

Influence of photonic crystal on Raman and SERS signal enhancement

Krajačić, Maria

Doctoral thesis / Doktorski rad

2024

Degree Grantor / Ustanova koja je dodijelila akademski / stručni stupanj: **University of Zagreb, Faculty of Science / Sveučilište u Zagrebu, Prirodoslovno-matematički fakultet**

Permanent link / Trajna poveznica: <https://um.nsk.hr/um:nbn:hr:217:252404>

Rights / Prava: [In copyright](#)/[Zaštićeno autorskim pravom.](#)

Download date / Datum preuzimanja: **2025-03-29**



Repository / Repozitorij:

[Repository of the Faculty of Science - University of Zagreb](#)





UNIVERSITY OF ZAGREB
FACULTY OF SCIENCE
DEPARTMENT OF PHYSICS

Maria Krajačić

**INFLUENCE OF PHOTONIC CRYSTAL
ON RAMAN AND SERS SIGNAL
ENHANCEMENT**

DOCTORAL THESIS

Zagreb, 2024



UNIVERSITY OF ZAGREB
FACULTY OF SCIENCE
DEPARTMENT OF PHYSICS

Maria Krajačić

**INFLUENCE OF PHOTONIC CRYSTAL
ON RAMAN AND SERS SIGNAL
ENHANCEMENT**

DOCTORAL THESIS

Supervisor:
Asst. Prof. Marko Škrabić

Zagreb, 2024.



SVEUČILIŠTE U ZAGREBU
PRIRODOSLOVNO-MATEMATIČKI FAKULTET
FIZIČKI ODSJEK

Maria Krajačić

UTJECAJ FOTONIČKOG KRISTALA NA POJAČANJE RAMAN I SERS SIGNALA

DOKTORSKI RAD

Mentor:
Doc.dr.sc. Marko Škrabić

Zagreb, 2024

To Dr. David Paul Mabwa

*who taught me that genuine friendship goes beyond earthly
dimensions*

*I always thought you were the best, I guess I always will,
I always felt that we were blessed, and I feel that way still.*

*Through every joy and tear I'd shared, you were my shining light,
In stormy times and in the rain, you'd made my world so bright.*

*With every smile and every cheer, our friendship always grew,
If I had only one friend left, I'd want it to be you.*

And remember, I am with you always, to the end of the age.

(Matthew 28:20)

Acknowledgements

First and foremost, I want to thank my supervisor, Asst.Prof. Marko Škrabić. Your dedication to my professional growth, profound knowledge, guidance and exceptional support have been crucial on this journey. I was incredibly lucky to have such an amazing mentor. Thank you for your patience and constant encouragement.

My sincere thanks go to Dr. Nikola Baran, Ana Medić, Dr. Lara Mikac, and Dr. Tanja Jurkin from Ruđer Bošković Institute for helping me with the instrumentation and measurements. A special thank you to Prof. Mile Ivanda, Head of the Laboratory for Molecular Physics and Synthesis of New Materials, for allowing me to access the laboratory instruments and facilities. Your support in securing project funding and acquiring necessary equipment has also been essential for my work. Finally, thank you for your valuable advice and insightful discussions.

I am particularly grateful to all members of the Department of Physics and Biophysics at the School of Medicine, especially to the Knopersići gang. Thank you for taking over my teaching classes whenever I needed to focus on my research and for the friendly atmosphere at work.

I also want to say thank you to Prof. Ivana Vinković Vrček, Prof. Hrvoje Buljan, and Asst.Prof. Vedran Đerek who were always available and willing to assist me when I needed help.

My sincere thanks goes to my best friend Marija. Thank you for your unwavering support, for making me laugh so many times, and for being my therapist in times of crisis. Your friendship means so much to me.

I extend my appreciation to Igor. You have been more like a family for the past few years. Thank you for being a voice of a common sense when I felt like losing mine, for numerous advices and for always being there.

Special thanks goes to my favourite people - David, Florence, Paul, Mary, Simon and Isaac. Thank you for your love, for encouragement, for prayers, laughter and support. You've been my inspiration and motivation.

*For all those times you stood by me, for all the truth that you made me see, for all the joy you brought to my life, for all the wrong that you made right, for every dream you made come true, for all the love I found in you, I'll be forever thankful. **

Finally, my deepest gratitude goes to my Family. Thank you for your unconditional love and support. Thank you for believing in me even when I didn't believe in myself, thank you for countless words of encouragement and even professional help. Thank you for being my biggest fans and my best friends.

You gave me wings and made me fly, you touched my hand, I could touch the sky. I lost my faith, you gave it back to me, you said no star was out of reach. You stood by me, and I stood tall, I had your love, I had it all...

*I'm everything I am because you loved me **

**(C. Dion, Because You Loved Me)*

Abstract

Photonic crystals are periodic dielectric structures that enable control and manipulation of light propagation, making them highly attractive for various optical applications. A central feature of photonic crystals is the photonic bandgap, which not only forbids the propagation of certain wavelengths but also decreases group velocity and modifies the density of states at the photonic bandgap edges. By careful design and optimization of various parameters, photonic crystals with desired optical properties can be created, leading to enhanced light-matter interactions.

This research demonstrates that the density of states increases while group velocity decreases at the high- and low-frequency edges of the photonic bandgap, enhancing light-matter interactions and thereby increasing the Raman scattering rate. Precise tuning of the photonic bandgap relative to the laser excitation wavelength is crucial for optimizing the enhancement conditions. Additionally, the integration of photonic crystals with metallic nanoparticles utilizes the strong localized electromagnetic fields generated by the nanoparticles to achieve even greater signal amplification.

Experimental results confirmed that photonic crystals enhance both Raman and SERS signals and showed that the alignment between the laser excitation and the photonic bandgap is crucial for achieving optimal enhancement, with the best results obtained at the photonic bandgap edges. This specific alignment intensifies the light-matter interaction due to the reduced group velocity of light and an increased local density of optical states.

Overall, this thesis offers a detailed analysis of how photonic crystals can enhance Raman and SERS signals, providing valuable insights for developing advanced optical sensors and analytical devices. The findings highlight the importance of photonic crystal design in achieving optimal enhancement conditions and offer guidelines for future research and applications in nanophotonics, biosensing, and material science.

KEYWORDS: photonic crystal, photonic bandgap, porous silicon, Raman scattering, surface-enhanced Raman scattering, signal enhancement

Prošireni sažetak

Fotonički kristali su periodične dielektrične strukture koje omogućuju kontrolu i manipulaciju širenja svjetlosti, što ih čini vrlo privlačnima za različite optičke primjene. Ključni pojam vezan uz fotoničke kristale je energetski zabranjeni pojas za fotone. Energetski zabranjeni pojas je spektralni raspon unutar kojeg je propagacija određenih valnih duljina svjetlosti zabranjena. Pažljivim dizajniranjem i optimizacijom različitih parametara je moguće kreirati strukture sa željenim optičkim svojstvima, koje omogućuju pojačanje interakcije između svjetlosti i materijala. Upravo zbog ovih jedinstvenih svojstava, fotonički kristali su postali ključne komponente u raznim optičkim primjenama, uključujući razvoj fotoničkih sklopova, visokoučinkovitih senzora i tehnologija za pojačanje optičkih signala.

No, osim što sprječava širenje određenih valnih duljina kroz fotoničku strukturu, zabranjeni pojas značajno utječe i na druge optičke karakteristike kao što su grupna brzina svjetlosti i gustoća optičkih stanja. Na rubovima zabranjenog pojasa dolazi do smanjenja grupne brzine svjetlosti i povećanja gustoće optičkih stanja, što rezultira pojačanom interakcijom svjetlosti i materije. Ova svojstva su od presudne važnosti za optimizaciju spektroskopskih tehnika, poput Ramanovog raspršenja i površinski pojačanog Ramanovog raspršenja, koje se oslanjaju na snažne interakcije svjetlosti i materije kako bi postigle visoku osjetljivost i preciznost.

Ovo istraživanje bavi se ulogom fotoničkih kristala u pojačanju Raman i SERS signala, s posebnim naglaskom na pažljivo dizajniranje i optimizaciju karakteristika fotoničkog zabranjenog pojasa u odnosu na valnu duljinu laserskog pobuđivanja. U istraživanju su primarno korišteni fotonički kristali izrađeni od poroznog silicija, koji su odabrani zbog svoje jednostavne izrade, mogućnosti podešavanja optičkih svojstava te kompatibilnosti sa silicijskom tehnologijom. Tip fotoničkih kristala koji su se koristili u ovom radu su tzv. naborani filtri (eng. *rugate filter*), koji su karakteristični po sinusoidnoj varijaciji indeksa loma. Takav profil fotoničkog kristala omogućuje stvaranje visoko-podesivih fotoničkih zabranjenih pojasa, čime se dodatno povećava njihova primjenjivost u različitim optičkim uređajima.

Jedan od ključnih aspekata ovog istraživanja bila je sustavna izrada uzoraka fotoničkih kristala od poroznog silicija. Uzorci su sortirani u šest različitih kategorija, pri čemu je svaka kategorija imala različiti položaj zabranjenog energetskog pojasa za fotone. Pripremljeni fotonički kristali zatim su uranjeni u otopinu probne molekule (metil ljubičasta 10B), te su snimljeni Raman spektri. U drugom dijelu istraživanja su fotonički kristali prekriveni zlatnim nanočesticama kako bi se dobila SERS podloga, a Rodamin 6G je korišten kao probna molekula. U oba

eksperimenta probna molekula se nalazila na površini uzoraka, ali je i djelomično ispunjavala unutrašnjost poroznog sloja, odnosno fotoničkih kristala. Dodatno, uz karakteristične vrpce probnih molekula, dobiveni Raman i SERS spektri također su sadržavali i vrpcu silicija na $\sim 520 \text{ cm}^{-1}$.

Cilj istraživanja bio je istražiti kako relativno pozicioniranje energetski zabranjenog pojasa za fotone u odnosu na valnu duljinu laserske pobude utječe na pojačanje Raman i SERS signala. Eksperimentalni rezultati pokazali su da poravnavanje laserske pobude s rubovima energetski zabranjenog pojasa dovodi do povećanja Ramanovog raspršenja, što se može pripisati smanjenju grupne brzine svjetlosti i odgovarajućem povećanju gustoće optičkih stanja u tom području. Precizno usklađivanje relativnog položaja između zabranjenog pojasa i laserske pobude omogućuje snažniju interakciju svjetlosti i materije, čime se pojačava Ramanov signal, a samim time i točnost i osjetljivost mjerenja.

Dodatno, korištenje SERS podloga baziranih na fotoničkim kristalima pokazalo je da uz lokalno značajno pojačano elektromagnetsko polje koje generiraju nanočestice, postoji i dodatno pojačanje signala od fotoničke strukture. Kombinacija fotoničkih kristala i metalnih nanočestica omogućuje dodatno poboljšanje osjetljivosti senzora, što je od velike važnosti za primjene u detekciji niskih koncentracija molekula, biosenzorici i drugim područjima u kojima je potrebno precizno mjerenje.

Međutim, iako su rezultati jasno pokazali da fotonički kristali mogu pojačati Raman i SERS signale, istraživanje je također naglasilo važnost relativnog poravnavanja laserske pobude i energetski zabranjenog pojasa za fotone. Najbolji rezultati pojačanja postignuti su u slučaju preklapanja lasera s rubovima zabranjenog pojasa, čime je potvrđena ključna uloga podešavanja položaja energetski zabranjenog pojasa tijekom procesa optimizacije uvjeta za pojačanje signala. Također, SERS signali su pokazali nešto veću varijabilnost u usporedbi s Raman signalima, što je vjerojatno posljedica složenije prirode mehanizma pojačanja kod SERSa. Faktori kao što su distribucija tzv. vrućih točaka (eng. *hotspots*) i adsorpcija probnih molekula dodatno doprinose ovoj varijabilnosti, naglašavajući potrebu za sustavnom kontrolom pripreme uzoraka i eksperimentalnih uvjeta.

Iako su rezultati dobiveni u ovom radu obećavajući, postoji prostor za daljnja istraživanja koja bi mogla pružiti još detaljniji uvid u utjecaj fotoničkih struktura na pojačanje Raman i SERS signala. Na temelju sadašnjih saznanja, buduća istraživanja mogla bi se usmjeriti na proširenje skupa uzoraka i optimizaciju eksperimentalnih protokola. Također, dodatna analiza utjecaja fotoničkih kristala različitih geometrija te dubine okupiranosti probnim molekulama na

intenzitet Raman i SERS signala mogla bi doprinijeti daljnjim poboljšanjima u dizajnu i primjeni ovih struktura.

Ova disertacija pruža detaljnu analizu potencijala fotoničkih kristala za pojačanje Raman i SERS signala, nudeći vrijedne uvide za razvoj naprednih optičkih senzora. Rezultati također daju praktične smjernice za buduća istraživanja usmjerena na daljnju optimizaciju tehnika pojačanja temeljenih na fotoničkim kristalima i istraživanje njihovih primjena u različitim znanstvenim i industrijskim domenama. Očekuje se da će daljnja istraživanja na ovom polju omogućiti razvoj novih tehnologija i uređaja koji će imati široku primjenu u naprednim optičkim sustavima i analitičkoj znanosti.

Disertacija je podijeljena u sedam poglavlja. Prvo poglavlje uvodi osnovne principe Ramanove spektroskopije, dok se drugo poglavlje fokusira na temeljne aspekte fotoničkih kristala, uključujući elektromagnetski opis fotoničkih kristala, formiranje energetski zabranjenog pojasa za fotone, te specifičnosti vezane uz zabranjeni pojas kao što su smanjena grupna brzina svjetlosti ili povećana gustoća optičkih stanja na njegovim rubovima. Treće poglavlje obrađuje izradu poroznog silicija i njegove optičke karakteristike, dok se četvrto poglavlje odnosi na pojačanje Ramanovog signala preko površinski pojačanog Ramanovog raspršenja i pomoću fotoničkih kristala. Peto poglavlje pruža pregled dosadašnjih istraživanja u području, dok šesto poglavlje opisuje materijale i metode korištene u eksperimentima. Sedmo poglavlje donosi rezultate i detaljnu diskusiju, uključujući usporedbu Raman i SERS signala te analizu utjecaja fotoničkih kristala na njihovo pojačanje.

KLJUČNE RIJEČI: fotonički kristal, fotonički zabranjeni pojas, porozni silicij, Ramanovo raspršenje, površinski pojačano Ramanovo raspršenje, pojačanje signala

List of abbreviations

EM - electromagnetic	1
PhC - photonic crystal	9
PBG - photonic bandgap	16
DOS - density of states	22
LDOS - local density of states.....	23
RF - rugate filter	34
cSi - crystal silicon	39
EtOH - ethanol	39
HF - hydrofluoric acid.....	39
pSi - porous silicon.....	39
pSi PhC - porous silicon photonic crystal	44
SERS - surface-enhanced Raman scattering	47
LSPR - localized surface plasmon resonance	48
EF - enhancement factor	58
NIR - near-infrared.....	64
SRS - stimulated Raman scattering	67
HAuCl ₄ - chloroauric acid	76
MQ - ultrapure Milique water	76
UV-Vis-NIR - ultraviolet-visible-near infrared	76
SEM - scanning electron microscope.....	77
EDS - energy-dispersive X-ray spectroscopy	78
CV - crystal violet	82
R6G - Rhodamine 6G.....	82
FWHM - full width at half maximum	88

Contents

Abstract.....	I
Prošireni sažetak	II
List of abbreviations.....	V
Contents.....	VI
Chapter 1. Raman spectroscopy	1
1.1 Classical description of Raman scattering	2
1.2 Quantum description of Raman scattering	4
1.3 Semi-classical description of Raman scattering.....	6
Chapter 2. Photonic crystals.....	9
2.1 Electromagnetic description of photonic crystals.....	10
2.2 Variational principle	15
2.3 Photonic bandgap	16
2.4 Group velocity.....	19
2.5 Density of states	22
2.6 Evanescent modes	27
2.7 One-dimensional PhCs	28
2.8 Rugate filters	34
Chapter 3. Porous silicon	39
3.1 Fabrication of porous silicon	39
3.2 Porous silicon photonic crystals	44
Chapter 4. Raman signal enhancement.....	47
4.1 Surface-enhanced Raman scattering	48
4.2 Photonic crystals as Raman and SERS signal enhancers	65
Chapter 5. Overview of the previous research	66
Chapter 6. Materials and Methods	70

6.1	Porous silicon photonic crystals fabrication	70
6.2	Deposition of gold nanoparticles on pSi and pSi PhC samples	76
6.3	UV-Vis-NIR spectroscopy	76
6.4	Scanning Electron Microscopy and Energy-Dispersive X-ray Spectroscopy	77
6.5	Raman spectroscopy	80
6.6	Probe molecules	82
6.7	Sample characterization conditions	83
Chapter 7.	Results and discussion.....	84
7.1	Porous silicon photonic crystals for Raman measurements	84
7.2	Raman signal.....	96
7.3	Gold-coated porous silicon photonic crystals for SERS measurements.....	130
7.4	SERS signal	135
Conclusion.....		150
Bibliography		155
Information about the supervisor		169
Curriculum vitae		170
List of publications		171

Chapter 1. Raman spectroscopy

In the right light, at the right time, everything is extraordinary.

(A. Rose)

Raman spectroscopy is a cornerstone technique in molecular analysis that offers insights into various materials' structural composition, chemical bonding, and vibrational dynamics. This fast and nondestructive analytical technique is an excellent tool with wide-ranging applications across numerous scientific disciplines, such as nanotechnology, biomedical research, forensics, pharmaceuticals, environmental science, etc.¹⁻³

The principle behind Raman spectroscopy lies in the interaction between monochromatic light and matter, i.e., between the incident electromagnetic (EM) radiation and molecular vibrations, phonons, or some other excitations in the system. When non-resonance radiation irradiates molecules, most of the incident light is elastically scattered (Rayleigh scattering), and energy and momentum are conserved. However, a small fraction ($1:10^8$) undergoes inelastic scattering, as predicted by Smekal in 1923 and a few years later experimentally shown by Raman^{4,5}, resulting in a frequency shift of an incident photon (Figure 1.1). These energy shifts are manifested as Raman bands in the Raman spectrum and provide a fingerprint-like signature of the molecular composition and structure, enabling precise identification and characterization of analytes. Raman spectrum has two contributions that arise from the vibrational transitions within molecules due to the interaction with light⁶. The first one is Stokes scattering, which occurs when incident light interacts with molecules and transfers energy to molecules to excite the molecule's vibrational modes. In this process, the molecule gains energy from the incident radiation, and as a result, the scattered light has slightly lower energy than the incident. Conversely, anti-Stokes scattering pertains to the case in which phonon is absorbed during the interaction, leading to energy transfer from the molecule to photons. Hence, the resulting EM radiation has higher energy than the incident. Since most molecules are usually in the ground state, the probability for Stokes scattering is much higher than for the anti-Stokes, so Stokes contribution is a dominant process and is, in most cases, more intense than the anti-Stokes.

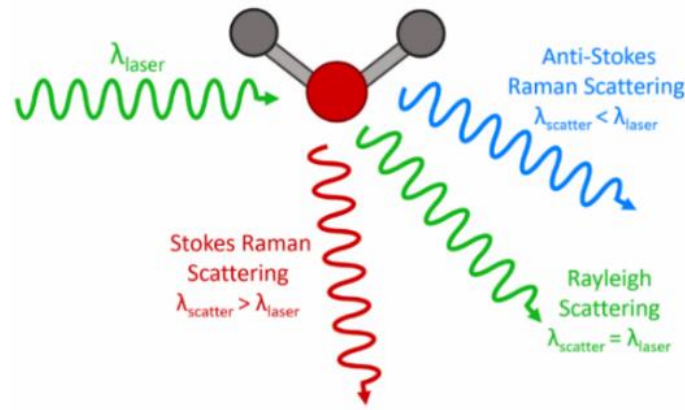


Figure 1.1 Illustration of scattering processes that occur in the interaction of light with a molecule⁷

1.1 Classical description of Raman scattering

The classical theory of Raman scattering, although not perfectly precise, gives a good basis for understanding the Raman effect^{6,8,9}. It was developed in the early 20th century by C.V. Raman, who was awarded a Nobel Prize in Physics in 1930 for his contribution. In this approach, both EM radiation and the molecule are treated classically.

When a molecule is placed into a static electric field, charges within the molecule separate, leading to the polarization of the molecule. The induced dipole moment $\vec{\mu}$ is proportional to the applied electric field \vec{E} , and the constant of proportionality is polarizability α , which can be understood as the molecule's susceptibility to distortion:

$$\vec{\mu} = \alpha \vec{E}. \quad (1.1)$$

When a molecule is subjected to an oscillating electric field of frequency ν_0 ,

$$\vec{E}(t) = \vec{E}_0 \cos(2\pi\nu_0 t) = \vec{E}_0 \cos(\omega_0 t), \quad (1.2)$$

the dipole moment of the molecule undergoes oscillations with the same frequency:

$$\vec{\mu}(t) = \alpha \vec{E}_0 \cos(2\pi\nu_0 t) = \vec{\mu}_0 \cos(\omega_0 t). \quad (1.3)$$

In this case, the molecule emits radiation of the same frequency as the incident excitation, and the whole process is called Rayleigh scattering.

In a more realistic case, when a molecule is not isotropic, the magnitude of the induced dipole moment varies across different directions, meaning that the polarizability α is not a pure scalar but a tensor quantity:

$$\alpha = \begin{pmatrix} \alpha_{xx} & \alpha_{xy} & \alpha_{xz} \\ \alpha_{yx} & \alpha_{yy} & \alpha_{yz} \\ \alpha_{zx} & \alpha_{zy} & \alpha_{zz} \end{pmatrix}. \quad (1.4)$$

In this notation, α_{ij} represents the component of the dipole moment induced in the direction i by an electric field in the direction j . The induced dipole moment can now be written as:

$$\mu_i = \sum \alpha_{ij} E_j. \quad (1.5)$$

It is important to note that polarizability is not a constant quantity. Instead, it depends on the thermal oscillations of atoms around their equilibrium positions, which allows us to expand it in Taylor series with respect to the normal coordinates of vibration

$$\alpha_{ij} = (\alpha_{ij})_0 + \sum_k \left(\frac{\partial \alpha_{ij}}{\partial Q_k} \right)_0 Q_k + \frac{1}{2} \sum_{kl} \left(\frac{\partial^2 \alpha_{ij}}{\partial Q_k \partial Q_l} \right)_0 Q_k Q_l + \dots \quad (1.6)$$

where $(\alpha_{ij})_0$ represents the value of α_{ij} in the equilibrium and $Q_{k,l}$ are normal coordinates of vibration associated with molecular vibration frequency $\omega_{k,l}$. In the case of small displacements from the equilibrium position, the harmonic approximation can be made to simplify calculations. The approximation allows neglecting all terms with powers of Q higher than one:

$$\alpha_k = \alpha_0 + \left(\frac{\partial \alpha}{\partial Q_k} \right)_0 Q_k \quad (1.7)$$

where the second term is called Raman tensor. Under the same (harmonic) assumption, time-dependent normal coordinates are given by:

$$Q_k = Q_{k_0} \cos(\omega_k t) \quad (1.8)$$

where Q_{k_0} is the amplitude of the normal coordinate. By combining expressions for polarization tensor (1.7) and electric field (1.2), the induced dipole moment can be written as follows:

$$\vec{\mu}(t) = \alpha_0 \vec{E}_0 \cos(\omega_0 t) + \left(\frac{\partial \alpha}{\partial Q_k} \right)_0 Q_{k_0} \cos(\omega_k t) \vec{E}_0 \cos(\omega_0 t) \quad (1.9)$$

With the help of trigonometry, the final expression becomes:

$$\begin{aligned} \vec{\mu}(t) &= \alpha_0 \vec{E}_0 \cos(\omega_0 t) \\ &+ \frac{1}{2} Q_{k_0} \vec{E}_0 \left(\frac{\partial \alpha}{\partial Q_k} \right)_0 [\cos(\omega_k + \omega_0)t + \cos(\omega_k - \omega_0)t] \end{aligned} \quad (1.10)$$

A closer look indicates that each term in equation (1.10) has a different frequency:

- frequency ω_0 in the first term corresponds to the Rayleigh scattering since the radiation frequency is the same as that of incident light
- the second and the third term show frequency shifts $\omega_k + \omega_0$ and $\omega_k - \omega_0$ that correspond to inelastic scattering, i.e., anti-Stokes and Stokes components, respectively. These frequency-shifted bands are symmetric around the Rayleigh band.

The intensity of Raman bands is proportional to the square of the induced dipole moment, which implies:

$$I \sim \left(\vec{E}_0 \left(\frac{\partial \alpha}{\partial Q_k} \right)_0 \right)^2 \quad (1.11)$$

Equation (1.11) indicates that the Raman active modes are those that cause the change of polarizability of the molecule, which means that condition $\left(\frac{\partial \alpha}{\partial Q_k} \right)_0 \neq 0$ leads to selection rules for Raman scattering^{6,10}. Moreover, the stronger the incident electric field vector, the stronger the Raman signal.

However, equation (1.11) also suggests that the intensity of Raman lines is proportional to the magnitude of $\left(\frac{\partial \alpha}{\partial Q_k} \right)_0$, and implies that the intensity of Stokes and anti-Stokes lines is the same.

This, however, is incorrect, as will be shown in the next section.

1.2 Quantum description of Raman scattering

Quantum theory offers a more detailed and accurate description of Raman scattering, characterizing the energy states and the transitions between them as quantized. Quantization means that electronic, vibrational, and rotational states have discrete values, and hence, transitions between the states can occur only if the excitation wavelength matches the energy difference between them.

In the quantum framework, Raman scattering can be understood as a two-photon process initiated by the interaction of an incident photon and a molecule. In this process, a molecule is excited from an initial state to an energetically higher *virtual* state. The virtual state is not an eigenstate of a molecular Hamiltonian, so it is not a real or stable state, meaning that the molecule almost immediately “emits” a photon and transitions to a real vibrational state. If the molecule returns to the original vibrational state $|\psi_i\rangle$, the scattered photon has the same energy

as incident one, resulting in Rayleigh scattering. However, in some cases, a molecule relaxes to a different vibrational state $|\psi_f\rangle$. The energy difference between the initial and final state is compensated by an energy difference between the incident and scattered photon. If the final vibrational state of the molecule is higher than the initial one, the scattered photon will have less energy than the incident one, and Stokes lines will be observed. Conversely, if the frequency of the scattered photon is higher than that of the initial one, the final state of the molecule will be lower in energy than the initial one, and anti-Stokes lines will be observed. Since most molecules are initially in the ground and not in the excited state, Stokes scattering is, at room temperature, more probable than anti-Stokes. Consequently, the intensity of Stokes lines will be higher than that of the anti-Stokes. The diagram of the different types of light scattering, together with the corresponding energy transitions and spectral shifts associated with the Raman process, is given in Figure 1.2, while a more rigorous mathematical explanation can be found in^{6,10,11}.

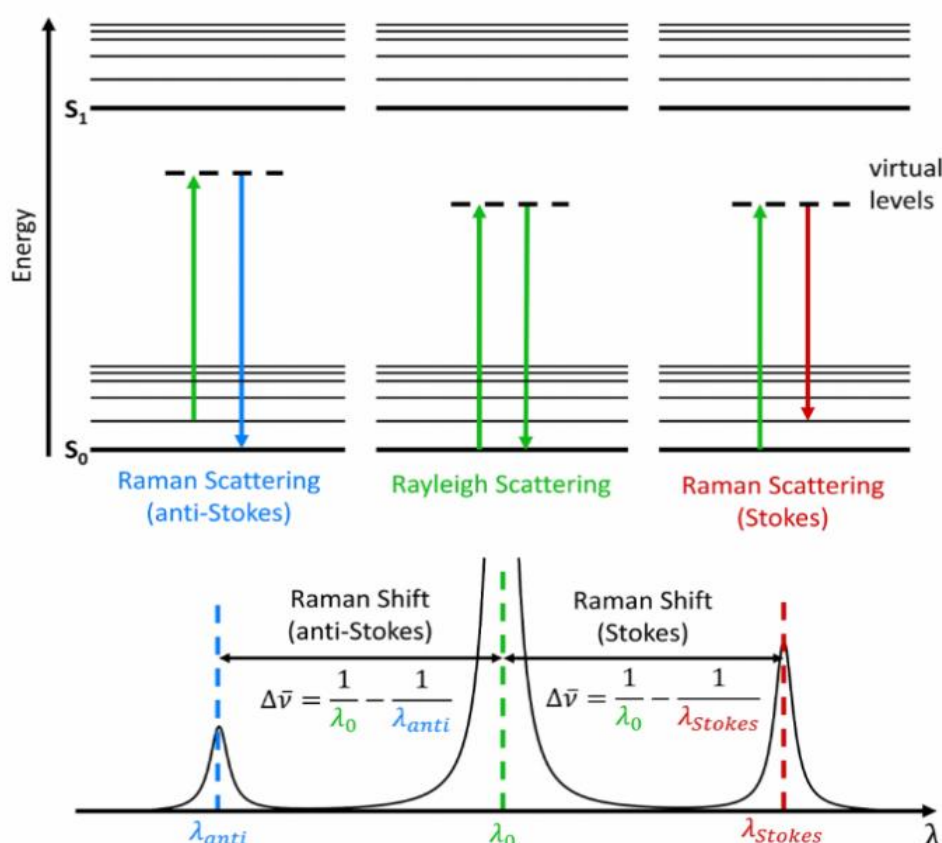


Figure 1.2 Jablonski diagram showing the origin of Rayleigh, Stokes, and anti-Stokes Raman scattering. Stokes and anti-Stokes scattering appear at higher and lower wavelengths than the incident⁷

1.3 Semi-classical description of Raman scattering

A semiclassical approach in which the electric field is treated classically, whereas a molecule is considered as a quantum-mechanical system, will be used to further analyze the Raman effect¹². As mentioned earlier, the interaction between the applied electric field

$$\vec{E} = \vec{E}_0 \cos(\omega t) \quad (1.12)$$

and a molecule induces a dipole moment that emits a secondary photon. Therefore, transitions between the states of the molecule have to be found, which can be done from

$$\mu_{i,f}(t) = \langle \psi_i | \alpha | \psi_f \rangle \quad (1.13)$$

where $|\psi_i\rangle$ and $|\psi_f\rangle$ are wavefunctions of the initial and final vibrational states, α is the polarizability tensor, and $\mu_{i,f}$ is transition dipole moment.

In this approach normal modes can be found by solving the time-dependent Schrödinger equation in which the interaction between the electric field and the dipole is treated as a small perturbation to the system:

$$\hat{H}' = -\mu \cdot E_0 \cos(\omega t) \quad (1.14)$$

The solution leads to the ratio of intensities between the Stokes and anti-Stokes scattering

$$\frac{I_{Stokes}}{I_{anti-Stokes}} = \frac{(\omega - \omega_k)^4}{(\omega + \omega_k)^4} \cdot e^{\beta \hbar \omega_k} \quad (1.15)$$

where $\beta = (k_B T)^{-1}$, with Boltzmann factor k_B and absolute temperature T , whereas ω and ω_k are an incident electric field and phonon frequencies, respectively. A key finding is that the intensities of Raman scattering are proportional to the fourth power of the incident EM radiation frequency. Furthermore, the ratio of Stokes to anti-Stokes intensities reflects ground and excited state populations, which follow the Bose-Einstein distribution. Since the ground state is usually more populated than higher excited states, Stokes scattering is more probable, resulting in approximately an order of magnitude more intense Stokes lines than the anti-Stokes. However, it is important to mention that this statement holds true for Raman shifts above $\sim 200 \text{ cm}^{-1}$, since the energy difference between the vibrational states is relatively small for those bands. At room temperature, the thermal energy $k_B T$ is $\sim 200 \text{ cm}^{-1}$ which makes it comparable to the vibrational energy for such small shifts. As a result, there is a more balanced population

between the ground and excited states for Raman shifts below 200 cm^{-1} , leading to smaller differences in intensity between Stokes and anti-Stokes lines.

In contrast, for larger Raman shifts (above 200 cm^{-1}), the energy difference ΔE becomes significantly larger than the available thermal energy at room temperature. According to the Bose-Einstein statistics, the population of molecules in the first excited state drops exponentially at high energies. Thus, for larger Raman shifts, almost all molecules are in the ground state, and very few are in excited states. This leads to a much larger probability of Stokes scattering (where molecules are excited from the ground state) compared to anti-Stokes scattering (which requires molecules to be initially in excited states). Consequently, the Stokes lines become significantly more intense than the anti-Stokes lines for Raman shifts above 200 cm^{-1} .

The process of Raman scattering can also be described using a differential scattering cross-section^{13,14}, which gives the probability of scattering into a particular solid angle. It is directly proportional to the Raman tensor (or Raman susceptibility tensor):

$$\frac{d\sigma}{d\Omega} \propto |\vec{e}_s \cdot \chi^{(2)} \cdot \vec{e}_i|^2 \quad (1.16)$$

In this equation, \vec{e}_i and \vec{e}_s unit vectors that represent the polarization of the incident and scattered light, respectively, while $\chi^{(2)}$ represents Raman susceptibility tensor. The Raman tensor is a mathematical tool that helps understand how effectively a molecule can undergo Raman scattering and is a link between the macroscopic Raman scattering and microscopic change of polarizability due to molecular vibrations and quantum transitions between the states, where $\chi^{(2)} \propto \left(\frac{\partial\alpha}{\partial Q_k}\right)$.

After rigorous mathematical derivations, the expressions for differential scattering cross section for Stokes and anti-Stokes scattering are given by:

$$\frac{d\sigma_s}{d\Omega} = \frac{\omega_s^4}{(4\pi\epsilon_0)^2 c^4} \left| \vec{e}_s \cdot \left(\frac{\partial\alpha}{\partial Q_k}\right) \cdot \vec{e}_i \right|^2 \frac{\hbar}{2\omega_v} (n+1) \quad (1.17)$$

$$\frac{d\sigma_a}{d\Omega} = \frac{\omega_s^4}{(4\pi\epsilon_0)^2 c^4} \left| \vec{e}_s \cdot \left(\frac{\partial\alpha}{\partial Q_k^*}\right) \cdot \vec{e}_i \right|^2 \frac{\hbar}{2\omega_v} n, \quad (1.18)$$

where ω_v represents the vibrational frequency of the mode, \hbar is reduced Planck's constant, n denotes the expected number of particles in a given vibrational state, ω_s is the frequency of the scattered photon, c is the speed of light, and the asterisk denotes the complex conjugate. From equation (1.16), it is clear that larger $\chi^{(2)}$ results in greater Raman scattering cross section and

consequently stronger intensity of Raman signal, that is, $I \propto |\chi^{(2)}|^2$. This relationship shows the importance of Raman susceptibility tensor in Raman scattering since it plays a crucial role in understanding the intensities of Raman lines and serves as a connection between the classical and quantum-mechanical description. It is an intrinsic property indicating the material's ability to undergo Raman scattering. From equations (1.17) and (1.18), it is clear that more populated states are included in Stokes scattering in which the cross-section is proportional to $(n + 1)$, while the cross-section in the case of anti-Stokes scattering is proportional n , resulting in more intense Stokes lines in the Raman spectrum.

Chapter 2. Photonic crystals

In the last few decades, an interest in controlling the optical properties of materials has rapidly increased, leading to the development of a new class of materials known as photonic crystals (PhCs). Photonic crystals are periodically structured materials that affect the motion of photons in a way similar to how ionic lattices affect the motion of electrons in solids^{15–17}. Seminal works of Yablonoitch and John^{18,19} in 1987, which investigated the creation and influence of photonic bandgap on light propagation within periodic structures, led to an increased interest in the field. Periodicity can be realized in one, two, or three dimensions (1D, 2D, or 3D PhCs), as shown in Figure 2.1, and is usually achieved by periodic variations of the material's index of refraction. Since the index of refraction and the geometry of the unit cell can be easily adjusted, various structures with a wide range of applications can be designed¹⁵.

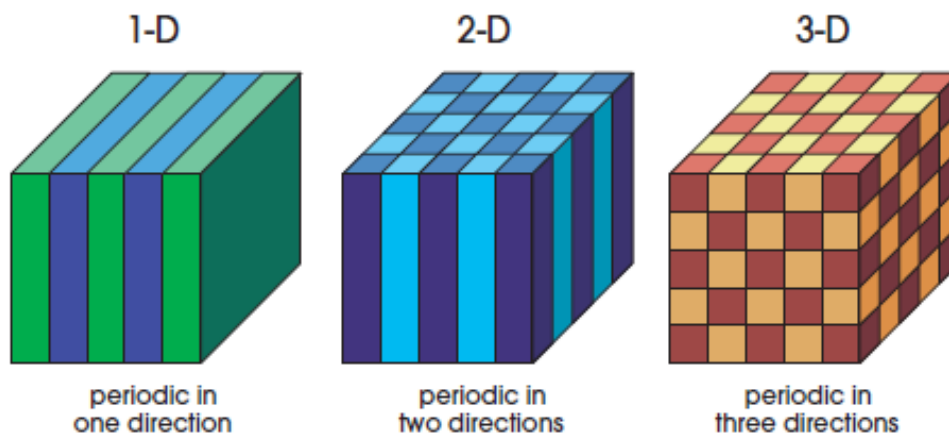


Figure 2.1 Illustration of 1D, 2D and 3D photonic crystal. Different colors represent materials with different dielectric functions¹⁵

It is well known that ionic lattices create the periodic potential that forms electronic band structures, confining electrons to specific energy levels¹⁶. Similarly, periodic variation of the material's dielectric function restricts the propagation of photons through the material to only certain energies. Frequency ranges that are not allowed are analog to bandgaps in electronic eigenstates and are called photonic bandgaps.

2.1 Electromagnetic description of photonic crystals

Physicists use the wave theory on Mondays, Wednesdays, and Fridays,

and the particle theory on Tuesdays, Thursdays, and Saturdays.

(Sir William Henry Bragg)

The behavior of light within photonic crystals can be described using Maxwell's equations^{15,16,20}:

$$\begin{aligned}\vec{\nabla} \cdot \vec{D} &= \rho & \vec{\nabla} \times \vec{E} + \frac{\partial \vec{B}}{\partial t} &= \vec{0} \\ \vec{\nabla} \cdot \vec{B} &= 0 & \vec{\nabla} \times \vec{H} - \frac{\partial \vec{D}}{\partial t} &= \vec{J}\end{aligned}\tag{2.1}$$

where \vec{E} and \vec{H} are macroscopic electric and magnetic fields, \vec{D} and \vec{B} are electric displacement and magnetic induction vectors, whereas ρ is free charge density and \vec{J} is the electric current density. In the case of macroscopic and isotropic material, electric displacement and magnetic induction vectors are given by constitutive relations:

$$\begin{aligned}\vec{D}(\vec{r}, \omega) &= \varepsilon_0 \varepsilon(\vec{r}, \omega) \vec{E}(\vec{r}, \omega) \\ \vec{B}(\vec{r}, \omega) &= \mu_0 \mu(\vec{r}, \omega) \vec{H}(\vec{r}, \omega)\end{aligned}\tag{2.2}$$

where ε and μ are permittivity and permeability of the medium and ε_0 and μ_0 are permittivity and permeability of the vacuum, respectively.

Generally, an electric displacement vector can be expressed as a power series expansion of an electric field. In terms of components:

$$D_i = \varepsilon_0 \sum_j \varepsilon_{ij} E_j + \varepsilon_0 \sum_{j,k} \chi_{ijk} E_j E_k + O(E^3)\tag{2.3}$$

The focus of this analysis is on a mixed dielectric medium that is characterized by regions of homogeneous dielectric material. However, due to the periodic arrangement of different materials, ε becomes a function of spatial coordinate, $\varepsilon = \varepsilon(\vec{r})$. Additionally, we consider the case in which there are no current sources or free charges within the material: $\rho = 0$, $\vec{J} = \vec{0}$. Moreover, for many dielectric materials, the following assumptions can be made¹⁵:

1. field intensities are sufficiently low, so the second and all higher-order terms in (2.3) can be neglected

2. explicit frequency dependence of a relative permittivity can be ignored; instead, we choose a value of the relative permittivity that is appropriate for the frequency range of the physical system
3. relative permittivity is a real and positive number, i.e., we focus on transparent materials.

Additionally, here, we do not work with magnetic materials, so we can assume $\mu(\vec{r}, \omega) \approx 1$. With all of the above assumptions, Maxwell's equations take the following form:

$$\vec{\nabla} \cdot [\varepsilon(\vec{r})\vec{E}(\vec{r}, t)] = 0 \quad \vec{\nabla} \times \vec{E}(\vec{r}, t) + \mu_0 \frac{\partial \vec{H}(\vec{r}, t)}{\partial t} = \vec{0} \quad (2.4)$$

$$\vec{\nabla} \cdot \vec{H}(\vec{r}, t) = 0 \quad \vec{\nabla} \times \vec{H}(\vec{r}, t) - \varepsilon_0 \varepsilon(\vec{r}) \frac{\partial \vec{E}(\vec{r}, t)}{\partial t} = \vec{0}$$

Since Maxwell's equations are linear, the solutions to these equations may be obtained by separating the spatial and temporal dependence :

$$\vec{E}(\vec{r}, t) = \vec{E}(\vec{r})e^{-i\omega t} = \vec{E}_0 e^{i\vec{k}\cdot\vec{r}} e^{-i\omega t} \quad (2.5)$$

$$\vec{H}(\vec{r}, t) = \vec{H}(\vec{r})e^{-i\omega t} = \vec{H}_0 e^{i\vec{k}\cdot\vec{r}} e^{-i\omega t} \quad (2.6)$$

By inserting equations (2.5) and (2.6) into divergence equations of (2.4), two conditions pertaining to the EM field are obtained: there are no point sources or sinks of electric and magnetic fields in the medium. Mathematically, this condition can be written as :

$$\vec{\nabla} \cdot [\vec{\varepsilon}(\vec{r})\vec{E}(\vec{r})] = 0 \quad (2.7)$$

$$\vec{\nabla} \cdot \vec{H}(\vec{r}) = 0 \quad (2.8)$$

Additionally :

$$\vec{\nabla} \cdot \vec{H}(\vec{r}) = \vec{\nabla} \cdot [\vec{H}_0 e^{i\vec{k}\cdot\vec{r}}] = 0 \quad (2.9)$$

which implies that $\vec{H}_0 \cdot \vec{k} = 0$. The analogous expression can be derived for the electric field, indicating that EM waves are transverse.

Curl equations, on the other side, say that :

$$\vec{\nabla} \times \vec{E}(\vec{r}) = i\omega\mu_0\vec{H}(\vec{r}) \quad (2.10)$$

$$\vec{\nabla} \times \vec{H}(\vec{r}) = -i\omega\varepsilon_0\varepsilon(\vec{r})\vec{E}(\vec{r}) \quad (2.11)$$

Decoupling these equations results in obtaining a master equation that describes the propagation of EM waves in a photonic crystal:

$$\vec{\nabla} \times \left(\frac{1}{\varepsilon(\vec{r})} \vec{\nabla} \times \vec{H}(\vec{r}) \right) = \left(\frac{\omega}{c} \right)^2 \vec{H}(\vec{r}) \quad (2.12)$$

where $c = \frac{1}{\sqrt{\mu_0 \varepsilon_0}}$ is the speed of light, and the relative permittivity has a periodic distribution, $\varepsilon(\vec{r}) = \varepsilon(\vec{r} + \vec{a})$, where \vec{a} is the lattice constant vector of a photonic crystal.

Similarly, it is possible to obtain an equation for the electric field :

$$\frac{1}{\varepsilon(\vec{r})} \vec{\nabla} \times (\vec{\nabla} \times \vec{E}(\vec{r})) = \left(\frac{\omega}{c} \right)^2 \vec{E}(\vec{r}) \quad (2.13)$$

Both equations, (2.12) and (2.13), can be written as an eigenvalue problem

$$\hat{\theta} \vec{H}(\vec{r}) = \left(\frac{\omega}{c} \right)^2 \vec{H}(\vec{r}) \quad (2.14)$$

$$\hat{\mathcal{E}} \vec{E}(\vec{r}) = \left(\frac{\omega}{c} \right)^2 \vec{E}(\vec{r}) \quad (2.15)$$

where $\vec{H}(\vec{r})$ and $\vec{E}(\vec{r})$ represent eigenfunctions, $\left(\frac{\omega}{c} \right)^2$ are the eigenvalues of the corresponding problem, while $\hat{\theta}$ and $\hat{\mathcal{E}}$ are the differential operators defined as:

$$\hat{\theta} = \vec{\nabla} \times \left(\frac{1}{\varepsilon(\vec{r})} \vec{\nabla} \times \right) \quad (2.16)$$

$$\hat{\mathcal{E}} = \frac{1}{\varepsilon(\vec{r})} \vec{\nabla} \times (\vec{\nabla} \times) . \quad (2.17)$$

Equations (2.14) and (2.15), together with (2.7) and (2.8), give all information about the magnetic and electric fields and lead to identical solutions. However, there is an important difference between the differential operators given by (2.16) and (2.17): the operator $\hat{\theta}$ is linear and Hermitian. Linearity ensures that if $\vec{H}_1(\vec{r})$ and $\vec{H}_2(\vec{r})$ are solutions of (2.14), then any linear combination of $\vec{H}_1(\vec{r})$ and $\vec{H}_2(\vec{r})$ is also a solution to the problem, which is important for finding more complex solutions from simpler ones. Hermiticity leads to two important results: firstly, the eigenvalues ω^2 must be real, which is important since they correspond to physically observable frequencies of the photonic modes; secondly, any two harmonic modes with different frequencies must be orthogonal, which means that EM waves in periodic structures exist only as discrete modes, and this orthogonality is precisely what we observe in Bloch modes within periodic structures.

The solutions of equations (2.14) and (2.15) give the allowed frequencies ω for different wavevectors k resulting in an infinite series of modes with discretely spaced frequencies $\omega_n(k)$.

All $\omega_n(k)$ create photonic band structure of a periodic dielectric configuration known as a dispersion relation. Figure 2.2a illustrates the first three branches of a dispersion relation for a 1D photonic crystal, while Figure 2.2b represents the dispersion relation for a 3D photonic structure. The regions where no eigenvalues exist correspond to photonic bandgaps, indicating that light with these frequencies cannot propagate through the photonic crystal.

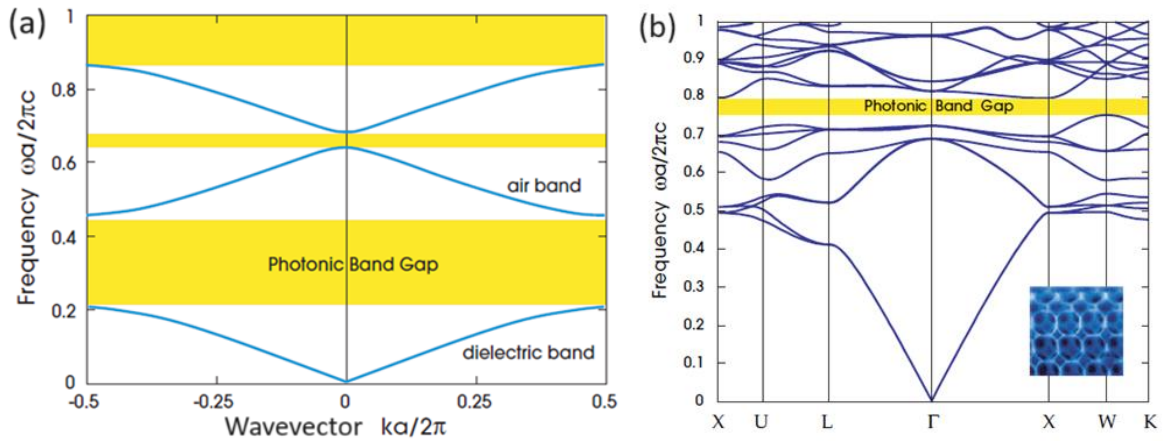


Figure 2.2 The photonic band structure of a) multilayer structure with lattice constant a b) 3D photonic structure¹⁵

The above eigenvalue problem is analogous to the well-known time-independent Schrödinger equation, $\hat{H}\psi(\vec{r}) = E\psi(\vec{r})$, which means that principles and results from quantum mechanics can be applied to problems related to the propagation of photons in photonic crystals. The analogy between physical quantities in the electrodynamic approach to solving the problem of light propagation in photonic crystals and in quantum mechanics is given in Table 2.1.

Table 2.1 The analogy between physical quantities in the electrodynamic approach to solving the problem of light propagation in photonic crystals and quantum mechanics²¹

EM in a periodic medium		QM in a periodic potential	
The magnetic and electric field vectors	$\vec{H}(\vec{r}, t) = \vec{H}(\vec{r})e^{-i\omega t}$ $\vec{E}(\vec{r}, t) = \vec{E}(\vec{r})e^{-i\omega t}$	The scalar wave function	$\psi(\vec{r}, t) = \psi(\vec{r})e^{-i\omega t}$
Master equations	$\hat{\theta}\vec{H}(\vec{r}) = \left(\frac{\omega}{c}\right)^2 \vec{H}(\vec{r})$ $\hat{\varepsilon}\vec{E}(\vec{r}) = \left(\frac{\omega}{c}\right)^2 \vec{E}(\vec{r})$	The Schrödinger equation	$\hat{H}\psi(\vec{r}) = E\psi(\vec{r})$
Periodic relative permittivity*	$\varepsilon(\vec{r}) = \varepsilon(\vec{r} + \vec{a})$	Periodic potential*	$V(\vec{r}) = V(\vec{r} + \vec{a})$
Bloch theorem*	$\vec{H}_k(\vec{r}) = \vec{H}_k e^{i\vec{k}\cdot\vec{r}}$ $\vec{H}_k(\vec{r}) = \vec{H}_k(\vec{r} + \vec{a})$ $\vec{E}(\vec{r}) = \vec{E}_k e^{i\vec{k}\cdot\vec{r}}$ $\vec{E}_k(\vec{r}) = \vec{E}_k(\vec{r} + \vec{a})$	Bloch theorem*	$\psi_k(\vec{r}) = u_k e^{i\vec{k}\cdot\vec{r}}$ $u_k(\vec{r}) = u_k(\vec{r} + \vec{a})$
The allowed values of \vec{k} lie in Brillouin zone		The allowed values of \vec{k} lie in Brillouin zone	
Frequencies of allowed harmonic modes are given by $\omega_n(k)$		Frequencies of allowed harmonic modes are given by $E_n(k)$	

*for lattice constant \vec{a}

As mentioned earlier, solving Maxwell's equations with the periodic boundary conditions imposed by the periodic structure gives the dispersion relation, which describes how frequency ω of EM waves varies with the wavevector \vec{k} , and is crucial for understanding the propagation characteristics of light within the photonic crystal. Figure 2.2 depicts the dispersion relation within the first Brillouin zone, which is the fundamental region of the reciprocal space in which the wavevector \vec{k} lies. In a one-dimensional photonic crystal, the first Brillouin zone extends from $-\frac{\pi}{a}$ to $+\frac{\pi}{a}$, where a is the lattice constant. The band structure is periodic in the reciprocal space, and the photonic bandgaps appear at the edges of the Brillouin zone.

For a three-dimensional photonic crystal, the Brillouin zone is more complex, often taking the shape of a polyhedron. The photonic bandgaps in such crystals depend on the symmetry and

geometry of the Brillouin zone. For example, the face-centered cubic (fcc) lattice has a nearly spherical Brillouin zone, making it favorable for the formation of complete photonic bandgaps. The analysis of photonic bandgaps and dispersion relations often requires both analytical and numerical methods. Analytical methods, such as the plane wave expansion method and the transfer matrix method, provide insights into the basic properties of the band structure, while numerical methods, such as the finite-difference time-domain (FDTD) method and the finite element method (FEM) offer detailed solutions for complex structures. The plane wave expansion method involves expanding the electromagnetic fields and the dielectric function in terms of plane waves. This transforms the wave equation into a matrix eigenvalue problem, which can be solved to obtain the band structure. On the other hand, the transfer matrix method uses the continuity of the electromagnetic fields at the interfaces between layers to derive the reflection and transmission coefficients, leading to the calculation of the bandgaps.

2.2 Variational principle

Before the analysis of the photonic bandgap and its physical origin, it is useful to understand some of the qualitative features of the harmonic modes. To gain a deeper insight, we need a theoretical approach, and the variational principle stands out as an effective tool that allows precise modeling and analysis of the behavior of harmonic modes within photonic crystals¹⁵. The variational principle is based on choosing a trial function that closely represents the EM modes within the photonic crystal. By minimizing the corresponding energy functional, it is possible to obtain approximate solutions that closely match the actual modes. The obtained solution is an approximation of the ground state function (mode), while the corresponding expectation value of the energy represents an upper limit for the ground energy state. This method simplifies complex calculations and gives valuable insights into the mechanisms behind photonic bandgaps.

In the context of photonic crystals, the lowest-frequency mode corresponds to the field pattern that minimizes the (EM) energy functional (also called Rayleigh quotient) given by¹⁵:

$$u_f(\vec{H}) = \frac{(\vec{H}, \hat{\theta}\vec{H})}{(\vec{H}, \vec{H})}. \quad (2.18)$$

where the terms in brackets denote the inner product given by :

$$(\vec{F}, \vec{G}) = \int d^3\vec{r} \vec{F}^*(\vec{r}) \cdot \vec{G}(\vec{r}). \quad (2.19)$$

Here, the asterisk denotes the complex conjugation. Knowing that

$$(\vec{H}, \vec{H}) \left(\frac{\omega}{c}\right)^2 = (\vec{H}, \hat{\theta}\vec{H}) = \int d^3\vec{r} \frac{1}{\varepsilon} |\vec{\nabla} \times \vec{H}|^2, \quad (2.20)$$

and by using the expressions given by (2.16), (2.10), and (2.11), the final form of the energy functional is given by :

$$U_f(\vec{H}) = \frac{(\vec{\nabla} \times \vec{E}, \vec{\nabla} \times \vec{E})}{(\vec{E}, \varepsilon(\vec{r})\vec{E})} = \frac{\int d^3\vec{r} |\nabla \times \vec{E}(\vec{r})|^2}{\int d^3\vec{r} \varepsilon(\vec{r}) |\vec{E}(\vec{r})|^2}. \quad (2.21)$$

It is clear that to minimize the functional $U_f(\vec{H})$, the expression in the denominator has to be maximized, which is achieved when the lowest mode of electric field (i.e., the lowest order eigenmode) is concentrated in the regions of high relative permittivity, as is shown in Figure 2.3. This result will be of great importance in the following section.

***E*-field for mode at the top of band 1**

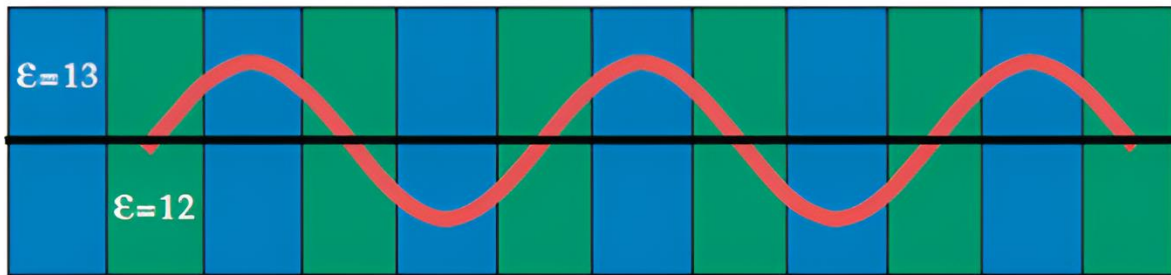


Figure 2.3 The distribution of the lowest electric field mode in a multilayer structure. Blue and green regions correspond to layers of higher and lower relative permittivity, respectively¹⁵

2.3 Photonic bandgap

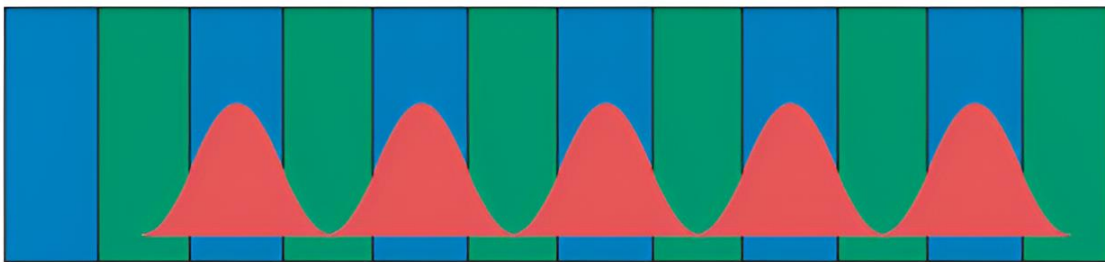
The photonic bandgap (PBG) is a central concept in studying photonic crystals. It refers to the range of frequencies of EM waves that are forbidden from propagating through the crystal.

To better understand the physical origin of the PBG, we will consider 1D PhC and recall three important principles:

1. Solutions to the Maxwell's equations in a periodic medium, also known as Bloch modes or Bloch waves, must have the same symmetry as periodic structure
2. The lowest-order mode of the electric field prefers to reside in high relative permittivity regions
3. EM modes must be orthogonal to each other

Bloch theorem states that the solutions to the wave equation can be written as a plane wave modulated by a periodic function, which in the case of EM modes in PhCs means that they must have the same periodicity as the photonic structure (Table 2.1). As depicted in Figure 2.4a, the first-order mode has the same periodicity as the structure itself. According to equation (2.21), the (intensity of the) first-order electric field mode prefers to be located in the high-dielectric regions. In contrast, the second-order mode, which has to be orthogonal to the first, primarily occupies regions of lower relative permittivity, as shown in Figure 2.4b.

(a) Local energy density in E -field, top of band 1



(b) Local energy density in E -field, bottom of band 2

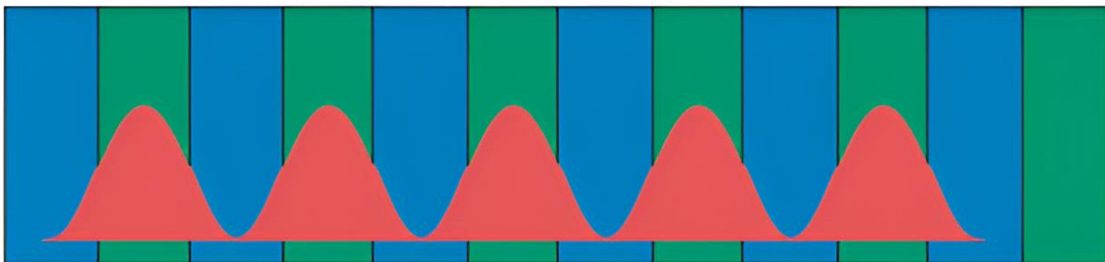


Figure 2.4 The distribution of the electric field energy density a) of the first band in a multilayer structure and b) of the second band in a multilayer structure. Blue and green regions correspond to layers of higher and lower relative permittivity, respectively¹⁵

As a result, two waves with the same periodicity are present, but the lower order mode experiences, on average, the higher refractive index due to its concentration in the high relative permittivity regions. In contrast, the second-order mode interacts more with low relative permittivity regions and, therefore, experiences, on average, a lower refractive index. These two waves have the same period, but experience refractive indices, so they can only coexist if their frequencies are different. This difference in frequency is represented in Figure 2.5 and is the origin of the PBG.

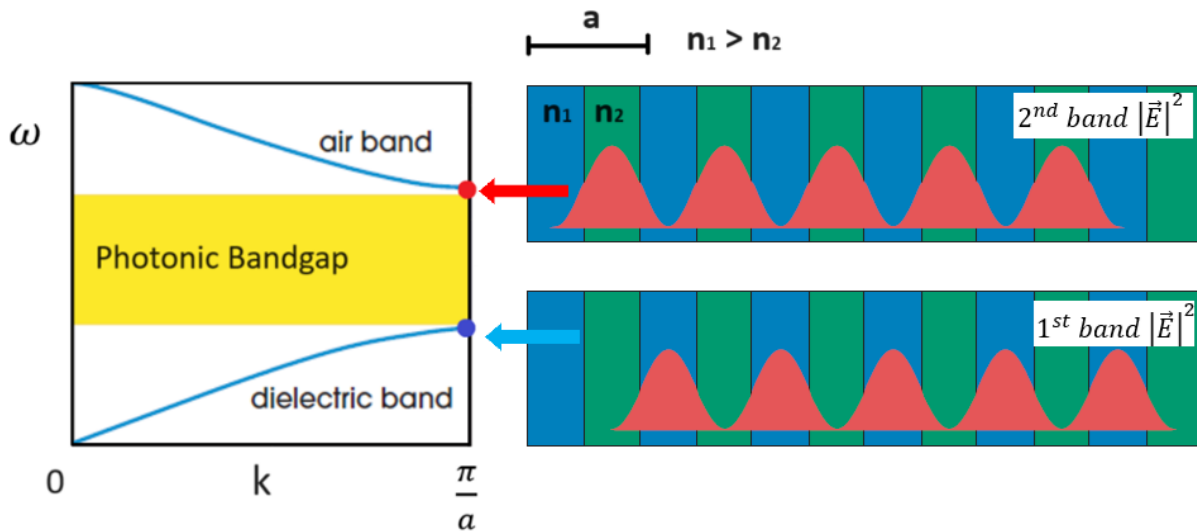


Figure 2.5 The origin of a photonic bandgap in a PhC. The electric field energy density distribution of the first and second bands in a multilayer structure presented on the right panel have the same period, but due to concentration in different refractive index regions, they can coexist only if their frequencies are different. This difference in frequency is represented on the left panel and shows the origin of the photonic bandgap. Blue regions on the right panel correspond to layers with a higher relative permittivity, while green areas correspond to layers with a lower relative permittivity¹⁵

The formation of a PBG can also be explained through the concept of Bragg scattering, which occurs when EM waves interact with a structure whose periodicity of the relative permittivity is of the order of the wavelength of light. Depending on the wavelength of light and the angle of incidence, diffracted waves can interfere destructively, leading to prohibited propagation directions and frequency ranges for which no photonic modes exist within the crystal.

The effect can be explained by considering 1D PhC, in which the periodic arrangement is achieved by layers of alternating high and low refractive indices. When light enters such a structure, it undergoes multiple reflections at the interfaces between different layers, as shown in Figure 2.6.

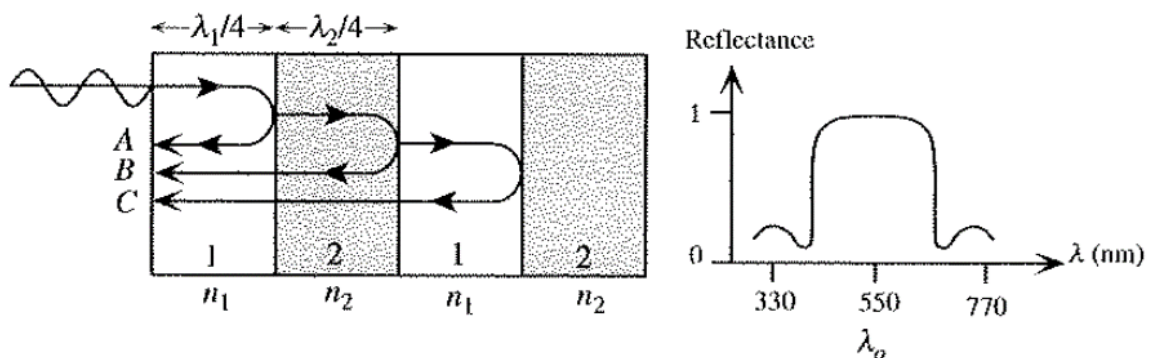


Figure 2.6 Schematic illustration of the principle of the dielectric mirror with high and low refractive index layers and corresponding reflectance spectrum²²

For certain wavelengths, a strong reflection of light, known as Bragg reflection, will occur. The condition for constructive interference of reflected light is given by Bragg condition:

$$m\lambda = 2nd \cos \theta \quad (2.22)$$

where m is an integer representing the order of the reflection, λ is the wavelength of light, n the refractive index of the material, d the thickness of the layers, and θ is the angle of incidence. Waves of frequencies that satisfy this condition are reflected from different layers, and they interfere constructively, leading to strong reflection (Figure 2.6) and, therefore, prohibition of propagation of those frequencies through the photonic structure, which means that a bandgap is formed. It is important to mention that the localization of EM modes contributes to the specific conditions under which constructive and destructive interference occur; the first mode will experience different scattering conditions compared to the higher-order modes that are localized in low relative permittivity regions. The difference in the interference pattern then either contributes to the formation of another bandgap or reinforces the existing one.

Both Bragg scattering and localization of EM modes explain the formation of the PBG. The localization of EM modes within different dielectric regions describes how the energy distribution within the photonic structure influences the creation of the PBG, while Bragg scattering explains the phenomenon through constructive and destructive interference within the structure.

2.4 Group velocity

One of the key parameters in the context of PhCs is the group velocity of light within the PhC. Group velocity characterizes the EM waves and gives insights into the speed at which energy and information are transmitted through the material.

There are three different kinds of velocities²⁰. Phase velocity describes the velocity with which the equi-phase surface propagates in space. However, it is less meaningful in the case of PhCs due to the complex nature of the eigenfunctions, which are superpositions of plane waves.

The energy velocity represents the velocity of the propagation of the EM energy through the medium and is defined using the Poynting vector \vec{S} and energy density U :

$$v_e = \frac{\langle \vec{S} \rangle}{\langle U \rangle} \quad (2.23)$$

where $\langle \rangle$ denotes the spatial average over a unit cell and

$$\vec{S} = \frac{1}{2} \text{Re}[\vec{E} \times \vec{H}^*], \quad U = \frac{1}{4} (\varepsilon |\vec{E}|^2 + \mu |\vec{H}|^2). \quad (2.24)$$

Finally, the group velocity is the energy-transport velocity in the case of a lossless medium, small material dispersion, and real wavevector¹⁵. It describes the propagation of a wave packet and is defined by the gradient of the angular frequency $\omega(\vec{k})$ given by the dispersion relation with respect to the wave vector \vec{k} :

$$v_g = \vec{\nabla}_k \omega(\vec{k}) \quad (2.25)$$

In the case of PhCs, the energy velocity is the same as the group velocity despite the periodically modulated dielectric constant^{15,20}.

Group velocity plays an important role in understanding the propagation of light through PhCs and their optical response, so its calculation is crucial for understanding the optical properties of PhCs. It serves as a direct link between the microscopic structure of the PhC and the macroscopic propagation characteristics of the waves that propagate through it.

The photonic band structure illustrated in Figure 2.2 shows that near the PBG edges, the dispersion relation flattens out. Calculation of the group velocity at these points, which involves calculating the first derivative of the frequency with respect to the wavevector, shows that group velocity approaches zero, leading to the effect of so-called slow photons or slow light. The top panel in Figure 2.7 shows the transmittance spectrum of a PhC as a function of normalized frequency. The regions of low (ideally zero) transmittance correspond to PBG. The bottom panel of the same figure shows the real and imaginary parts of a group velocity. The real part of the group velocity is zero within the PBG, and therefore, there is no propagation of light in these frequency ranges. Outside the PBG, the real part of the group velocity increases, which means that light can propagate through a PhC. Contrarily, the imaginary part shows a spike at the center of the PBG that corresponds to evanescent modes (which will be discussed later in the chapter) and strong attenuation of light within the PBG. It is important to mention that within the PBG, the wavevector becomes a complex number with real and imaginary parts, $k = k_R + ik_I$ ²³. As defined in (2.25), group velocity can be found by calculating the gradient of an angular frequency with respect to the wavevector. Within the PBG, ω is purely real (representing the frequency of evanescent waves), while k is purely imaginary, so inside the PBG, the group velocity will have a non-zero imaginary component.

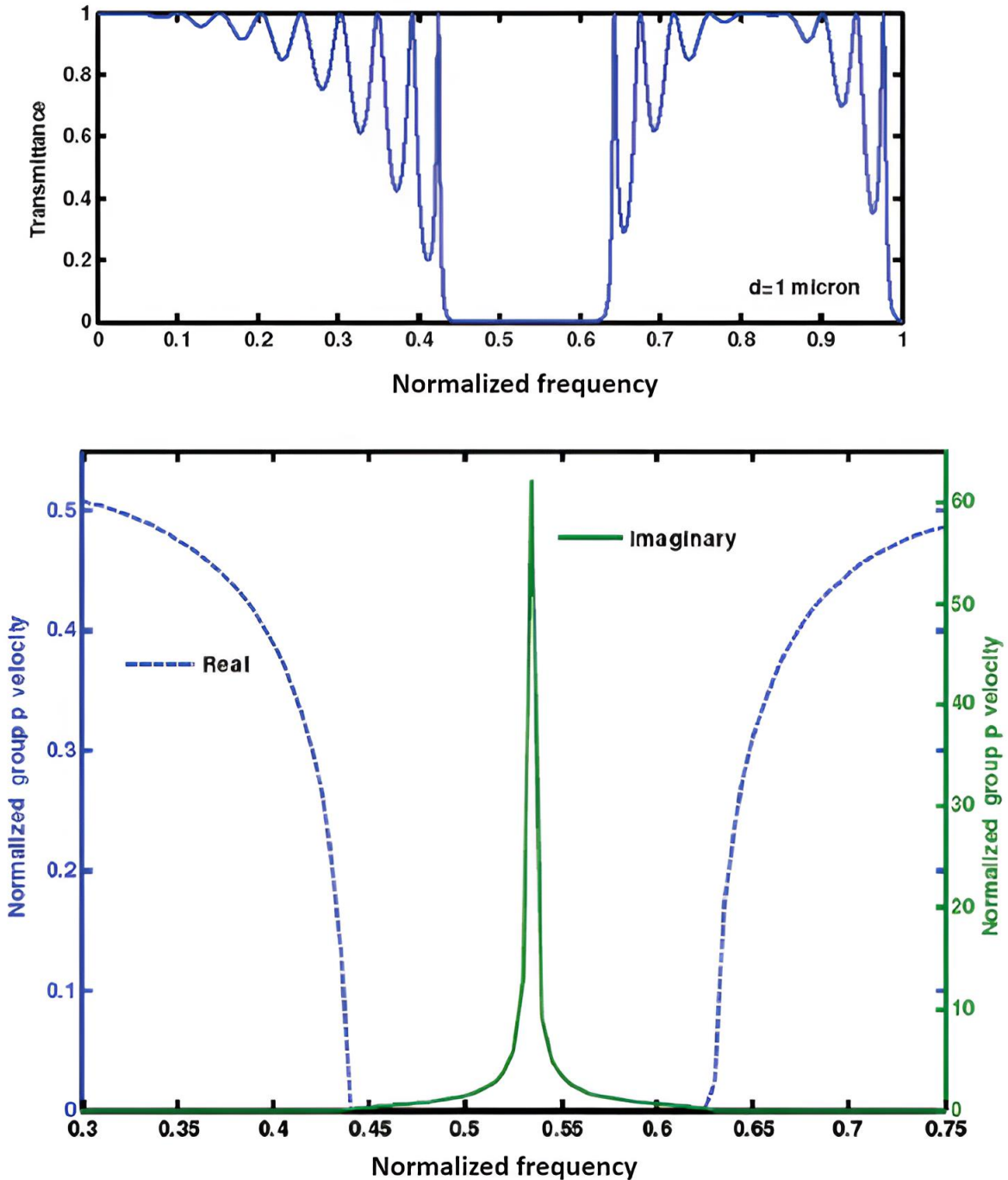


Figure 2.7 The top panel illustrates the transmittance spectrum for a multilayer structure as a function of a normalized frequency, where regions with zero transmittance correspond to the PBG. The bottom panel shows the corresponding normalized group velocity, where the dashed blue line represents the real part of normalized group velocity, while the solid green line represents the imaginary part. The sharp peak in the imaginary part indicates the presence of evanescent modes within the PBG¹⁷

The significantly reduced group velocity at the edge of the PBG results in effectively enhanced light-matter interaction due to longer light-matter time interaction, which means that various optical processes are enhanced. Additionally, the fact that group velocity approaches zero at the

edges of the PBG reinforces the fact that within the PBG, group velocity is zero, meaning that propagation of certain frequencies is entirely forbidden inside the PBG.

To conclude, it is important to note that by manipulation of the dispersion relation through careful design of photonic structures, it is possible to utilize unique properties of group velocity that can improve the performance of various PhC-based devices.

2.5 Density of states

Density of states (DOS) is another important concept in the study of photonic crystals that describes the number of available EM modes within a small frequency interval²⁴:

$$D(\omega) = \frac{dN(\omega)}{d\omega}, \quad (2.26)$$

where $D(\omega)$ represents the density of states at frequency ω , while $N(\omega)$ is a number of EM modes (or photonic states) with frequencies in a range $(\omega, \omega + d\omega)$, as shown in Figure 2.8.

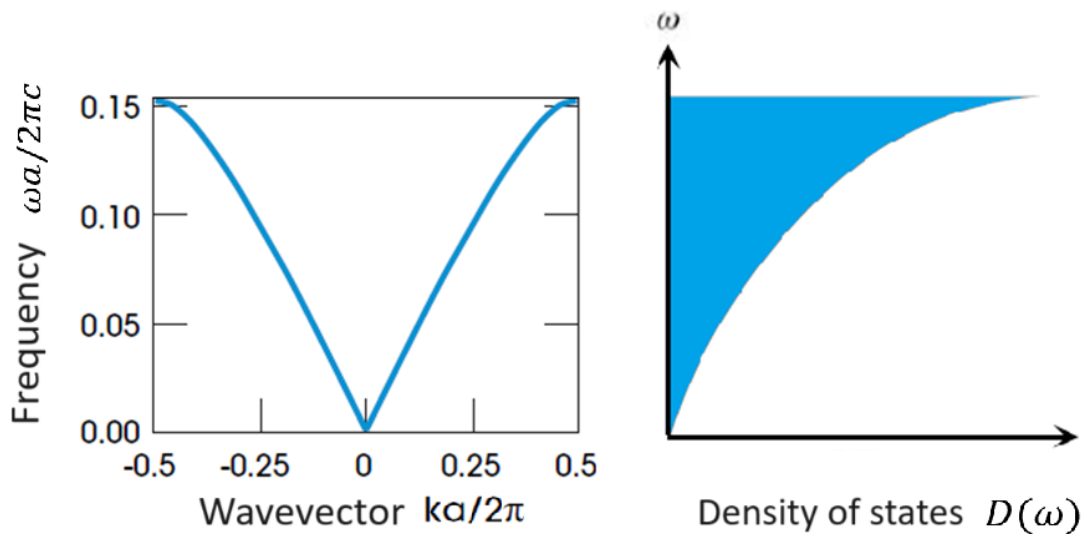


Figure 2.8 The dispersion relation (on the left) and the corresponding density of states (on the right) in a 1D PhC. At the edge of the first Brillouin zone, the dispersion relation flattens out, resulting in an increase in the number of available photonic modes within a small frequency interval¹⁵

The probability of spontaneous photon emission or photon scattering for a certain frequency depends on the DOS at that frequency, which is why this concept is important in the study of both Raman scattering and photonic crystals. Structures whose spatial variation of relative permittivity is of the order of photon wavelength modify the DOS and, consequently, all the processes related to photon emission and photon scattering²⁵.

The probability for Raman scattering with frequency ω' by a structure in a continuous medium is given by²⁵:

$$W(\omega', \omega) = \frac{2\pi^2}{\hbar^2} \omega' \omega N(\omega') |S|^2 \left[N(\omega) + \frac{1}{4\pi} D(\omega) \right], \quad (2.27)$$

where ω is a frequency of a Raman mode, $N(\omega')$ and $N(\omega)$ are numbers of photons with frequencies ω' and ω , respectively and S is a transition matrix element. The first term in the square brackets represents stimulated, while the second represents spontaneous scattering processes. DOS depends on the dimensionality of the structure, so the expressions for 3D, 2D, and 1D cases are, respectively:

$$D_3(\omega) = \frac{\omega^2 n^3}{2\pi^2 c^3}, \quad D_2(\omega) = \frac{\omega n^2}{2\pi c^2}, \quad D_1(\omega) = \frac{n}{\pi c}. \quad (2.28)$$

By inserting these expressions into (2.27), the probability for spontaneous Raman scattering in a continuous 3D, 2D and 1D medium is:

$$W_3(\omega', \omega) = \frac{1}{\hbar^2} \omega' N(\omega') |S|^2 \frac{1}{4\pi} \frac{\omega^3}{c^3} n^3, \quad (2.29)$$

$$W_2(\omega', \omega) = \frac{1}{\hbar^2} \omega' N(\omega') |S|^2 \frac{1}{2} \frac{\omega^2}{c^2} n^2, \quad (2.30)$$

$$W_1(\omega', \omega) = \frac{2\pi}{\hbar^2} \omega' N(\omega') |S|^2 \frac{\omega}{c} n. \quad (2.31)$$

The influence of DOS on the probability for Raman scattering results from the fact that the scattering rate ($\sim \omega D(\omega)$), depends on the index of refraction and the dimensionality of the medium²⁵. It is important to notice that the well-known relation $W(\omega', \omega) \propto \omega^4$ in the case when $\omega - \omega' \ll \omega$ is not valid for low-dimensional structures. Instead, the probability for Raman scattering is proportional to the third power of frequency in the case of 2D medium and to its square in the 1D case. In general

$$W(\omega', \omega, n, d) \propto \omega' (n\omega)^d, \quad (2.32)$$

where d denotes the dimensionality of the medium. In the case when $\omega - \omega' \ll \omega$:

$$W(\omega', \omega, n, d) \propto \omega^{d+1} n^d. \quad (2.33)$$

When dealing with non-continuous media, Raman scattering depends on the local density of states (LDOS) in the vicinity of a molecule²³. In the case of PhCs, the DOS is a complicated function of frequency and coordinate. According to Barnett²⁶, DOS redistributes within the frequency spectrum, but the total DOS remains constant. Examples of the 3D and 2D cases are depicted in Figure 2.9, where DOS for continuous medium is presented by solid lines, while

DOS corresponding to a photonic structure is presented by dashed lines. The dip representing the PBG, where in perfect cases, no allowed modes should exist, is compensated by the increase at the ends of the PBG. Additionally, Figure 2.10 shows DOS for a 1D multilayer structure as a function of a normalized frequency, where the solid line represents the DOS and highlights the redistribution of states. There is a significant increase in the DOS at the edges of the PBG, while the lack of available states characterizes the PBG. The dashed line shows the corresponding transmittance spectrum.

This analysis suggests that due to the increased DOS, Raman scattering should be enhanced at the edges of the PBG. It is also important to mention that in the case of 3D structures with 1D or 2D periodicity, the PBG suppresses the DOS in one or two dimensions while enhancing it in the remaining dimensions²⁵.

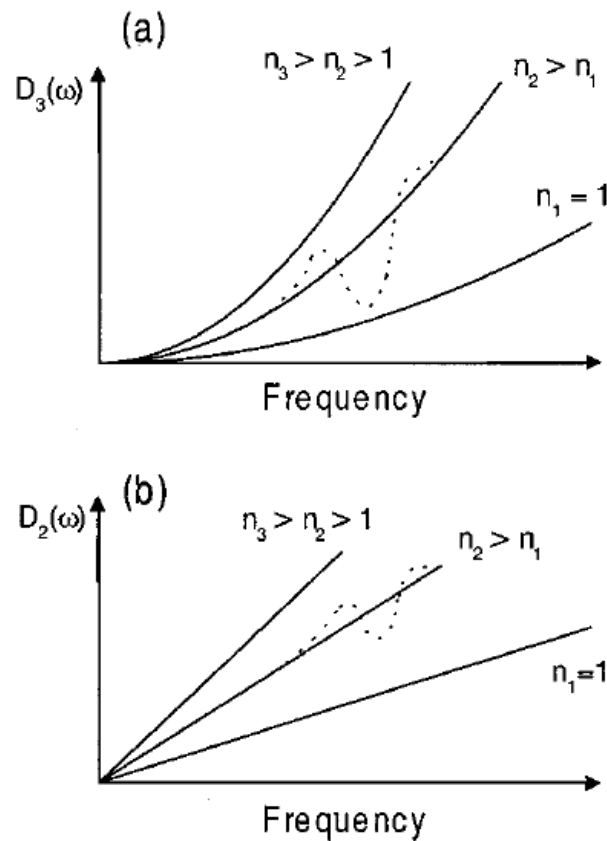


Figure 2.9 Density of states in a) three-dimensional and b) two-dimensional spaces. Solid lines represent continuous media with different refractive indices, while dashed lines illustrate the redistribution of DOS in photonic structures²⁵

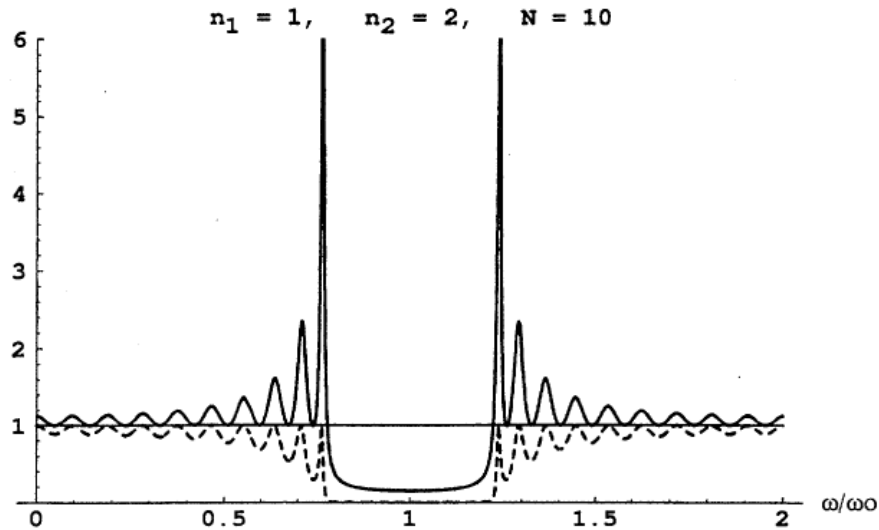


Figure 2.10 Representation of the dimensionless DOS as a function of frequency (solid line) and the corresponding transmittance spectrum (dashed line) for a 1D PhC²⁴

As mentioned earlier, the concept of DOS is directly related to the band structure, i.e., the dispersion relation of a photonic crystal: within the allowed bands, the DOS can significantly vary depending on the dispersion relation, as illustrated in Figure 2.11, while near the edges of the PBG, it usually increases since there are many states within a small frequency range. In contrast, within the PBG, the DOS is zero, confirming that no photonic states are allowed within that particular frequency range.

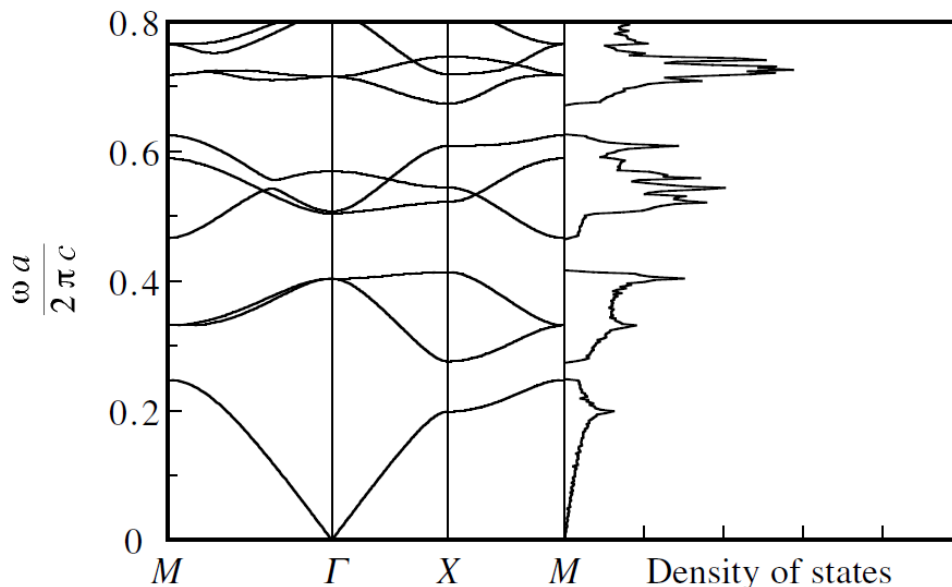


Figure 2.11 Band structure for a 2D square lattice composed of circular cylinders, obtained through numerical calculation. The relative permittivities of the cylinders and the background were $\epsilon = 9$ and $\epsilon = 1$, respectively, with a lattice constant to cylinder radius of 1:0.38. Labels on the x-axis denote the center of the first Brillouin zone (Γ), its edge (M), and the middle point (X)²⁰

However, in real cases, when defects are present in the photonic structure, the DOS within the PBG can be different from zero. Irregularities in the photonic structure can introduce localized states within the PBG and allow the existence of frequencies that would be forbidden in the case of a perfect structure.

The importance of the concept lies in the fact that the optical properties of atoms and molecules strongly depend on DOS, which means that by modifying the DOS, it is possible to change the characteristics of the radiation field²⁰.

At the end of this section, it is important to clarify an essential point that was quietly implied in the discussion above: our focus was on the probability of detecting the Raman signal, not on the occurrence of the Raman scattering event itself. While Raman scattering can occur regardless of the DOS, it is the availability of photonic states that determines whether the scattered photon can propagate and be observed.

It is essential to distinguish between the generation of Raman-scattered photons and their propagation through the photonic crystal. Raman scattering itself is a localized event that occurs when an incident photon interacts with the molecular vibrations of the material. This scattering process does not directly depend on the availability of photonic states, so Raman scattering can still occur even if the scattered photon's frequency lies within the PBG.

However, once the Raman-shifted photon is generated, its ability to propagate through the photonic crystal depends on the DOS at that frequency. In the case of a 1D PhC, if the frequency of the scattered photon falls within the PBG where the DOS is zero, the photon cannot propagate in the direction perpendicular to the PhC's surface. This restriction occurs because a 1D PhC creates a photonic band gap that blocks light in the direction perpendicular to the layers and therefore, a detector positioned above the sample would not directly capture this scattered photon due to the lack of available states for it to travel upward.

However, alternative propagation paths may allow some scattered photons to reach the detector. For example, if the Raman-scattered photon is generated within the superficial layers, it might propagate in the other two directions where the DOS is different from zero, bypassing the propagation restriction in the direction perpendicular to the surface. Additionally, light in a photonic crystal can experience partial reflections within the structure, meaning that some scattered photons may reflect at different angles within the layers and eventually find a path that enables them to escape.

2.6 Evanescent modes

In subsections 2.3, 2.4, and 2.5, we showed that the EM modes with frequencies in the PBG region are not allowed to propagate through the ideal photonic structure. This is because the propagation of normal modes is forbidden in such cases, and no real wavevectors exist. However, as mentioned earlier and depicted in Figure 2.7, the wavevector is a complex quantity, and the non-zero imaginary part determines the exponential decay of the wave amplitude within the PhC¹⁵:

$$\vec{H}(\vec{r}) = e^{i\vec{k}\vec{z}}\vec{u}(z)e^{-Kz} \quad (2.34)$$

These modes are similar to Bloch modes with a complex wavevector, $k + iK$, where the imaginary part determines the exponential decay at the length scale of $1/K$. This means that the energy of the mode rapidly decreases upon entering the PBG, and therefore, such modes do not transport energy over long distances.

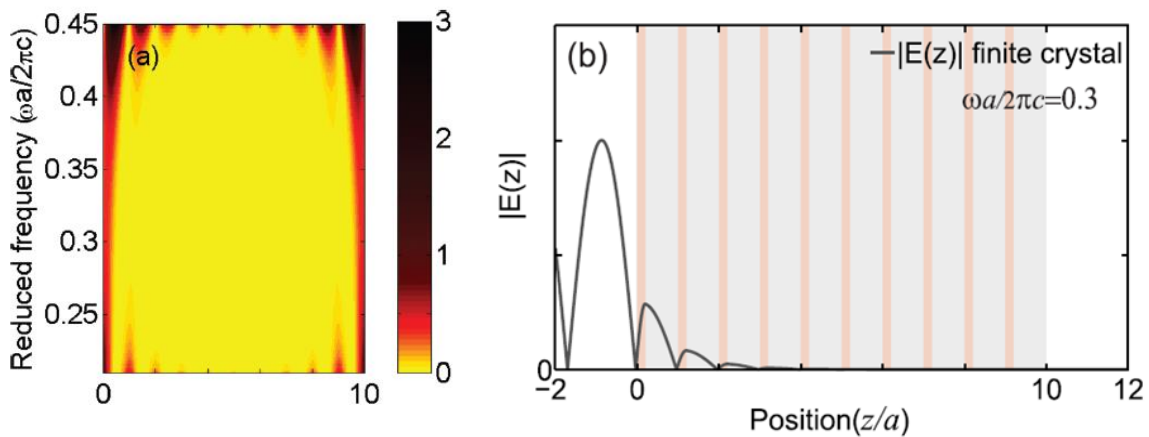


Figure 2.12 a) Heat map representing LDOS within the frequency range of the PBG for a 20-layer PhC. Local DOS decays exponentially inside the PBG with a minimum at the center of the PBG due to the maximum imaginary component of the wavevector. b) Absolute value of the electric field at a frequency $\omega a / 2\pi c = 0.3$ that corresponds to the approximately center of the PBG. At this frequency, the field inside the structure is damped. The lattice constant is given by a , and z represents the position within the photonic structure²³

The origin of the evanescent modes can be explained with the help of the dispersion relation. If, near the PBG, we write the second band as the expansion of $\omega_2(k)$ in the powers of k around the edge of the first Brillouin zone, where $k = \frac{\pi}{a}$, and take into account the time-reversal symmetry that implies that the expansion cannot contain odd powers of k , then

$$\Delta\omega = \omega_2(k) - \omega_2\left(\frac{\pi}{a}\right) \approx \alpha \left(k - \frac{\pi}{a}\right)^2 = \alpha(\Delta k)^2 \quad (2.35)$$

where α is a constant that depends on the curvature of the specific band. If $\Delta\omega > 0$, then Δk is purely real and $\omega_2(k) > \omega_2\left(\frac{\pi}{a}\right)$, which means that the mode is within the second band. Contrarily, if $\Delta\omega < 0$, then $\omega_2(k) < \omega_2\left(\frac{\pi}{a}\right)$. In that case, the frequency $\omega_2(k)$ corresponds to the mode within the PBG, Δk is purely imaginary, and the states decay exponentially since $\Delta k = iK$.¹⁵ As the frequency of the photonic modes approaches the center of the PBG, the value of K increases. Conversely, K decreases for frequencies further away from the center and towards the edges of the PBG and finally disappears at the edges of the bandgap. This means that the photonic structures with wide PBG have greater K in its center, resulting in a more rapid exponential decay of the modes within the PBG and minimal penetration into the structure.

It is interesting to note that equation (2.34) shows that evanescent modes diverge as z goes to $\pm\infty$ (depending on the sign of K). This implies that evanescent modes cannot be physically excited unless there is a defect within the photonic structure. From the mathematical perspective, defects eliminate the divergence and, thus, sustain the evanescent mode.

2.7 One-dimensional PhCs

One-dimensional (1D) PhCs are optical structures that are characterized by a periodic variation of relative permittivity in only one dimension. Just as in the case of 2D and 3D PhCs, the periodicity creates a PBG that forbids the propagation of certain wavelengths of light. The simplest 1D PhC is a Bragg reflector (also known as a multilayer structure, Bragg stack, or Bragg mirror), which is composed of alternating layers of materials with discrete relative permittivity, as shown in Figure 2.1. This type of multilayer structure was first produced by Vincent²⁷ in 1994, which initiated a big interest in the development of (porous silicon) PhCs.

The design of a Bragg reflector ensures that the waves reflected from each interface interfere constructively, resulting in high reflectivity for a certain wavelength range, which corresponds to the formation of a PBG. A simple case where a layer of thickness d whose index of refraction is n_1 , is placed between two infinite different media whose indices of refraction are n_0 and n_T as illustrated in Figure 2.13, can be described using a matrix approach as follows²⁸ :

$$\begin{bmatrix} 1 \\ n_0 \end{bmatrix} + \begin{bmatrix} 1 \\ -n_0 \end{bmatrix} \frac{E_R}{E_0} = \begin{bmatrix} \cos kd & \frac{-i}{n_1} \sin kd \\ -in_1 \sin kd & \cos kd \end{bmatrix} \times \begin{bmatrix} 1 \\ n_T \end{bmatrix} \frac{E_T}{E_0} \quad (2.36)$$

where $k = 2\pi n_1/\lambda$, the amplitude of the incident electric field is E_0 , that of a reflected beam is E_R and E_T is the amplitude of the transmitted beam.

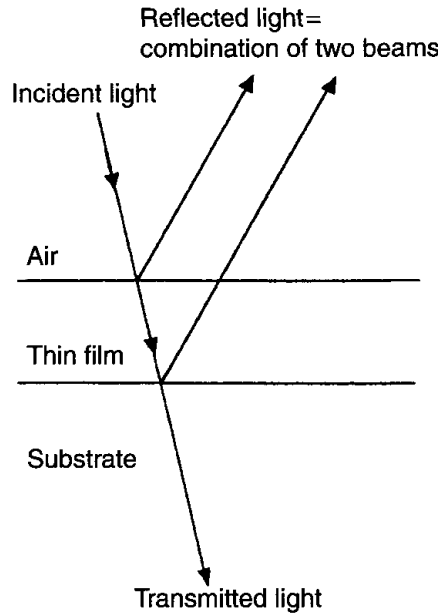


Figure 2.13 Reflection and transmission of light by a thin film²⁹

Introduction of the reflection and transmission coefficients, r and t , simplifies the above expression to :

$$\begin{bmatrix} 1 \\ n_0 \end{bmatrix} + \begin{bmatrix} 1 \\ -n_0 \end{bmatrix} r = M \begin{bmatrix} 1 \\ n_T \end{bmatrix} t \quad (2.37)$$

where M is a matrix that relates the reflected and transmitted beams, known as the transfer matrix.

In the case of a multilayer structure (Figure 2.14), where N layers are present, each layer having an index of refraction n_i and thickness d_i , we can write :

$$\begin{bmatrix} 1 \\ n_0 \end{bmatrix} + \begin{bmatrix} 1 \\ -n_0 \end{bmatrix} r = M_1 M_2 \dots M_N \begin{bmatrix} 1 \\ n_T \end{bmatrix} t = M \begin{bmatrix} 1 \\ n_T \end{bmatrix} t \quad (2.38)$$

where M_i are transfer matrices for each particular layer.

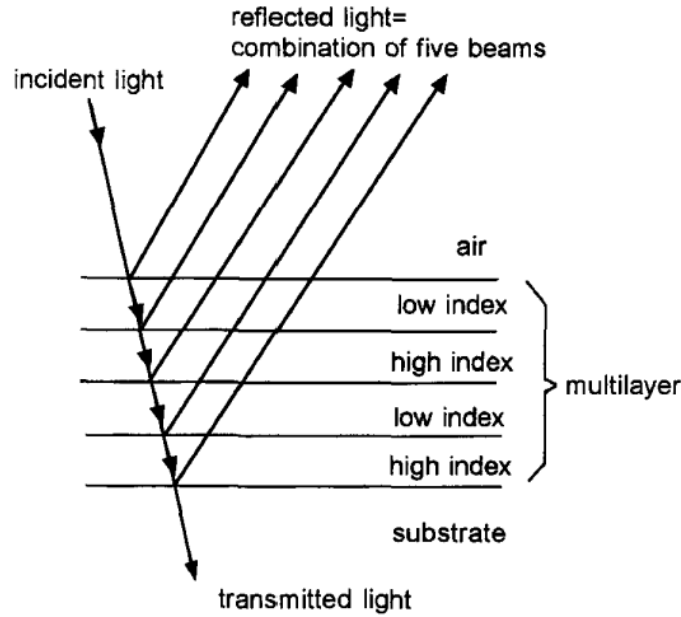


Figure 2.14 Reflection and transmission of light by a multilayer²⁹

If we define the overall transfer matrix M as $M = \begin{bmatrix} A & B \\ C & D \end{bmatrix}$, equation (2.38) can be solved for r and t :

$$r = \frac{An_0 + Bn_T n_0 - C - Dn_T}{An_0 + Bn_T n_0 + C + Dn_T} \quad (2.39)$$

$$t = \frac{2n_0}{An_0 + Bn_T n_0 + C + Dn_T} \quad (2.40)$$

The reflectance R and transmittance T can then easily be calculated using $R = |r|^2$ and $T = |t|^2$, respectively. In the case of a high-reflectance multilayer film with $2N$ layers, in which the relation between the thickness and the index of refraction is given by $\lambda = 4n_i d_i$, the transfer matrix of the whole multilayer structure will be given by

$$M = \begin{bmatrix} \left(-\frac{n_H}{n_L}\right)^N & 0 \\ 0 & \left(-\frac{n_L}{n_H}\right)^N \end{bmatrix} \quad (2.41)$$

where n_H and n_L are high and low refractive indices. Under the assumption that n_0 and n_t are both equal to one, the reflectance is given by:

$$R = \left[\frac{\left(\frac{n_H}{n_L}\right)^{2N} - 1}{\left(\frac{n_H}{n_L}\right)^{2N} + 1} \right]^2. \quad (2.42)$$

It is visible that the reflectivity of a Bragg reflector increases with the number of layers and for large N it approaches unity around a certain central wavelength. This is due to reflection at multiple interfaces and the fact that all reflected beams have the same phase when they reach the top of the structure and, therefore, interfere constructively.

In addition to increasing the peak reflectivity, the number of layers N and the contrast between refractive indices also play a crucial role in determining the width, sharpness, and overall shape of the reflectance peak²⁸. As we increase N :

- the reflectance peak becomes wider and sharper
- the value of R in the bandgap increases with respect to the value of R in the side-lobes

As we increase the contrast between the refractive indices :

- bandgap becomes wider and sharper
- overall reflectance becomes higher, both in the bandgap and in the side lobes

The above relationships are illustrated in Figure 2.15 and Figure 2.16.

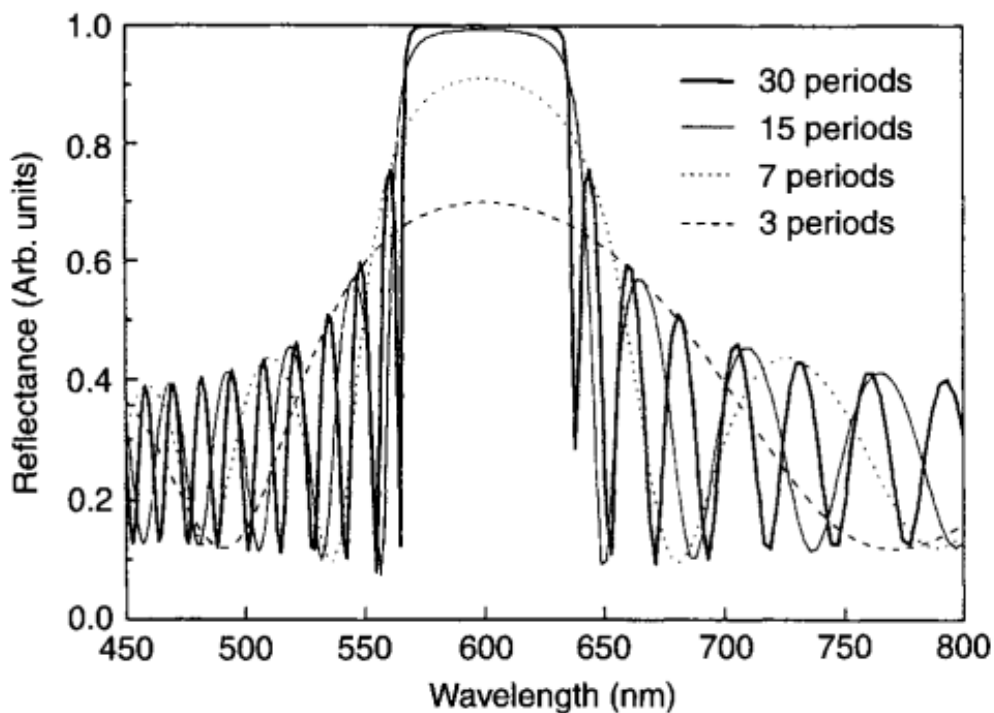


Figure 2.15 Reflectance spectra of Bragg reflector with varying number of periods. The high and low reflective indices are 1.5 and 1.27²⁹

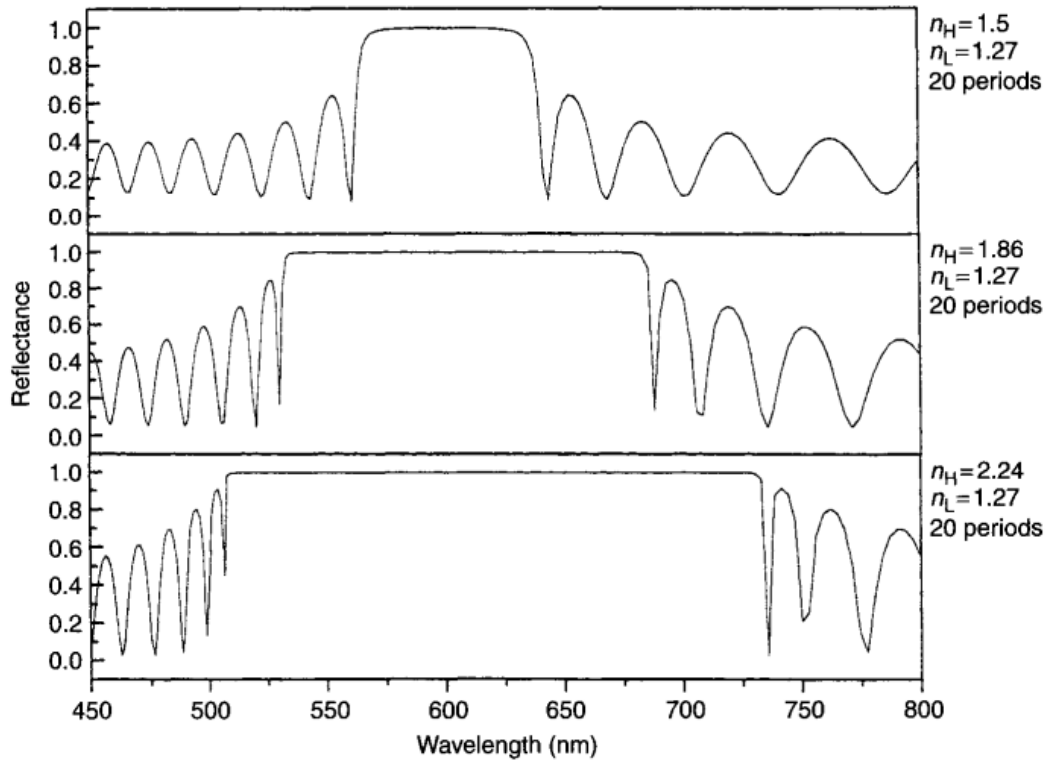


Figure 2.16 Reflectance spectra of Bragg reflector with a fixed number of periods and varying ratios between the high and low refractive indices²⁸

With that being said, it is clear that the design of a PhC requires considering several factors to achieve the desired bandgap properties, such as refractive index contrast, periodicity, and geometry. In addition, variations such as introducing defects into the structure or adding a third layer are also possible. Defects can be in the form of a missing layer, a layer of altered thickness, or a layer with a different refractive index, as shown in Figure 2.17, and their introduction into the structure results in the creation of localized modes within the PBG.

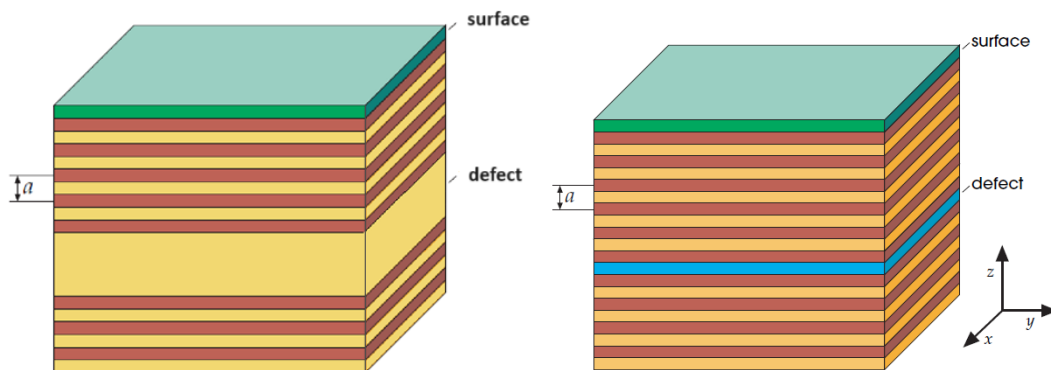


Figure 2.17 Schematic illustration of defects introduced in a 1D PhC, either by removing a layer (left), by adding a layer with a refractive index different from those of the other layers (right), or by modifying the surface layer (left and right). These modifications break the symmetry of the structure and result in localized states within the PBG¹⁵

By manipulating the nature and the position of defects, it is possible to create precisely tuned PhC-based cavities and filters. Defects allow the propagation of a very narrow range of frequencies within the PBG in the case of PhC-based filters and confine specific wavelengths within the PBG in the case of cavities. An example of a current density profile required to obtain a microcavity within the photonic structure and the corresponding reflectance spectra are presented in Figure 2.18.

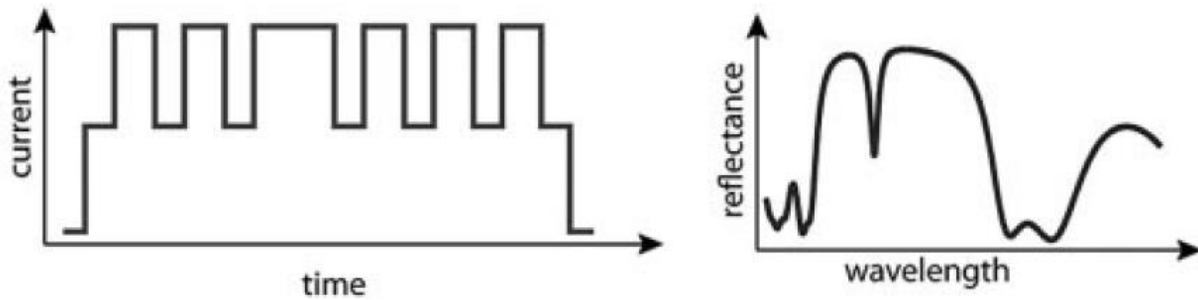


Figure 2.18 Current density profile as a function of time for a microcavity and the corresponding reflectance spectra³⁰

Another variation is a PhC with three different layers known as ternary 1D PhC. Similarly to previous configurations, by careful design of the thickness and refractive indices of the layers, it is possible to get various PBGs. Such structures are useful for enhancing the efficiency of light-emitting devices, improving the performance of sensors, creating more efficient waveguides, etc.³¹⁻³³

Additionally, graded refractive index profiles can also be achieved, where the smooth transition between the layers reduces the scattering losses and enhances the performance of the PhC. One example of such structures is rugate filters, which will be discussed in the next section.

All the abovementioned modifications enable the construction of various structures with a range of different properties and the precise control of PBG, which influences the propagation and localization of light. This offers a new way to improve and create new and advanced optical devices.

2.8 Rugate filters

Rugate filters (RFs) are a class of photonic crystals characterized by the continuous sinusoidal modulation of the refractive index. Unlike Bragg reflectors or microcavity structures, which consist of discrete different refractive index layers, RFs have smooth transitions between the layers^{34,35}, resulting in cleaner and more defined spectral characteristics, as depicted in Figure 2.19.

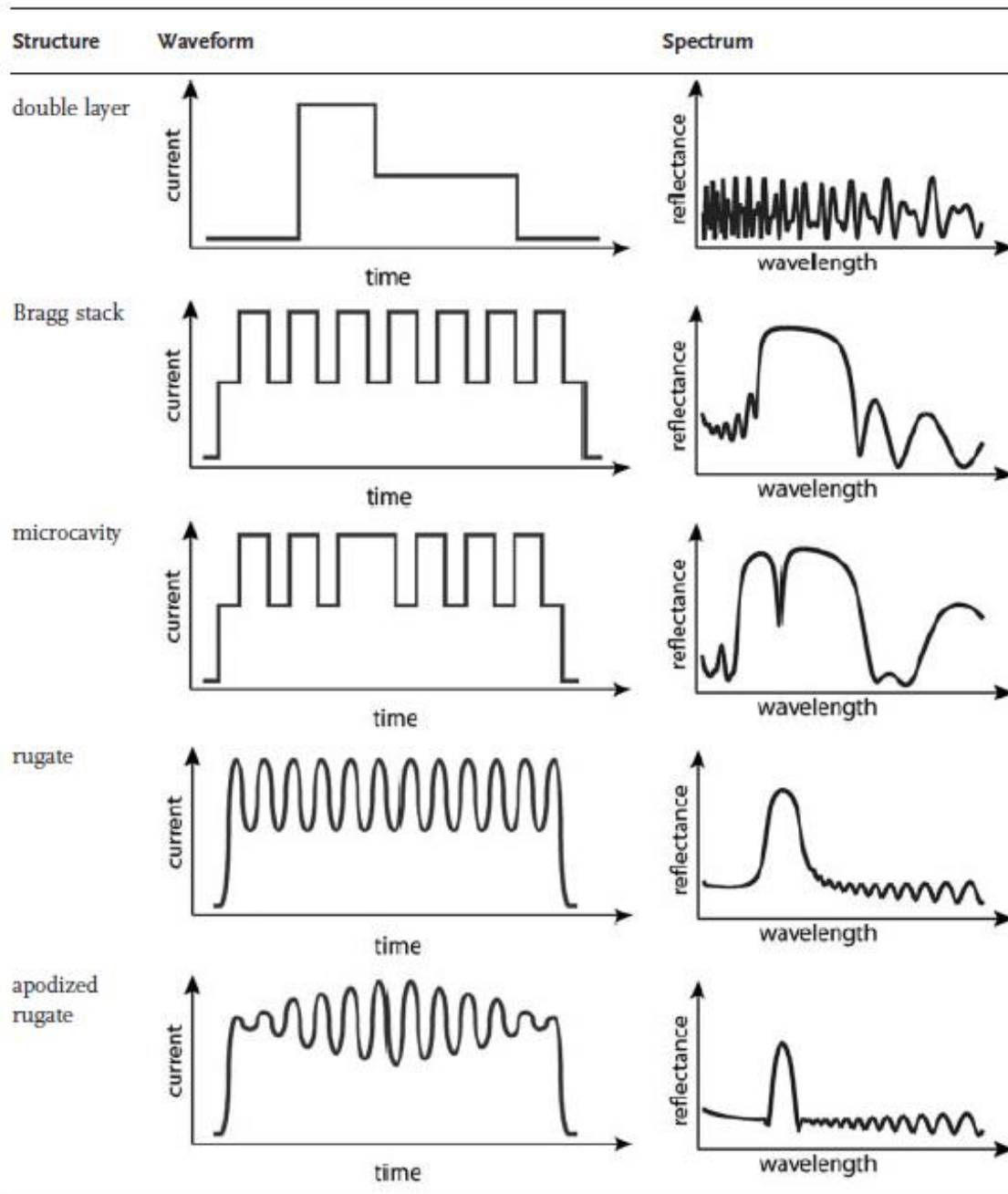


Figure 2.19 Examples of the most important 1D pSi periodic structures obtained by the modulation of porosity.

The corresponding current density profiles over time are shown on the left, and their reflectance spectra are given on the right³⁰

Fabrication of a RF is based on precise control of the electrochemical etching process, in which porous silicon is a commonly used substrate. The key to creating a rugate filter is sinusoidal modulation of the current density that results in sinusoidal variation in porosity and, therefore, sinusoidal variation in the index of refraction. To produce such modulation, sophisticated equipment that enables an application of a time-varying current profile is required.

Rugate filters possess unique optical properties that enable precise control of light reflection and transmission. Just as with the other types of PhCs, periodic variation in the refractive index of a RF creates a PBG that prohibits the propagation of a certain narrow range of wavelengths, as shown in Figure 2.20.

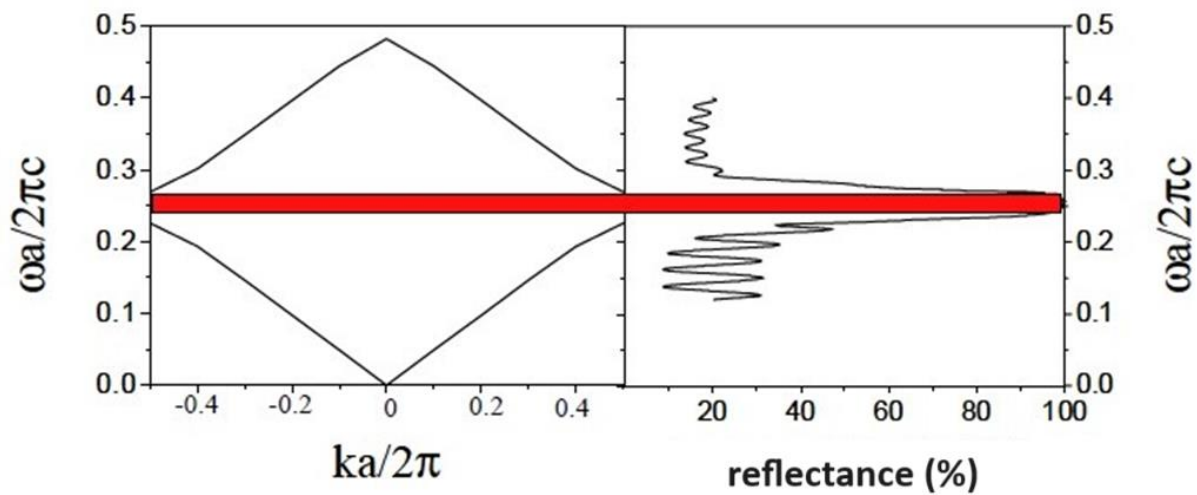


Figure 2.20 Comparison of the theoretically calculated band structure and the experimentally obtained reflectance spectrum of a pSi Bragg reflector³⁶

The reflectance peak position is influenced by the average current density and the frequency of the applied sinusoidal waveform. Figure 2.21 shows how it depends on the average current density, while the relationship between the frequency of the sinusoidal waveform and the position of the PBG is presented in Figure 2.22³⁰. The frequency of the sinusoidal current determines the periodicity of the refractive index modulation, i.e., the periodicity of the PhC, which influences the position of the PBG. The above relationships can mathematically be expressed by^{30,37}:

$$\lambda_{rugate} = 2n_{ave}d. \tag{2.43}$$

The wavelength λ_{rugate} represents the wavelength of the main reflectance peak, the average index of refraction is given by n_{ave} and reflects the influence of the average current density,

while periodicity d gives information about the impact of the frequency of the sinusoidal waveform.

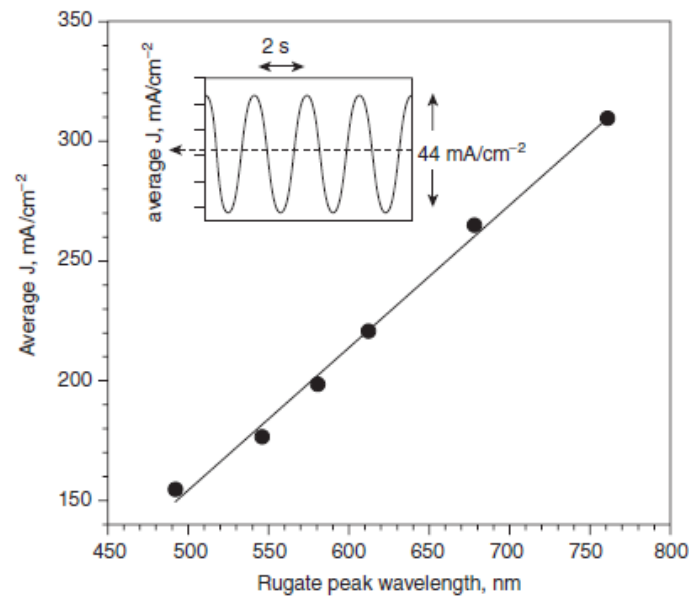


Figure 2.21 Effect of average current density on the position of the main reflectance peak of a RF³⁰

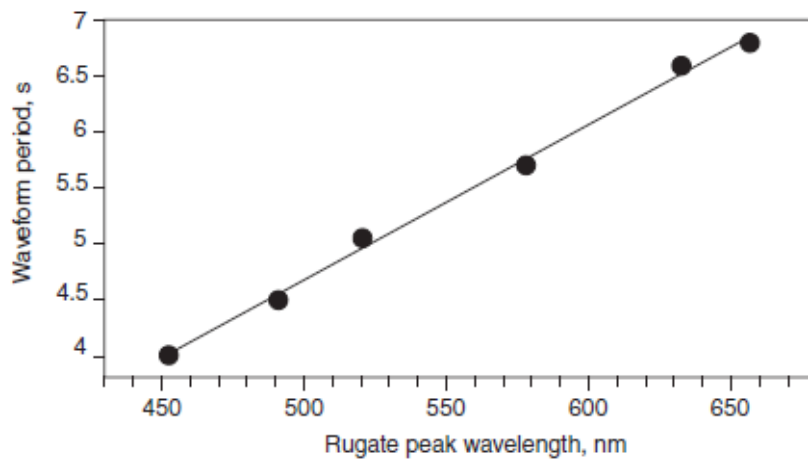


Figure 2.22 Effect of the period of a waveform on the position of the main reflectance peak of a RF³⁰

Additionally, the central position of the main reflectance peak is also influenced by the angle of incidence of the light^{38,39}. The relationship can be expressed as:

$$\lambda_{\theta} = \lambda_0 \cos \theta_a = \lambda_0 \sqrt{1 - \frac{(\sin \theta)^2}{n_{avg}^2}}, \quad (2.44)$$

where λ_{θ} denotes the wavelength of the main reflectance peak at an angle of incidence θ , while λ_0 represents the peak wavelength when the light is incident at a normal angle. The angle θ_a

corresponds to the propagation angle of light through the RF. Expression (2.44) is derived under the assumption that light enters the photonic structure from the air and indicates that an increase in the angle of incidence causes a blue shift of the reflectance peak position.

As mentioned in the previous section, the peak width can be controlled by the refractive index contrast and the number of cycles (repeats) in the waveform. Figure 2.23 illustrates how the current density values influence the porosity of the layers. Higher current density results in higher porosity and, consequently, a lower refractive index, meaning that by adjusting minimum and maximum value of the sinusoidal current density profile, it is possible to achieve the desired refractive index contrast. A higher amplitude of the sinusoidal wave results in a greater refractive index contrast, which consequently leads to a broader stopband, while the lower contrast yields a narrower reflectance peak. Mathematically, the relationship can be written as ^{30,34,35} :

$$\frac{\Delta\lambda}{\lambda} \propto \ln \frac{n_{max}}{n_{min}} \tag{2.45}$$

where n_{max} and n_{min} are maximum and minimum values of the refractive index in a cycle, respectively.

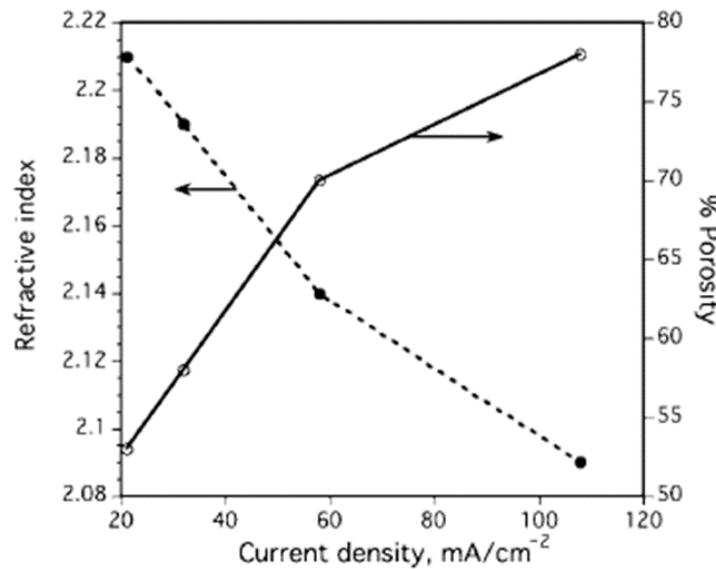


Figure 2.23 Empirically obtained relationship between the refractive index and porosity as a function of etch current density³⁰

It is important to mention that the dependence of the refractive index on the average current density follows the power law. However, for most highly-doped p-type silicon samples

(denoted as p^+ for moderately high doping and p^{++} for very high doping), the relationship can be approximated as linear function.

Additionally, the higher the number of repeats of the sinusoidal cycle results in a clearer and more pronounced reflectance peak, as shown in Figure 2.24.

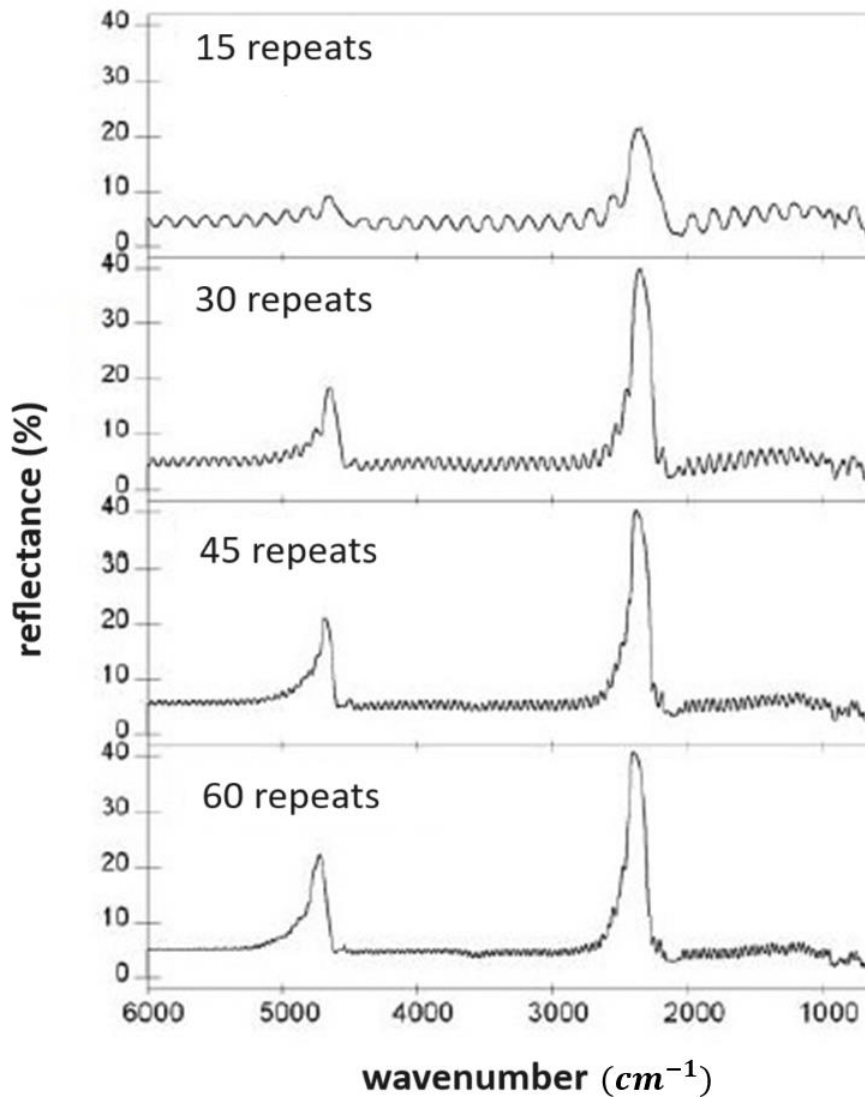


Figure 2.24 Comparison of the experimentally obtained reflectance spectra of RFs with the same period ($T = 43.7$ s), but different numbers of repeats³⁷

All of the above-mentioned parameters that influence the position and the shape of the RF's main reflectance peak indicate that the position of the reflectance peak of a rugate filter can be easily tuned by adjusting the etching process parameters, which makes them attractive for various applications.

Chapter 3. Porous silicon

There is a crack in everything; that's how the light gets in.

(L. Cohen)

3.1 Fabrication of porous silicon

Porous silicon (pSi) is a dielectric sponge-like material whose optical, electrical, and chemical properties have been investigated during the past three decades. Since its discovery in the 1950s, pSi has attracted much attention in various scientific fields, including photonics, electronics, biomedical devices, etc.^{30,40–42} Porous silicon is especially interesting due to its huge specific area, the ability to control pore dimensions and the depth profile, compatibility with silicon technology, biodegradability, and other interesting and distinct properties^{30,42}.

The most common method for the fabrication of porous silicon is electrochemical etching (anodization). This simple and reproducible technique involves the use of hydrofluoric acid (HF), usually diluted in ethanol (EtOH) a platinum electrode, and a silicon wafer that is to be etched, as shown in Figure 3.1

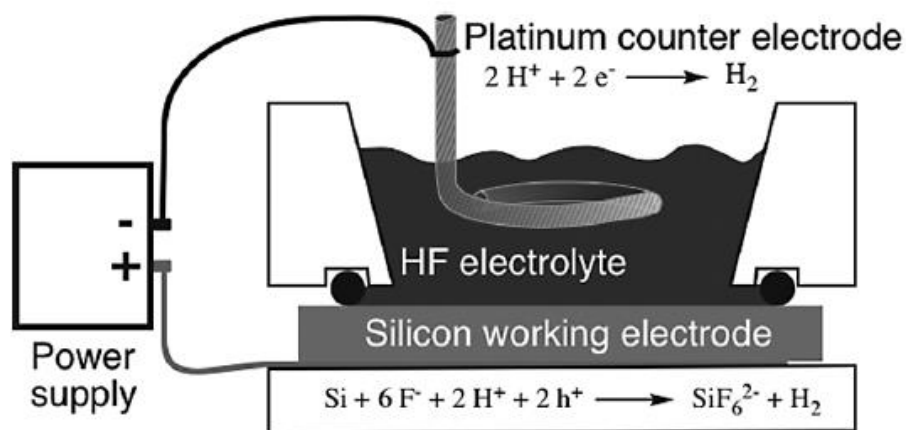


Figure 3.1 Schematic representation of a two-electrode electrochemical cell used to make pSi³⁰

In this process the electric current passes through a silicon wafer that is immersed in a HF solution and dissolves crystal silicon (cSi). By varying various etching parameters (electric current density, electrolyte composition, temperature, etc.), it is possible to create samples with specific morphology, pore dimensions, and optical and electrical properties³⁰.

According to IUPAC, there are three different types of porous silicon structures. Microporous silicon is highly reactive due to its large surface area, which results from pore dimensions

smaller than 2 nm and is usually produced at low current densities. Mesoporous silicon is characterized by pores whose size is between 2 and 50 nm and is formed with moderate current densities. Finally, macroporous silicon structures have pores larger than 50 nm, and high current densities are required for their production. It is important to mention that the etching process is not the same for all current densities. Instead, there is a characteristic current-voltage relationship for silicon depicted in Figure 3.2^{28,30,42}.

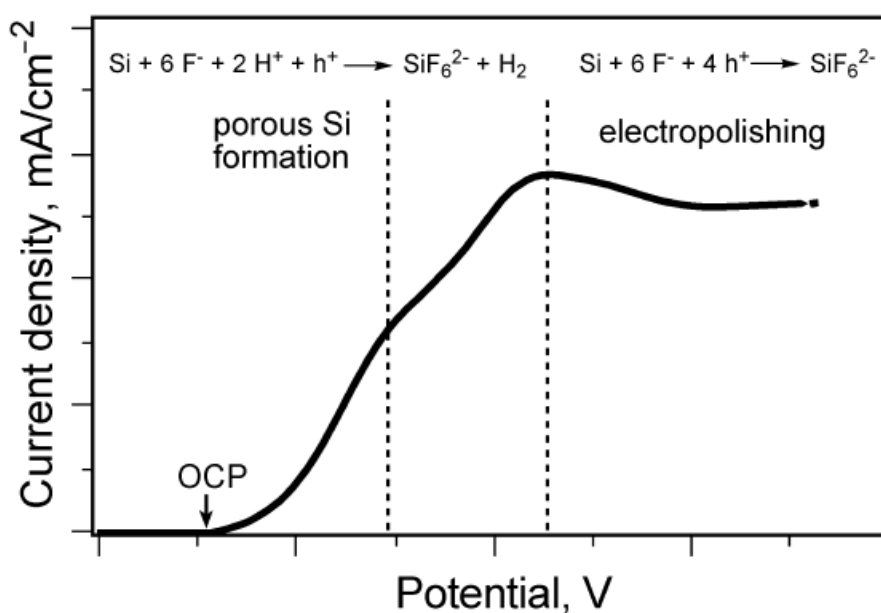
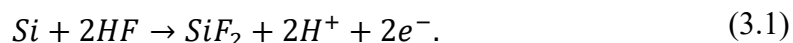


Figure 3.2 Current density as a function of applied potential for electrochemical etching of moderately doped p-type silicon in an HF electrolyte showing two different regimes for pSi formation and electropolishing. OCP stands for open circuit potential, or rest potential of the silicon electrode³⁰

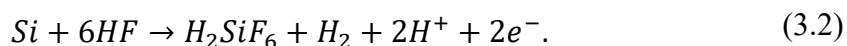
The curve shows the initial exponential rise in current with the applied potential that reaches a maximum, after which it decreases a bit and then continues to rise more slowly as the applied potential increases. The described behavior of the current-potential curve indicates that three different regions can be defined: the first represents the region of formation of pSi characterized by the nucleation and growth of pores within the silicon substrate. This region is followed by a transitional region in which pores can still be formed, but its surface coverage is not uniform. Finally, the electropolishing regime refers to a region where silicon substrate undergoes dissolution at a high rate under the influence of an applied high voltage and current density.⁴⁰

The etching process includes several important chemical reactions and is well explained by Lehmann and Gösele⁴³. The surface of the silicon wafer used in the process is usually covered with an oxide layer (SiO_2). When the Si wafer is immersed in an HF solution, the SiO_2 layer dissolves, which leaves Si surface reactive. On the other hand, in the etching process, an aqueous solution of HF is used, which partially dissociates in water. In this process, hydrogen

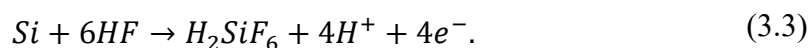
(H^+) and fluoride ions (F^-) are obtained, while some HF remains in its undissociated form. The H^+ ions can either bond with water molecules to form hydronium ions (H_3O^+) or directly interact with the silicon surface. When H^+ ions interact with Si atoms, they form Si-H bonds, which temporarily stabilize the surface. In the next step, as illustrated in Figure 3.3, F^- ions attack the Si-H bonds, displacing the hydrogen atoms and leading to the formation of Si-F bonds. The sequence of reactions that involves the attack of fluoride ions on Si-H bonds, and leads to the creation of Si-F bonds and generation of hydrogen gas (H_2) is represented by:



As F^- ions continue to attack the Si surface, the SiF_4 molecules are formed, which further react with excess of HF in the solution and eventually form H_2SiF_6 . The hexafluorosilicic acid (H_2SiF_6) formed in the process represents the portion of silicon that has been removed from the crystalline silicon. Additionally, hydrogen gas (H_2) is released as a byproduct of the reduction reaction. The anodic semi-reaction involving the dissolution of silicon in HF can be written as:



By increasing the voltage towards the electropolishing, the creation of hydrogen atoms starts to decrease, and it completely stops in the electropolishing regime²⁸. The electropolishing phase is characterized by the use of four electrons per every silicon atom. The high potential creates a strong driving force that oxidates the Si atoms, which is necessary for the Si to fully react with the F^- ions and eventually H_2SiF_6 is formed. In this regime, the process of Si dissolution is rapid due to the applied high voltage, so the removal of Si atoms is more uniform. Moreover, rapid dissolution prevents the formation of porous surfaces, which results in a smooth, polished, and more homogeneous layer. The anodic semi-reaction, in this case, is given by:



In both reactions, the final and stable product is hexafluorosilicic acid (H_2SiF_6). It is noteworthy that the electrochemical behavior of silicon shows two regimes: during the pore formation, only two out of four available silicon electrons participate in an interface charge transfer, while all four electrons are electrochemically active during the electropolishing.

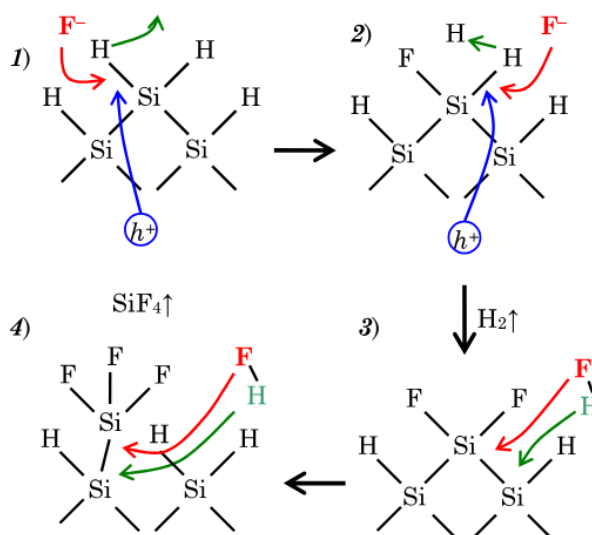


Figure 3.3 Diagram of the stages of electrochemical etching of silicon according to the Lehmann and Gösele model⁴⁴

It is important to note that as the silicon surface is being covered by hydrogen atoms, it becomes resistant to additional attacks by F^- ions since Si-H bonds are relatively stable and do not easily react with F^- ions^{43,45}. As can be seen from Figure 3.3, holes (h^+) are essential for overcoming this problem. In p-type silicon, holes are available due to the doping. When an anodic voltage is applied, these holes are pushed to the silicon-electrolyte interface, and they oxidize silicon atoms. In this process, positively charged silicon atoms (Si^+) are created. These silicon atoms are more likely to be attacked by F^- ions, which supports the continuation of the dissolution. When holes oxidize Si-atoms, the resulting Si^+ atoms have a greater tendency to attract electron pairs from F^- , which makes Si-Si bonds weaker. This makes holes crucial for maintaining the dissolution reaction since they keep silicon atoms in the oxidized state, which is more reactive. Without holes, the Si-atoms would be in a neutral, less reactive state^{40,46}. The schematic representation of the final pSi structure is given in Figure 3.4. The figure shows a cross-sectional view of the resulting porous silicon structure where white regions indicate the etched pores within the cSi substrate.

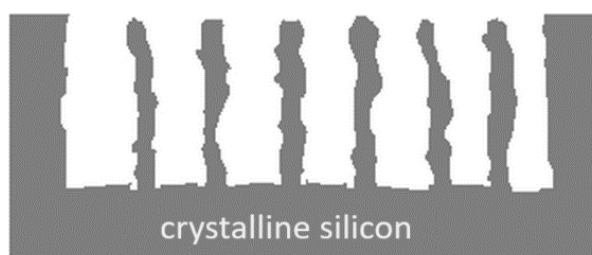


Figure 3.4 Cross-sectional view of pSi structure. The grey pillars represent Si walls, the grey area at the bottom represents the bulk cSi, and the white regions illustrate pores formed during electrochemical etching⁴⁷

It is important to mention that once etched, the porous structure is stable, and the walls between the pores are protected from further dissolution. This stability arises from the selective etching of silicon at the pore tips, rather than along the pore walls, primarily due to the formation of a depletion region and the effects of band bending at the Si-HF interface. Generally, bringing the semiconductor and the electrolyte into contact causes a redistribution of charges, as the Fermi level in the semiconductor and the redox level in the electrolyte equalize. In the semiconductor, this leads to band bending and depletion of charge carriers near the surface.⁴⁸

When p-type silicon is immersed in HF, a depletion region forms at the interface as holes, the majority carriers in p-type silicon, are repelled by the electric field created by charge redistribution at the surface. This electric field points from the electrolyte towards the silicon, pushing holes away from the interface and creating a potential barrier along the pore walls. The potential barrier acts as a self-limiting mechanism in the dissolution process by inhibiting charge transfer between the silicon and the electrolyte and reducing hole concentration along the pore walls, making them less reactive to fluoride ions and resistant to further etching.

The band bending induced by this field further increases the potential energy of holes near the walls, making it energetically unfavorable for holes to accumulate there, which significantly reduces their reactivity to fluoride ions. At the pore tips, however, the curved geometry of the tips causes the electric field to focus, concentrating the field strength and promoting hole accumulation. This localized field concentration affects the band bending, which results in a slightly lower potential barrier at the tips than along the pore walls, allowing more holes to accumulate at the tips. These accumulated holes drive the oxidation of silicon at the tips, initiating the etching process and allowing HF to dissolve the oxidized silicon. As a result, etching progresses primarily at the pore tips, where the potential barrier is locally reduced, while the pore walls remain depleted of holes and are less reactive. This selective hole depletion stabilizes the pore walls and protects them from further dissolution, thus maintaining the porous structure.

The fabrication of porous silicon through electrochemical etching involves several critical parameters that determine the resulting properties of the material^{30,40-42}. One of the most important factors is electrolyte composition since it controls the chemical reactions during the etching process. The concentration of HF directly influences the etching rate and porosity of the sample. Higher HF concentration means that more fluoride ions are available, which accelerates the dissolution of silicon and, therefore, the etching process. Fast etching results in a greater number of small pores, while slower etching, resulting from lower HF concentration,

creates a smaller number of larger pores, so the porosity profile is also influenced by the electrolyte concentration.

Current density is another important parameter that influences the porosity profile in a way that higher current densities generally give higher porosity and smaller pore sizes, whereas lower current densities result in larger pores but lower overall porosity. Additionally, the etching time is directly proportional to the depth of the porous structure, where a longer etching time results in a deeper porous layer. Furthermore, the characteristics of silicon wafers, including their doping type, resistivity, and crystalline orientation, significantly affect the etching process. In the case of n-type silicon illumination, it is often required to generate charge carriers that help the etching process, so the light intensity and wavelength are necessary.

Temperature affects both the rate of chemical reactions and the morphology of the pores, so the control of this parameter is crucial for reproducible results. The uniformity of the etching process can be improved by stirring the electrolyte solution during the etching process so that homogeneous pore distribution is obtained³⁰. Also, pre-etching cleaning of the silicon wafer is necessary to achieve uniform pores. On the other hand, after the etching process, an oxide layer is formed on the top surface of the pSi sample, and this oxidation process also modifies the properties of the sample. By precise control of the abovementioned parameters, pSi samples with desired structural and functional characteristics can be produced.

3.2 Porous silicon photonic crystals

Porous silicon photonic crystals (pSi PhCs) are advanced materials created by periodic variations of porosity in silicon structure, which can be achieved in one, two, or three dimensions. The porosity profile is directly related to the index of refraction since higher porosity corresponds to more air-filled voids, which consequently decreases the index of refraction of the particular structure. This fact is important because the periodic porosity profile leads to the periodic arrangement of layers with different refractive indices and, thus, the creation of the PBG in PhCs.

As mentioned earlier, the fabrication of pSi structures and pSi PhCs requires precise control of various etching parameters. One of the most important factors is the current density, which highly impacts the porosity of the structure. Periodic modulation of current density results in periodic modulation of porosity, which means that layers with alternating refractive indices can

be obtained. Such structures are periodic in one dimension and are called one-dimensional porous silicon photonic crystals (1D pSi PhCs).

Precise adjustment of etching parameters is necessary to obtain high-quality pSi PhCs with desired properties. Figure 3.5 shows how the position of the PBG can be precisely tuned by the optimization of required parameters.

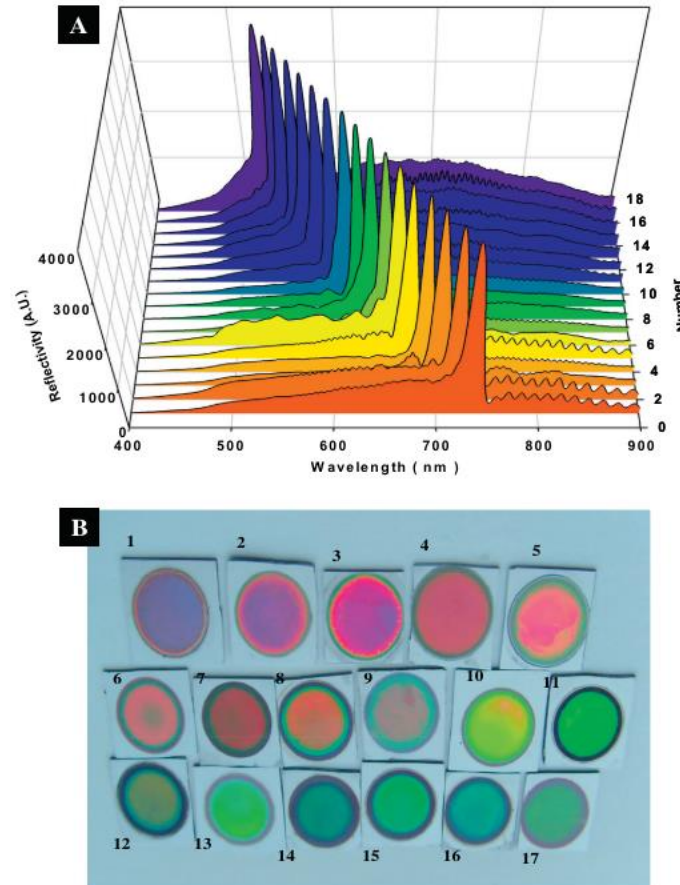


Figure 3.5 a) Reflection spectra of 1D pSi PhC obtained by various etching parameters b) Photograph of the corresponding samples illustrating the variation in color due to changes in the photonic structure⁴⁹

Porous silicon PhCs are particularly interesting due to their unique properties that distinguish them from other PhCs and even other porous material-based PhCs. Porous silicon is fabricated from silicon wafers, meaning that pSi PhCs are compatible with silicon technology, especially silicon-based microelectronics and micro-electro-mechanical system technologies. Moreover, the fabrication process is relatively simple and low-cost compared to production methods of other types of PhCs and also enables precise control of the etching parameters, which is important for fine-tuning the refractive index profile and obtaining the desired optical properties such as PBG position. Porous silicon is also specific for its high surface area and biocompatibility, which make pSi PhCs desirable for biosensing and chemical sensing

applications. Additionally, pSi PhCs can be easily integrated with various optoelectronic devices, such as LEDs, solar cells, photodetectors, etc. Unlike other porous material-based PhCs, such as porous alumina PhCs, pSi PhCs are more stable, which makes them suitable for long-term and high-performance applications^{42,50-53}.

Chapter 4. Raman signal enhancement

Alone we can do so little; together we can do so much.

(H. Keller)

As mentioned earlier, Raman spectroscopy is a powerful technique for the analysis and characterization of various compounds and samples, however, its inherently very weak signal is a challenge when it comes to sensitivity and detection limits. For this reason, various signal enhancement techniques have been developed to make Raman spectroscopy an acceptable choice for sensing, nanotechnology, and materials science. The enhancement of the Raman signal is crucial for the detection of low-concentration analytes and the improvement of the signal-to-noise ratio, which is important for obtaining good-quality spectra.

One of the first methods of enhancing the Raman signal was resonance Raman spectroscopy. The main condition in this technique is to match the laser excitation wavelength with the electronic transition of the molecule under study, which results in increased intensity of the Raman signal by several orders of magnitude.

Another approach is coherent anti-Stokes Raman spectroscopy in which two laser beams, the pump beam and Stokes beam, of different frequencies are used to excite the sample. Their interaction with the molecules in the sample excites specific vibrational modes of molecules. When the third laser beam, the probe beam, is introduced to the system, it interacts with the excited vibrational mode of a molecule and generates a coherent anti-Stokes signal of Raman scattering at a frequency that is higher than the original pump frequency by the amount equal to the vibrational frequency of the molecule. This technique has high spatial resolution and is very important in biological and medical research.

Although these techniques are valuable in certain fields of research, the highest Raman signal enhancement is achieved through surface-enhanced Raman scattering (SERS). In this technique, molecules of interest are adsorbed on the rough metal surfaces (usually gold or silver nanoparticles). Generally, nanostructured materials such as metal-coated substrates and nanomaterials play a significant role in the field of Raman signal enhancement. Other techniques like tip-enhanced Raman spectroscopy combine SERS and scanning probe microscopy in which a metal-coated tip is used to enhance Raman signal from a very small volume.

4.1 Surface-enhanced Raman scattering

Surface-enhanced Raman scattering is a powerful technique that significantly enhances the signal of Raman scattering by molecules adsorbed on or near rough metal surfaces or nanoparticles. The technique was discovered in the 1970s, and since then, it has significantly decreased the detection limit, enabling even the detection of single molecules^{54,55}. The enhancement of signal is primarily attributed to two main mechanisms: electromagnetic and chemical⁵⁶.

Chemical enhancement arises from an increase in the polarizability of a molecule due to charge transfer between the molecule and a metal surface, which increases the Raman scattering cross-section, as explained in Chapter 1. In this process, an electron from the metal nanoparticle near the molecule can form ionic or covalent bonds with the molecule, or charge transfer between the nanoparticle and the molecule can occur⁵⁷. These interactions increase the polarizability of the molecule, so the electron cloud becomes more easily distorted by the external EM field. This increased polarizability induced a stronger dipole, leading to a stronger interaction with the external field and, consequently, an enhanced Raman scattering signal.

On the other hand, electromagnetic enhancement originates from the excitation of localized surface plasmon resonance (LSPR) in metallic nanoparticles. The interaction of light and nanoparticles results in coherent oscillations of free electrons relative to the crystal lattice of positive ions. These oscillations are analogous to the oscillations of electron clouds in bulk materials, but since they are limited by the position and the size of nanoparticles, they are called localized surface plasmons. When the frequency of incident radiation matches the natural frequency of these oscillations, the resonance condition is satisfied, which leads to the great enhancement of the local EM field and, consequently, Raman scattering⁵⁸. It is important to mention that by careful choice of geometrical parameters such as the size and the shape of metallic nanoparticles, it is possible to obtain desired optical properties for specific applications in various fields. A significant interest in the field of plasmonics since the early 2000s resulted in the synthesis of various types of nanoparticles, such as nanospheres, nanorods, nanostars, nanoshells, etc., that have found applications in various fields, from biomedical diagnostics to photonics, and from medical imaging to solar cells and polarizers^{59,60}.

4.1.1 Localized surface plasmon resonance

The theoretical background of EM enhancement was explained by Gustav Mie, who provided an analytical solution to Maxwell's equations for scattering of the EM waves by metallic nanoparticles. To better understand the physical concept behind the enhancement, metal structures can be modeled as homogeneous isotropic metallic spheres, and the oscillating electric field can be modeled as a stationary plane wave given by:

$$E_0 = E_0' \sin(\omega_0 t) \quad (4.1)$$

When an incident light interacts with metallic nanoparticles, the electric field induces oscillations of conducting electrons that have the same frequency as the incident electric field. An illustration of such oscillations is presented in Figure 4.1.

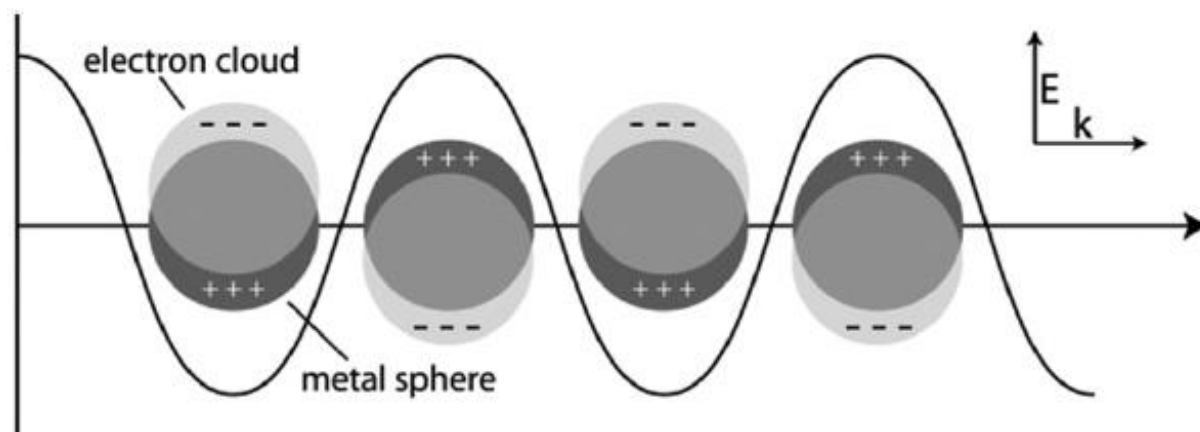


Figure 4.1 Schematic illustration of localized surface plasmon polaritons. E denotes the electric field vector, and k the wavevector⁶¹

In the case when the frequency of the incident light matches the natural oscillation frequency of localized surface plasmons in metallic nanoparticles, the resonance condition is achieved. This resonance leads to significant enhancement of the local EM field and is, therefore, crucial for the enhancement of the Raman signal.

Assuming that the particles are much smaller than the wavelength of the incident light (dipole approximation⁶²), the field within the nanoparticle will be uniform when placed in an external field. As a result, the nanoparticle will exhibit a dipole moment without higher-order multipole moments.

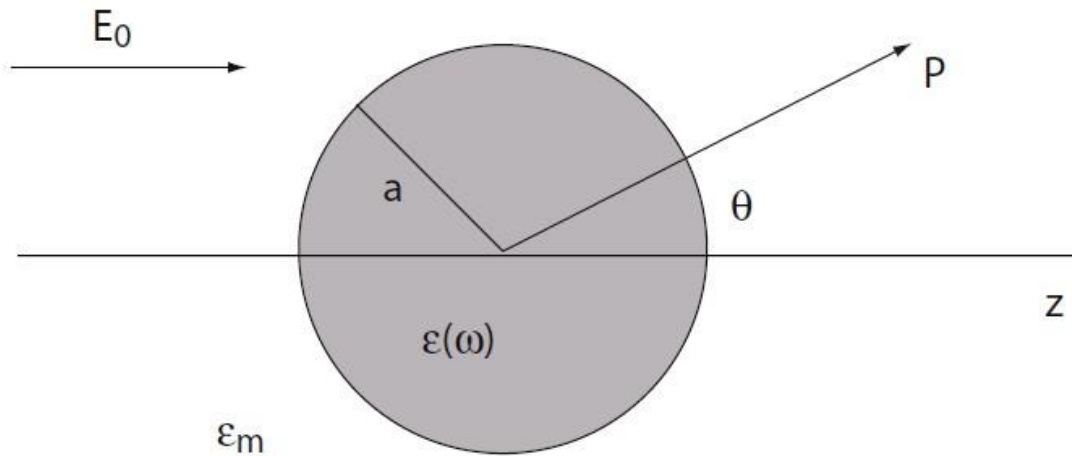


Figure 4.2 Representation of a homogeneous sphere placed into an electrostatic field. Electric field lines are parallel to the z-direction at a sufficient distance from the sphere. The surrounding medium of the relative permittivity ϵ_m is non-absorbing and isotropic, while the dielectric response of the sphere is described by the relative permittivity $\epsilon(\omega)$ ⁶³

In this case, solving Laplace’s equation with the appropriate boundary conditions gives the scalar potential both inside and outside of the sphere. However, since the molecule of interest is placed near or on the metal nanoparticle, we are primarily interested in the potential outside the sphere^{63,64} :

$$\Phi_{out} = -E_0 r \cos\theta + g \frac{a^3}{r^3} E_0 r \cos\theta , \tag{4.2}$$

where

$$g = \frac{\epsilon(\omega) - \epsilon_m}{\epsilon(\omega) + 2\epsilon_m} . \tag{4.3}$$

In these equations, a is the radius of the nanoparticle, E_0 is the incident electric field, ϵ_m is the complex relative permittivity of the surrounding medium, $\epsilon(\omega)$ is the complex frequency-dependent relative permittivity of the metallic nanoparticle and θ is the angle between the incident electric field and the specific point in space where the potential is to be determined. Equation (4.2) shows that the potential outside the particle has two contributions: the first resulting from the incident field and the second from the scattering. To understand the influence of the local field on a nearby molecule, we need to determine the electric field outside the sphere, which can be derived from $\vec{E} = -\vec{\nabla}\Phi$. The scattered electric field at a point r is given by:

$$\vec{E}_{sc} = g \frac{a^3}{r^3} E_0 (2\cos\theta\hat{r} + \sin\theta\hat{\theta}). \quad (4.4)$$

Comparing the equation (4.4) with the expression for the electric field obtained from an ideal dipole placed in the center of the sphere

$$\vec{E}_p = \frac{p}{4\pi\epsilon_0 r^3} (2\cos\theta\hat{r} + \sin\theta\hat{\theta}), \quad (4.5)$$

leads to a conclusion that the induced dipole moment p is given by

$$p = 4\pi\epsilon_0 g a^3 E_0. \quad (4.6)$$

Recalling the expression that links the dipole moment with the external electric field, $\vec{p} = \alpha\vec{E}_0$, and combining it with (4.6) gives the polarizability α :

$$\alpha = 4\pi\epsilon_0 g a^3. \quad (4.7)$$

Equation (4.7) is a very important result that gives the expression for the polarizability of a small sphere, whose diameter is smaller than the wavelength of the incident light (electrostatic approximation). The expression shows that the polarizability is proportional to the volume of the nanoparticle and factor g . This factor g is crucial for the local enhancement of the electric field, as will be shown shortly.

The resonance condition for localized surface plasmons is determined by the singularity of the expression (4.3). The singularity condition requires that:

$$\epsilon(\omega) + 2\epsilon_m = 0. \quad (4.8)$$

Generally, relative permittivity of metallic nanoparticles describes the response of electrons in metallic structures on the incident EM field. In dipole approximation, the relative permittivity consists of two parts: one from Drude model and the other that includes corrections due to possible transitions of bound electrons into higher bands^{63,65}:

$$\epsilon = \epsilon_\infty - \frac{\omega_p^2}{\omega^2 + i\gamma\omega} \quad (4.9)$$

where ϵ_∞ represents the response due to interband transitions, ω is the angular frequency of the incident radiation, γ is the frequency of electron collisions with the crystal lattice and ω_p is plasmon frequency of free electrons in bulk material defined as

$$\omega_p = \sqrt{\frac{Ne^2}{\epsilon_0 m_e}}. \quad (4.10)$$

From equation (4.10) it can be seen that the plasmonic frequency is related to the number of free electrons N in a particular metal and also depends on band structure within the metal through the effective mass of the electrons m_e .

It is important to notice that the relative permittivities are complex quantities, but the real part gives the condition for the plasmon resonance

$$Re[\varepsilon(\omega)] = -2\varepsilon_m \tag{4.11}$$

while the imaginary part gives information about the absorption losses in real metals. The condition (4.11) is known as the Fröhlich condition and the corresponding oscillating field mode is called the dipole surface plasmon of the metallic nanoparticle. Equation (4.11) also implies that the resonant frequency strongly depends on the dielectric constant of the surrounding medium: the higher the relative permittivity of the surroundings, the lower the resonant frequency^{63,66,67}.

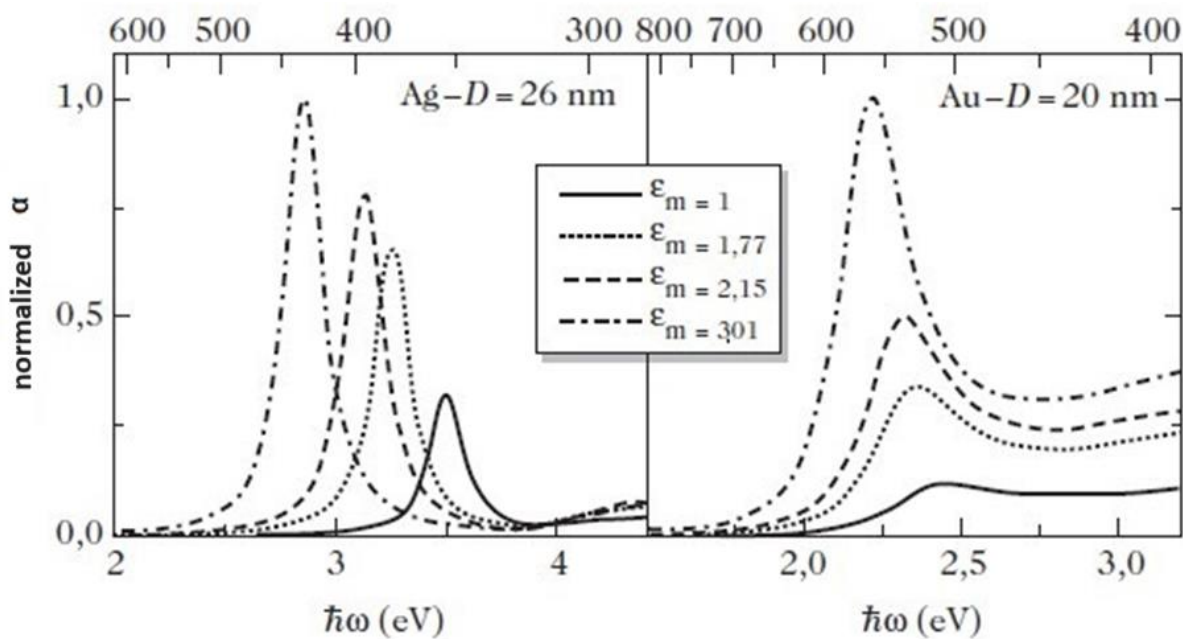


Figure 4.3 Absorption spectra calculated within the quasistatic approximation for silver (diameter $D = 26 \text{ nm}$) and gold nanospheres (diameter $D = 20 \text{ nm}$) in various media: vacuum ($\varepsilon_m = 1$), water ($\varepsilon_m = 1,77$), silicon dioxide ($\varepsilon_m = 2,15$) and aluminium ($\varepsilon_m = 3,01$)⁶⁸

The origin of this effect lies in the fact that changing the relative permittivity of the surrounding medium influences its ability to adapt to the charge oscillations within the nanoparticle. When the frequency of the incident light meets the condition given by (4.11), the factor g drastically increases, and plasmon resonance is achieved. This resonance leads to high polarizability and significant enhancement of the field around the metallic nanoparticle, as shown in equation (4.4).

The resonance frequency for surface plasmons in the case of noble and alkali metals is given by⁶⁹:

$$\Omega_{LSPR} = \frac{\omega_p}{\sqrt{\varepsilon_1^{ib}(\omega) + 2\varepsilon_m}} \quad (4.12)$$

where ε_1^{ib} is the real part of the dielectric function corresponding to interband transitions. For free electrons, $\varepsilon_1^{ib} = 1$, and in a vacuum ($\varepsilon_m = 1$), the Frölich condition is met at the frequency

$$\omega_0 = \frac{\omega_p}{\sqrt{3}}, \quad (4.13)$$

where ω_p is the frequency of the plasmons in the bulk of the material. This is in good agreement with the experimentally obtained data, however, due to interband transitions that are energetically close to the surface localized plasmon resonance, gold and copper show deviations from the theoretically derived data^{70,71}. In the case of silver, due to its unique electronic structure, which minimizes energy losses through interband transitions⁶³, the corresponding damping of the surface plasmons is not so pronounced, so silver shows the strongest LSPR intensity, as presented in Figure 4.4.

As mentioned earlier in the text, the real part of the dielectric function determines the frequency of the plasmon resonance and indicates how strongly the material is polarized by an external EM field. Contrarily, the imaginary part is responsible for the broadening of the resonance peak as it accounts for the various loss mechanisms such as material absorption, electron-electron scattering, and other non-radiative processes that dampen the plasmonic oscillations, so the balance between the real and imaginary part defines the overall efficiency and the intensity of the LSPR. In general, a narrower plasmon line width is attributed to electrons that are less influenced by the ionic core potential, which implies a higher LSPR intensity⁷².

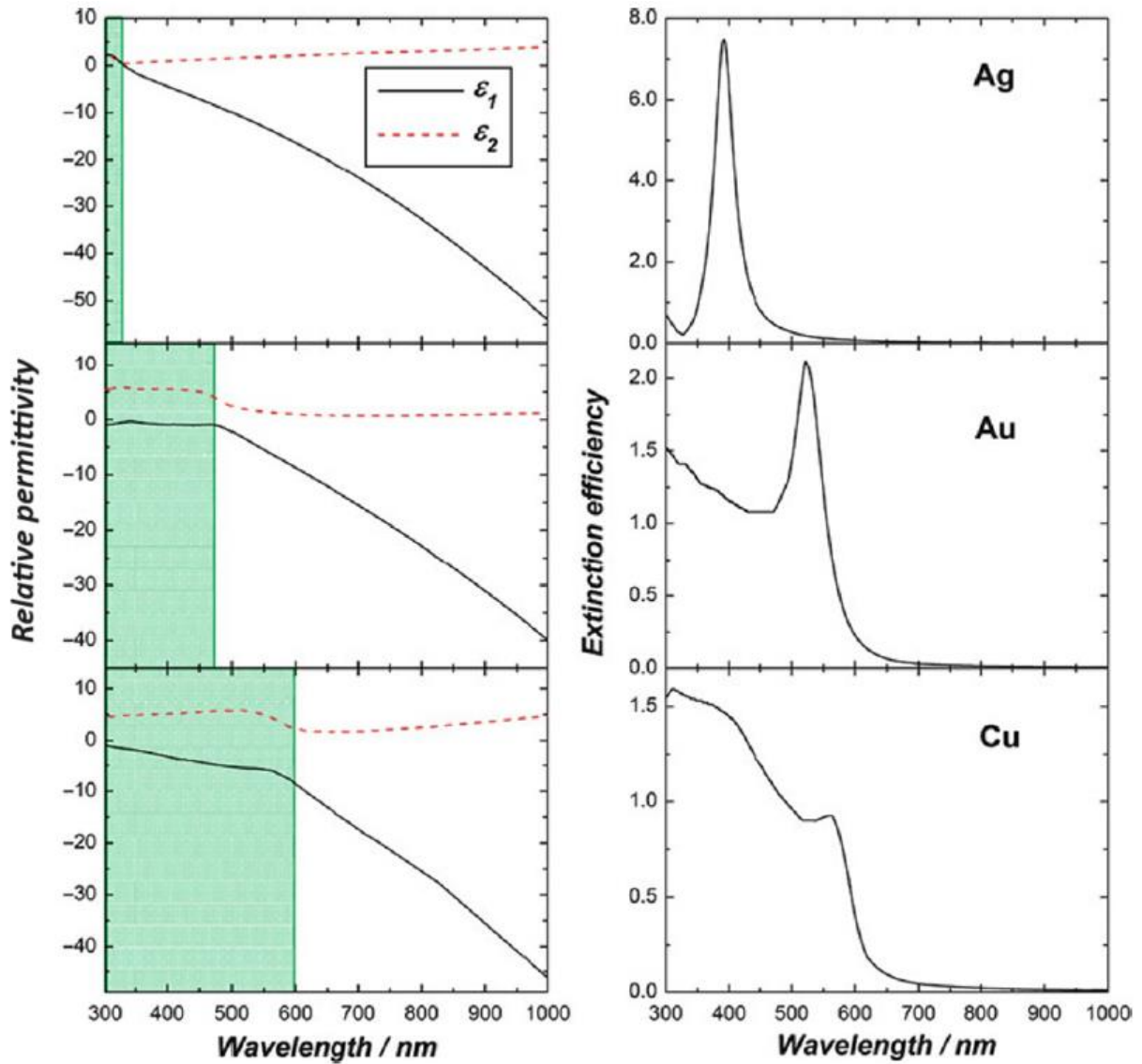


Figure 4.4 Relative permittivities and the calculated extinction spectra of a silver, gold, and copper nanosphere (diameter $D = 30nm$). The green areas represent the wavelength ranges where the real part of the relative permittivity is negative⁷³

4.1.2 Raman signal enhancement

As explained in Chapter 1, Raman scattering by a molecule is a result of the interaction between an incident EM radiation and the induced dipole moment within a molecule. The dipole moment is influenced by the external electric field, vibrational frequency of the molecule, and polarizability of the molecule, and the final expression is given by (see (1.10)) :

$$\vec{p}_M = \alpha_0 \vec{E}_0 \cos(\omega_0 t) + \frac{1}{2} Q_{k_0} \vec{E}_0 \left(\frac{\partial \alpha}{\partial Q_{k_0}} \right)_0 [\cos(\omega_k + \omega_0)t + \cos(\omega_k - \omega_0)t] \quad (4.14)$$

where the first term corresponds to Rayleigh scattering, while the second and the third correspond to Raman scattering. Additionally, in this context $\vec{\mu}(t)$ is replaced by \vec{p}_M .

From the previous discussion, it is important to emphasize the following key points:

- scattering of the electric field by the metallic nanoparticle does not change the frequency of the light; however, it significantly enhances the electric field. This enhancement is the main property of the metal nanoparticles in SERS
- scattering by the molecule results in a frequency shift that produces the Raman signal.

When a molecule of polarizability α_M is placed in an enhanced electric field E_{sc} resulting from the scattering of EM radiation on the metallic nanoparticle, it can be described as a new dipole with a dipole moment p_1 :

$$p_1 = \alpha_M E_{sc} . \quad (4.15)$$

This dipole oscillates with the frequency of the incident electric field ω_0 and creates a field $E_{dip}(\omega)$. This field is a scattered field and can be calculated similarly as E_{sc} described in the section 4.1.1. However, its frequency is different from the frequency of the incident electric field. This new field $E_{dip}(\omega)$ now polarizes the metal sphere and induces another dipole p_2 :

$$p_2(\omega) = 4\pi\epsilon_0 g' a^3 E_{dip}(\omega) \quad (4.16)$$

The potential outside the sphere, in this case, is similar to the equation (4.2), and the electric field in radial direction is given by:

$$\vec{E}_{tot} = E_{dip} \cos\theta \hat{r} + 2g' \frac{a^3}{r^3} E_{dip} \cos\theta \hat{r}. \quad (4.17)$$

Therefore, for molecules located in regions of maximum enhancement, where $\theta = 0^\circ, 180^\circ$:

$$E_{tot} \sim g' E_{dip} \sim g' \alpha_M E_{sc} \sim g' \alpha_M g E_0, \quad (4.18)$$

or

$$E_{tot} \sim g' g \alpha E_0 \quad (4.19)$$

if the change in the polarizability of the molecule by the metal nanoparticle is $\alpha_M \rightarrow \alpha$. To conclude, there are two contributions to the Raman signal: the first from the dipole p_1 that creates the electric field $E_{dip}(\omega_{Raman})$, and the other from the dipole p_2 that oscillates at the Raman frequency ω . Since the intensity of the total scattered radiation, I_{SERS} , is proportional to the square of the resultant electric field, $I \sim E_{tot}^2$:

$$I_{SERS} \sim E_{tot}^2 \approx g'^2 g^2 \alpha^2 E_0^2. \quad (4.20)$$

In the case of low-frequency modes and when the laser excitation overlaps with the plasmonic resonance, g and g' are similar, so the intensity of the SERS signal is proportional to the fourth power of the factor g :

$$I_{SERS} \sim g^4 \alpha^2 I_0 \quad (4.21)$$

This approximation is not valid for the high-frequency modes ($\geq 500 \text{ cm}^{-1}$), for which the frequency difference between the incident and scattered photons is relatively high⁶⁵, generally resulting in weaker enhancement. The enhancement of high-frequency modes is influenced not only by their frequency but also by the degree of overlap between the laser excitation and the plasmonic resonance. When the plasmonic resonance aligns closely with the laser excitation and the Stokes line, significant amplification can still occur, regardless of the mode frequency. It has been shown^{74,75} that the maximum SERS amplification is expected when the laser excitation is slightly blue-shifted relative to the LSPR, placing the LSPR peak between the laser and the Stokes Raman emission. However, more recent studies indicate that as the excitation moves from the visible to the near-infrared region, the optimum condition shifts, requiring the excitation to be red-shifted from the LSPR peak^{76,77}.

Following the explanation of SERS, it is important to consider factors that affect enhancement efficiency with which the metallic nanoparticle scatters or absorbs the incident radiation. The corresponding cross-sections are given by⁶³:

$$C_{sc} = \frac{k^4}{6\pi} |\alpha|^2 = \frac{8\pi a^6}{3\lambda^4} \left| \frac{\varepsilon - \varepsilon_m}{\varepsilon + 2\varepsilon_m} \right|^2 \quad (4.22)$$

$$C_{abs} = k \text{Im}|\alpha| = \frac{4\pi a^3}{\lambda} \text{Im} \left| \frac{\varepsilon - \varepsilon_m}{\varepsilon + 2\varepsilon_m} \right|. \quad (4.23)$$

When considering small nanoparticles, specifically those with radii significantly less than the wavelength of incident light, the predominant occurrence is absorption rather than scattering. This is because the efficiency of absorption is directly proportional to the volume of the nanoparticle, whereas the efficiency of scattering is proportional to the square of the volume. Therefore, for very small particles, absorption is the dominant process due to its stronger dependence on the volume compared to scattering. If we assume that the relative permittivities of the metal and the surrounding medium are non-dispersive, the scattering cross-section is Rayleigh-type scattering. In this case, the scattering intensity increases with the fourth power

of frequency, which means that shorter wavelengths (higher energies) scatter much more efficiently than longer wavelengths.

Additionally, as the size of the nanoparticle increases beyond the quasistatic approximation limit ($a \leq \frac{\lambda}{10}$), the interaction of the incident EM wave and the spherical nanoparticle must be analyzed using the more general Mie theory. An important prediction of Mie theory is the redshift of the LSPR frequency with the increase of the size of nanoparticles. This redshift occurs due to retardation effects, such as delays in the response of the electrons in the nanoparticle to the oscillating EM field^{63,78}. Moreover, with increasing the size of the nanoparticle, higher-order multipole resonances (quadrupole, octupole, and even higher-order modes) start to appear⁷⁹. These higher-order modes become more pronounced and contribute to the overall scattering and absorption spectra of the nanoparticles.

In summary, small nanoparticles primarily absorb light with minimal scattering, while larger nanoparticles exhibit significant scattering and more complex interactions with light. As nanoparticle size increases, the LSPR shifts to lower frequencies due to retardation effects, and higher-order resonance modes appear.

The total extinction cross-section C_{ext} for a metallic spherical nanoparticle with a dielectric function $\varepsilon = \varepsilon_1 + i\varepsilon_2$ in the quasistatic approximation is proportional to the volume of the particle⁶³:

$$C_{ext} = 9 \frac{a^3}{\lambda} \sqrt{\varepsilon_m^3} \frac{\varepsilon_2}{(\varepsilon_1 + 2\varepsilon_m)^2 + \varepsilon_2^2} \quad (4.24)$$

This equation shows that the extinction cross-section is directly proportional to the volume of the particle, indicating that larger particles have a greater cross-section and, therefore, greater capacity to interact with incident light. This interaction is influenced by both the intrinsic properties of the material of the nanoparticle, described by the dielectric function, and the extrinsic properties of the surrounding medium.

When two or more metallic nanoparticles are in close proximity, near-field effects come into play. The electric field that each nanoparticle experiences is not just from the incident light but a combination of an incident field and fields generated by neighboring particles. This superposition of EM fields leads to coupled plasmonic oscillations^{62,71,79,80}, which can modulate the plasmon oscillation frequency and shift it to lower (red-shift) or higher (blue-shift) values. The coupling strength and resulting frequency shift depend on the distance between the particles and the polarization of the incident light. The red-shift phenomenon suggests that lower energy is required for plasmon excitation, which can be advantageous in applications such as sensing,

where shifts in resonance frequency can be used to detect changes in the environment or the presence of specific molecules. The shift in the resonance frequency of surface localized plasmons is also highly dependent on the polarization of the incident light relative to the distance between the nanoparticles. When the light is polarized parallel to the axis that connects two nanoparticles, the LSPR shifts to lower-frequency values. Additionally, studies^{71,79,81} have shown that for polarization parallel to the axis connecting two nanoparticles, the red-shift in the resonance frequency of surface localized plasmons is exponential with the decrease in distance between the nanoparticles. This behavior is consistent regardless of the size of the nanoparticles, their shape, metal composition, or the surrounding medium. This fundamental observation is referred to as the "universal scaling law."

In conclusion, the extinction cross-section of metallic nanoparticles and the near-field effects arising from their proximity are crucial in determining their optical properties. The coupling of plasmonic oscillations leads to significant shifts in resonance frequencies, which are dependent on the inter-particle distance and the polarization of the incident light.

Finally, after discussing the theoretical background, it is important to define the measure by which the Raman signal enhancement can be determined. The enhancement factor (EF) can be defined as:

$$EF = \frac{I_{SERS}}{I_R} \quad (4.25)$$

where the I_R is the intensity of the Raman signal. In the ideal case, the EF can be of the order 10^{10} or 10^{11} , which enables the detection of one molecule. For comparison, the chemical contribution usually results in an enhancement factor of $\leq 10^3$, which is significantly lower than the EM contribution, so the EM part prevails. It is important to note that determining the intensity of Raman spectra can be challenging due to the low Raman scattering cross-section of the probe molecule or due to the inherent photoluminescence at certain wavelengths, which can produce a strong background that can cover the Raman signal¹². This has led to a broad range of reported EFs in the literature, which can be challenging to obtain or reproduce. Therefore, it is important to accurately estimate the Raman signal intensity.

4.1.3 Porous silicon as SERS substrate

While significant progress has been made in improving and optimizing SERS substrates through the development of nanoscience and related techniques, there are still challenges that prevent the quantitative analysis of SERS and its application in fields such as clinical diagnostics and technological investigations⁸². The main challenge is the development of substrates that can consistently meet the request for strong and uniform EF, chemical stability, and cost-effective, reproducible production methods. The need for the perfect SERS substrate continues to motivate researchers to explore new materials and fabrication techniques to overcome these limitations. The goal is to create substrates that provide reliable and high-performance SERS signals for a wide range of applications.

Generally, SERS substrates can be divided into three major groups^{12,41} :

1. **Suspensions of metal nanoparticles (colloidal suspensions)** consist of a uniformly dispersed phase in a dispersing medium and are among the most commonly used SERS substrates. They can be easily prepared in a straightforward way by chemical reduction of metal salts. However, the issue with colloids is their stability and the tendency of nanoparticles to aggregate, which makes the SERS signal unstable and/or poorly reproducible.
2. **Nanostructures produced directly on solid substrates** include irregular metallic surfaces on which the SERS effect was initially discovered. These nanostructures are commonly produced by electrochemical techniques. However, despite their effectiveness, their application has decreased due to the discovery of new, simpler, and more reproducible methods. Modern advancements have introduced techniques that not only simplify the fabrication process but also enhance the consistency and uniformity of the resulting substrates. Methods such as physical vapor deposition and chemical vapor deposition have gained popularity, providing more controlled nanostructure formation. Additionally, these newer techniques often allow better integration with existing technology. As a result, the focus has gradually moved towards these innovative approaches that promise improved performance and ease of production.
3. **Metal nanoparticles deposited on solid substrates** can be organized or disorganized metal films. Organized metal films are created using lithographic techniques, which ensure high reproducibility. However, the lithographic process is relatively slow and expensive, limiting its practicality for large-scale applications. On the other hand,

disorganized metal films, which can be either continuous or discontinuous, are fabricated using various deposition methods. The simplest method involves drying a prepared colloidal solution on a particular substrate. This approach is relatively simple, but it also presents challenges, such as limited control over the deposition process. This lack of control can lead to poor reproducibility and inconsistent performance of the substrates. Despite these challenges, research is ongoing to improve the deposition techniques for disorganized films.

In this study, a metal-coated pSi was used as a SERS substrate, which is part of the third group in the abovementioned classification. The main advantage of pSi as a SERS substrate is its high specific surface area, which can host a significantly larger number of metal nanoparticles compared to standard flat substrates such as glass^{83,84}. Due to the cost-effective and straightforward fabrication process of SERS substrates, intense research and development efforts have been focused on SERS-active substrates based on pSi templates, as summarized in a review article by Bandarenka⁸⁵.

As mentioned earlier in this work, one of the main properties of pSi is that its surface morphology depends on the etching parameters. The surface morphology, in turn, dictates the morphology of the deposited metal nanostructures. In the literature, there are various examples of metal structures deposited on pSi, as represented in Figure 4.5. The methods used to make these structures vary and are affected by several factors, such as the etching conditions, the type and doping of the pSi, and the methods and conditions used for metal deposition. These factors significantly impact the distribution, size, and density of metal nanoparticles deposited on the pSi surface, so by fine-tuning these parameters, it is possible to optimize the SERS enhancement factor and achieve more consistent and reproducible results.

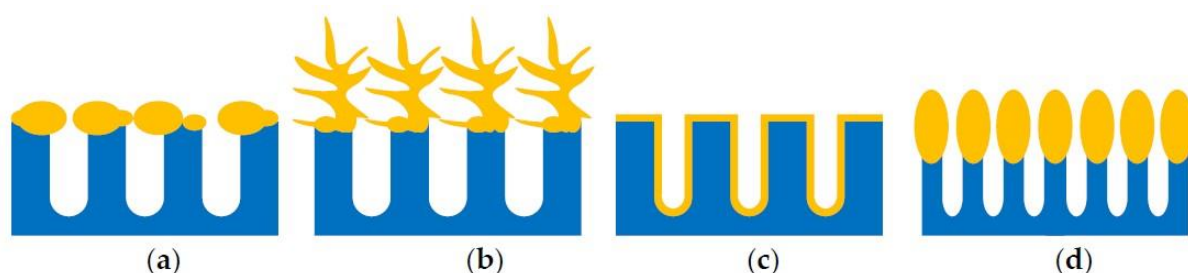


Figure 4.5 The schematic view of plasmonic structures formed on pSi: a) metallic particles b) metallic dendrites on the outer surface of the porous layer c) conformal metallic film on the pore walls d) oval-shaped metallic nanoparticles on the top of the silicon nanowires⁸⁵

Moreover, pSi allows the deposition of various metal nanoparticles, such as gold, silver, and platinum. Each of them offers unique plasmonic properties that can be used for different analytical applications.

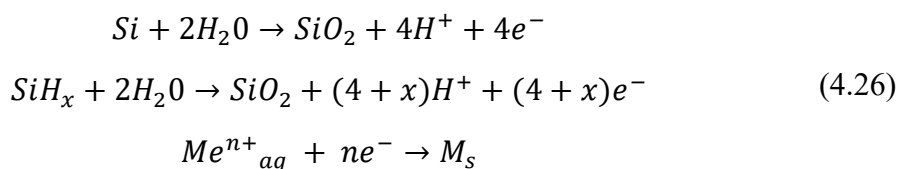
There are various methods to deposit plasmonic metal nanostructures onto pSi, which can be roughly categorized into dry and wet processes^{85,86}. Dry processes involve techniques such as vacuum evaporation, metal sputtering, physical vapor deposition, and pulsed laser ablation. On the other hand, wet processes include methods like thermal decomposition, drop coating from colloidal solutions, chemical and electrochemical deposition, and immersion plating (or dip coating), where immersion plating is the most common one.

Immersion plating is particularly popular for depositing metal nanoparticles on pSi due to its simplicity and low cost. This method does not require special experimental equipment or special conditions like high temperatures, lighting, vacuum conditions, or the application of external potentials⁸⁷. However, the important parameters that influence the morphology of the nanoparticles have to be precisely controlled. Those are the deposition conditions, with the most critical factors being the duration of immersion and the concentration of the metal salt solution^{41,85}.

The high specific surface area of pSi is an important property that is utilized in the immersion plating technique since it offers a large number of available electrons and surface states. When pSi is immersed in an aqueous solution of metal salt, it spontaneously reduces metal ions with a positive reduction potential relative to hydrogen⁸⁸. Metals like gold, silver, and copper have this property, and they provide a cost-effective way to produce reliable SERS-active substrates from pSi.

The process of preparing the pSi SERS substrate begins with the immersion of the pSi in the solution of metal salt, resulting in a simultaneous reduction of metal ions and oxidation of the pSi through coupled redox reactions. This dual reaction mechanism efficiently deposits metal nanoparticles and contributes to the stability and functionality of the resulting SERS substrate. By fine-tuning the immersion conditions, it is possible to achieve high control over the size, distribution, and density of the metal nanoparticles, which helps to optimize SERS substrates for good performance in various applications.

As previously mentioned, when pSi is immersed in aqueous solution of metal salt, a simultaneous reduction of metal ions and oxidation of the pSi occurs through coupled redox reactions:



Here, M represents a specific metal, and the subscripts 'aq' and 's' indicate aqueous solution and crystalline state, respectively. Moreover, the first two equations represent the oxidation processes, while the third describes the reduction process. As illustrated in Figure 4.6, metal deposition occurs simultaneously at various sites across the entire surface of the pSi. This deposition is influenced by the morphology of the pSi in a way that surface defects like scratches and irregularities serve as preferred sites for metal deposition⁸⁸. Consequently, metal deposition on pSi is much faster and more pronounced compared to cSi, which has a smooth surface with fewer surface defects.

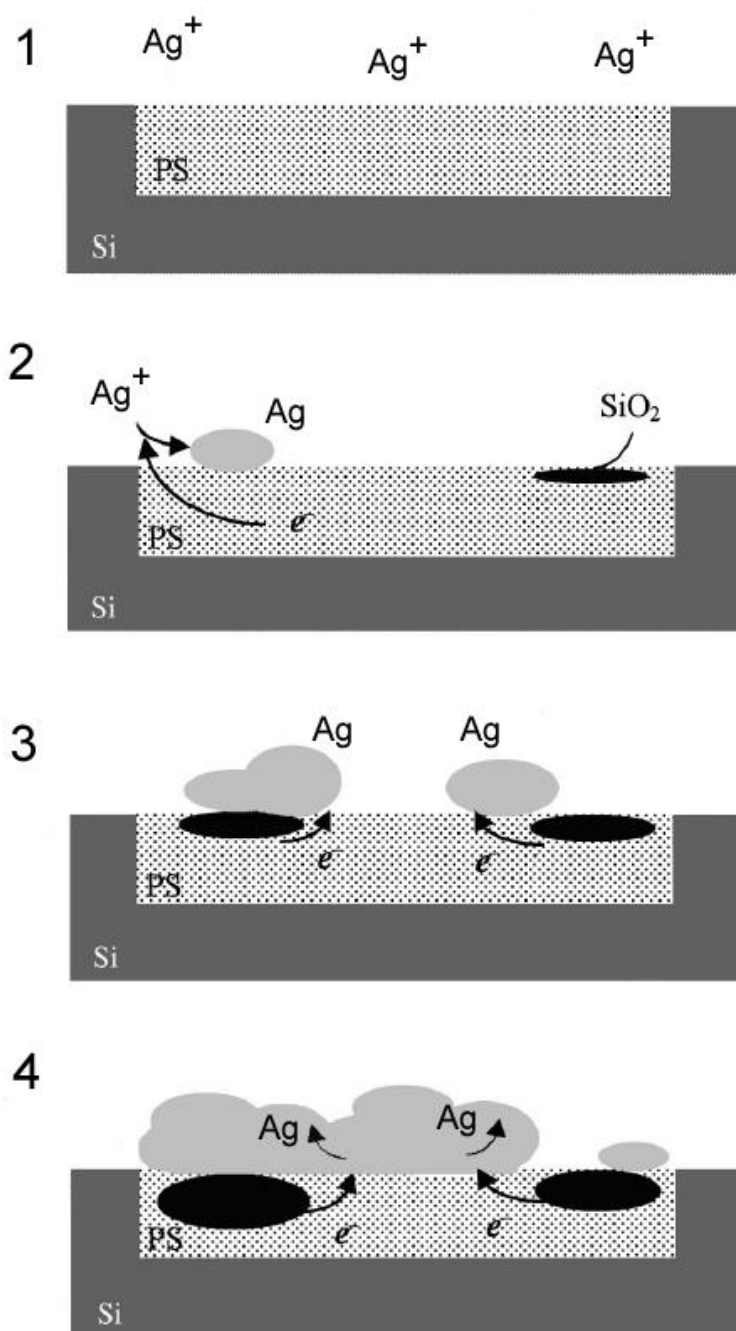


Figure 4.6 Formation process of a nanostructured silver film on porous silicon. Silver ions are reduced, while porous silicon is oxidized, leading to the formation of silver and silicon oxide. As the process continues, numerous silver nanoparticles are formed, leading to the formation of nanostructured silver film⁴⁷

The effectiveness of metal deposition on pSi can be improved by optimizing various parameters in the immersion process. For instance, adjusting the concentration of the metal salt solution, immersion time, and temperature can all significantly improve the quality and uniformity of the metal nanoparticle layer. Additionally, the initial surface treatment of pSi, such as surface roughening or functionalization, further improves the efficiency of metal deposition.

Surface roughening enhances the number of reactive sites available for metal ion reduction, which increases the density of deposited nanoparticles. Functionalization, on the other hand, can introduce specific chemical groups that enhance the affinity between the pSi surface and the metal ions, which ensures a more uniform and controlled deposition. Moreover, advanced deposition techniques, such as pulsed laser deposition and magnetron sputtering, can provide even more precise control over nanoparticle characteristics, although they are more complex and costly. Traditional methods like immersion plating are relatively simple and affordable, and their optimization continues to improve, which is crucial for developing high-performance SERS substrates that can be used in various applications, from biosensing to environmental monitoring.

4.1.4 SERS with NIR laser excitation

For a given excitation frequency ω , the intensity of Raman scattering is proportional to its fourth power, $I \sim \omega^4$. Since the Raman signal is inherently weak due to the small cross-section (low probability of inelastic scattering), it is a good idea to use high-energy lasers in Raman spectroscopy to maximize signal intensity. Additionally, the resonances of localized surface plasmons, which are crucial for the SERS effect, typically occur in the visible range.

However, in recent years near-infrared (NIR) lasers have attracted much attention^{54,89–92} especially in the analysis of biological samples^{93,94}. While they operate at lower energies and therefore produce weaker Raman signals, the reduced energy of the laser beam helps minimize fluorescence interference, which is a common issue in Raman spectroscopy. This makes NIR laser excitations particularly suitable for biological and medical applications without altering the properties of the sample. Despite the advantages of NIR lasers, it is essential to adapt SERS substrates to ensure sufficient Raman signal intensity under NIR excitation. Traditional SERS substrates optimized for visible light may not perform well under NIR excitation due to the different plasmonic properties required to enhance the Raman signal at longer wavelengths. Therefore, developing substrates specifically optimized for NIR excitation is essential to maximize the advantages of this approach across various fields.

4.2 Photonic crystals as Raman and SERS signal enhancers

In Chapter 2, we have introduced photonic crystal structures and explored the fundamental principles of PhCs and their ability to control and manipulate light propagation, which makes them very attractive for various optical applications. The central term in the discussion about PhCs is photonic bandgap, which not only prohibits the propagation of a specific range of wavelengths but also significantly reduces group velocity and modifies DOS at its edges. As discussed in 2.5, the DOS is significantly increased at the edges of the PBG, leading to an increased probability of light-matter interactions, which in turn enhances the scattering rate and, consequently, the intensity of the Raman signal. Moreover, PhCs slow down the propagation of light, leading to a reduced group velocity at the edges of the PBG, which increases the interaction time between the incident excitation and the Raman-active molecules. Similar to the effect of increased DOS, the longer light-matter interaction time increases the probability of Raman scattering, resulting in an enhanced Raman signal. Furthermore, when a probe molecule is placed on the surface of a photonic structure, and the laser excitation is aligned with the center of the PBG, the incident light passes through the probe molecule, before being reflected by the photonic structure. This reflection causes the light to pass through the probe molecule a second time, which should ideally double the chances for the Raman scattering due to the increased interaction with the probe molecule.

As mentioned earlier, precise tuning of the position of the PBG can be achieved by careful design, which allows precise control over the enhancement conditions. Additionally, PhCs can be combined with other nanostructures, such as metallic nanoparticles in SERS, to further enhance the Raman signal.

The potential to adjust the PBG position and the associated optical properties means that it is possible to position the PBG to align with the desired excitation wavelengths for Raman spectroscopy. Furthermore, the integration of PhCs with metallic nanoparticles in SERS applications takes advantage of the strong localized EM fields generated by the nanoparticles. This approach combines the specific properties of PhCs, such as the high DOS and reduced group velocity, and the intense local field enhancements obtained by the metal nanoparticles, which leads to even greater Raman signal amplification.

Chapter 5. Overview of the previous research

The important thing is not to stop questioning. Curiosity has its own reason for existing.

(A. Einstein)

The enhancement of Raman and SERS signals using photonic crystal structures has been of great interest in the past few decades, and has resulted in numerous theoretical and experimental studies that contributed to the field. However, a comprehensive review of the existing research reveals a lack of systematic analysis. The biggest challenge in the literature concerns the alignment of the excitation wavelength relative to the PBG. Some researchers claim that the highest enhancement of Raman signal is achieved when the laser excitation is aligned with the center of the PBG, or when there is an overlap between the Raman-shifted bands and the PBG. This is attributed to the maximum backward reflection from the photonic structure^{95,96}. Others argue that the greatest signal enhancement is obtained when the excitation is aligned with the edges of the PBG, which is explained through the concept of the decreased group velocity and increased local density of optical states that intensify the light-matter interaction^{97–100}. Furthermore, there is an inconsistency in the literature regarding the definition of the PBG edges, while some studies do not even provide information about the relative position between the laser and the PBG^{95,101–103}. Additionally, the reported enhancement factors vary widely from as low as $2^{102,104,105}$ to as high as $100^{97,101,106}$. Moreover, some studies have reported Raman signal enhancement originating from the materials constituting the PhCs^{23,24,95,97,98,105–111}, while others have focused on enhancement from molecules either embedded within or attached to the surface of photonic structures^{96,99,101–103,110}. In addition, the literature presents different reports on the impact of dimensionality of PhCs (1D, 2D or 3D) on the Raman signal, as well as inconsistent reports on the maximum reflectances associated with the PBGs, while some studies did not define these parameters at all. Special issue presents the fact that the results about the signal enhancement were reported based on the analysis of only one Raman band or a limited number of spectra. To provide a clearer overview, Table 5.1 and Table 5.2 highlight and summarize these issues.

Table 5.1 A summary of the previous experimental explorations on Raman signal enhancement by photonic crystals

EXPERIMENT	REF.	DIMENSIONALITY	EMPTY PhC*	PROBE MOLECULE **	EF***	RAMAN BANDS ANALYZED	STRONGEST ENHANCEMENT****
	95	3D	✓	x	x	whole spectrum	~Center
	96	3D	x	✓	50	1	Center
	97	1D	✓	x	10	1	Edge
	98	1D	✓	x	4	1	Edge
	99	3D	x	✓	4 orders of magnitude	x	Edge
	100	1D	x	✓	SRS gain >10†	„new bands appeared“	Edge
	101	3D	x	✓	SRS threshold reduced by several orders of magnitude‡	„new bands appeared“	Not defined
	102	3D	x	✓	2.3	1	~Center
	103	1D	x	✓	10	1	~Center

* analysis of Raman bands of PhC constituent material

** analysis of Raman bands of probe molecules that were infiltrated into or absorbed on the surface of PhC

*** Raman enhancement obtained by comparing the intensity of Raman bands recorded with and without PhCs

**** relative position between the excitation and PBG for which the strongest enhancement was recorded

† experiment with stimulated Raman scattering; enhancement due to both PBG and non-linear effects

‡ experiment with stimulated Raman scattering; reported detection threshold reduction (not enhancement factor)

Table 5.2 A summary of the previous theoretical explorations on Raman signal enhancement by photonic crystals

THEORY	REF.	DIMENSIONALITY	EMPTY PhC*	PROBE MOLECULE **	EF***	RAMAN BANDS ANALYZED	STRONGEST ENHANCEMENT****
	104	2D	✓	✓	2.5	x	Center
	105	1D, 3D	✓	x	1-2	x	Edge
	106	2D, 3D	✓	x	2 orders of magnitude	x	Edge
	24	1D	✓	x	x	x	Edge
	107	1D	✓	x	5	x	Edge
	108	3D	✓	x	x	x	Edge
	109	2D, 3D	✓	x	x	x	Edge
	23	1D	✓	x	x	x	Edge
	110	1D	✓	x	1 order of magnitude	x	Edge
111	1D	✓	x	x	x	Edge	
112	1D	✓	x	x	x	Edge	

* analysis of Raman bands of PhC constituent material

** analysis of Raman bands of probe molecules that were infiltrated into or absorbed on the surface of PhC

*** Raman enhancement obtained by comparing the intensity of Raman bands recorded with and without PhCs

**** relative position between the excitation and PBG for which the strongest enhancement was recorded

It is also worth noting that similar uncertainties persist in studies that investigate the combined effects of PhCs and SERS. For instance, Ashurov, Yan, and Wu^{113–115} claim that the highest EF is achieved when the laser excitation overlaps with the center of the PBG, while Nguyen, Chen, Gudalla, and Gorelik^{100,116–118} reported the strongest signal enhancement when the excitation is aligned with the edges of the PBG. In addition, Gudalla¹¹⁸, reported differences between the high- and low-frequency side of the PBG. Bi¹¹⁹ also claims that the strongest SERS signal enhancement is achieved when the laser excitation is aligned with the edge of the PBG, however, the edge of the PBG is not defined as the very bottom of the reflectance peak but as the approximately 85% of the reflectance peak height. Yue reported the enhancement when the laser overlapped with approximately 50% of the reflectance peak height, which once again reinforces the statement that there is an inconsistency in the literature regarding the definition of the PBG edges. Additionally, some researchers reported that the highest enhancement was obtained when the Raman-shifted band was aligned with the center of the PBG and the laser excitation coincided with its high-frequency edge¹²⁰, while some studies do not provide information about the relative position between the laser and the PBG¹²¹. Similar to the reports that investigate the influence of PhC on the Raman signal, the enhancement factors on the SERS signal were sometimes not reported or were estimated based on just a few spectra or using only one peak^{99,113,114,117,118,120,122–127}. Moreover, the literature presents different reports on the impact of dimensionality of PhCs (1D, 2D, or 3D) on the Raman signal, as well as inconsistent reports on the maximum reflectances associated with the PBGs, while some studies did not define these parameters at all. Finally, the reported enhancement factors vary widely from as low as 2¹¹⁵ to as high as 1000¹⁰³.

Chapter 6. Materials and Methods

An experiment is a question which science poses to Nature, and a measurement is the recording of Nature's answer.

(M. Planck)

6.1 Porous silicon photonic crystals fabrication

In this work, pSi PhC samples were prepared using commercially available (Siegert Water GmbH, Germany) p-type boron-doped silicon wafers. The wafers were single-side polished, and their resistivity was $< 0.005 \Omega\text{cm}$. The crystal orientation was $< 100 > \pm 0.05^\circ$, and the thickness $(525 \pm 20) \mu\text{m}$. Before etching, silicon wafers were cut into approximately $2 \times 2 \text{ cm}^2$ squares.

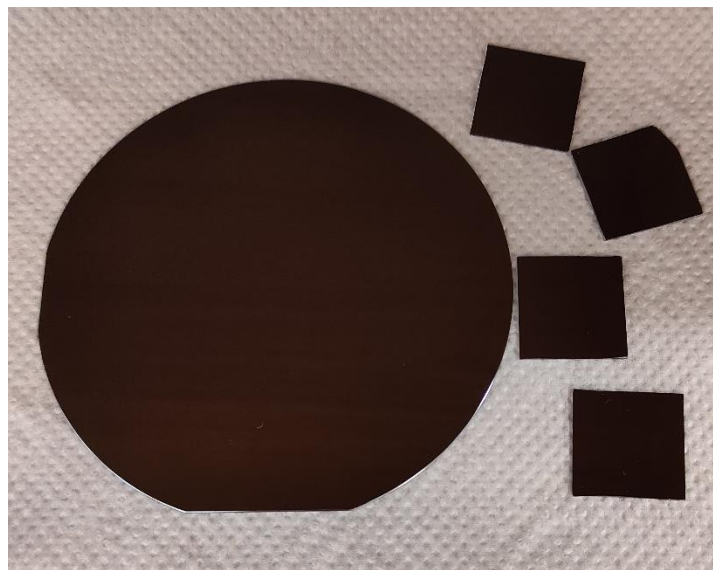


Figure 6.1 An example of the silicon wafer used in this work and the $\sim 2 \times 2 \text{ cm}^2$ square samples cut out from the wafer for subsequent etching

Even though the silicon wafers appear to be clean and well polished when unpacked, they contain impurities and an oxide layer on their surface that have to be removed to produce homogeneous and high-quality pSi PhC samples. For that reason, a sacrificial layer was removed before etching. Both the etching process and the removal of the sacrificial layer were conducted using a homemade Teflon electrochemical etch cell, with a piece of aluminum foil as a back-contact and a platinum mesh as a counter-electrode suspended at a fixed height above the silicon wafer³⁰.

The etch cell consists of a base that supports a platform for the sample, a top piece designed to hold the electrolyte and a platinum electrode. To establish an electrical connection with the cSi wafer, an aluminum foil was placed on the platform. The cSi wafer was then carefully positioned on the foil, and the top piece of the etching cell was placed to keep the position of the wafer fixed. Additionally, a HF-resistant O-ring was put on the polished side of the silicon wafer to prevent leakage of HF solution from the cell. The diameter of the O-ring was ~ 1.78 cm, meaning that approximately 2.5 cm^2 of the cSi wafer was exposed to the electrolyte. Apart from the O-ring, the top piece of the etching cell contained the electrolyte, a drainage valve, and a hollow specifically designed to accommodate the platinum electrode. The platinum electrode was a horizontal mesh with a surface area slightly larger than that of the silicon wafer that was exposed to the etching process. This design was crucial for ensuring a uniform flow of electric current through the electrolyte to the silicon electrode, which was essential for the electrochemical reactions to occur evenly. Moreover, the platinum electrode was held at a fixed height, approximately 5 mm, above the crystalline silicon wafer. This fixed height was crucial for obtaining reproducible samples since it ensured that the electric current and the chemical processes were uniform across the surface of the silicon wafer. The overall design and the precise arrangement of all components were important for the consistent and reproducible etching of the pSi PhC samples, leading to reliable and reproducible experimental results.

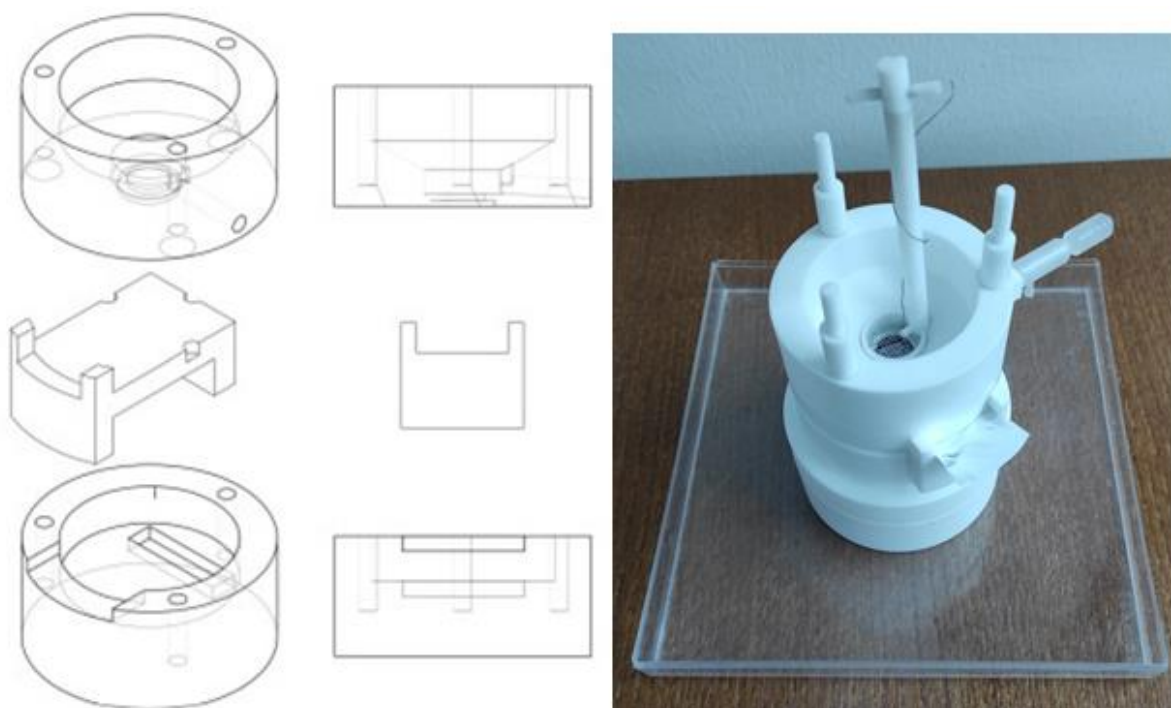


Figure 6.2 Schematic representation of the etching cell (left) and a photograph of the actual etching cell (right)¹²⁸

In all experiments, 10 mL of the 3:1 mixture of 40 wt% HF (Sigma-Aldrich, Germany) and 99.8% v/v ethyl alcohol was used. Ethanol was primarily used to reduce the surface tension of the electrolyte, allowing it to enter into very small pores, which was crucial for obtaining a homogeneous surface of the sample. The aluminum foil, along with the wafer that was placed on it, was connected to the positive pole, so it served as the anode, while the platinum electrode was connected to the negative pole of the power source. For this process, a high-precision current-voltage source (2601B SourceMeter, Keithley Instruments, USA) was used, and it was controlled by LabVIEW (National Instruments, USA) software. This setup ensured precise regulation and monitoring of the etching process. Additionally, the voltage drop across the platinum electrode-electrolyte-cSi wafer system was monitored using a UT60E digital multimeter (Uni-Trend Technology, China) to ensure consistency. The entire etching process was carried out in a homemade fume hood to ensure the removal of the highly toxic HF fumes.

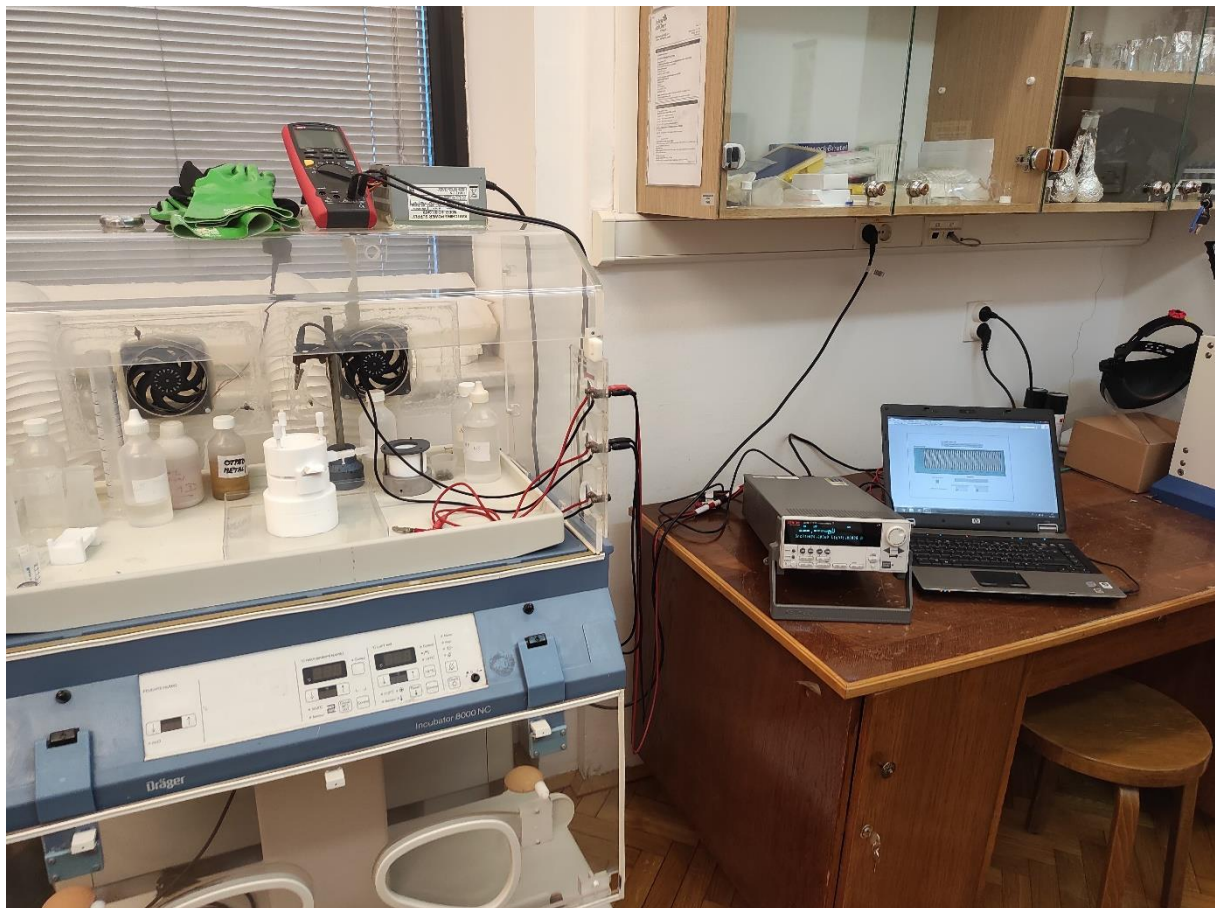


Figure 6.3 Experimental setup for the fabrication of pSi samples

To obtain clean and reproducible silicon wafer surfaces, a sacrificial layer was removed using a strong base. This technique takes advantage of the pSi property to dissolve in strongly basic solutions³⁰. The silicon wafer was etched using the previously mentioned 3:1 HF-EtOH solution

applying a constant current density of 175 mA/cm^2 for 30 s. HF solution was then removed, and the pSi sample was soaked in 1 M aqueous solution of NaOH for 5 minutes. The NaOH solution was then removed from the cell, and the wafer was thoroughly rinsed with EtOH to ensure that all residues were removed. Cleaning silicon wafer surfaces in this way significantly increases the reproducibility of the samples and prevents the formation of parasitic surface film. This is crucial for the homogeneous deposition of metallic nanoparticles on the surfaces of pSi and pSi PhC samples.

Following the cleaning procedure, both the standard pSi and pSi PhC samples were prepared using the same 3:1 HF-EtOH solution. The pSi samples (sample category A) underwent etching at a constant current density of 25.5 mA/cm^2 for 250 s. In contrast, pSi PhCs, being rugate filters, were etched with a sinusoidally modulated current density ranging from 1 to 50 mA/cm^2 applied for 50 cycles.

Five different sample categories of pSi PhC samples were prepared (B, C, D, E, and F), with all parameters kept constant, except for the period of the sinusoidal current profile. This period varied between 4.386 for sample category F to 4.95 s for sample category D to obtain RFs with different specific positions of the reflectance peak relative to the laser excitation wavelength. Following the etching procedure, all samples were rinsed twice in EtOH and dried using a gentle stream of liquid nitrogen gas. The preparation of samples was conducted in a well-lit room and at a constant temperature of $(22.0 \pm 0.1)^\circ\text{C}$ to ensure consistency and reproducibility. For each of the six sample categories, four samples were prepared and labeled A1, A2, A3, A4, B1, and so on up to F4, which is 24 samples in total. Each sample was then cut into three small rectangles, i.e. A1-1, A1-2, A1-3, A2-1, A2-2, A2-3, etc. Each of these small rectangles had a surface area of approximately 6 mm^2 . As a result, a total of 72 rectangular specimens were available for the subsequent measurements and analysis. A photograph of the prepared pSi and pSi PhC samples is given in Figure 6.4, while the corresponding etching parameters are presented in Table 6.1. The schematic view of the division of all 6 sample categories into samples and rectangular specimens, on which the measurements were recorded, is given in Figure 6.5.

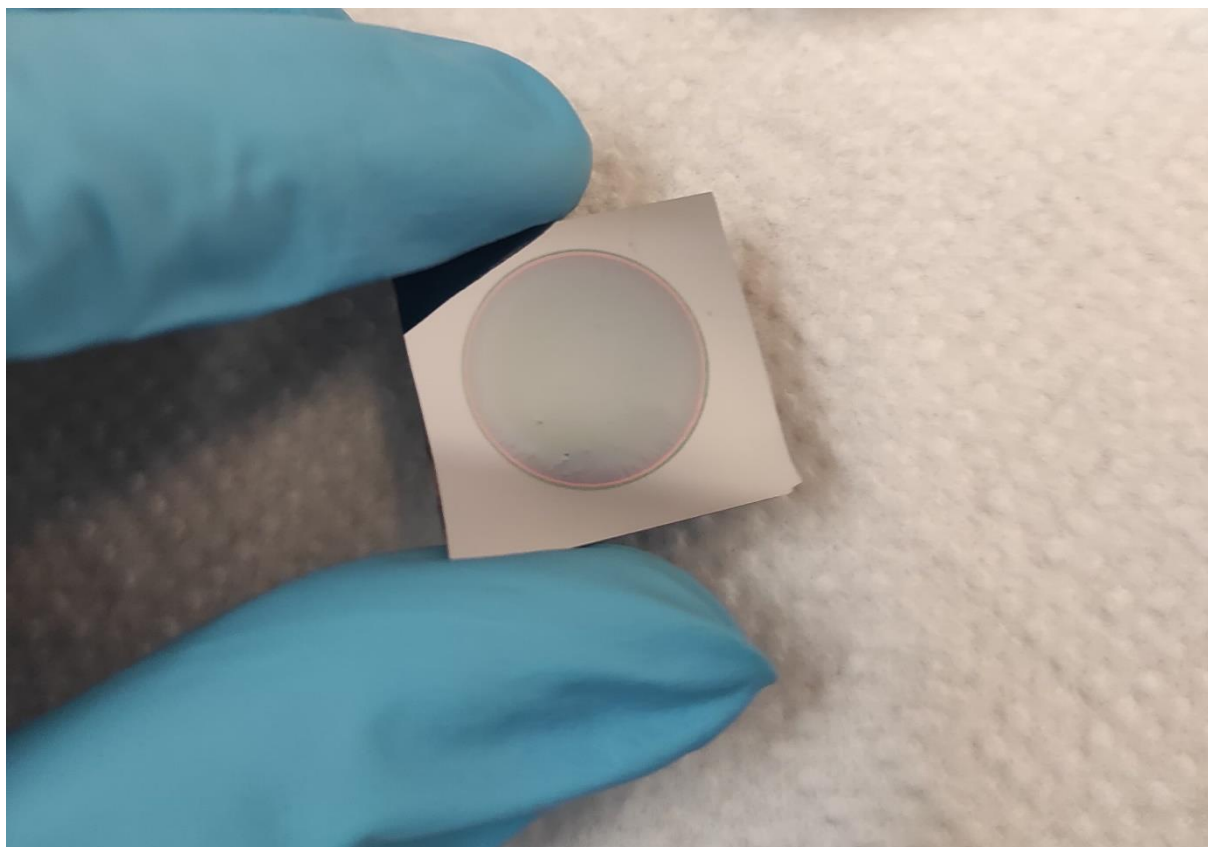


Figure 6.4 Photograph of the prepared pSi PhC sample, with a porous layer surface area of $\sim 2.5 \text{ cm}^2$

Table 6.1 Etching parameters for the pSi sample and pSi PhC samples of rugate type used in the study

Sample category	Period [s]	J [mA/cm ²]	Number of cycles
A	<i>n/a</i>	25.5	<i>n/a</i>
B	~ 4.65	1 – 50	50
C	~ 4.75	1 – 50	50
D	~ 4.90	1 – 50	50
E	~ 4.55	1 – 50	50
F	~ 4.40	1 – 50	50

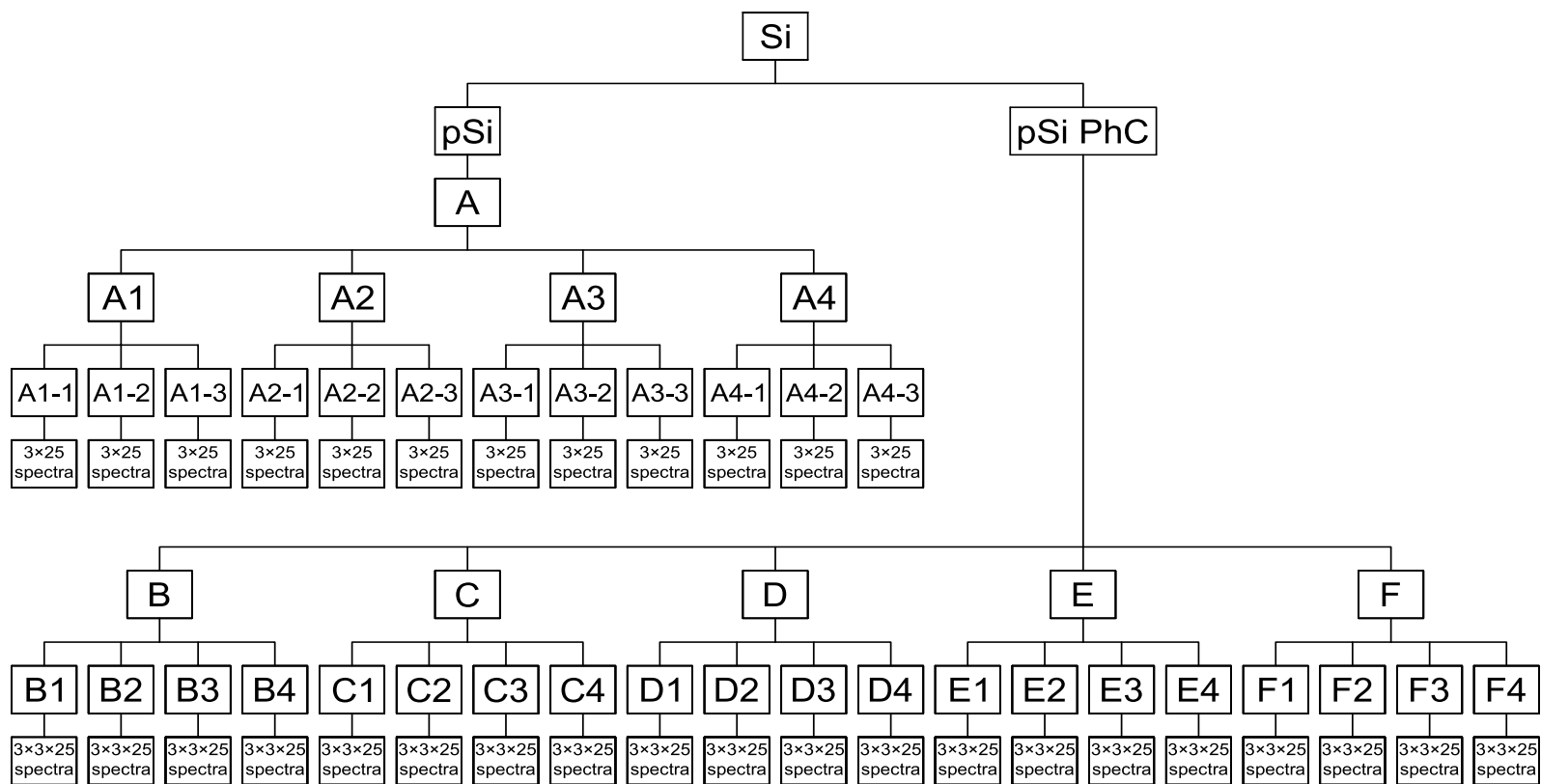


Figure 6.5 Schematic view of the division of pSi and pSi PhCs into sample categories A-F, 4 samples (A1-A4, B1-B4, C1-C4, D1-D4, E1-E4, F1-F4), 12 rectangular specimens (from A1-1 to F4-3), 3 randomly chosen positions on each rectangular specimen (from A1-1-1 to F4-3-3), and ~25 recorded Raman spectra on each mapping area

6.2 Deposition of gold nanoparticles on pSi and pSi PhC samples

Synthesis of gold nanoparticles was performed by immersion of pSi and pSi PhC samples into an aqueous solution of commercially available salts of chloroauric acid, HAuCl_4 (Alfa Aesar, SAD). Prior to immersion, samples were cut into approximately $2 \times 3 \text{ mm}^2$ pieces and immersed into a 2 wt% solution of hydrofluoric acid to remove the surface oxide layer. This was followed by rinsing samples twice in 99.8% ethanol. The prepared samples were then immersed into 1 mL of $5 \cdot 10^{-2} \text{ M}$ HAuCl_4 aqueous solution at a constant temperature of $22.0 \pm 0.5 \text{ }^\circ\text{C}$. After 60 seconds, samples were removed from the solution, rinsed in ultrapure MQ water, and left to dry in the air.



Figure 6.6 Photograph of pSi and pSi PhC samples during the synthesis of gold nanoparticles

6.3 UV-Vis-NIR spectroscopy

Spectral dependence of reflection of pSi PhC and pSi PhC-based SERS substrates was investigated using UV-Vis-NIR spectroscopy in reflectance mode. Spectra were obtained using a UV-3600 Shimadzu spectrometer at Ruđer Bošković Institute, in the range from 500 to 1000 nm. The spectrometer is equipped with multiple light sources and three different detectors: a photomultiplier tube for the ultraviolet, visible, and near-infrared range (200 – 870) nm and InGaAs and PbS detectors for the rest of the near-infrared range (870 – 2600) nm. Detector calibration was performed using a BaSO_4 substrate that gives 100% reflectance in the range of interest.



Figure 6.7 UV-3600 Shimadzu UV-Vis-NIR spectrometer from the Division of Materials Chemistry at Ruđer Bošković Institute

6.4 Scanning Electron Microscopy and Energy-Dispersive X-ray Spectroscopy

Scanning electron microscope (SEM) is a type of microscope that uses focused beams of electrons to produce highly detailed images of the surfaces of samples. Since this type of microscope uses electron beams that have much shorter wavelengths than optical microscopes, much higher resolutions can be achieved, revealing fine details of the examined structures.

In this work, JEOL JSM-7000 SEM located at Ruđer Bošković Institute was used to study the morphologies of pSi and pSi PhC samples with and without gold nanostructures on their surfaces. At the operating voltage of 30 kV, the device offers a maximum magnification of 500 000 times and a resolution of 1.2 nm.

A beam of electrons is produced by an electron gun that consists of an electron source that usually includes thermionic or field emission. In the case of a thermionic emission source,

electrons in a heated tungsten filament have enough energy to overcome the work function of the material and are, therefore, emitted into the surrounding vacuum. On the other hand, a field emission source uses a sharp tungsten tip in a strong electric field to extract electrons by quantum tunneling, which finally provides higher brightness and better spatial resolution. The generated beam is then accelerated towards the sample by the electric field created by the potential difference between the cathode (the electron source) and the anode and focused into a fine spot using a series of EM lenses. The focused beam is then directed by scanning coils that deflect the beam across the sample surface in a raster pattern. The beam interacts with atoms on the surface of samples, and the interaction gives a signal that is captured by a detector. Finally, signals are converted into electrical signals that are processed and used to modulate the brightness of a display screen. To prevent electron scattering by air molecules, the whole process must occur in a high vacuum chamber, while the only requirement regarding sample preparation is that samples are electrically conductive to prevent charging under the electron beam. In the case of non-conductive samples, a thin layer of conductive material is typically applied as a coating.

Energy-dispersive X-ray spectroscopy (EDS) is an analytical technique for chemical characterization of samples. The interaction of high-energy electrons and a sample in SEM results in the ejection of inner-shell electrons from atoms in the sample. A vacancy is then filled with another electron from a higher energy state, and the transition releases energy in the form of characteristic X-rays that are specific to the element from which they were emitted. The EDS detector then captures emitted X-rays and converts them into electrical signals that produce an energy spectrum. Each peak in the spectrum corresponds to the energy of a detected X-ray, and since these emitted X-rays are characteristic of the elements present in the sample, the energy spectrum acts as a unique fingerprint for the sample. This means that by analyzing the spectrum, various elements within the sample can be identified. Moreover, the intensity of the peaks gives quantitative information about the concentration of the elements, where higher intensity means higher concentration and vice versa.



Figure 6.8 JEOL JSM-7000 scanning electron microscope together with energy-dispersive X-ray spectroscopy device from the Division of the Materials Chemistry at Ruđer Bošković Institute

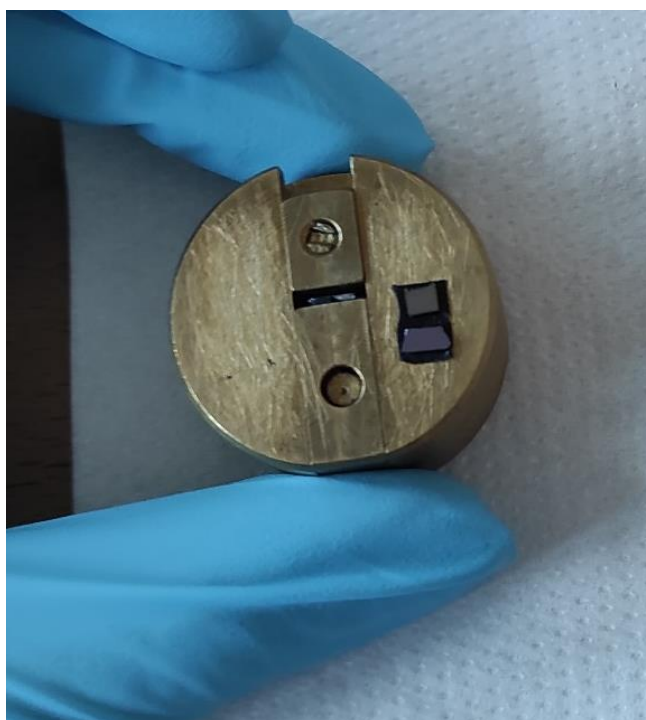


Figure 6.9 pSi PhC samples prepared for SEM and EDS analysis

6.5 Raman spectroscopy

Raman and SERS measurements were performed at Ruđer Bošković Institute using the inVia™ Raman microscope from Renishaw plc, Wotton-under-Edge, UK. For the measurements, an unpolarized near-infrared 785 nm laser excitation was used with a Leica x10 NPLAN objective and numerical aperture of 0.25. The measurement process begins with the laser being directed through the optical components within the microscope. The laser is then focused on a small spot on the sample where scattering occurs (the focusing is typically made by a microscope objective lens). The scattered light (both Rayleigh and Raman components) is then collected by the same objective lens that was used to focus the laser on the sample and directed back through the optical path to the spectrometer. Before reaching the spectrometer, the scattered light passes through a notch filter that blocks the intense Rayleigh scattered light and allows only the much weaker Raman scattered light to pass through. The filtered Raman light then enters the dispersive spectrometer. Inside the spectrometer, the light falls on a diffraction grating, which separates the light based on its wavelength. After being dispersed by the grating, the light then reaches the detector. The detector is a charge-coupled device (CCD), which is a highly sensitive type of detector that consists of light-sensitive elements (pixels). The pixels detect the intensity of light at different frequencies. The detected signals are then sent to a computer, where they are processed to create a Raman spectrum that displays the intensity of the Raman scattering as a function of Raman shift.



Figure 6.10 inVia™ Raman microscope from the Division of Materials Physics, Ruđer Bošković Institute



Figure 6.11 Photograph of SERS substrates prepared for Raman measurements

It is important to note that the absorption depth, defined as the depth for which the intensity decreases to $1/e$ of its initial value, for the 785 nm laser used in this study in silicon is $\sim 10 \mu\text{m}$, as represented in Figure 6.12. This indicates that the absorption depth for porous silicon is somewhat greater, which will be important in the interpretation of our results.

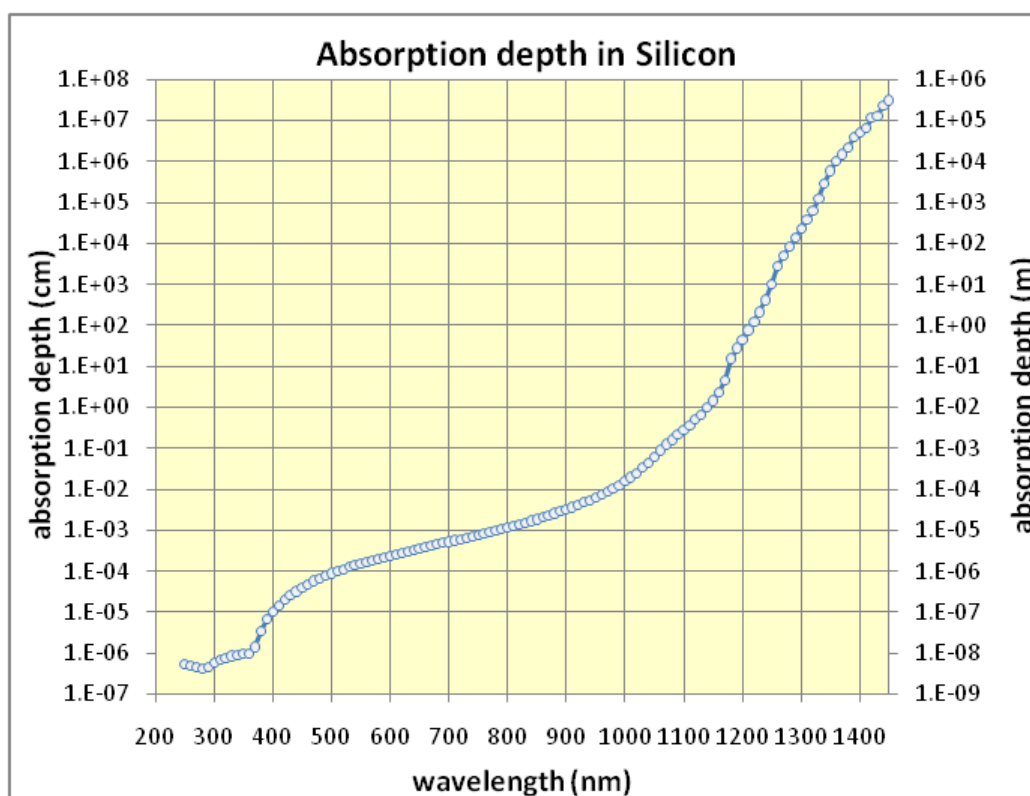


Figure 6.12 The absorption depth of laser excitation into silicon as a function of laser excitation wavelength¹²⁹

6.6 Probe molecules

To determine the influence of pSi PhC on Raman and SERS signal enhancement, it is important to use the well-known probe molecules that remain chemically unmodified when they bind to Raman or SERS surfaces. In this work, commercially available crystal violet (CV) and Rhodamine 6G (R6G) molecules from Sigma-Aldrich, Germany, were used for Raman and SERS measurements, respectively.

Crystal violet ($C_{25}N_3H_{30}Cl$) is a synthetic dye that belongs to the triarylmethane family. Since it binds well to various substrates, it is widely used in different fields, including Raman and SERS studies. In this work, the CV molecule solution of the concentration 10^{-2} M was used for Raman measurements. The solution was prepared by dissolving the CV powder in ultrapure MQ water. Porous silicon and pSi PhC samples were immersed in 200 μ L of the solution for a time period of 90 minutes. At the end of the incubation time, the samples were taken out of the solution and left to dry in the air. Dry samples were then fixed on a glass slide for Raman measurements.

Rhodamine 6G ($C_{28}H_{31}N_2O_3Cl$) is a highly fluorescent and photostable dye that is also widely used in various scientific and industrial applications. In this study, R6G molecule solution was used for SERS measurements. The $1 \cdot 10^{-4}$ M solution was prepared by dissolving a powder in a 1:1 volumetric mixture of 99.8% ethanol and ultrapure MQ water. SERS substrates were immersed and incubated in the solution for 30 minutes, followed by rinsing in ultrapure MQ water and air drying. SERS samples prepared in this way were then fixed to a glass slide for measurements.

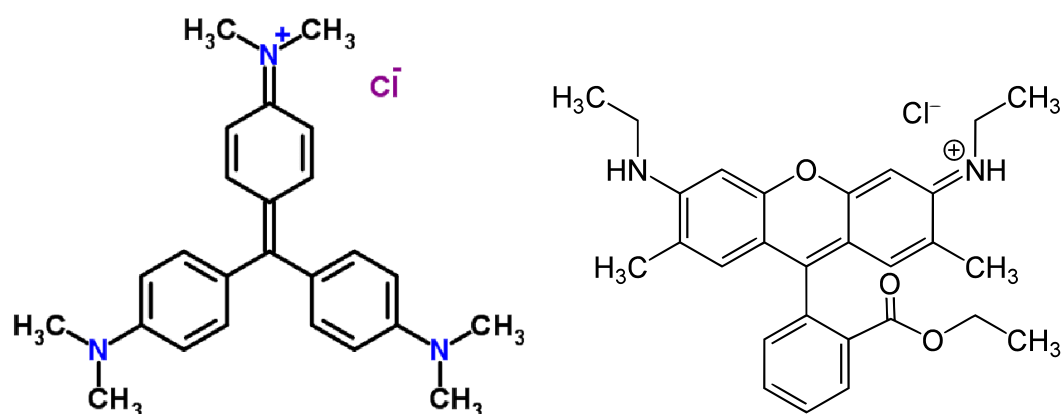


Figure 6.13 Molecular structure of crystal violet (left) and Rhodamine 6G (right)^{130,131}

6.7 Sample characterization conditions

UV-Vis-NIR spectra of pSi and pSi PhC samples were recorded in reflectance mode over the 500-1000 nm spectral range, with a resolution of 1 nm and aperture of ~ 13 nm. The angle of incidence for the reflectance measurements was 7° .

The morphology and thickness of the prepared pSi and pSi PhC structures were examined using FE-SEM operating in the range of 5-15 kV, with a working distance between 4.8 and 10 mm. The magnifications were in the range 2 200 to 100 000 times.

Raman and SERS spectra were recorded using the unpolarized near-infrared 785 nm laser excitation from the inViaTM Raman microscope with a Leica x10 NPLAN objective and numerical aperture of 0.25. At the beginning of each experiment, the spectrometer was calibrated with an internal cSi (110) sample measured at 520.5 cm^{-1} . To avoid intensity differences of transversal-optical phonon scattering at the center of the Brillouin zone of $\langle 100 \rangle$ cSi (and even pSi) due to in-plane orientation^{132,133} the angular position of every rectangular specimen was fixed to provide the strongest Raman signal. The Raman spectra were acquired from three different randomly chosen positions on every rectangular specimen, with 24-25 spectra recorded at each mapping area. The step size was fixed at $20\ \mu\text{m}$, so the average surface area covered during each Raman measurement was approximately $0.01\ \text{mm}^2$. The laser spot diameter was approximately $8\ \mu\text{m}$ and the laser power was set to 10%, which is about 3 mW. The integration time was 1 s with 5 accumulations, and all spectra were recorded in a spectral range between 350 and $1700\ \text{cm}^{-1}$.

Chapter 7. Results and discussion

It is the glory of God to conceal things, but the glory of kings is to search things out.

(Proverbs 25:2)

7.1 Porous silicon photonic crystals for Raman measurements

The investigation of the influence of photonic crystals (PhCs) on Raman and SERS signal enhancement is motivated by the unique properties of PhCs and their potential to enhance signals in vibrational spectroscopy. In this work, we utilized a type of PhCs known as rugate filters (RFs). RFs are characterized by a dielectric function that varies sinusoidally in a direction perpendicular to the PhC surface, and the reason why this type of PhCs was used is primarily due to the simplicity of its fabrication process. While Bragg reflectors are a common choice for 1D PhC, their production requires precise calibration of optical layer widths, which complicates the fabrication process. On the other side, RFs offer a more straightforward production approach, which is why they were a good alternative for this research. The variation in relative permittivity was achieved by the modulation of current density during the etching process. The current density directly influences the porosity profile of the RF, which means that minimum and maximum values determine the corresponding porosity of the layers and, consequently, their refractive indices. The difference between the minimum and maximum current density values influences the width of the reflectance peak of a RF, where a greater difference results in a wider reflectance peak. On the other hand, the number of layers significantly influences the height of the reflectance peak. As the number of layers increases, constructive interference of light within the crystal is enhanced, thus increasing the reflectance towards unity, which indicates perfect reflection and an ideal photonic structure. Together with current density, the frequency of sinusoidal variation is the key aspect in the production of RFs. The frequency or period of the sinusoidal function directly influences the position of the center of the reflectance peak, meaning that the precise position can be adjusted by modulation of the frequency of the sinusoidal current density profile.

Parameters for the RF fabrication were selected to obtain an optimal reflectance performance. Current densities ranging from 1 to 50 mA/cm² were chosen to avoid the electropolishing regime while still providing distinct refractive index contrasts necessary for the PBG. A total of 50 repeats was applied giving 50 layers and providing sufficient thickness to achieve strong

reflectance, while the periodicity was carefully adjusted to center the reflectance peak at the desired wavelength. This approach ensured that the RFs met the specific optical requirements of this study.

In this work, five different sets of PhCs (sample categories) were prepared, with each set having the center of the reflectance peak at a different wavelength, as shown in Figure 7.1. Photonic crystals that belong to sample category B are those with the center of the reflectance peak at 785 nm. Sample categories C and E have reflectance peaks slightly shifted to the higher and lower wavelengths, respectively, so that the laser excitation falls at approximately 50% of the reflectance peak at the high- and low-frequency side. Finally, sample categories D and F correspond to the case in which laser excitation falls at the edge of the reflectance peak on the high- and low-frequency side, respectively, meaning that PhCs that belong to sample categories D have reflectance peak centered around 835 nm, while those that belong to sample category F have reflectance peak at approximately 735 nm. Illustration of the relative alignments between the laser excitation and the reflectance peak for each particular sample category (B-F) is presented in Figure 7.1, while the relative position between the laser excitation and each particular sample category is given in Figure 7.2. Frequencies of the corresponding sinusoidal current density profiles were in the range (0.202 – 0.228) Hz, while their amplitudes were sinusoidally varied between 1 and 50 mA/cm².

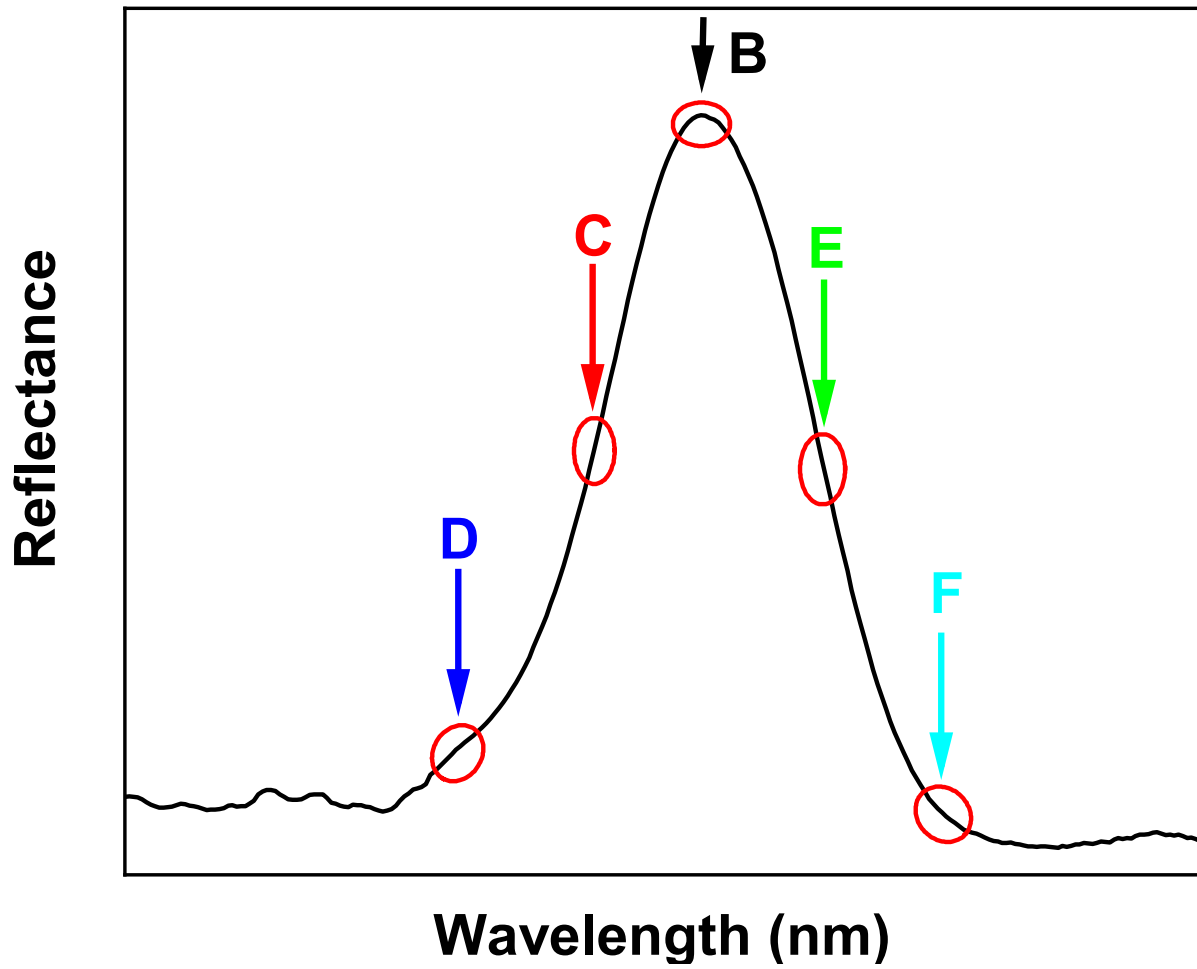


Figure 7.1 Illustration of the relative alignments between the laser wavelength and the reflectance peak of a pSi PhC for sample categories B to F

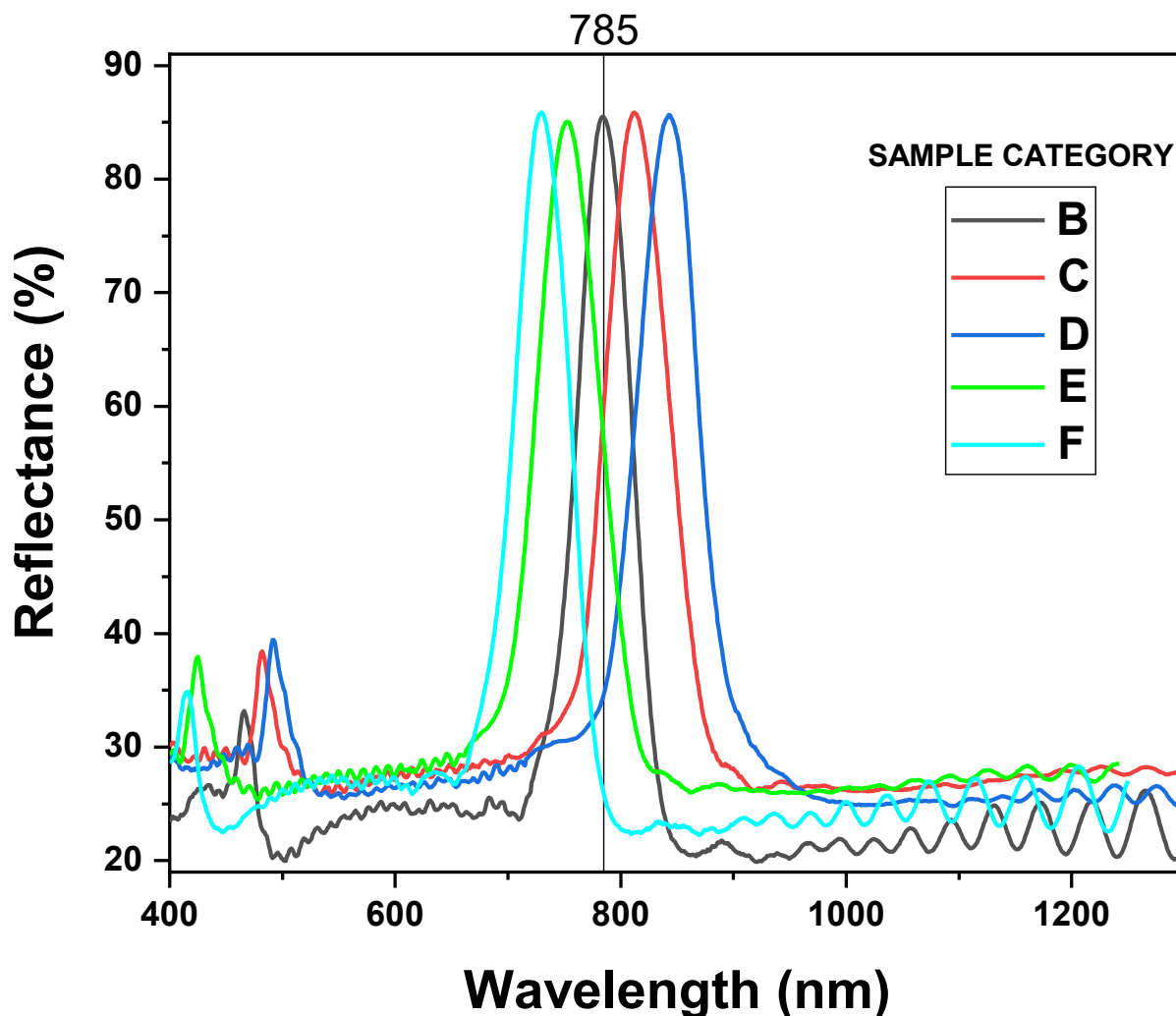


Figure 7.2 Reflectance spectra of pSi PhC representing 5 sample categories (B-F). The vertical line indicates the 785 nm laser excitation

The reflectance spectra represented in Figure 7.2 show a high reflectance peak that represents the first stopband of the RFs. Additionally, there are significantly weaker second-order stopbands located at approximately half the wavelength of the primary stopbands. In other regions, the reflectance remains minimal, while at higher wavelengths, Fabry-Perot interference fringes become evident. The height of the reflectance peak reached approximately 85%, which, although slightly below the theoretical value of 100%, represents a highly satisfactory result. The deviation from the ideal value can be attributed to two main factors. Firstly, theoretical predictions often suggest ideal values that are unattainable in experiments due to various factors that influence the system and inherent imperfections, so typical experimental values for the reflectance peaks are often below 95%. Additionally, the theoretical predictions are based on the analysis of Bragg reflectors. However, in the case of RFs, the ease of their production comes

at the cost of the reduced reflectance peaks and narrower stopbands compared to the Bragg reflectors¹³⁴.

From Figure 7.2, it is visible that the FWHM of the reflectance peaks remained nearly constant, at (60 ± 5) nm indicating that the optical thickness throughout the PhCs was uniform and reinforcing the claim that our PhCs were of good quality. However, a more specific approach to determining the reflectance efficiency involves the calculation of the Bragg attenuation length, for which information about the depth of the porous layers is needed. For this reason, the discussion about the quality of our samples will be continued after the physical structure of the samples is examined using the SEM images presented later in the text.

The reflectance of pSi, which is not depicted in Figure 7.2, remained relatively constant at around 20-25% across the spectrum but began to rise in the lower wavelength region, below 450 nm. It is important to mention that the reflectance spectra measurements were conducted at an angle of incidence of 7° , which results in a shift of the actual position of each reflectance peak towards higher wavelengths by a factor of $\cos(7^\circ)$ ^{134,135}. Conducting measurements at a non-zero angle of incidence introduces a shift in the reflectance peaks, which must be considered in practical applications to ensure accurate reflectance peak position. Additionally, the reflectance measurements were performed immediately after sample fabrication to prevent any potential oxidation and to ensure that the effects of oxidation or other environmental factors did not influence samples in any way. Moreover, it is important to highlight that the same FWHM for all sample categories reinforces the claim of PhCs' homogeneity, meaning the optical properties of the samples were maintained. This consistency is crucial for applications that rely on precise optical responses. Contrarily, the recording of Raman spectra was not conducted on the same day, meaning that pSi and pSi PhCs samples had to be dipped in a low concentration of HF solution to remove native oxides from the surfaces before any preparation for measurement. This treatment caused a slight but noticeable blueshift in the position of the reflectance peak; specifically, a 30 s dip in 2 wt% HF aqueous solution shifted the reflectance peak towards lower wavelengths by 2-3 nm. This blueshift results from the replacement of oxygen with fluorine atoms and from the chemical etching effect, which slightly increases the porosity of the etched porous layer. Consequently, this increases the porosity and slightly lowers the refractive index, shifting the reflectance peak positions to shorter wavelengths³⁰.

Furthermore, sample incubation in a solution with a high concentration of CV and subsequent air-drying led to the visible adsorption of probe molecules on the pSi and pSi PhC surfaces and

potential infiltration into their structures. This fact was not an issue for the pSi samples, however in the case of pSi PhCs, this adsorption caused a blueshift of the reflectance peak center by approximately 15 nm and a decrease in the peak reflectance by approximately 3%. However, the width of the reflectance peak that corresponds to the width of the PBG did not change after the immersion, indicating that the uniformity of optical reflectance across the samples was preserved. The blueshift due to the CV coating implies that the primary contribution to the reflection peak position arises from the newly formed layer of adsorbed molecules. This means that the possible increase in the effective refractive index of the PhC due to molecules infiltrated into the photonic structure is a minor effect.

Considering the various parameters that influence the position of the PBG, and to ensure the precise overlap of the excitation wavelength and the PBG position, it was essential to incorporate all these effects into our analysis. For that reason, all the abovementioned corrections are summarized in Table 7.1 and had to be taken into account when adjusting the frequency of the sinusoidal etch current density.

Table 7.1 Experimental corrections for the reflectance peak position in Raman experiment – example for peak initially measured at 785 nm

	Peak center (nm)	Shift (nm)	Direction
1° C increase during etching	-	~ 7-10	Redshift
UV-Vis-NIR $\rightarrow \lambda_{0=7^\circ}$	785	-	-
Angle correction $\rightarrow \lambda_0$	791	~ 6	Redshift
2% HF for 30s	788	~ 2-3	Blueshift
10 ⁻² M CV for 90 minutes	773	~ 15	Blueshift

It is also important to mention that the FWHM of the reflectance peak for our samples was approximately 60 nm. Therefore, even a small deviation, such as 10 nm, from a specific position can significantly alter the relative alignment between the incident radiation and the PBG. For this reason, only small uncertainty wavelength intervals of ± 2 nm around each predefined position corresponding to sample categories B to F were allowed.

Additionally, the room temperature during the etching process and incubation significantly influences the position of the reflectance peak¹³⁶. Temperature changes of even ± 2 °C drastically changed the position of the PBG. Therefore, temperature had to be carefully

maintained at a constant value to ensure the accuracy and reliability of the measurements, allowing only the changes as small as ± 0.5 °C. This precise temperature control was crucial for achieving consistent and reproducible reflectance peak positions.

After discussing the PhCs and their reflectance spectra, as well as the parameters that influence their quality, it is important to get information about the physical characteristics of the samples. For that purpose, scanning electron microscopy was used to examine the morphology of the porous surfaces. Figure 7.3 shows a high-magnification top-view FE-SEM image of the pSi PhC samples and reveals a typical mesoporous morphology with pore diameters 10 – 20 nm, often observed when highly doped p-type cSi wafers are used for the production of pSi and pSi PhC samples. Since the average etching current density was the same for all samples, pSi and pSi PhC samples show the same morphology of the surface³⁰.

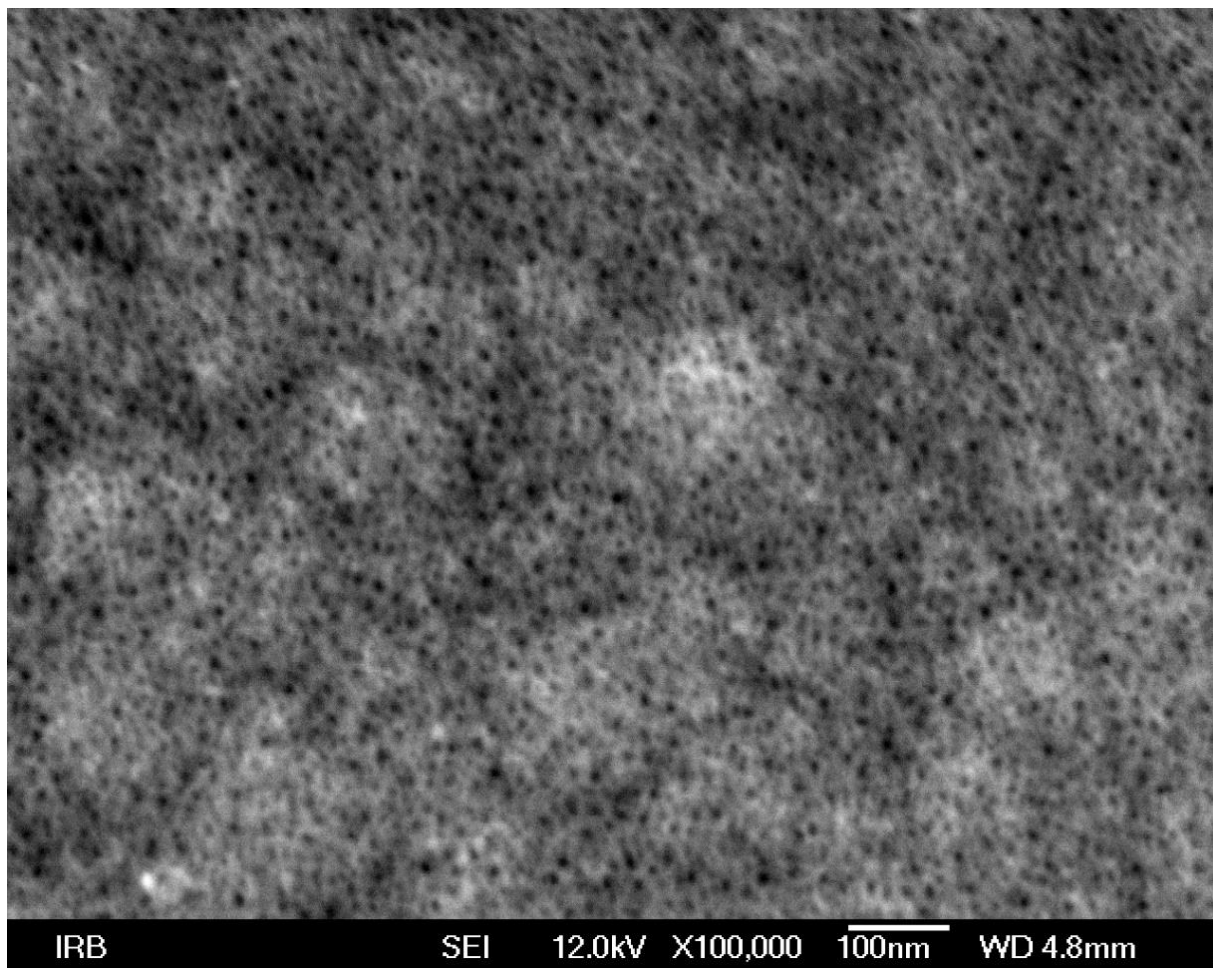


Figure 7.3 Top view FE-SEM image of an as-etched pSi PhC sample showing the pores on the surface

Figure 7.4 shows the cross-sectional view of the pSi PhC structure. Smooth variations between the layers of high and low index of refraction, perpendicular to the surface of the RF, can be

easily recognized. The periodic pattern is maintained throughout the entire photonic structure, which consists of 50 periods. The thickness of the porous section is approximately 7.5 μm .

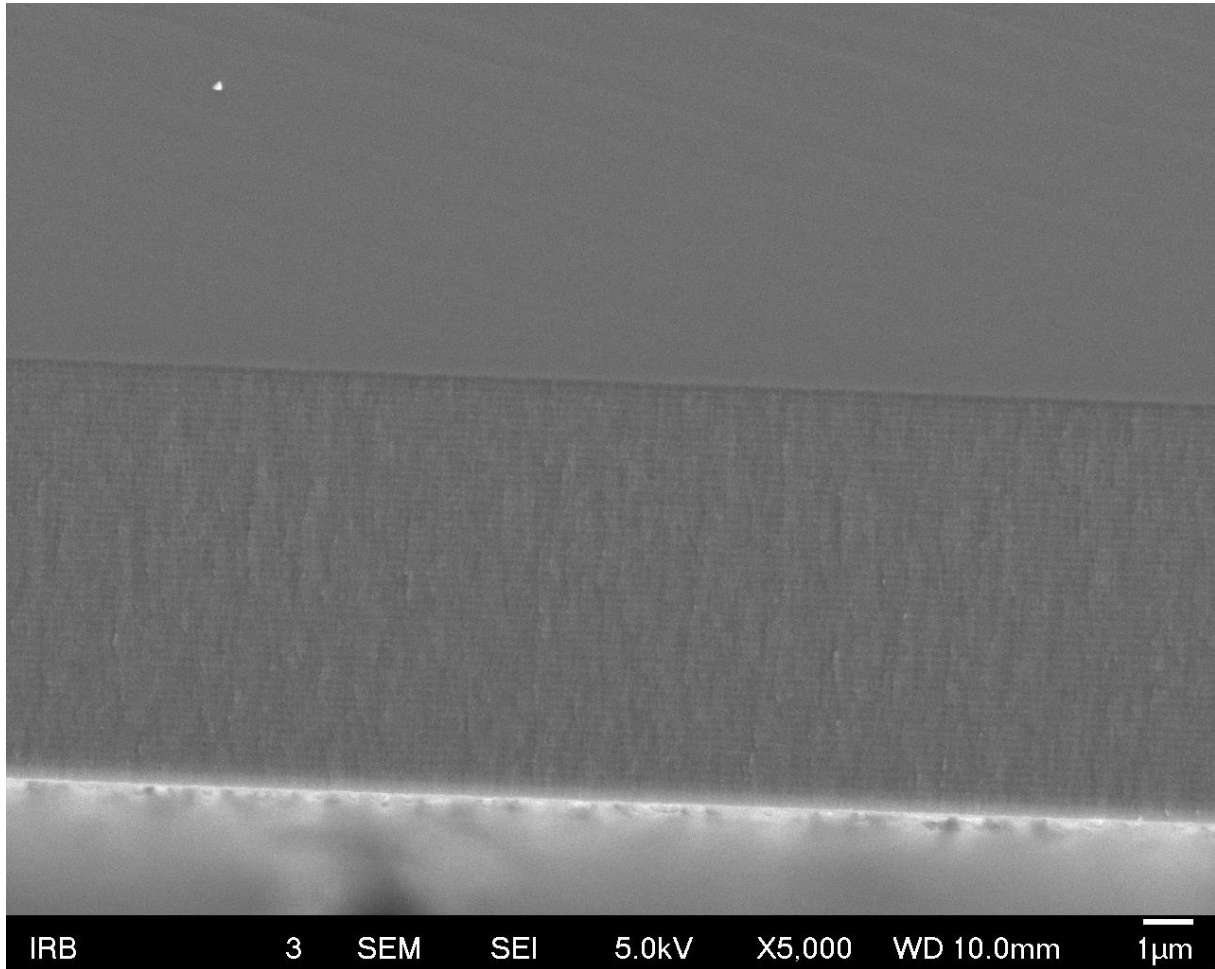


Figure 7.4 FE-SEM image of a cross-section of an as-etched sample showing the whole rugate structure

Having determined the depth of the PhCs, we can now return to the discussion of Bragg attenuation length. The depth and uniformity of the porous layers, as revealed in Figure 7.4, play an important role in understanding why an 85% reflectance, though slightly below the ideal, is still a strong indicator of the quality of these samples.

The Bragg attenuation length corresponding to the maximum reflectance was calculated using the relation^{137–139}:

$$l_B^{-1} = -\frac{\langle \ln T \rangle}{L}, \quad (7.1)$$

where T denotes the transmission coefficient, and L represents the thickness of the sample. The maximum reflectance of our samples with 50 cycles (50 rugate layers) is approximately 85% (Figure 7.2), meaning that about 15% of the incident light is either absorbed or transmitted.

According to Figure 6.12, the absorption coefficient of silicon at 785 nm given is $\sim 10^3 \text{ cm}^{-1}$, suggesting that the value for porous silicon is somewhat lower.

For the 15% of non-reflected incident light, calculations for the whole photonic crystal depth indicate that approximately half of the non-reflected light will be absorbed, meaning that the corresponding value for porous silicon is expected to be a bit lower. Consequently, it is estimated that only about 7-8% of the incident radiation is transmitted through the photonic crystal, resulting in a value of (2.8 – 3.0) μm for the Bragg attenuation length of our samples and for the specific case of the alignment of the laser with the center of the PBG. The obtained value supports the claim that despite the slightly lower reflectance peak height, our samples were of good quality since it shows that the majority of the incident light was reflected within the top 40% of the porous layer.

After this discussion about the quality of the PhC samples, we can now return to SEM images and continue the structural examination of the samples. Low-magnification SEM image of the porous surface after a 90-minute incubation in a 10^{-2} M CV aqueous solution is presented in Figure 7.5. This image reveals that the top surface is entirely covered with a continuous CV film, which blocks the pores and prevents the acquisition of clear, high-magnification images. The high concentration of probe molecules was found to be optimal for counteracting the weak Raman signal and achieving a decent signal-to-noise ratio. Examination of the cross-sectional view of the incubated sample showed that it was visually similar to samples that had not been incubated in the probe molecule. This similarity indicates that samples with and without CV coating exhibit very similar, if not identical, cross-sectional appearances. Consequently, it is impossible to visually determine whether the CV molecules have infiltrated the porous structure based only on SEM images.

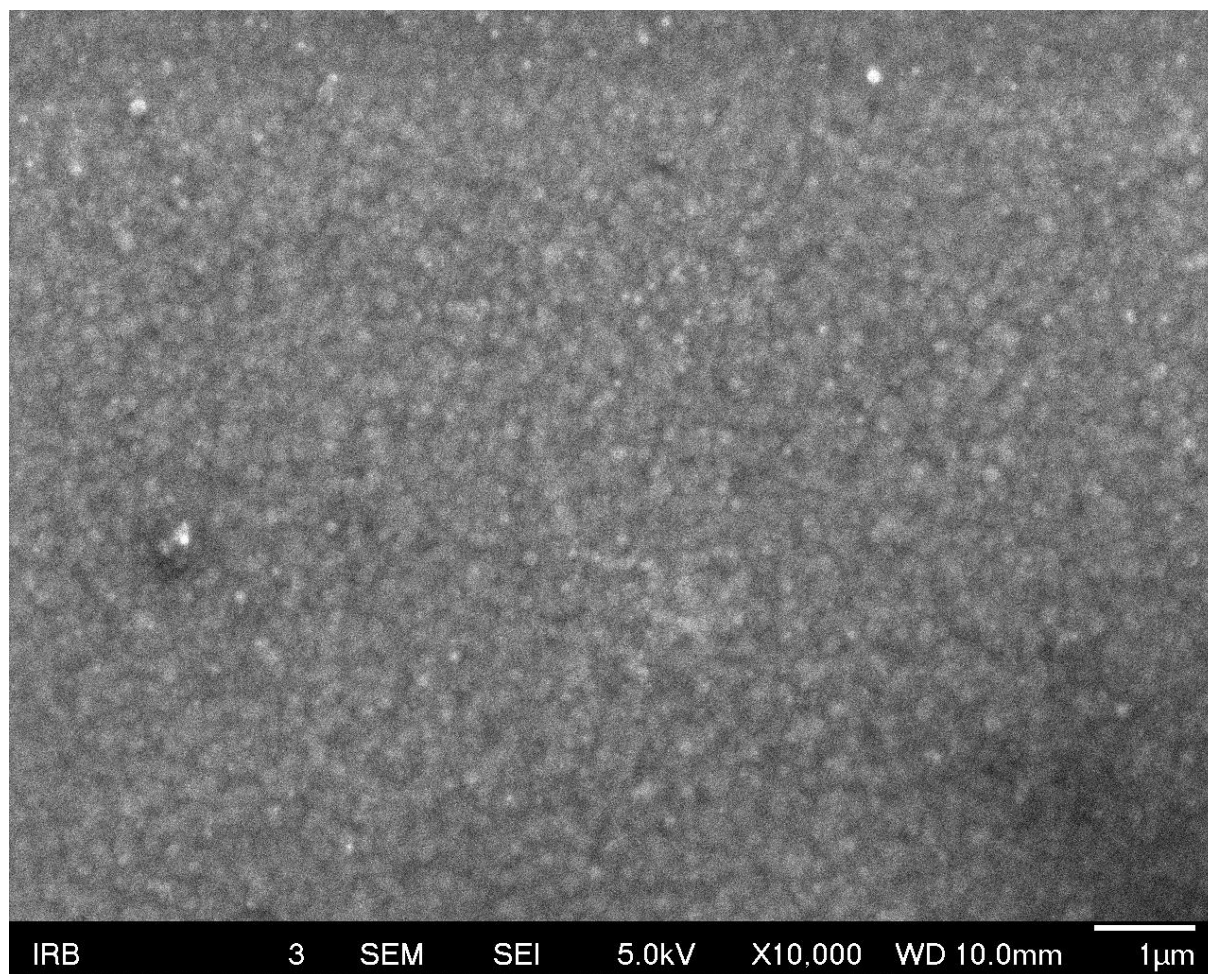


Figure 7.5 FE-SEM image of the top view of the sample incubated in 10^{-2} M CV with continuous CV film over the pores

To overcome this issue, the EDS technique was employed. This method enabled the identification of the differences in the elemental composition between the samples with and without CV coating, as shown in Figure 7.6.

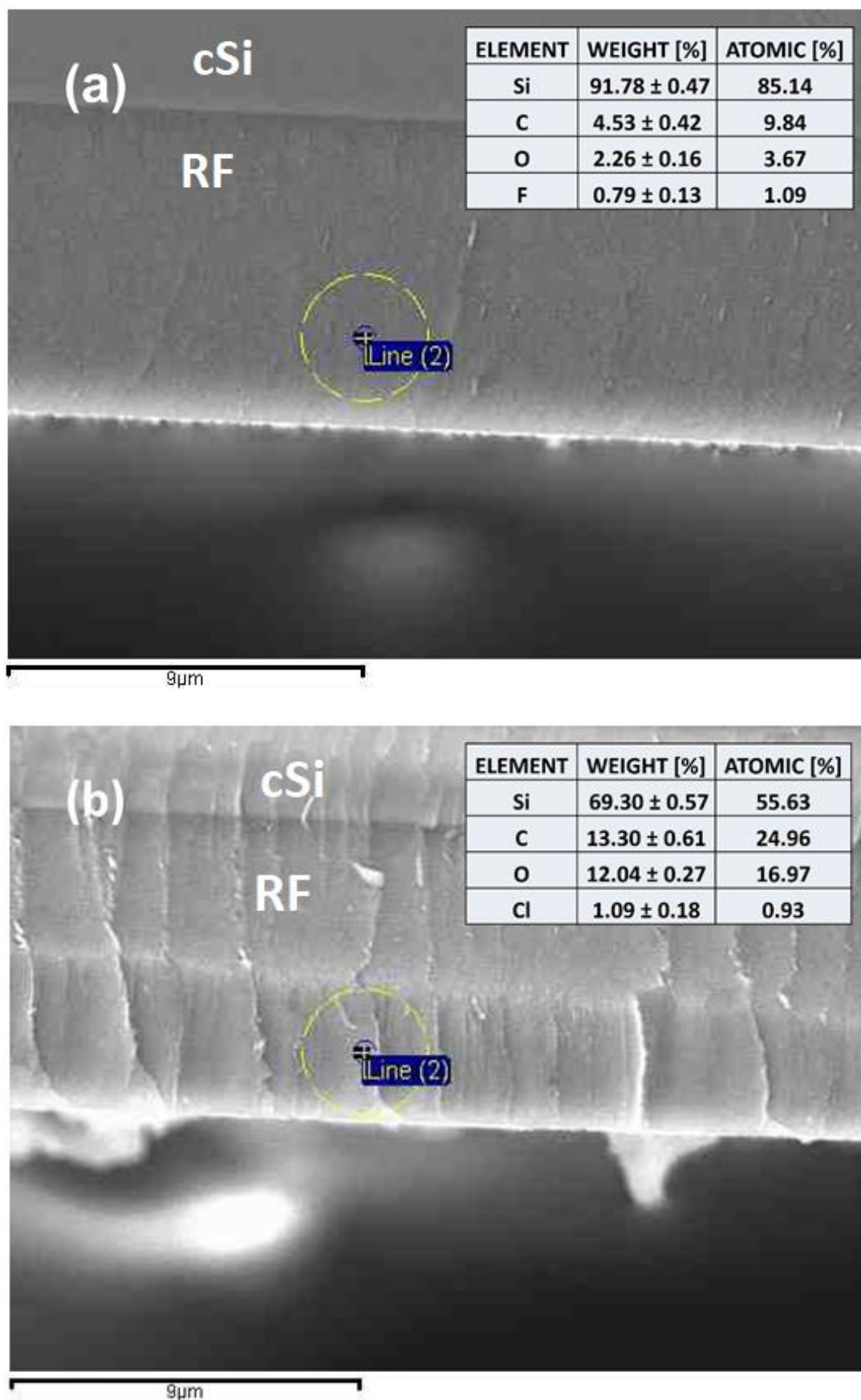


Figure 7.6 FE-SEM cross-section images with corresponding EDS elemental analysis of (a) as-etched pSi PhC sample and (b) pSi PhC sample incubated in 10^{-2} M CV

The EDS measurements, presented by yellow circles in both images, examined an equivalent sample depth of less than 3 μm . These yellow circles indicate the areas on which the compositional analysis was conducted. By focusing on these regions, it was possible to ensure that the depth analysis of the elemental composition across samples was consistent, which allowed the direct comparison of the results. Moreover, it ensures that the gathered EDS data provide reliable results and meaningful insights into the presence and distribution of different elements within the samples. The inset tables in Figure 7.6 show that there was a significant increase in the number of carbon atoms (approximately 2.5 times) in the incubated samples. Carbon atoms are the primary constituents of CV molecules, so this increase indicates that the CV molecules penetrated into the porous structure. Additionally, the detection of 1% of fluorine atoms in the samples that were not incubated in CV can be attributed to residuals from the etching process. This is a common occurrence since the etching process often leaves a small amount of fluorine atoms in the samples. On the other hand, the presence of 1% of chlorine atoms in the incubated samples is a clear indicator of the CV molecules since chlorine is a component of the CV molecules. Moreover, chlorine atoms were not present in samples that were not incubated in CV, so this further supports the conclusion that CV molecules have infiltrated the porous structure. Inset tables in Figure 7.6 also show approximately four times higher concentration of oxygen atoms, which is likely due to the differences in the treatment of the samples. Specifically, both samples were initially exposed to an HF solution to remove any existing oxide layer. However, after this step, the CV samples were incubated in an aqueous CV solution, which may have led to oxidation due to exposure to water.

The key insight obtained by the EDS analysis is that the presence of CV molecules was not restricted to the surface of the photonic structure, but rather, they penetrated into it. This is in agreement with the expectations since the molecule's dimensions are approximately $1.4 \times 1.4 \text{ nm}^{140}$, while the average pore size ranges from 10 to 20 nm, indicating that the pores are roughly one order of magnitude larger. Additionally, the analysis of the deeper regions of the porous layer revealed that the molecules did not penetrate too deep into the structure, but rather, they diffused into approximately 40% of the thickness of the porous layer.

7.2 Raman signal

Measurements of the Raman signal were performed using a 785 nm laser excitation. Spectra were acquired from 3 mapping areas on each sample, with approximately 25 spectra recorded in each mapping area. The main reason why it was not possible to record the same number of spectra on each mapping area is the constraints of the experimental setup, which allowed the definition of the mapping area and the step size but not the number of spectra to be recorded. Additionally, some data sets contained one or two outliers, characterized by much stronger or weaker Raman signals compared to others, so after removing these outliers, 23 to 25 spectra were available for further analysis.

The outliers can originate from two different sources: either from the Raman signal of the CV molecule or from the Raman signal of the constituent material, which is characterized by significantly different intensity of $\sim 520\text{ cm}^{-1}$ band. An example of a dataset containing an outlier corresponding to the Raman signal of the CV molecule is presented in Figure 7.7.

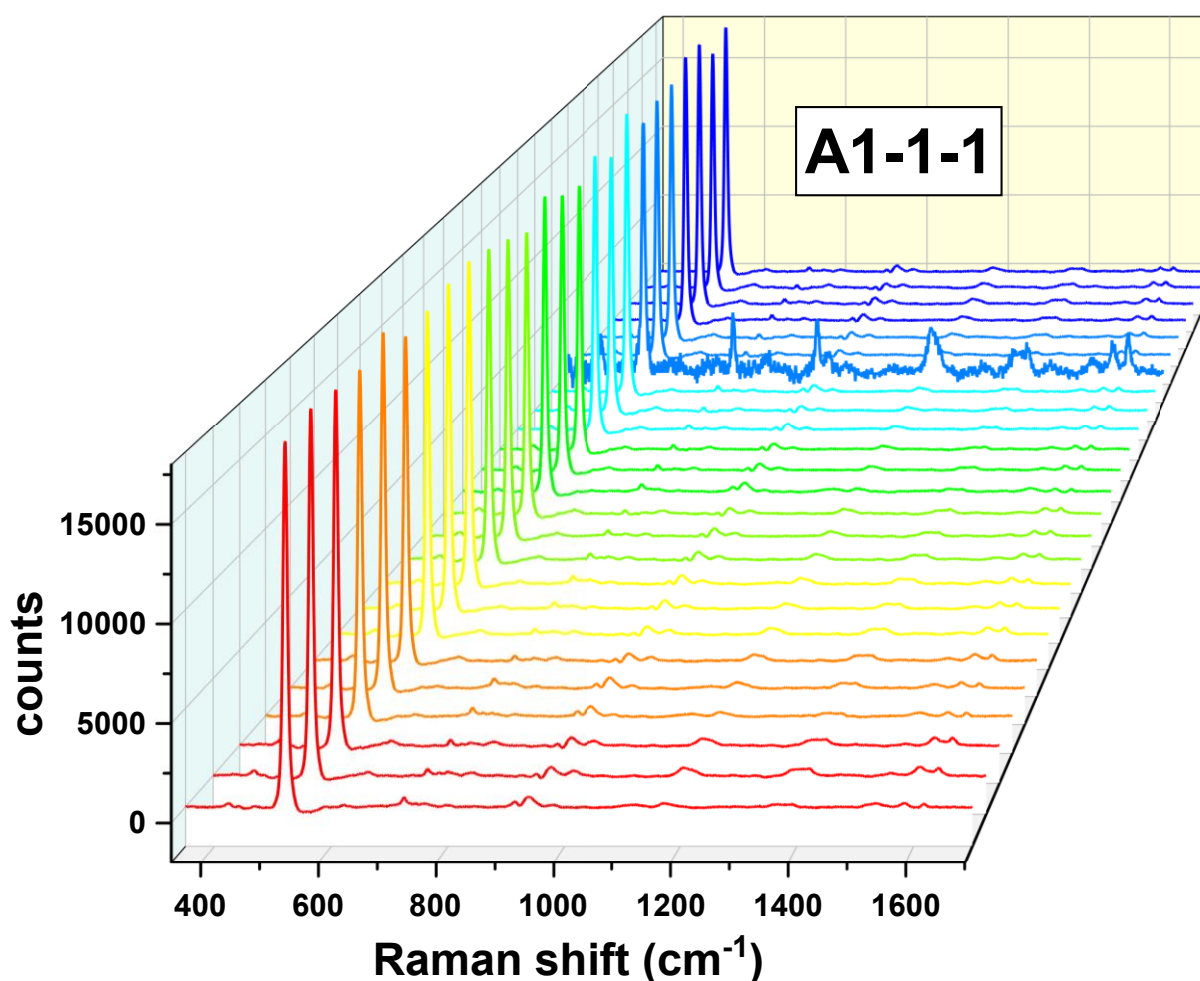


Figure 7.7 The data set of 25 Raman spectra recorded in one mapping area shows one outlier regarding signal intensity from the probe molecule

The outliers associated with the silicon peak at $\sim 520\text{ cm}^{-1}$ can be explained by considering the experimental setup for the etching procedure. Aluminum backside contact with the silicon wafer placed on it typically results in homogeneous PhC layers in the middle of the wafer. The reflectance spectra shown in Figure 7.2 represent a macroscopic characteristic of samples since they were recorded on an area of approximately $6.5 \times 6.5\text{ mm}^2$. In contrast, the Raman laser spot size was much smaller, with a radius of less than $4.5\text{ }\mu\text{m}$. Consequently, the outliers in the $\sim 520\text{ cm}^{-1}$ band were likely caused by minor inhomogeneities in the local electric field during the etching process. These inhomogeneities created regions with different refractive indices compared to the rest of the sample, which altered the defined sample category at that particular spot on the sample. This claim is validated by considering the spectra obtained from samples that belong to sample category A, which represents the ordinary pSi sample. In this case, no outliers in the $\sim 520\text{ cm}^{-1}$ peak were found, and the variation in the intensity of the $\sim 520\text{ cm}^{-1}$ peak was less than 15% of the mean value. It is also important to mention that despite the local inhomogeneities, the PhCs in this work were of good quality. Another parameter confirming this claim (apart from the Bragg attenuation length) is the width of the reflectance peak of our RFs. According to theory, high-quality RFs typically exhibit narrow peaks with low FWHM values. In this work, the FWHM values for our RFs were about 60 nm indicating good quality of our PhCs.

In contrast, the outliers corresponding to the intensity of the CV peaks likely originated from the local accumulations or deaccumulations of CV molecules, both inside the sample and on its surface. These imperfections in the distribution of the probe molecule at a certain spot on the sample are attributed to imperfections in the incubation method. An optical image shown in Figure 7.8, recorded by a Raman microscope, shows a typical rectangular specimen coated with CV molecules. Black spots covering the surface of the sample are local imperfections in the distribution of the CV molecules. The white rectangle presents an example of a randomly selected mapping area on which ~ 25 spectra were recorded. The spot-to-spot intensity variation across all CV Raman bands in over 90% of spectra for each mapping area was less than 25%, indicating that the quasi-uniform coating by CV molecules was achieved. Despite this overall uniformity, it is important to note that most outliers corresponded to significantly different Raman signals of the CV molecules rather than the Raman signal of the silicon band. This indicates that local variations in the distribution of the CV molecules are indeed present. However, these variations are limited to the outliers, and a meaningful analysis can be conducted after removing a few compromised spectra.

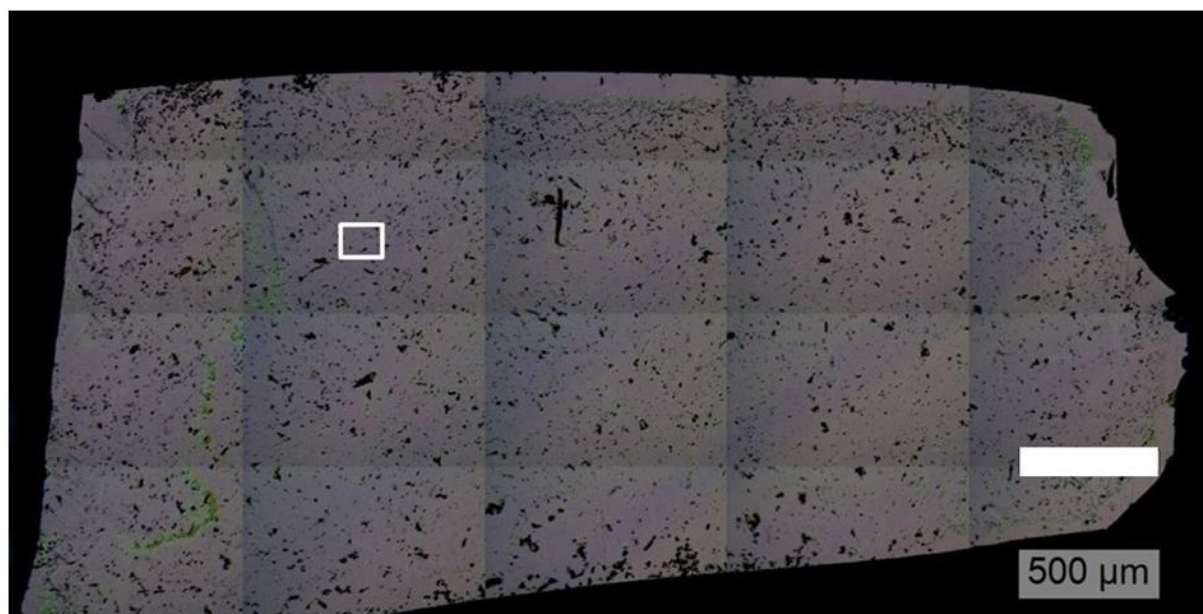


Figure 7.8 Optical image of a typical rectangular specimen showing surface coating by CV molecules. The white rectangle represents one randomly selected mapping area, and the black spots are local accumulations of CV molecules

This observation highlights a significant issue in quantifying Raman enhancement by PhCs. As mentioned in Chapter 5, most previous studies reported results based on only a few spectra. This limited approach can be problematic as some reported enhancements may have resulted from outliers or spectra with unrepresentative Raman signals. For instance, when only a few spectra are analyzed, an anomalous signal could cause misinterpretation, leading to incorrect conclusions about the performance of PhCs, so any study with only a few spectra should not be considered as a validation of the PhCs' influence on Raman signal enhancement. Therefore, a comprehensive statistical approach is necessary to obtain meaningful insights about the influence of PhCs on Raman signal enhancement. By analyzing a large number of spectra and considering the distribution of signal intensities across multiple peaks, the risk of drawing wrong conclusions based on anomalous data points is significantly reduced.

To overcome this issue and ensure a comprehensive analysis, a large number of spectra was recorded, and the results obtained from every level in the schematic representation in Figure 6.5 were analyzed and compared with each other to check for consistency and reliability of the findings. After eliminating outliers from the datasets, 23-25 spectra were available for further analysis from each mapping area. Spectra from one mapping area were averaged, so the averaging procedure resulted in 9 mean spectra for each of the four samples within a particular sample category (3 mapping areas on 3 rectangular specimens). These mean spectra were then baseline corrected, using the same positions of zero points across all sample categories, and the results for the typical sample are given in Figure 7.9.

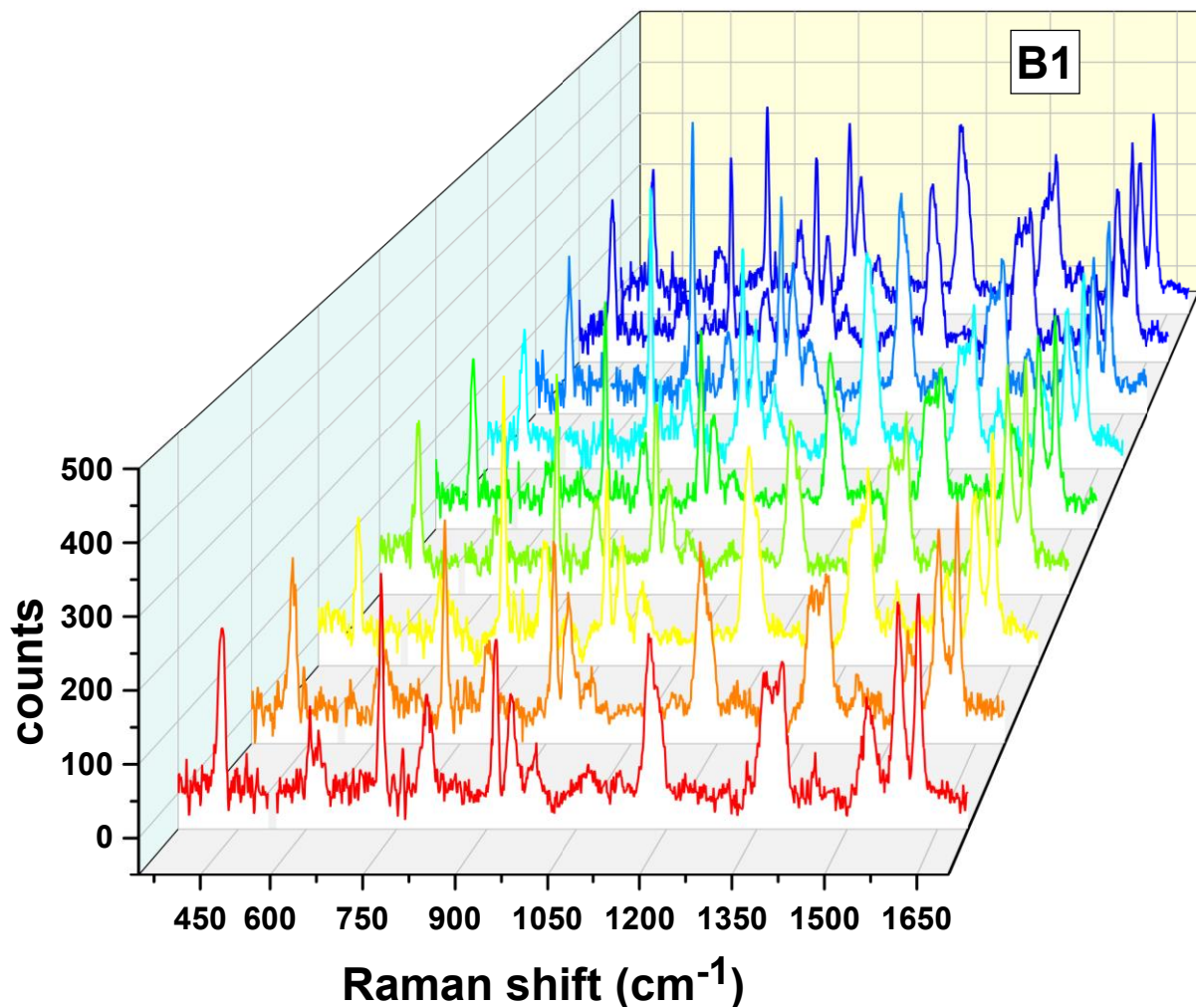


Figure 7.9 The data set consisting of 9 mean Raman spectra obtained from sample B1. The ~ 520 cm⁻¹ silicon peak is removed for clarity of the y-axis

For further analysis, the ten most prominent CV Raman bands, whose assignments are given in previous works^{141,142}, were used. The typical Gaussian fitting results obtained using Origin software are shown in Figure 7.10, where the maximum height values were used for further analysis.

Peak Analysis

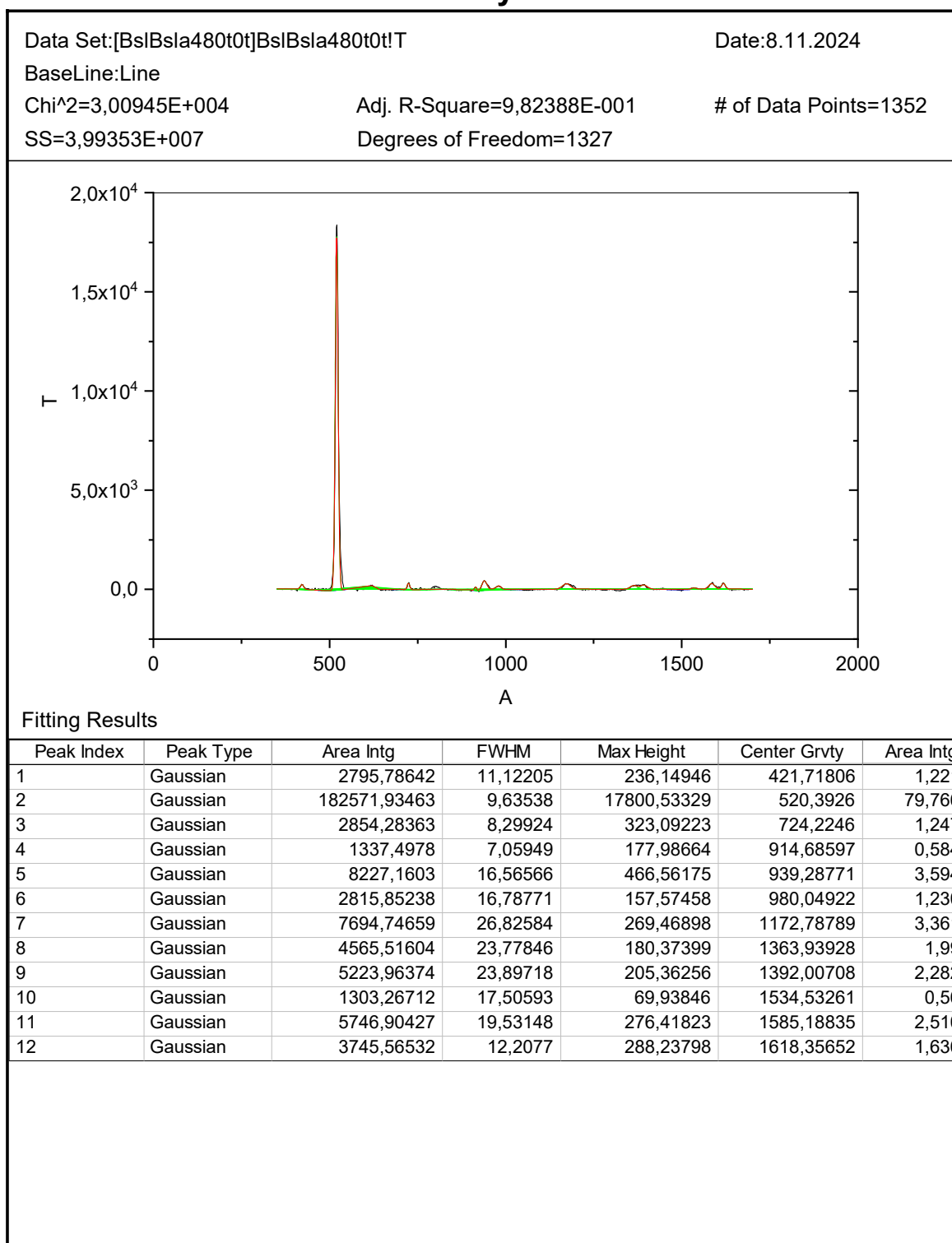


Figure 7.10 Gaussian fitting results for silicon and the most prominent CV Raman peaks, showing peak area, full width at half maximum (FWHM), maximum height, center of gravity, and area integral (IntgP) for each peak. The results were obtained using Origin software, with the peak characteristics summarized in the table below the plot.

To present these results visually, Figure 7.11 displays bar plot of the mean Raman band intensities across all four samples and six sample categories. The corresponding numerical data can be found in Table 7.2 to Table 7.4. It should be noted that the results in all tables are rounded for clarity: the standard deviation was rounded to the first significant digit, and the mean values were rounded to match this level of precision. Consequently, due to this rounding, the relative error may sometimes be larger than it would be with unrounded data.

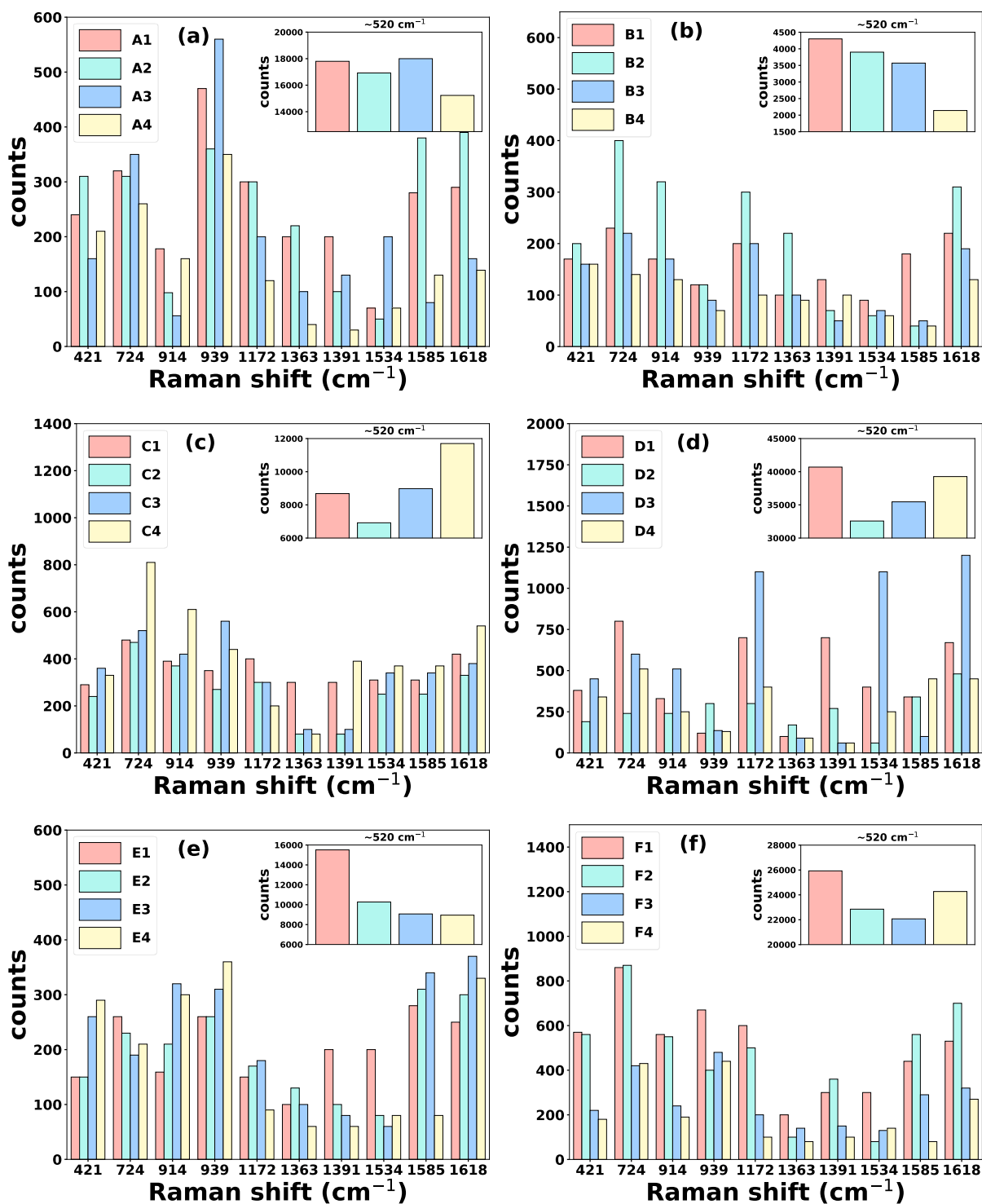


Figure 7.11 Bar plots representing mean intensities of Raman bands recorded on 4 different samples (A1-A4, etc.) within 6 different sample categories (A – F). Images (a) – (f) show data for sample categories A, B, C, D, E, and F

Table 7.2 Numerical values representing the intensity of the main CV Raman bands and $\sim 520 \text{ cm}^{-1}$ Si band for four samples across sample categories A and B, obtained by Gaussian fitting

Intensity for a given sample (counts) / CV Raman bands (cm^{-1})	I_{A1}	I_{A2}	I_{A3}	I_{A4}	I_{B1}	I_{B2}	I_{B3}	I_{B4}
421	240 ± 20	310 ± 40	160 ± 20	210 ± 30	170 ± 30	200 ± 20	160 ± 30	160 ± 40
520	17800 ± 20	16920 ± 20	18000 ± 20	15230 ± 20	4300 ± 20	3900 ± 20	3570 ± 20	2140 ± 20
724	320 ± 10	310 ± 10	350 ± 20	260 ± 10	230 ± 10	400 ± 10	220 ± 10	140 ± 10
914	178 ± 8	98 ± 4	300 ± 30	160 ± 9	170 ± 10	320 ± 30	170 ± 10	130 ± 20
939	470 ± 50	360 ± 30	560 ± 70	350 ± 50	120 ± 40	200 ± 60	90 ± 30	70 ± 50
1172	300 ± 100	300 ± 200	200 ± 100	120 ± 70	200 ± 100	300 ± 200	200 ± 200	100 ± 90
1363	200 ± 100	220 ± 90	100 ± 200	40 ± 100	100 ± 100	200 ± 100	100 ± 100	90 ± 100
1391	200 ± 100	300 ± 100	130 ± 30	80 ± 20	130 ± 50	220 ± 70	130 ± 70	90 ± 50
1534	70 ± 60	50 ± 40	200 ± 100	70 ± 50	90 ± 100	60 ± 100	70 ± 100	60 ± 100
1585	280 ± 70	380 ± 90	190 ± 30	110 ± 10	180 ± 60	200 ± 50	170 ± 40	110 ± 40
1618	290 ± 30	380 ± 60	160 ± 10	139 ± 8	220 ± 20	310 ± 30	190 ± 20	130 ± 20

Table 7.3 Numerical values representing the intensity of the main CV Raman bands and $\sim 520 \text{ cm}^{-1}$ Si band for four samples across sample categories C and D, obtained by Gaussian fitting

Intensity for a given sample (counts) CV Raman bands (cm^{-1})	I_{C1}	I_{C2}	I_{C3}	I_{C4}	I_{D1}	I_{D2}	I_{D3}	I_{D4}
421	290 ± 30	240 ± 40	360 ± 40	330 ± 20	380 ± 30	190 ± 40	450 ± 50	340 ± 40
520	8680 ± 20	6920 ± 20	8980 ± 20	11700 ± 20	40700 ± 20	32570 ± 20	35460 ± 20	39270 ± 20
724	480 ± 10	470 ± 20	520 ± 10	810 ± 10	800 ± 10	240 ± 10	600 ± 20	510 ± 10
914	390 ± 20	370 ± 20	410 ± 10	610 ± 20	330 ± 20	240 ± 30	510 ± 20	250 ± 40
939	350 ± 60	270 ± 70	280 ± 50	440 ± 50	200 ± 100	160 ± 80	136 ± 6	130 ± 30
1172	400 ± 100	300 ± 200	400 ± 200	600 ± 200	700 ± 200	300 ± 100	1100 ± 200	400 ± 200
1363	200 ± 100	200 ± 100	200 ± 100	300 ± 100	600 ± 100	170 ± 90	1000 ± 100	90 ± 70
1391	300 ± 80	300 ± 100	260 ± 80	390 ± 60	700 ± 100	270 ± 60	1200 ± 100	210 ± 50
1534	100 ± 90	100 ± 100	150 ± 90	180 ± 80	100 ± 40	60 ± 10	300 ± 100	60 ± 5
1585	310 ± 60	250 ± 50	340 ± 40	370 ± 30	600 ± 100	340 ± 60	1100 ± 100	250 ± 30
1618	420 ± 30	330 ± 30	380 ± 20	540 ± 20	670 ± 50	480 ± 40	1200 ± 50	450 ± 20

Table 7.4 Numerical values representing the intensity of the main CV Raman bands and $\sim 520 \text{ cm}^{-1}$ Si band for four samples across sample categories E and F, obtained by Gaussian fitting

Intensity for a given sample (counts) CV Raman bands (cm^{-1})	I_{E1}	I_{E2}	I_{E3}	I_{E4}	I_{F1}	I_{F2}	I_{F3}	I_{F4}
421	150 ± 20	150 ± 20	260 ± 20	290 ± 40	570 ± 20	560 ± 20	220 ± 10	180 ± 20
520	15510 ± 20	10270 ± 20	9070 ± 20	8950 ± 20	25930 ± 20	22850 ± 20	22070 ± 20	24270 ± 20
724	260 ± 30	230 ± 20	190 ± 10	210 ± 20	860 ± 10	870 ± 10	420 ± 10	430 ± 10
914	159 ± 8	210 ± 20	320 ± 20	300 ± 20	560 ± 10	550 ± 10	240 ± 10	190 ± 7
939	260 ± 40	260 ± 60	310 ± 50	360 ± 50	670 ± 50	400 ± 30	480 ± 50	440 ± 50
1172	150 ± 80	170 ± 90	200 ± 100	200 ± 100	600 ± 100	500 ± 100	220 ± 90	200 ± 100
1363	100 ± 90	150 ± 90	300 ± 100	200 ± 100	200 ± 100	300 ± 100	140 ± 80	100 ± 80
1391	100 ± 30	150 ± 60	320 ± 90	300 ± 100	300 ± 40	360 ± 50	150 ± 50	130 ± 40
1534	200 ± 100	100 ± 100	80 ± 60	60 ± 40	300 ± 80	300 ± 100	120 ± 90	200 ± 100
1585	280 ± 50	310 ± 70	340 ± 80	250 ± 60	440 ± 30	560 ± 60	290 ± 50	270 ± 40
1618	250 ± 20	300 ± 30	370 ± 40	330 ± 30	530 ± 10	700 ± 20	320 ± 20	270 ± 10

The graphical representation clearly shows comparable intensities of all Raman bands across different samples within each sample category, apart from a few bands in sample categories A and D. Each column in the bar plot represents the average of 9 mean spectra obtained for each of the four samples within one sample category. For example, the average of the 9 spectra depicted in Figure 7.9 corresponds to sample B1 in Figure 7.11b, represented by the red column. To enhance clarity, the y-axis scales in Figure 7.11a to Figure 7.11f are adjusted differently to compare the mean intensities of each Raman band across four different samples. Since the $\sim 520\text{ cm}^{-1}$ silicon peak intensities are roughly two orders of magnitude higher than those of the CV bands, each image includes an inset where the silicon peak alone is presented.

Although the overall reproducibility of the samples is rather good, with variability of 15 to 25% within one category, confirming the reliability of the data, a closer examination reveals some anomalies in the mean intensities of certain CV bands. For example, 7 out of 10 CV bands on sample B2 have the highest intensities, followed by samples B1, B3, and B4 in descending order. Conversely, in sample categories C and E, the mean intensities of Raman bands do not display a consistent trend, where one sample consistently shows the highest and or the lowest intensity. Additionally, samples F3 and F4 stand out with significantly lower intensities for several CV bands compared to the samples F1 and F2. This deviation might indicate localized imperfections or variations in the sample preparation. Furthermore, the relative ratios of the mean intensities of the ten observed CV bands differ across various sample categories, likely depending on how the molecules arrange themselves on the surface. This variation highlights the complexity of the analysis of the Raman signal enhancement from different PhC samples. These observations highlight the importance of the comprehensive statistical approach employed in this study. The variability and specific trends identified in different sample categories highlight the necessity of using a large dataset to draw reliable conclusions. Only by analyzing multiple Raman bands across various samples and sample categories is it possible to get meaningful and reliable results. This approach ensures that the findings are not skewed by outliers or anomalies and that they reflect the true information about the influence of the PhCs on Raman signal enhancement.

To get an insight into the consistency of our results, the exact average values and corresponding standard deviations for all wavenumbers in each sample category were calculated and depicted in Figure 7.12 and Figure 7.13. The analysis includes approximately 900 spectra per sample category. The discrepancy between the fitted values given in Figure 7.11 and the exact values given in Figure 7.12 is, for most bands across all sample categories, less than 15%, with the

exception of several bands in sample category D. Additionally, the standard deviation across all Raman bands within a single sample category is typically much less than 25%, except for the bands at 914 cm^{-1} , 1363 cm^{-1} , and 1391 cm^{-1} in sample categories D and F.

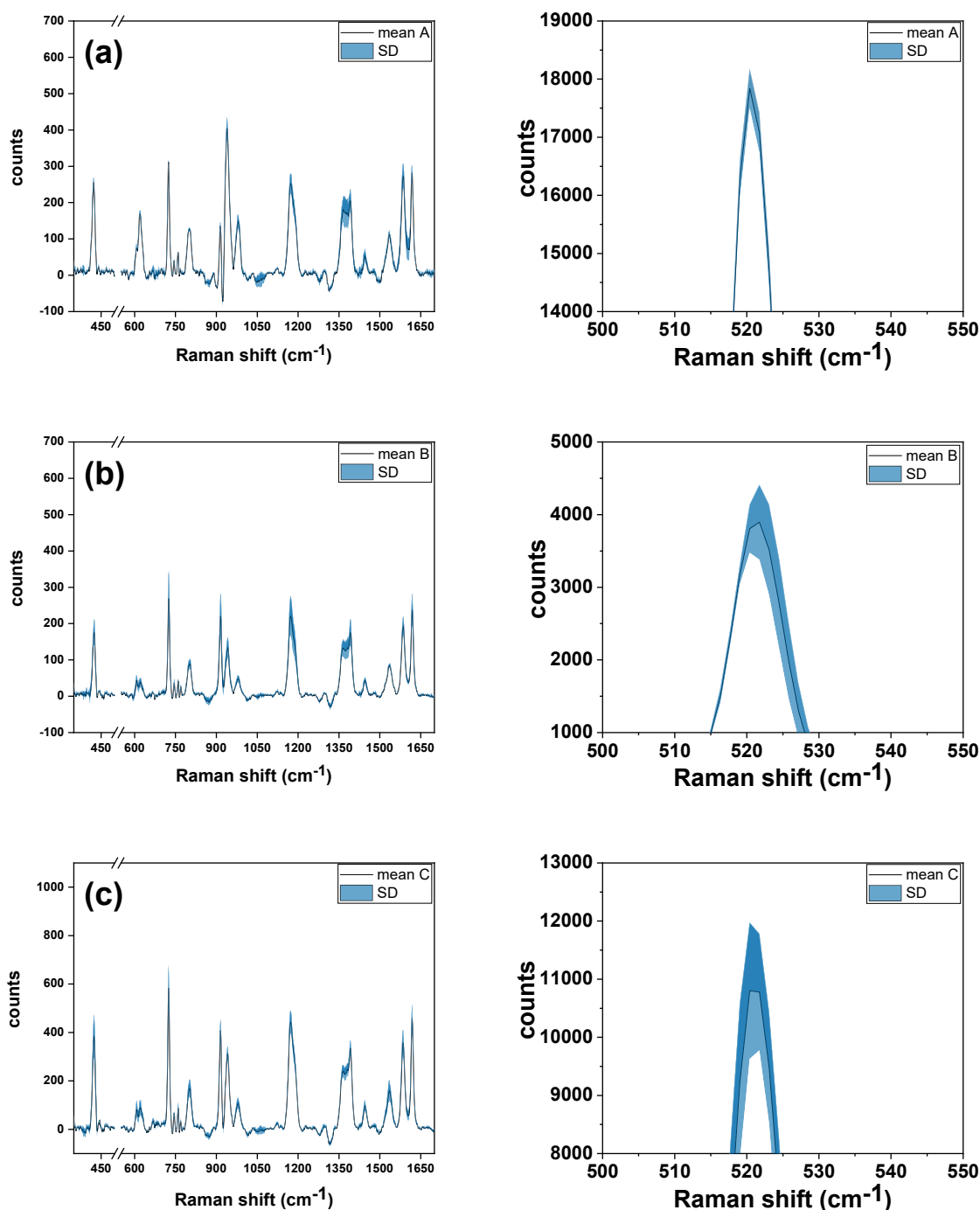


Figure 7.12 Mean CV Raman spectra obtained from 4 different samples across 3 sample categories (A-C) and corresponding standard deviation, computed in Matlab. The mean Raman intensity and corresponding standard deviation for $\sim 520\text{ cm}^{-1}$ silicon band are depicted on the right panels

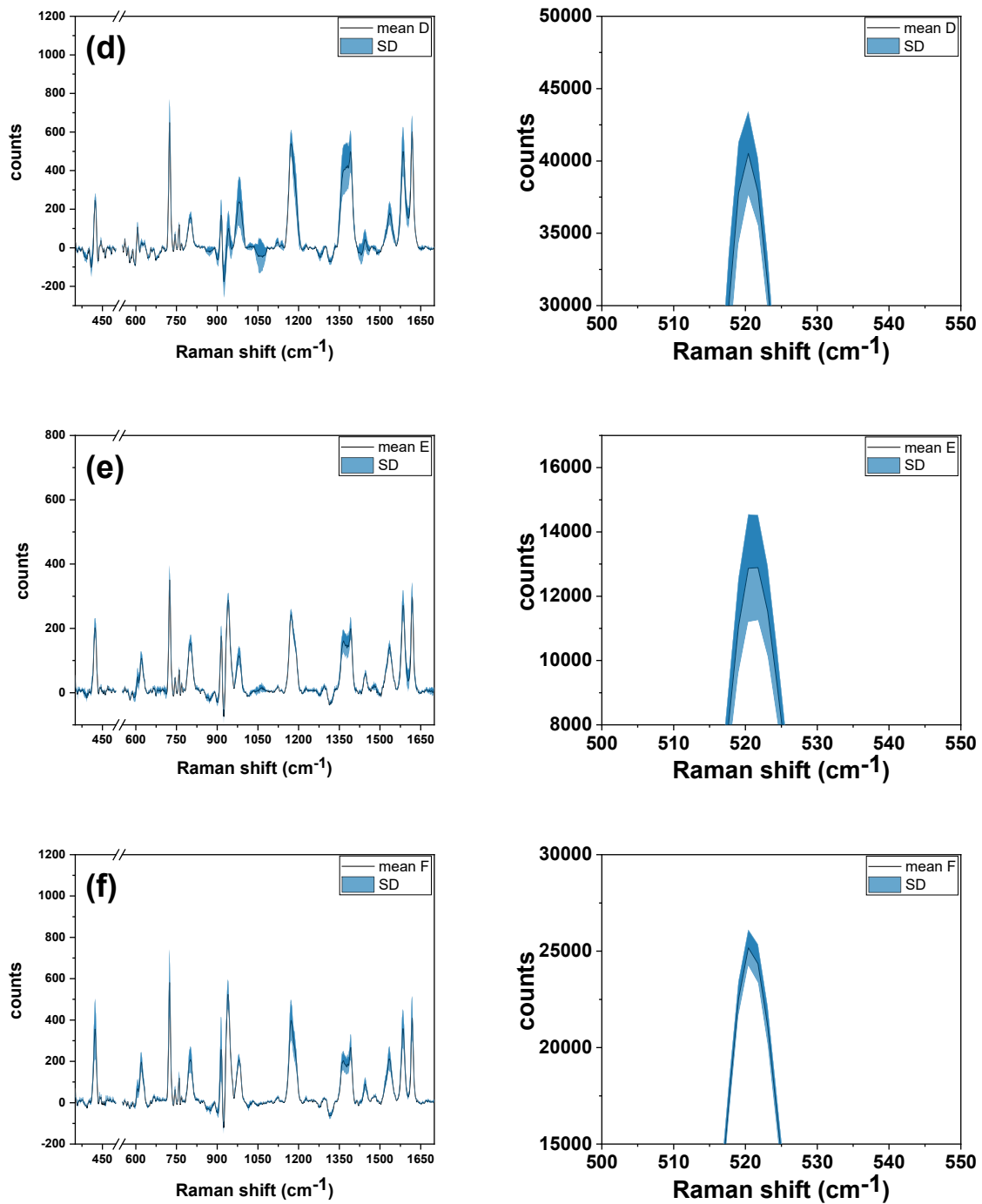


Figure 7.13 Mean CV Raman spectra obtained from 4 different samples across 3 sample categories (D-F) and corresponding standard deviation, computed in Matlab. The mean Raman intensity and corresponding standard deviation for $\sim 520 \text{ cm}^{-1}$ silicon band are depicted on the right panels

Additionally, the Student's t-test was used to evaluate whether there are statistically significant differences in Raman intensities between the reference sample category A and the remaining categories, for each Raman peak. The results of these comparisons are presented in Table 7.5. Furthermore, pairwise comparisons between all combinations of categories (B to F) were performed to assess the differences between them. The results of these pairwise analyses are provided in Table 7.6 to Table 7.9, offering a comprehensive view of the statistical distinctions across sample categories.

Table 7.5 Results of the Student's t-test for comparing Raman silicon peak intensity and CV Raman peak intensities of sample categories B to F with the reference sample category A. Each row represents a specific CV Raman peak, with t-statistic and p-value reported for each sample comparison. The t-statistic indicates the ratio of the difference in sample means to the variability in the data, while p-values $p < 0.05$ indicate statistically significant differences in intensity between the groups at the corresponding Raman peak

CV Raman Peak	B_T-Statistic	B_P-Value	C_T-Statistic	C_P-Value	D_T-Statistic	D_P-Value	E_T-Statistic	E_P-Value	F_T-Statistic	F_P-Value	
0	421	1.755435	0.129712	-1.841727	0.115102	-1.739253	0.132647	0.363096	0.728982	-1.383152	0.215886
1	520	17.167931	0.000003	6.756516	0.000513	-10.264162	0.000050	3.609758	0.011234	-6.420633	0.000674
2	724	1.081518	0.321007	-3.137620	0.020129	-1.932674	0.101467	3.655631	0.010635	-2.608630	0.040194
3	914	-1.475730	0.190470	-5.242117	0.001934	-3.056332	0.022330	-2.631202	0.038997	-2.552729	0.043331
4	939	6.538530	0.000612	0.376473	0.719519	4.008754	0.007048	2.490584	0.047125	-0.803669	0.452244
5	1172	0.502331	0.633334	-1.172106	0.285583	-2.136176	0.076554	1.717911	0.136618	-0.946713	0.380335
6	1363	0.238095	0.819730	0.000000	1.000000	0.589945	0.576754	0.948847	0.379333	0.200000	0.848087
7	1391	0.698971	0.510742	-1.223835	0.266889	-1.016702	0.348526	0.106399	0.918734	-1.591322	0.162642
8	1534	0.781079	0.464450	-5.120666	0.002177	-1.547690	0.172663	-0.159373	0.878604	-1.104634	0.311636
9	1585	1.820717	0.118503	-1.361353	0.222306	-0.891315	0.407080	-0.386609	0.712385	-1.005783	0.353344
10	1618	0.462346	0.660125	-2.336705	0.058105	-2.483251	0.047595	-1.058230	0.330682	-1.823037	0.118122

Based on the Student's t-test results comparing Raman peak intensities between the reference sample category A and sample categories B to F, the 520 cm^{-1} silicon peak consistently shows statistically significant differences across categories, highlighting the fact that it can be used to identify sample categories. The high t-statistics observed for the 520 cm^{-1} peak emphasize the robustness of these differences, making it a critical indicator of unique characteristics in each sample category.

The analysis also reveals significant differences across a range of other Raman bands, with p-values often falling below the 0.1 threshold. These differences suggest that, at a 90% confidence level (or even higher for some bands), the Raman profiles of categories B, C, D, E, and F are distinct from the reference category A. Large t-statistics (e.g., $t > |5|$) in several bands further highlight that these distinctions are unlikely due to random variation. However, some peaks,

specifically in categories B and E, do not show significant differences compared to category A, indicating less pronounced variation for those peaks.

Table 7.6 Results of the Student's t-test for comparing Raman silicon peak intensity and CV Raman peak intensities between sample category B and sample categories C, D, E, and F

CV Raman Peak	B_vs_C_T-Statistic	B_vs_C_P-Value	B_vs_D_T-Statistic	B_vs_D_P-Value	B_vs_E_T-Statistic	B_vs_E_P-Value	B_vs_F_T-Statistic	B_vs_F_P-Value	
0	421	-4.791853	0.003026	-3.005361	0.023843	-1.058080	0.330746	-1.978800	9.518211e-02
1	520	-5.113747	0.002192	-17.608524	0.000002	-4.616315	0.003629	-20.918119	7.773908e-07
2	724	-3.307692	0.016251	-2.257932	0.064732	0.441081	0.674604	-2.873859	2.828394e-02
3	914	-3.610006	0.011231	-1.794030	0.122965	-0.880316	0.412556	-1.748605	1.309430e-01
4	939	-4.807473	0.002978	-1.600557	0.160593	-7.345527	0.000326	-6.514716	6.236395e-04
5	1172	-1.732051	0.133975	-2.306300	0.060575	1.153104	0.292727	-1.192079	2.782357e-01
6	1363	-0.202168	0.846466	0.411435	0.695046	0.879883	0.412773	-0.061430	9.530123e-01
7	1391	-1.667329	0.146496	-1.218200	0.268873	-0.630641	0.551524	-2.196501	7.044096e-02
8	1534	-9.313137	0.000087	-1.685940	0.142784	-1.067490	0.326807	-1.919221	1.033778e-01
9	1585	-5.611573	0.001366	-2.824869	0.030160	-2.572093	0.042216	-2.431380	5.106651e-02
10	1618	-3.509276	0.012683	-2.744302	0.033544	-2.210878	0.069060	-2.286524	6.224013e-02

In the pairwise comparisons between sample category B and categories D to F, clear patterns also appear, as represented in Table 7.6. For example, the 520 cm^{-1} silicon peak, serving as a control, consistently shows significant differences between categories, which reinforces its value in distinguishing sample categories. Other peaks also often reveal substantial differences. However, a closer look at the pairwise comparisons show some inconsistencies. For instance, in the comparison of B with E, seven out of ten peaks do not exhibit significant differences (peaks at 421, 724, 914, 1172, 1363, 1391, and 1534 cm^{-1}), suggesting some overlap in the Raman profiles of these categories. On the other hand, categories B and C, as well as B and F, display strong statistical differences across most peaks, indicating more distinct Raman profiles.

Table 7.7 Results of the Student's t-test for comparing Raman silicon peak intensity and CV Raman peak intensities between sample category C and sample categories D, E, and F

	CV Raman Peak	C_vs_D_T-Statistic	C_vs_D_P-Value	C_vs_E_T-Statistic	C_vs_E_P-Value	C_vs_F_T-Statistic	C_vs_F_P-Value
0	421	-0.576046	0.585527	2.060863	0.084955	-0.712001	0.503196
1	520	-13.348137	0.000011	-1.023469	0.345567	-11.295573	0.000029
2	724	0.229678	0.825971	4.232903	0.005483	-0.498250	0.636042
3	914	1.379862	0.216844	2.992760	0.024234	0.552832	0.600353
4	939	3.087214	0.021464	1.611870	0.158116	-1.071826	0.325005
5	1172	-1.763641	0.128248	3.349492	0.015429	-0.397360	0.704853
6	1363	0.483157	0.646109	0.766679	0.472350	0.167444	0.872522
7	1391	-0.325625	0.755764	1.309459	0.238284	-0.102441	0.921745
8	1534	-0.591564	0.575737	5.182541	0.002049	2.863912	0.028655
9	1585	0.127906	0.902403	1.013586	0.349896	-0.234533	0.822370
10	1618	-1.575382	0.166238	2.041306	0.087286	-0.344517	0.742212

When comparing sample category C and E the results continue to show significant differences in many peaks. However, comparisons with sample category D and especially F do not show significant differences across most of the peaks implying similarities between categories C and D, as well as C and F. Additionally, the comparison of C with E shows similarity in the 520 cm^{-1} silicon peak, which is expected since for both of these categories the laser is aligned with similar reflectance conditions. This alignment results in similar intensities at this particular peak, while still allowing some differences in other regions.

Table 7.8 Results of the Student's t-test for comparing Raman silicon peak intensity and CV Raman peak intensities between sample category D and sample categories E and F

	CV Raman Peak	D_vs_E_T-Statistic	D_vs_E_P-Value	D_vs_F_T-Statistic	D_vs_F_P-Value
0	421	1.931763	0.101596	-0.356783	0.733466
1	520	10.814359	0.000037	6.509670	0.000626
2	724	2.688366	0.036131	-0.624326	0.555394
3	914	1.166189	0.287792	-0.449393	0.668926
4	939	-2.562108	0.042787	-4.428718	0.004429
5	1172	2.640665	0.038506	1.275854	0.249171
6	1363	0.623289	0.556031	-0.534263	0.612366
7	1391	1.055041	0.332026	0.276368	0.791539
8	1534	1.517367	0.179968	1.251491	0.257337
9	1585	0.582590	0.581387	-0.275305	0.792317
10	1618	2.208360	0.069300	1.225128	0.266436

The comparative analysis of sample category D with categories E and F reveals statistically significant differences across multiple Raman peaks, particularly when compared with category E. These distinctions reinforce the unique profiles of these categories. Notably, the 520 cm^{-1} silicon peak displays highly significant p-values ($p = 0.000037$ for D vs. E, and $p = 0.000626$ for D vs. F), confirming its value as a control for identifying sample differences. Most other peaks do not show significant differences when comparing D with F, suggesting an overlap in Raman profiles for these categories. This result aligns with the expectation, since both categories correspond to the alignment of the laser excitation with the PBG edge.

Table 7.9 Results of the Student's t-test for comparing Raman silicon peak intensity and CV Raman peak intensities between sample category E and sample category F

	CV Raman Peak	E_vs_F_T-Statistic	E_vs_F_P-Value
0	421	-1.519767	0.179379
1	520	-7.263363	0.000346
2	724	-3.302739	0.016352
3	914	-1.302824	0.240400
4	939	-3.106162	0.020951
5	1172	-1.677459	0.144464
6	1363	-1.079591	0.321799
7	1391	-1.709750	0.138167
8	1534	-1.001263	0.355355
9	1585	-0.756262	0.478123
10	1618	-1.391901	0.213358

Finally, when sample category E is compared with F, the comparison reveals statistically significant differences at several peaks, including 520 cm^{-1} , 724 cm^{-1} , and 939 cm^{-1} , suggesting distinct profiles between the two. Even peaks like 421 cm^{-1} , 914 cm^{-1} , 1172 cm^{-1} , 1391 cm^{-1} and 1618 cm^{-1} do show differences within the confidence interval of approximately 80%. This nuanced profile of significant and non-significant differences reflects both unique and overlapping characteristics in the Raman intensities of categories E and F.

Considering the results obtained in this analysis, it can be concluded that while each category exhibits a largely unique Raman profile, specific peaks reveal similarities. These findings suggest that while the overall profiles are distinct, certain bands may represent shared compositional or structural features among the categories, emphasising once again that the

analysis of one or a few Raman bands is insufficient for scientifically verifying the photonic crystal's influence on Raman signal intensity.

The enhancement of the Raman signal by PhCs was determined using the final results presented in Table 7.10 and Table 7.11, and depicted in Figure 7.14. The mean intensity for the 10 most prominent Raman bands in the spectrum was calculated by averaging approximately 900 spectra per sample category, resulting in a total of around 5400 spectra across all six categories. The results are rounded according to the previously mentioned rule. Error bars in Figure 7.14 indicate the standard deviation for each band. The enhancement factors (EFs) were determined by dividing the number of counts for a particular band and a particular sample category by the corresponding number of counts for sample category A. In contrast to this study, previous research typically reported findings based on the analysis of only a few spectra, often focusing on a single Raman band (as shown in Table 5.1).

Table 7.10 Mean intensities and the corresponding standard deviations of the main CV Raman bands and ~520 cm⁻¹ Si band for sample categories A, B and C. Corresponding enhancement factors were calculated with respect to the sample category A

CV Raman bands (cm ⁻¹)	Mean Raman intensity (counts) and EFs	I _A	I _B	EF (B)	I _C	EF (C)
421		200 ± 10	180 ± 10	0.89 ± 0.08	320 ± 20	1.6 ± 0.1
520 (Si)		17000 ± 600	3400 ± 500	0.20 ± 0.03	9000 ± 1000	0.53 ± 0.06
724		302 ± 7	235 ± 6	0.78 ± 0.03	574 ± 7	1.90 ± 0.05
914		119 ± 3	174 ± 8	1.46 ± 0.08	450 ± 9	3.8 ± 0.1
939 (?)		400 ± 20	110 ± 20	0.27 ± 0.06	330 ± 30	0.83 ± 0.08
1172		180 ± 50	150 ± 60	0.8 ± 0.4	410 ± 80	2.3 ± 0.8
1363		160 ± 50	130 ± 60	0.8 ± 0.5	230 ± 60	1.5 ± 0.6
1391		100 ± 20	130 ± 30	1.3 ± 0.4	320 ± 40	3.1 ± 0.7
1534		70 ± 30	70 ± 60	1.0 ± 0.9	140 ± 50	2 ± 1
1585		123 ± 9	160 ± 20	1.3 ± 0.2	330 ± 20	2.7 ± 0.3
1618		157 ± 6	190 ± 10	1.22 ± 0.08	450 ± 10	2.8 ± 0.1

Table 7.11 Mean intensities and the corresponding standard deviations of the main CV Raman bands and $\sim 520\text{ cm}^{-1}$ Si band for sample categories D, E and F. Corresponding enhancement factors were calculated with respect to the sample category A

CV Raman bands (cm^{-1}) \ / \ Mean Raman intensity (counts) and EFs	I_D	EF (D)	I_E	EF(E)	I_F	EF(F)
421	340 ± 20	1.7 ± 0.1	180 ± 10	0.90 ± 0.07	343 ± 8	1.7 ± 0.1
520 (Si)	37000 ± 2000	2.2 ± 0.1	11000 ± 2000	0.64 ± 0.09	23800 ± 800	1.40 ± 0.07
724	515 ± 6	1.70 ± 0.04	209 ± 9	0.69 ± 0.03	623 ± 6	2.06 ± 0.05
914	360 ± 10	3.0 ± 0.1	198 ± 7	1.67 ± 0.07	308 ± 5	2.59 ± 0.08
939 (?)	136 ± 6	0.34 ± 0.03	290 ± 20	0.74 ± 0.07	490 ± 20	1.22 ± 0.09
1172	550 ± 80	3 ± 1	180 ± 50	1.0 ± 0.4	340 ± 50	1.9 ± 0.6
1363	330 ± 50	2.0 ± 0.7	190 ± 50	1.1 ± 0.5	180 ± 50	1.1 ± 0.5
1391	390 ± 30	3.8 ± 0.8	140 ± 30	1.3 ± 0.3	240 ± 20	2.3 ± 0.5
1534	61 ± 5	0.9 ± 0.4	80 ± 30	1.2 ± 0.7	230 ± 50	4 ± 2
1585	330 ± 20	2.7 ± 0.3	290 ± 30	2.3 ± 0.3	380 ± 20	3.1 ± 0.3
1618	560 ± 20	3.6 ± 0.2	290 ± 10	1.8 ± 0.1	425 ± 7	2.7 ± 0.1

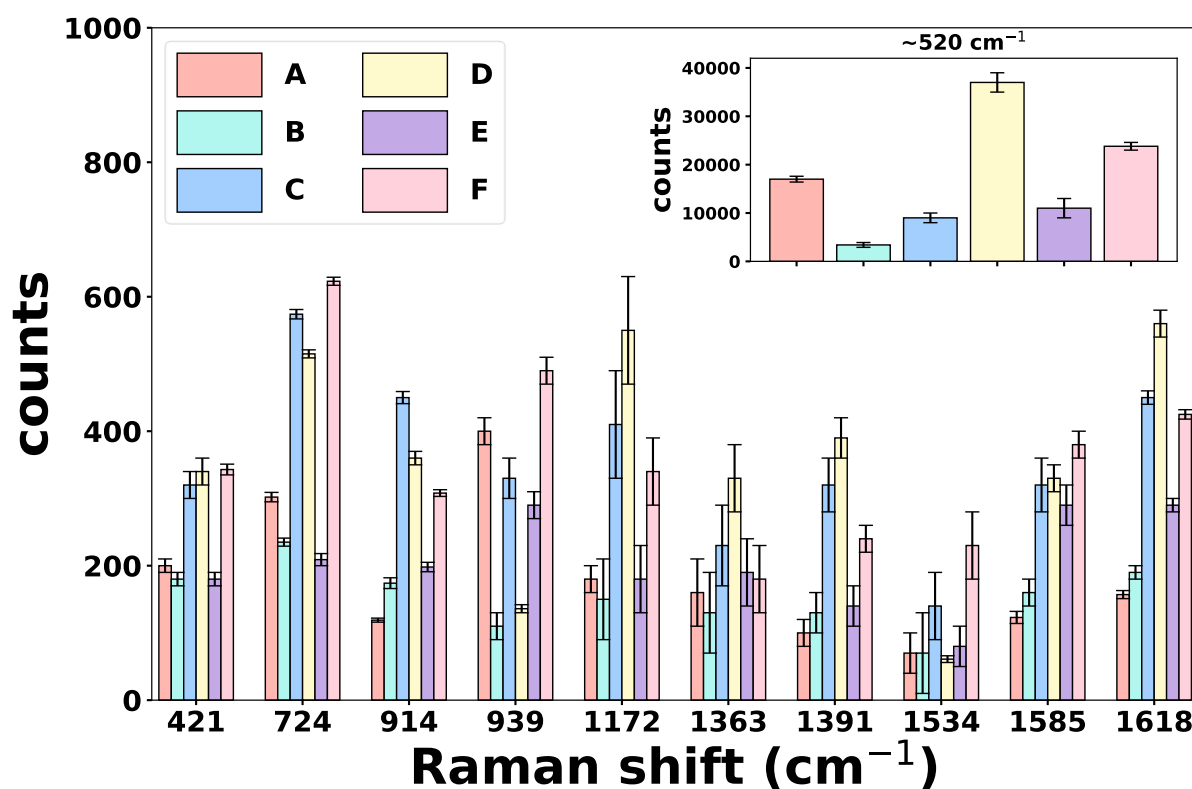


Figure 7.14 Bar plot illustrating the final mean intensities of the main CV Raman bands for six sample categories and $\sim 520 \text{ cm}^{-1}$ band highlighted in the inset. Error bars represent the standard deviation for each band

The analysis of the signal enhancement is structured in two sections: the first part pertains to the examination of the intensity of the $\sim 520 \text{ cm}^{-1}$ peak that corresponds to the Raman peak of silicon. This section gives information about the changes in the intensity of the Raman signal obtained from the constituent material. The second part investigates the Raman signal from the probe molecule. Both sections of the analysis focus on the effect of the alignment of the laser excitation with the specific position of the PBG. Additionally, the influence of the PBG on the Raman-shifted bands is also discussed.

7.2.1 Silicon $\sim 520 \text{ cm}^{-1}$ Raman band

The intensity of the Raman silicon band at $\sim 520 \text{ cm}^{-1}$, which is associated with scattering by transversal-optical phonons at the Brillouin zone center, allows the verification of the relative position between the laser excitation and the PBG. When the laser aligns with the center of the PBG, most of the incident radiation is reflected, resulting in a lower Raman signal. At the PBG edges, the increased density of states and minimal reflectance enhance the intensity of the signal, while positions within the PBG at approximately 50% of the reflectance peak show varying degrees of reflectance and transmission, leading to moderate Raman intensities. This variation in intensity for sample categories from B to F serves as a control for sample categories. The consistent position and shape of this band across all sample categories suggest that phonon confinement effects were negligible. This finding is crucial as it ensures that the variations in Raman intensity originate from the differences in the relative position between the laser excitation and the PBG and not from any intrinsic differences in the samples.

For the ordinary pSi, corresponding to sample category A, the intensity of the $\sim 520 \text{ cm}^{-1}$ Raman peak varied by less than 10% between samples A1 to A4, as can be concluded from Figure 7.11 and Table 7.2. Table 7.10 shows that the average intensity of the $\sim 520 \text{ cm}^{-1}$ silicon peak is ~ 17000 counts, meaning that the variation within the sample category A is $\pm 5\%$ from the average value. This small variation indicates a high degree of reproducibility in the preparation and measurements of these samples. The penetration depth of 785 nm laser excitation into pSi samples is about $10 \mu\text{m}$. Given that the thickness of the porous layer is approximately $7.5 \mu\text{m}$, at least one-quarter of the mean number of counts for $\sim 520 \text{ cm}^{-1}$ peak in sample category A originated from scattering in the underlying cSi. This assumption is important for accurate interpretation of the Raman data since it shows that the intensity of $\sim 520 \text{ cm}^{-1}$ Raman band has two contributions: one from the porous layer and another from the substrate.

For sample category B, the laser excitation aligns with the center of the reflectance peak, which corresponds to the center of the PBG, resulting in more than 80% of the incident radiation being reflected, as shown in Figure 7.2. Consequently, only a small fraction of the incident radiation penetrates the PhC and contributes to Raman scattering. As expected, the mean intensity of the $\sim 520 \text{ cm}^{-1}$ Raman peak is, in this case, five times lower compared to sample category A, resulting in ~ 3400 counts on average. This significant reduction in the Raman signal of the

$\sim 520\text{ cm}^{-1}$ band is consistent with the high reflectivity of the PhC at the PBG center, which effectively reduces the amount of light available for generating Raman scattering.

The decrease in the Raman signal from the material forming the PhC has been reported previously⁹⁵. It highlights the effectiveness of the PhC structure in reflecting incident light when the laser excitation falls within the PBG and reducing the Raman signal intensity. The 5 nm wavelength range that was the allowed variation in the relative position between the laser excitation and the PBG, corresponding to the predetermined uncertainty interval for each sample category, resulted in approximately 25% variability in intensity obtained from samples B1 to B4. When using laser excitation at 785 nm, the silicon band at 520 cm^{-1} is observed at 818 nm. Since the FWHM of the reflectance peak for our PhC samples is approximately 60 nm, the 818 nm position corresponds to a reflectance of around 40%, indicating that the intensity of the silicon band is partially suppressed by the photonic structure, as shown in Figure 7.15.

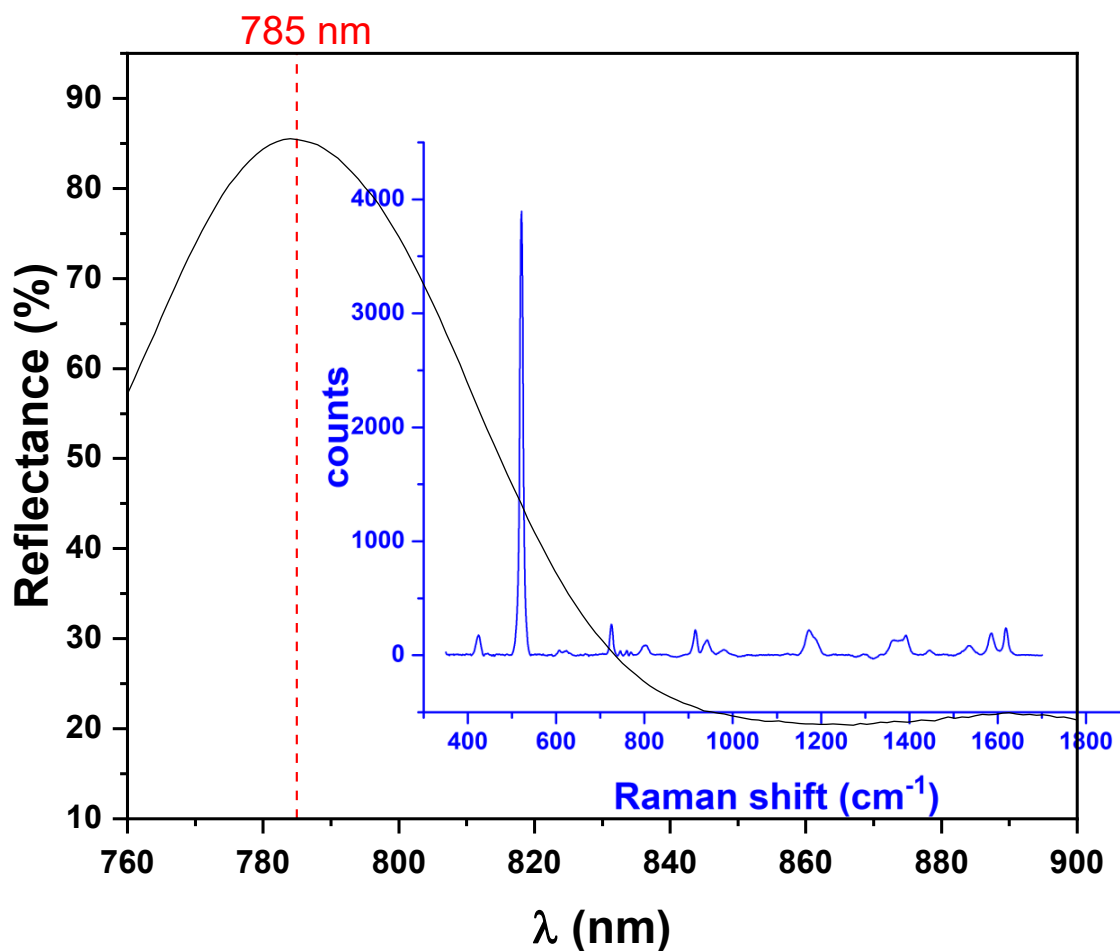


Figure 7.15 Overlay of the reflectance spectra of the PhC for sample category B with the Raman spectra of the CV probe molecule, along with the 785 nm laser excitation wavelength (indicated by the red dashed line). In this sample, the laser overlaps with the top of the reflectance peak, illustrating how different Raman bands experience varying levels of reflection from the PhC, which may impact the enhancement observed for each band

However, quantifying this suppression was not possible, as the silicon peak is subject to varying degrees of reflectance across different PhC samples. Only in the case of sample category F does the peak lie outside the PBG as shown in Figure 7.16.

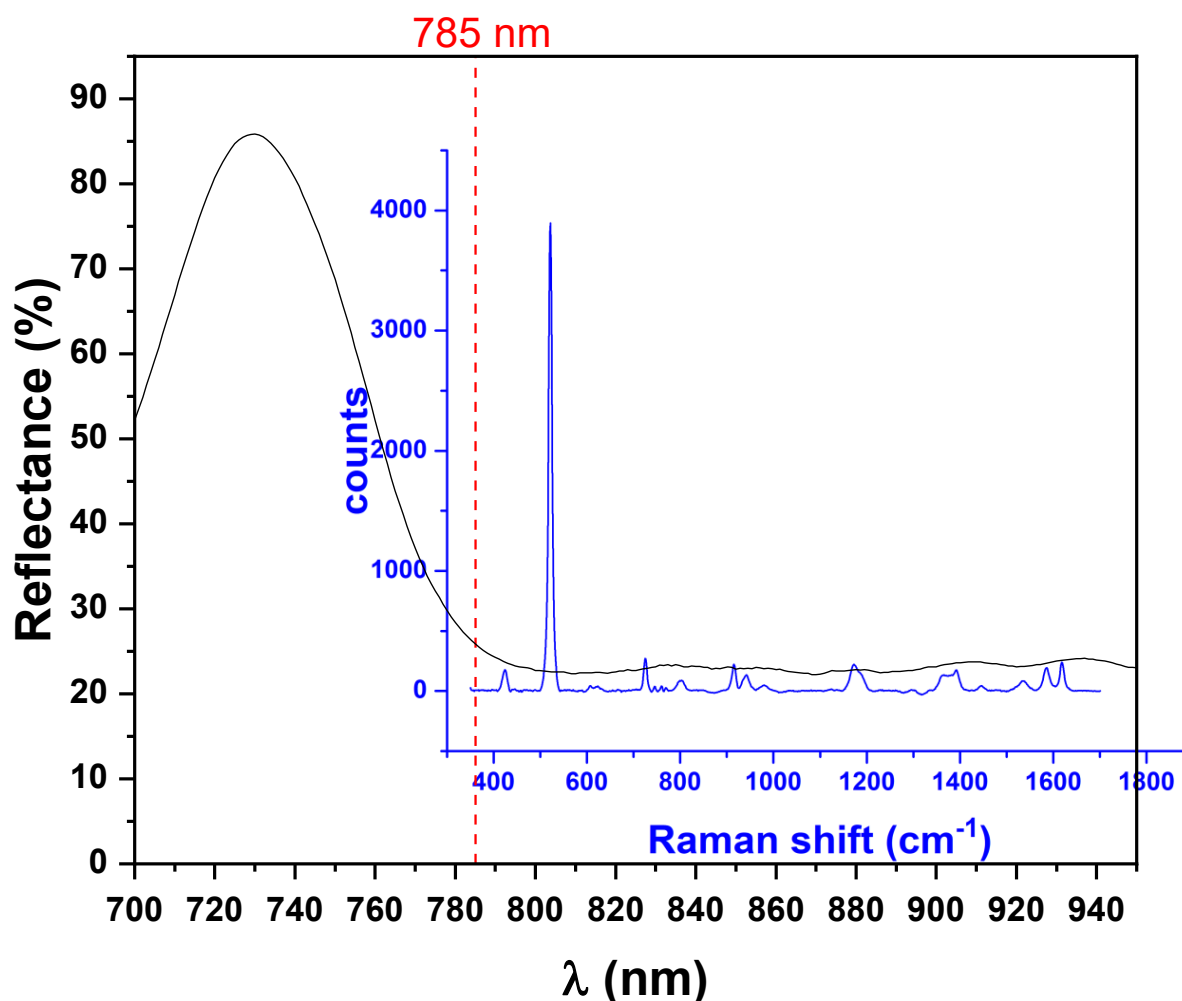


Figure 7.16 Overlay of the reflectance spectra of the PhC for sample category F with the Raman spectra of the CV probe molecule, along with the 785 nm laser excitation wavelength (indicated by the red dashed line). In this sample, the laser overlaps with the low-frequency edge of the reflectance peak

However, in that case the laser is aligned with the low-frequency edge of the reflectance peak, resulting in extended light-matter interaction. Consequently, the intensity of the 520 cm^{-1} band is influenced by both the reflectance and the enhanced light-matter interaction, making it challenging to isolate and quantify the specific impact of the reflectance alone.

The mean intensity of the $\sim 520\text{ cm}^{-1}$ Raman peak for sample categories D and F is higher compared to the control category A, as can be seen from Figure 7.14. Sample category D shows an increase of (2.2 ± 0.1) times, while an increase of (1.40 ± 0.07) times was obtained for category F, even though the reflectances of all three are similar. This enhancement of the silicon band, representing the Raman signal of the constituent material of PhC, in the case when the

laser excitation aligns with the edge of the PBG, has been theoretically predicted and experimentally observed in the past. However, the EFs covered a wide range of values, as shown in Table 5.1.

As mentioned in Chapter 1, Compaan and Trodahl¹⁴ showed that the rate of Raman-scattered photons is directly proportional to the square of the Raman susceptibility, as presented by equation (1.16). On the other side, according to the theory of photonic crystals, the light-matter interaction is significantly enhanced when the laser excitation coincides with the edge of the PBG. This enhancement can be attributed to either light localization or the longer light-matter interaction time (due to the increased density of optical states or significantly decreased group velocity at the PBG edge). As a result, in sample categories D and F, a higher probability of Raman scattering implies an increase in Raman susceptibility of either the PhC's constituent material or any molecule infiltrated into the PhC. This phenomenon was experimentally confirmed by a Russian group in several papers^{97,98,143}, which reported an increase in effective Raman susceptibility and estimated two orders of magnitude longer light-matter interaction time for pSi PhC. In their papers, this increase resulted in an almost tenfold enhancement of the $\sim 520 \text{ cm}^{-1}$ silicon peak.

Our results support the existence of an enhancement of the $\sim 520 \text{ cm}^{-1}$ peak, but with modest EFs. In the case of the alignment of the laser excitation with the high-frequency edge of the PBG, the EF was ~ 2.2 , while the intensity of the $\sim 520 \text{ cm}^{-1}$ Raman peak was enhanced ~ 1.4 times when the laser and the edge of the PBG overlapped on the low-frequency side of the corresponding reflectance peak.

The variation in EFs between the high- and low-frequency edges of the PBG is not easy to explain. Calculations show that the Raman shift of $\sim 520 \text{ cm}^{-1}$ falls just below the top of the reflectance peak for sample category D, while it is further away from the PBG edge for sample category F, as shown in Figure 7.17 and Figure 7.16.

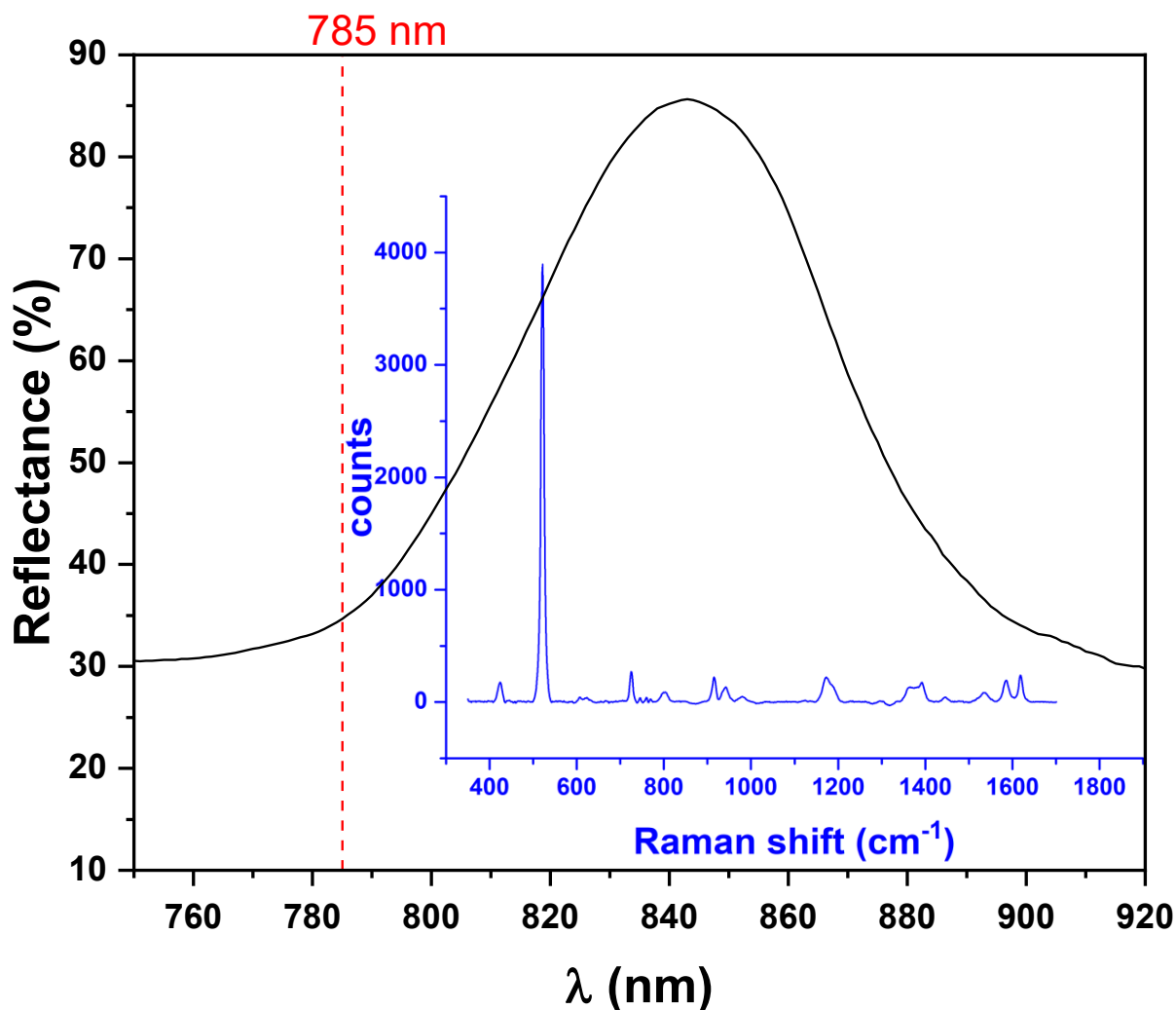


Figure 7.17 Overlay of the reflectance spectra of the PhC for sample category D with the Raman spectra of the CV probe molecule, along with the 785 nm laser excitation wavelength (indicated by the red dashed line). In this sample, the laser overlaps with the high-frequency edge of the reflectance peak, illustrating how different Raman bands experience varying levels of reflection from the PhC, which may impact the enhancement observed for each band

The reflectances at these specific positions are approximately 65% and 22%, respectively. Several reports in the literature indicate that the PBG inhibits the transmission of Raman-scattered photons through the PhC when the laser approaches the PhC surface at the normal incident angle due to Bragg reflection caused by the periodic multilayer structure^{115,120}.

Once Raman scattering occurs, the scattered photons attempt to propagate in all directions. However, if Raman-shifted wavelengths overlap with the PBG, their propagation is forbidden along the direction perpendicular to the PhC layers. Therefore, instead of transmitting through the crystal along this perpendicular direction, these photons are either back-reflected by the photonic structure or redirected to propagate in other available directions. Back-reflection leads to constructive interference caused by multiple reflections within the surface layers, which

should amplify the recorded intensity of Raman bands that are aligned with the PBG. For this reason, when certain Raman-shifted bands overlap with the PBG, constructive interference of back-reflected Raman-scattered light should enhance the recorded intensity for these bands. Considering this, the intensity of the silicon $\sim 520 \text{ cm}^{-1}$ band should be higher for sample category D. If this explanation holds true, it is important to note that most detected Raman-shifted photons likely originate from scattering in layers closer to the surface, as photons generated deeper within the PhC structure would be influenced by the PBG both above and below, affecting their transmission and detection. This complex interaction underscores the subtle nature of light-matter interactions in PhCs and the impact of structural and optical properties on Raman scattering efficiency.

Finally, sample categories C and E represent the alignment of the laser excitation with approximately half of the reflectance peak's height on the high- and low-frequency sides, respectively, as illustrated in Figure 7.1. These particular categories were included in the analysis because of the inconsistencies in the literature regarding the definition of the PBG edge and its potential contribution to the Raman signal enhancement. As graphically illustrated in the bar plots in Figure 7.14 and numerically represented in Table 7.10 and Table 7.11, the mean intensity of the silicon peak is about 50% lower for category C, with the EF of (0.53 ± 0.06) , and about 40% lower for category E, with the EF of (0.64 ± 0.09) compared to the sample category A, which serves as the control category. This decrease in intensity is in good agreement with the reflectance differences between these two sample categories and ordinary pSi. Figure 7.1 shows that the reflectance on the high-frequency edge of the PBG is approximately 5% higher than that on the low-frequency edge, leading to different half-heights on each side of the reflectance peak, which causes small variations in reflectance for sample categories C and E. These variations may be the cause of the observed differences in mean intensities between sample categories C and E. It is important to note that aligning the laser excitation with the specific position on the reflectance peak in the case of sample categories C and E was challenging, as even small variations led to significantly different reflectance due to its rapid increase and decrease on both sides. For that reason, only small variations from the central value were allowed. For example, Figure 7.11 shows that the variability in the intensity of the $\sim 520 \text{ cm}^{-1}$ peak was highest for sample category E, where sample E1 significantly increased the mean intensity of the silicon peak for that category. Contrary to the earlier explanation regarding the influence of the PBG on the $\sim 520 \text{ cm}^{-1}$ Raman-shifted band, the mean intensity for category E is unexpectedly higher than that for category C. This finding is

confusing since the Raman shift of $\sim 520 \text{ cm}^{-1}$ falls at the very top of the reflectance peak for sample category C where the reflectance is higher than 80%, as shown in Figure 7.18.

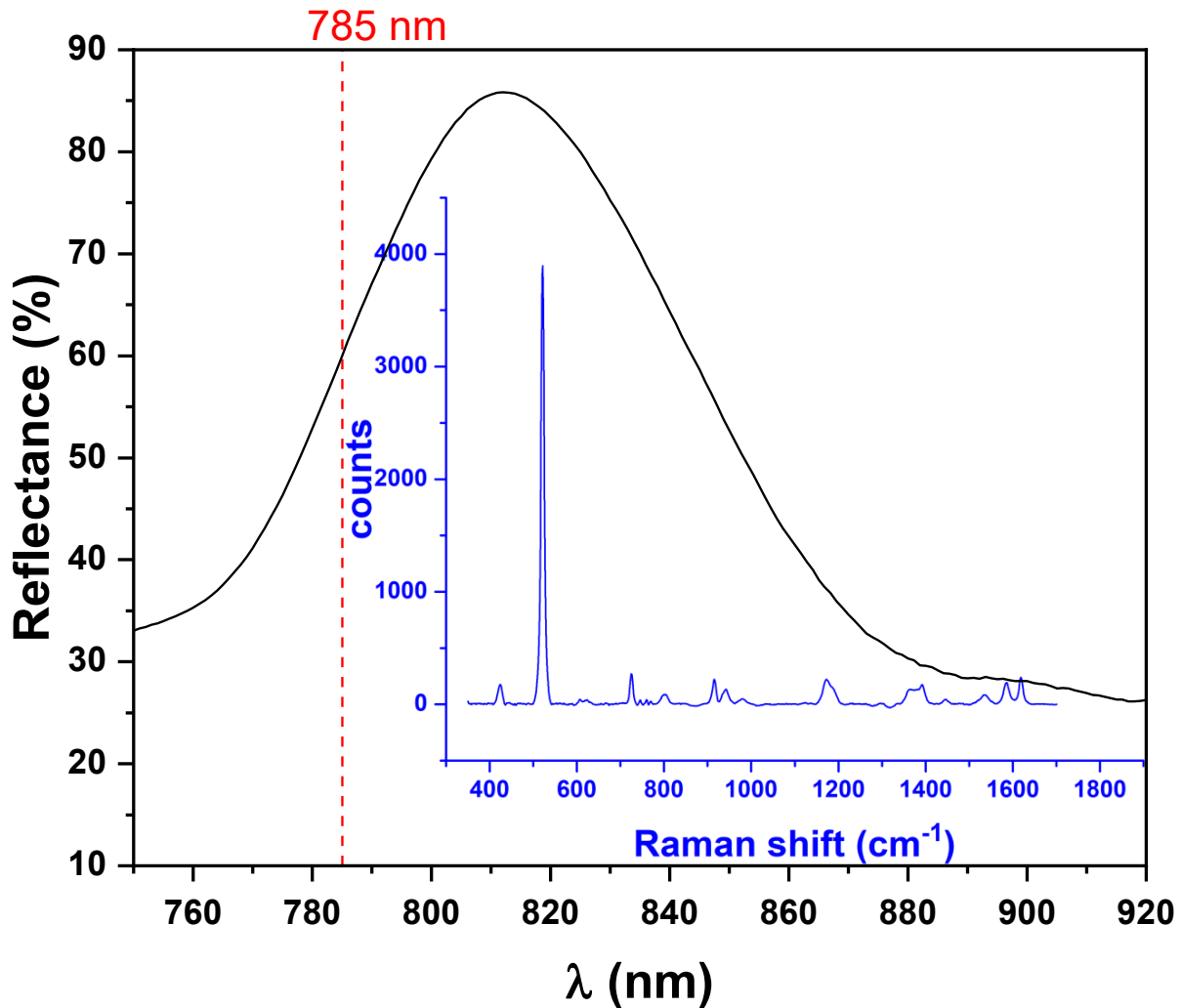


Figure 7.18 Overlay of the reflectance spectra of the PhC for sample category C with the Raman spectra of the CV probe molecule, along with the 785 nm laser excitation wavelength (indicated by the red dashed line). In this sample, the laser overlaps with the half-height of the reflectance peak on high-frequency side, illustrating how different Raman bands experience varying levels of reflection from the PhC, which may impact the enhancement observed for each band.

At this high reflectance, nearly all Raman-shifted photons generated in the superficial layers of the pSi PhC should be reflected back and increase the total number of counts.

In contrast, for sample category E, the Raman shift of $\sim 520 \text{ cm}^{-1}$ aligns precisely with the low-frequency edge of the PBG (Figure 7.19). This positioning results in a longer light-matter interaction time, which, in theory, enhances the Raman intensity due to the increased probability for the Raman scattering within the PhC structure.

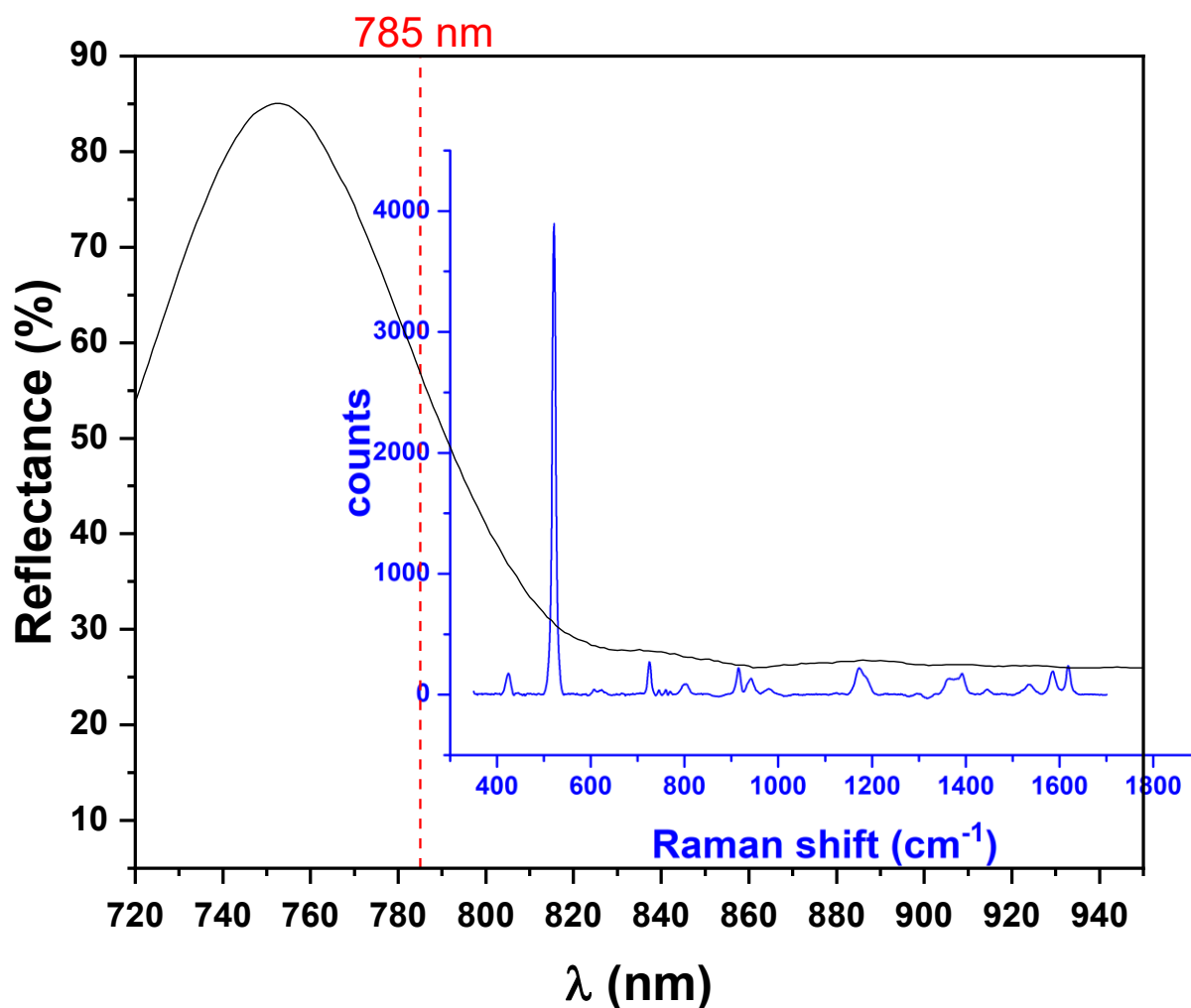


Figure 7.19 Overlay of the reflectance spectra of the PhC for sample category E with the Raman spectra of the CV probe molecule, along with the 785 nm laser excitation wavelength (indicated by the red dashed line). In this sample, the laser overlaps with the half-height of the reflectance peak on low-frequency side, illustrating how different Raman bands experience varying levels of reflection from the PhC, which may impact the enhancement observed for each band

Thus, there are two competing mechanisms: the high reflectance in sample category C, which should theoretically enhance Raman intensity by back-reflection, and the extended interaction time in sample category E, which suggests higher probability of scattering. The unexpected observation that the intensity of $\sim 520 \text{ cm}^{-1}$ in the sample category E is higher than in sample category C suggests that the enhancement due to the longer light-matter interaction at the PBG edge may overshadow the effect of high reflectance in amplifying the Raman signal for category C.

This analysis highlights an interplay between the effects of high reflectance and longer light-matter interaction time on Raman shifted bands within different regions of the PBG. However, it was not possible to isolate the effects of reflectance and interaction time independently, so

quantifying their individual contributions to the overall enhancement of the Raman-shifted bands was not achievable.

7.2.2 Ten most prominent CV Raman bands

The analysis of the intensity of the CV Raman bands is more complex due to the number of the observed bands. Figure 7.14 shows that the signal enhancement across CV Raman bands is not uniform since some bands show significantly different behavior compared to others, such as the band at 939 cm^{-1} . In the following analysis of the signal enhancement, the mean intensities from sample category A will serve as a reference.

When the center of the PhC's reflectance peak is aligned with the laser excitation, high reflectance suggests that the chance for Raman scattering to occur is almost doubled. This assumption is based on the fact that there are two contributions to the signal: one from the incident and the other from the back-reflected light. In the case of sample category B, a high reflectance of approximately 85% is observed, meaning that the contribution from the back-scattered light is significant and almost the same as the one from the incident beam. This doubled chance for Raman scattering primarily affects CV molecules adsorbed as a continuous film on the surfaces of pSi PhCs, as shown in Figure 7.8. Therefore, an expected enhancement factor for CV Raman bands was slightly lower than 2. Surprisingly, and contrary to several published studies (Table 5.1), the mean intensities for most observed CV bands are almost the same as those obtained from ordinary pSi. The differences in the signal intensity between sample categories A and B are relatively minor, as they fall within the range of standard deviation for several peaks. While the Student's t-test reveals statistically significant differences at certain peaks (e.g., 520 cm^{-1} and 939 cm^{-1}), many other bands do not show significant variations, suggesting that the Raman profiles of A and B are not entirely distinct. This unexpected result raises questions about the efficacy of using 1D pSi PhCs to provide additional photonic enhancement in SERS measurements, as the metal nanostructures intended for enhancement are typically deposited only on top of the photonic structure. One possible explanation for the absence of the expected enhancement could be in the dimensionality of the PhCs used in this work. One-dimensional PhCs create PBG in only one dimension, which is exclusively in the direction perpendicular to the surface. According to Gaponenko²⁵, in the case of such 1D PhCs, Raman scattering is, in the ideal case, inhibited along the direction of the periodicity of the structure, while it could be enhanced in the other two directions due to the

angular redistribution of the photon DOS. In our experimental setup, the objective was positioned perpendicular to the surface of the sample, so the analysis of the signal in the other two directions was impossible. Nevertheless, the aforementioned hypothesis could be applicable to the interior of the PhC and the molecules within it. Molecules adsorbed on the photonic crystal's surface experience limited influence from the periodicity of the structure in the direction perpendicular to the surface, since they interact primarily with back-reflected light rather than the internal photonic structure. In this context, the thickness of the CV layer and its absorption properties could influence the signal in a way that if the CV layer is thick or highly absorptive, it may attenuate both incident and back-reflected light, reducing the potential enhancement by limiting light transmission to the PhC and back. However, since all samples were prepared in the same way, any absorption effects from the CV layer should impact all samples equally and therefore may not fully explain the lack of observed enhancement. Additionally, it is important to note that the numerical aperture of the objective was relatively low and equal to 0.25, but it was not changed throughout the experiment, so the lack of the expected enhancement cannot be attributed to variations in the objective's numerical aperture. Instead, it is probably due to the inherent limitations of the 1D PhC structure to enhance Raman signals along the direction perpendicular to the PhC's surface. While this dimensional limitation primarily affects molecules within the PhC by restricting DOS, it also indirectly influences molecules on the surface, since they rely on the ability of photonic structure to enhance back-reflection and interaction with incident light. Thus, the restricted ability of the 1D structure to amplify signals in the direction perpendicular to the surface may contribute to a general lack of enhancement for surface-bound molecules as well.

Similar to the case of the $\sim 520\text{ cm}^{-1}$ silicon band, the strongest Raman signal enhancement was observed when the laser excitation was aligned with the edge of the PBG. Among the ten analyzed CV bands, four exhibited the strongest enhancement when the laser was aligned with the high-frequency edge of the PBG, and three when the excitation was aligned with low-frequency edge, while the band at 421 cm^{-1} showed the same enhancement in the case of the alignment with the high- and low-frequency edges. By averaging the EFs over the entire spectrum but without the outlier band at 939 cm^{-1} , the calculated EFs for sample categories D and F were approximately (2.5 ± 0.2) and (2.3 ± 0.2) , respectively.

The variations in enhancement observed when the laser aligns with the high- or low-frequency edges of the PBG can also be interpreted with the help of the theory of PhCs. All pSi PhCs used in this work were etched using a sinusoidally modulated current density ranging from 1 to 50

mA/cm^2 . The etching process started at $25 \text{ mA}/\text{cm}^2$, increased to the maximum value, and then sinusoidally decreased to the minimum of $1 \text{ mA}/\text{cm}^2$. Consequently, the photonic structure starts with a highly porous and low-refractive index layer, after which comes a high-refractive index layer, and the pattern repeats over the whole photonic structure, so the sections within the photonic part can be categorized into low-refractive index sections that are closer to the surface and high-refractive index sections that are further away from the surface. Additionally, the diffusion of CV molecules into the PhC likely creates a concentration gradient in the direction perpendicular to the surface. This gradient implies that low-refractive index sections were filled with more CV molecules than the high-refractive index sections.

According to principles explained in Chapter 2, sections 2.2 and 2.3, and specifically according to equation (2.21) and Figure 2.5, the lower-order modes prefer to be located in the high-dielectric regions, while the higher-order modes primarily occupy lower dielectric constant regions. This means that the Raman signal enhancement should be slightly higher for the high-frequency edge, which corresponds to sample category D. Furthermore, the Raman spectrum of CV was recorded in the range $(350 - 1700) \text{ cm}^{-1}$, which means that it completely falls within the PBG width in the case of sample category D, as presented in Figure 7.17. However, due to the use of RFs with narrow FWHM and rapid change of the reflectance on both sides of the reflectance peak, each Raman-shifted band experiences different PBG reflectance. Additionally, the density of optical states varies significantly at the edges of the PBG, where higher DOS values allow the increased scattering and potentially enhance Raman intensity. This detailed analysis reveals that there is an interplay between the distribution of the CV molecule, the localization of EM modes within the photonic structure, and the DOS, and all of them affect the enhancement of the Raman signal.

Finally, aligning the laser excitation with half of the reflectance peak's height on the high- and low-frequency sides resulted in higher EFs for almost all CV bands in the case of sample category C compared to the reference sample category A. The CV band at 939 cm^{-1} , however, showed completely inexplicable intensities: it was the strongest band in the Raman CV spectrum for sample category A, but showed a diminished intensity for all sample categories except in the case of sample category F. The EFs for 5 CV bands in sample category C were even higher than those obtained from sample category F. Additionally, the two low-frequency Raman bands at 421 cm^{-1} and 724 cm^{-1} showed signal intensities comparable to the intensities obtained from categories D and F, while the band at 914 cm^{-1} exhibited the highest overall EFs when sample category C was used. These three Raman-shifted bands, overlapped

with the top of the reflectance peak (Figure 7.18), which might explain their high mean intensities. A closer examination of Table 7.10 reveals that the EFs for all bands in sample category C show an interesting pattern: higher EFs are present for low-frequency bands as well as the high-frequency bands above 1392 cm^{-1} , while bands between 940 and 1363 cm^{-1} show much smaller EFs. This suggests that the low-frequency bands might be under the influence of the strong PBG effect, as they fall within the bottom of the reflectance peak. On the other hand, bands above 1392 cm^{-1} fall near the edge of the reflectance peak, where longer light-matter interaction occurs, potentially increasing their intensity. This suggests that both the central position within the peak (for low-frequency bands) and the boundary location (for high-frequency bands above 1392 cm^{-1}) play distinct but complementary roles in signal enhancement, highlighting the influence of the reflectance profile on Raman signal enhancement.

Interestingly, sample category C consistently shows stronger intensities across all Raman bands compared to sample category E. This result is somewhat counterintuitive, since low-frequency bands align with the low-frequency edge of the PBG in the case of sample category E, where longer light-matter interaction is generally expected to enhance signal intensities. The most probable explanation for the observed stronger enhancement in sample category C is the localization of high-frequency EM modes within the low-refractive-index regions of the PhC structure. Consequently, while the reflectance profile and PBG characteristics clearly influence Raman signal intensities, the complex interplay of EM mode localization within the PhC structure complicates definitive conclusions about the PBG's direct impact on specific Raman-shifted bands.

Despite this uncertainty, several important insights can still be derived from the above findings regarding the necessary conditions for Raman signal enhancement. Firstly, the relative position between the laser excitation wavelength and the photonic bandgap is crucial for observing Raman signal enhancement. The results obtained in this work indicate that the enhancement is predominantly associated with molecules that have penetrated inside the 1D photonic structure, and no significant enhancement was obtained for molecules adsorbed on the surface. This conclusion is based on the observation that enhancement was achieved only when the laser was aligned with the edges of the PBG. At these points, the density of optical states is increased, allowing stronger interaction with molecules embedded into the photonic structure. In contrast, molecules on the surface are less influenced by the internal DOS and PBG effects, resulting in minimal enhancement. Thus, the ability of the photonic structure to enhance the Raman signal

is effective for molecules within the PhC, where the interplay of DOS and photonic confinement is strongest. Additionally, the analysis based on more than 5000 recorded spectra suggests that the maximum enhancement from the 1D PhC structure for most observed Raman bands is up to 150%, which is significantly lower than theoretical expectations.

Moreover, it is evident that a single Raman band or a small number of spectra recorded on a limited number of samples cannot be scientifically accepted as verification of the PhC influence on Raman signal enhancement due to the presence of outliers, signal fluctuations, and specific experimental conditions. Furthermore, since the EF for sample categories C and E is generally weaker for most Raman bands, including the prominent $\sim 520\text{ cm}^{-1}$ silicon peak, compared to sample categories D and F, it can be concluded that the PBG edge and its increased DOS should be precisely defined as the position at the very bottom of the reflectance peak rather than the position at half of the reflectance peak's height.

Additionally, insights from EDS measurements suggest that the probe molecule penetrated up to approximately $3\text{ }\mu\text{m}$ into the PhC structure, implying that the effect of longer light-matter interaction occurs within roughly 40% of the total PhC thickness. Considering this, there is a possibility that if the probe molecule could infiltrate the entire porous structure, the EF for sample category D could increase compared to the ordinary pSi. In general, if the EM field is not confined to the first PhC layers¹⁴⁴, then the deeper the penetration of both the laser and probe molecules into the PhC, could result in the higher Raman EF, especially when the laser excitation aligns with the PBG edge. This hypothesis will hopefully be experimentally confirmed in our future work, which will involve the use of pSi PhCs with various thicknesses, lasers with different penetration depths into pSi, and various infiltration depths of probe molecules. Through these experiments, we aim to further optimize the design and application of PhCs in Raman spectroscopy since such studies should provide more detailed insights into the mechanisms of Raman signal enhancement in PhCs.

7.3 Gold-coated porous silicon photonic crystals for SERS measurements

While section 7.2 highlighted the role of photonic crystals in enhancing the Raman signal, this section will examine their influence on the enhancement of the SERS signal, where the interplay between photonic and plasmonic effects occurs. As discussed earlier, the analysis of the 1D pSi PhC's influence on Raman signal enhancement showed that the edge of the PBG is defined as the very bottom of its reflectance peak on both high- and low-frequency sides, corresponding to sample categories D and F, so sample categories C and E were excluded from the SERS experiment. Furthermore, since the previous analysis showed that the Raman signal intensity from sample category B was almost the same as for the reference sample category A, with no significant enhancement observed, the following analysis will focus on the influence of PhCs on SERS signal enhancement when the laser excitation is aligned with the high- and low-frequency edges of the PBG, meaning the signals obtained from sample categories A, D, and F will be analyzed, with sample category A serving as a reference. The schematic plan of samples and sample categories used in the SERS experiment is schematically illustrated in Figure 7.20. SERS substrates were prepared by the deposition of gold nanoparticles onto the surface of the pSi and pSi PhCs samples. The concentration of HAuCl_4 used was $5 \cdot 10^{-2}$ M, and the samples were incubated for 60 seconds. This short incubation time was purposefully chosen to balance the density of nanoparticles on the samples' surfaces and to maintain the interplay between photonic and plasmonic effects. It is important to note that stronger signal enhancement would be achieved with longer incubation times since this would result in a greater number of nanoparticles on the surface of our samples (i.e., more efficient surface morphology), which would significantly increase the plasmonic effect. However, increasing the density of the nanoparticles to the point where a gold layer is formed, or even further to increase the thickness of the gold layer, would completely overshadow the photonic effect inherent to the pSi PhCs structures^{136,145}. By choosing a shorter incubation time and, consequently, a smaller number of nanoparticles on PhCs' surfaces, we ensured that the plasmonic effect remained pronounced while still allowing the photonic properties of the substrates to contribute to the overall signal enhancement. This approach ensured that the photonic effect of the SERS substrates in our experiments could have been quantified.

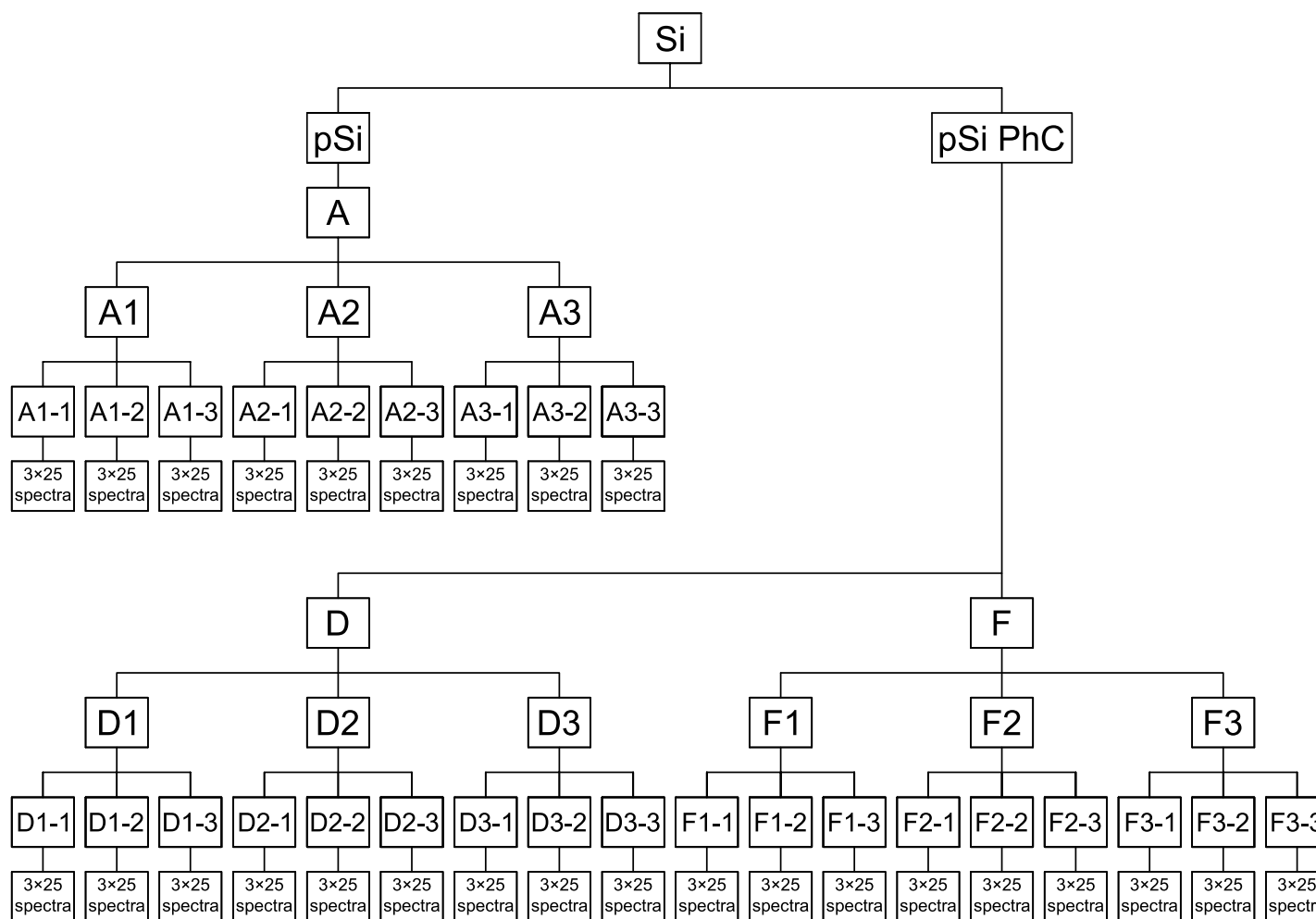


Figure 7.20 Schematic view of the division of pSi and pSi PhC SERS substrates used in the SERS experiment. Three samples from sample categories A, D, and F (A1, A2, A3, D1, D2, D3, and F1, F2, F3) were used. Each sample was divided into 3 rectangular specimens, and 3 random positions were selected on each rectangular specimen.

Approximately 25 Raman spectra were recorded on each mapping area

In addition to changing the substrate, a new probe molecule, Rhodamine 6G (R6G), was used in this part of the study instead of CV. This change was necessary because the CV molecule has a Raman band at $\sim 520 \text{ cm}^{-1}$, which coincides with the first-order Raman band of silicon. It is important to emphasize once again that the intensity of the $\sim 520 \text{ cm}^{-1}$ silicon Raman band served as a reference for different sample categories, and variations in its intensity were attributed to the differences in the relative position between the laser excitation and the PBG. The CV Raman band at $\sim 520 \text{ cm}^{-1}$ associated with transversal-optical phonons at the center of the Brillouin zone is very weak, so its influence on the intensity of the $\sim 520 \text{ cm}^{-1}$ silicon peak could have been easily neglected. However, this band becomes very pronounced in SERS, meaning that it would highly affect the intensity of the $\sim 520 \text{ cm}^{-1}$ silicon peak in SERS measurements, making it impossible to use the silicon band as a consistent reference for different sample categories. For this reason, the R6G molecule was used for SERS measurements.

The abovementioned changes introduced new parameters that affect the position of the PBG, and their impact had to be considered and taken into account in our analysis. Similar to Table 7.1, these corrections are summarized in Table 7.12. All other preparation and measurement conditions, as well as the equipment used for the SERS experiment, were the same as in the earlier analysis of the Raman signal.

Table 7.12 Experimental corrections for the reflectance peak position in SERS experiment – example for peak initially measured at 785 nm

	Peak center (nm)	Shift (nm)	Direction
1° C increase during etching	-	$\sim 7-10$	Redshift
UV-Vis-NIR $\rightarrow \lambda_{0=7^\circ}$	785	-	-
Angle correction $\rightarrow \lambda_0$	791	~ 6	Redshift
2% HF for 30 s	-	$\sim 2-3$	Blueshift
$5 \cdot 10^{-2} \text{ M H AuCl}_4$ for 60 s	-	$\sim 1-5$	Redshift
10^{-4} M R6G for 30 minutes	-	$\sim 2-3$	Blueshift

To gain insight into the morphology of the SERS substrates, SEM images were analyzed. Figure 7.21 shows both low- and high-magnification top-view FE-SEM images of the pSi PhC SERS substrates. The low-magnification view shows that the gold nanoparticles uniformly covered the entire surface of the PhC. This uniform coverage is due to the high density of gold nanoparticles, which formed as a result of their rapid growth rate. A large number of gold

nanoparticles can be attributed to the high density of suitable nucleation sites with dangling bonds on the mesoporous surface, which enabled the growth of nanoparticles. However, the high-magnification view reveals the presence of gaps between the nanoparticles, which is important since complete coverage would hinder the influence of photonic effects, as previously explained.

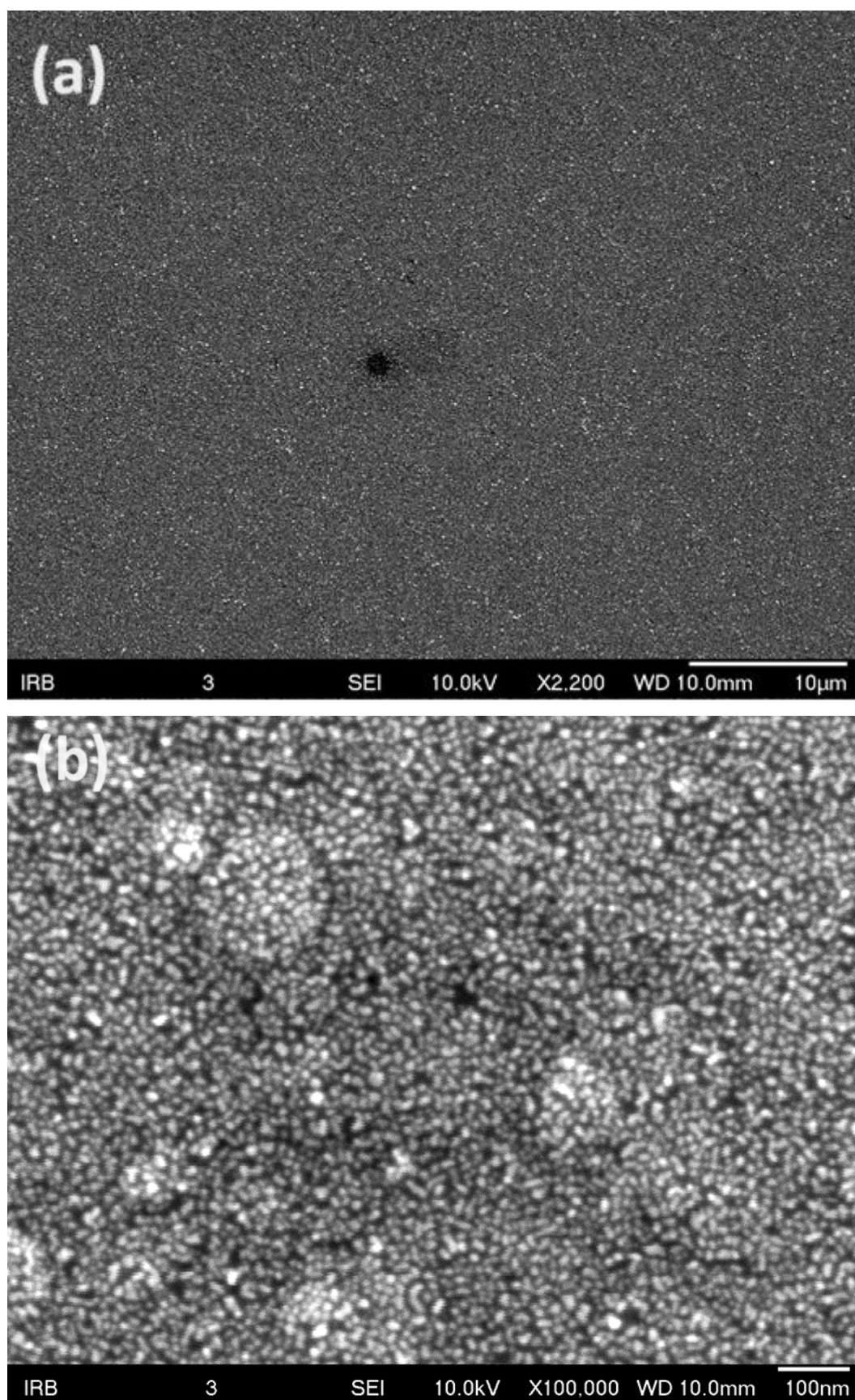


Figure 7.21 (a) Low-magnification view and (b) high-magnification view of the gold nanoparticles on the PhC surface obtained after the incubation of pSi PhC samples in $5 \cdot 10^{-2}$ M HAuCl_4 for 60 s

7.4 SERS signal

Measurements of the SERS signal were performed using the same 785 nm laser excitation, and the spectra were acquired in the same way as in the Raman experiment: from 3 mapping areas on each sample, with approximately 25 recorded spectra on each area. An optical image representing an example of a typical rectangular specimen showing the surface of the pSi PhC covered with gold nanoparticles and R6G probe molecule is given in Figure 7.22. The image indicates that the deposition of gold nanoparticles is not perfectly uniform and mechanical damage caused by handling the sample with tweezers is visible on the right side of the specimen. However, to ensure consistent and reliable results, mapping areas where spectra were recorded were always selected from undamaged areas.

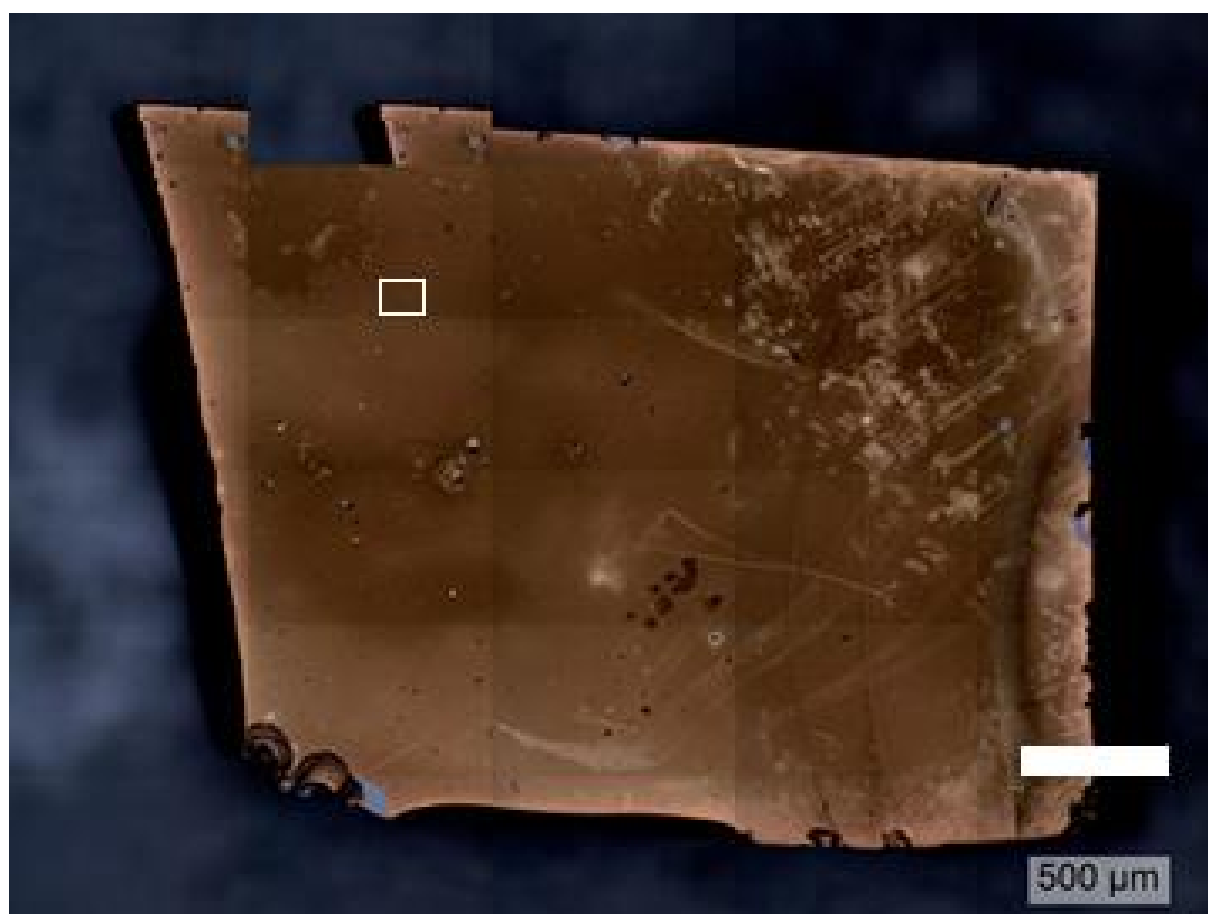


Figure 7.22 Optical image of a typical rectangular specimen showing gold-coated pSi PhC's surface. The white rectangle represents one randomly selected mapping area. The visible scratches are due to mechanical damage

Similar to the Raman measurements, sets of SERS spectra recorded from specific mapping areas sometimes contained a few outliers. In addition to the previously discussed sources of outliers, such as non-uniform deposition of a probe molecule or inhomogeneities in the

refractive index due to the imperfect etching process, SERS outliers can also result from the non-uniform metal deposition of metal nanoparticles or, as a result of recording in regions of exceptionally strong EM field on SERS substrates. The low-magnification SEM image in Figure 7.21a shows that the surfaces of the pSi and pSi PhC SERS substrates were uniformly covered with gold nanoparticles, suggesting that the outliers most likely originated from regions of extremely enhanced EM field. When laser excitation intersects with these regions where the EM field is significantly enhanced, it can occasionally lead to the detection of much stronger signals. After removing outliers from the datasets, 23-25 spectra from each mapping area were available for further analysis. However, it is important to note that an approximately 20% variability between the samples within the same sample category was observed. This variability likely originated from the imperfect environmental conditions, such as the inability to precisely control the room temperature and the need to transport samples between different locations for preparation and measurements, introducing a time gap that was difficult to control. These issues could potentially be resolved by using a clean room environment, which would enable more precise control over sample preparation conditions and help overcome these inconsistencies.

The abovementioned challenges highlight the importance of a comprehensive analysis. Similar to the Raman experiment, accurately quantifying the influence of PhCs on SERS signal requires a thorough statistical analysis. As previously mentioned, information obtained from a dataset with very few spectra can be misleading since they could contain outliers or unrepresentative spectra that can skew the results. To avoid drawing incorrect conclusions about the influence of PhCs on SERS signal enhancement and to improve the reliability of the findings, it is necessary to analyze a large number of spectra. A comprehensive statistical approach minimizes the risk of misinterpretation due to anomalous spectra and provides a more accurate assessment of the PhC's influence on SERS signal enhancement.

The analysis of the acquired data was performed in a similar way as for Raman measurements, with the difference being that SERS spectra were recorded on three samples within each sample category rather than four (i.e., A1, A2, A3, D1, D2, D3, F1, F2, F3). After eliminating outliers from datasets, 23-25 spectra were available for further analysis from each mapping area. The spectra from one mapping area were averaged, resulting in 9 mean spectra for each of the three samples within a particular sample category (3 mapping areas on 3 rectangular specimens). These mean spectra were then baseline corrected, and the results for the typical sample are given in Figure 7.23. It is important to mention that the results obtained from every level in the

schematic representation in Figure 7.20 were analyzed and compared with each other to check for the consistency and reliability of the findings.

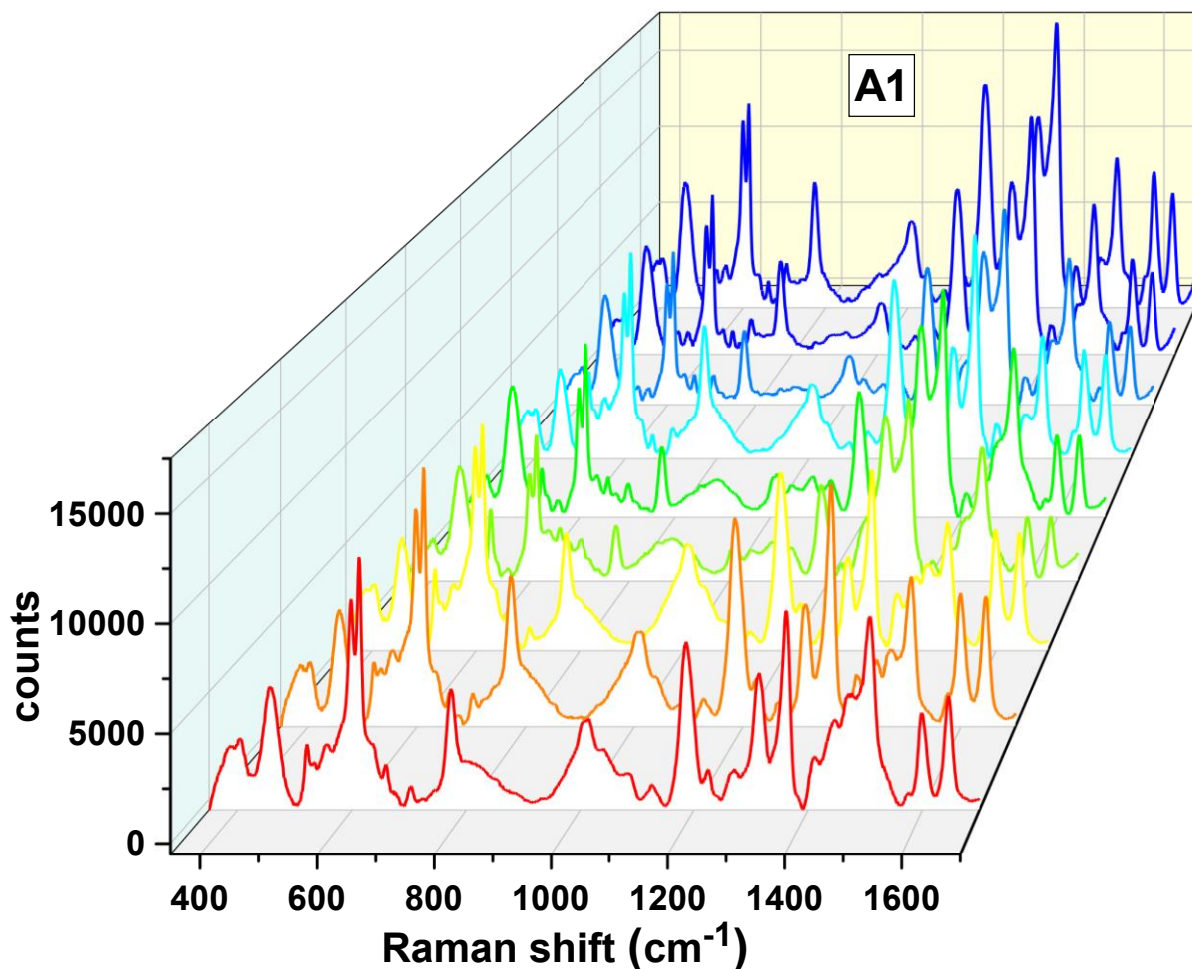


Figure 7.23 The baseline corrected data set consisting of 9 mean SERS spectra obtained from sample A1

For further analysis, the eight most prominent R6G SERS bands, whose assignments are given in^{146,147}, were selected. To visualize the results, a bar plot representing the mean SERS band intensities for the three samples within three sample categories of interest, obtained through Gaussian fitting using Origin software, is given in Figure 7.24, while the corresponding numerical data are given in Table 7.13 to Table 7.15. Just as in the analysis of Raman signals, the results in all tables are rounded for clarity: the standard deviation was rounded to the first significant digit, and the mean values were rounded to match this level of precision. Consequently, due to this rounding, the relative error may sometimes be larger than it would be with unrounded data.

Each column in the bar plot represents the average of 9 mean spectra obtained for each of the three samples within one sample category (the average of the 9 spectra depicted in Figure 7.23 corresponds to sample A1 in Figure 7.24, represented by the red column). To enhance clarity,

the y-axis scales in Figure 7.24 are adjusted differently to compare the mean intensities of each SERS band across three different samples.

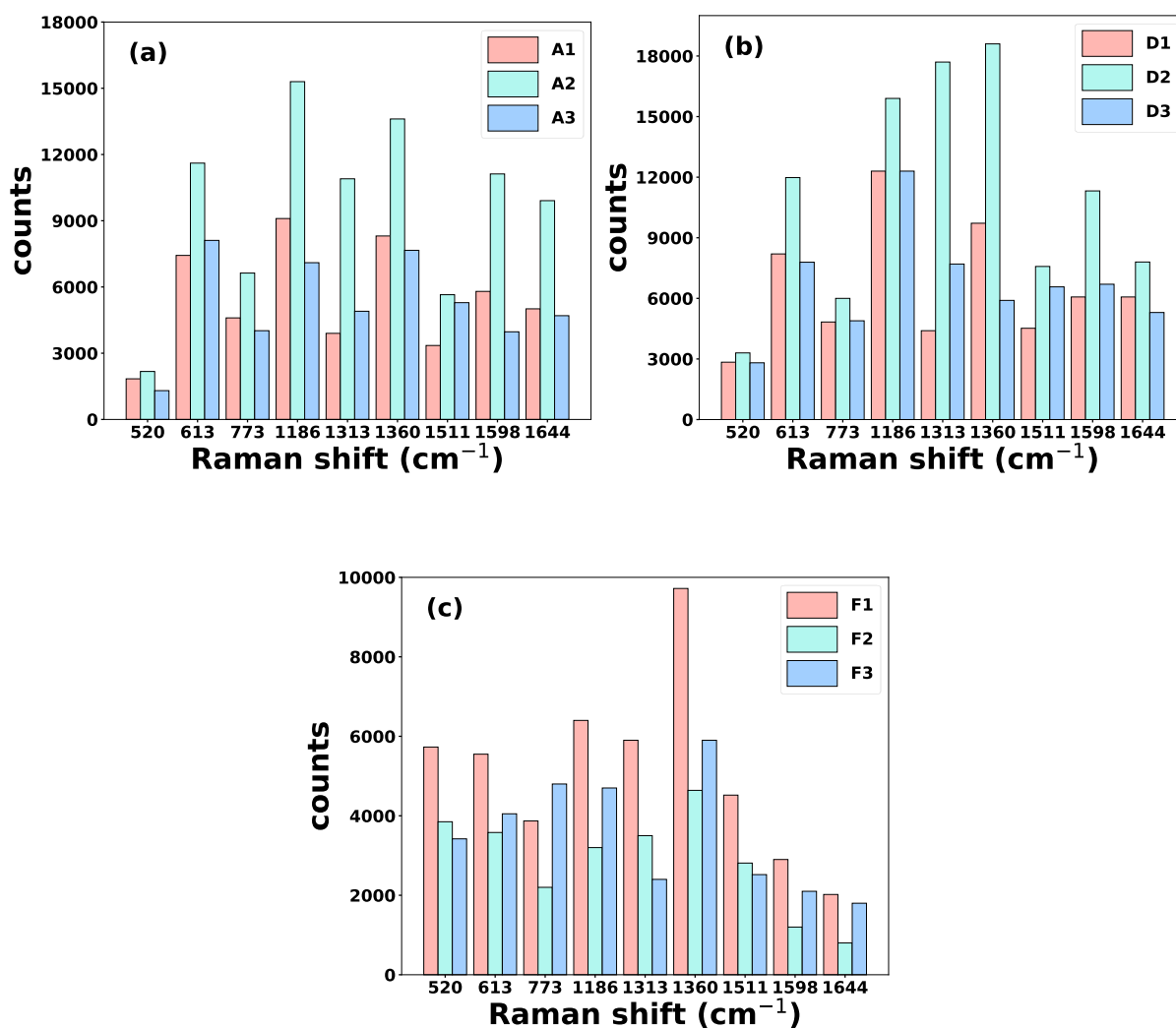


Figure 7.24 Bar plots representing mean intensities of SERS bands recorded on 3 different samples (A1-A3, etc.) within 3 different sample categories (A, D, and F). Images (a) – (c) show data for sample categories A, D, and F

Table 7.13 Numerical values representing the intensity of the main R6G SERS bands and $\sim 520 \text{ cm}^{-1}$ Si band for three samples across sample category A, obtained by Gaussian fitting

Intensity for a given sample (counts) R6G SERS bands (cm^{-1})	I_{A1}	I_{A2}	I_{A3}
520	1840 ± 10	2170 ± 20	1305 ± 6
613	7430 ± 20	11610 ± 20	8110 ± 20
773	4600 ± 100	6630 ± 60	4020 ± 50
1186	9100 ± 300	15300 ± 200	7100 ± 100
1313	3900 ± 100	10900 ± 600	4900 ± 100
1360	8310 ± 80	13610 ± 70	7660 ± 60
1511	3350 ± 40	5650 ± 40	5290 ± 50
1598	5800 ± 100	11120 ± 80	3970 ± 70
1644	5010 ± 60	9910 ± 60	4700 ± 50

Table 7.14 Numerical values representing the intensity of the main R6G SERS bands and $\sim 520 \text{ cm}^{-1}$ Si band for three samples across sample category D, obtained by Gaussian fitting

Intensity for a given sample (counts) R6G SERS bands (cm^{-1})	I_{D1}	I_{D2}	I_{D3}
520	2840 ± 50	3300 ± 10	2810 ± 40
613	8200 ± 20	11980 ± 20	7790 ± 10
773	4830 ± 60	6000 ± 40	4890 ± 70
1186	12300 ± 200	15900 ± 200	12300 ± 200
1313	4400 ± 100	17700 ± 700	4400 ± 100
1360	9720 ± 80	18600 ± 90	9700 ± 80
1511	4520 ± 50	7580 ± 50	4530 ± 50
1598	6700 ± 100	10700 ± 90	6700 ± 100
1644	6070 ± 70	7800 ± 50	6070 ± 70

Table 7.15 Numerical values representing the intensity of the main R6G SERS bands and $\sim 520 \text{ cm}^{-1}$ Si band for three samples across sample category F, obtained by Gaussian fitting

Intensity for a given sample (counts)	I_{F1}	I_{F2}	I_{F3}
R6G SERS bands (cm^{-1})			
520	5730 ± 20	3850 ± 20	3420 ± 20
613	5550 ± 20	3580 ± 20	4050 ± 30
773	3870 ± 50	2200 ± 100	1800 ± 30
1186	6400 ± 100	2030 ± 80	4700 ± 400
1313	5900 ± 500	3500 ± 900	2400 ± 100
1360	9720 ± 80	4640 ± 60	5900 ± 100
1511	5340 ± 50	2810 ± 60	2820 ± 50
1598	2900 ± 80	1200 ± 100	2100 ± 200
1644	2020 ± 30	800 ± 40	1800 ± 100

The graphical representation given in Figure 7.24 shows that the intensities for almost all SERS bands are comparable across different samples for sample category F, while some anomalies are present in the case of sample categories A and D. For example, sample A2 shows about 30% higher intensity for 3 bands, while approximately 2 times higher signal is obtained for 4 bands. On the other hand, sample D2 shows the strongest intensity for almost all SERS bands, while bands at 1313 and 1360 cm^{-1} stand out with significantly stronger intensities. This deviation might indicate variations in sample preparation. Additionally, the relative ratios of the mean intensities of the eight observed R6G bands are different within the sample category D. For instance, samples D1 and D3 show similar and about 30% weaker intensities than D2 for bands at 613, 1186 cm^{-1} , 1598 cm^{-1} and 1644 cm^{-1} , while completely different behavior is present for bands at 1313 cm^{-1} and 1360 cm^{-1} where D2 is almost two times stronger than D2 and D3, which have comparable intensities. On the other hand, the intensities obtained from all three samples are comparable for bands at 773 and 1511 cm^{-1} . These observations once again highlight the importance of the comprehensive statistical approach, which ensures that the findings are not skewed by anomalies and that they accurately reflect the influence of the PhCs on SERS signal enhancement.

Additionally, the Student's t-test was used to evaluate whether there are statistically significant differences in SERS intensities between the reference sample category A and categories D and

F for each peak, including the differences between D and F. The results of these comparisons are presented in Table 7.16.

Table 7.16 Results of the Student's t-test for comparing SERS peak intensities of R6G probe molecule and Raman peak of silicon across sample categories A, D, and F. Each row represents a specific peak, with t-statistics and p-values reported for each comparison. Statistically significant differences ($p < 0.05$) indicate distinct intensity profiles between the categories at the corresponding peaks.

	SERS Peak (cm^{-1})	A_vs_D_T-Statistic	A_vs_D_P-Value	A_vs_F_T-Statistic	A_vs_F_P-Value	D_vs_F_T-Statistic	D_vs_F_P-Value
0	520	-4.069207	0.021418	-3.403184	0.055707	-1.857486	0.192734
1	613	-0.147042	0.890218	3.268491	0.051521	3.376906	0.048809
2	773	-0.178448	0.870189	1.330232	0.254320	1.900982	0.155308
3	1186	-1.093019	0.356895	2.205139	0.114861	5.217556	0.006498
4	1313	-0.738802	0.512033	1.089163	0.359475	1.452842	0.269416
5	1360	-0.367599	0.738004	1.280796	0.272226	1.146106	0.344890
6	1511	-1.270516	0.276053	1.053363	0.354317	2.100049	0.103649
7	1598	-0.393777	0.715055	2.225837	0.143838	3.454344	0.059060
8	1644	0.081425	0.940681	2.892462	0.091098	5.849887	0.010265

The comparison of SERS peak intensities between sample categories A, D, and F reveals mixed results in terms of statistical significance. The 520 cm^{-1} peak shows a pronounced difference between categories A and D, as well as A and F, with significant p-values in both cases ($p = 0.021418$ when A and D are compared, while $p = 0.055707$ when A and F are compared), indicating that this peak is sensitive to structural or compositional changes between these samples. This suggests that the photonic crystal structure or the metal nanostructure deposition in these categories might have an impact on the SERS enhancement at this specific peak.

Other peaks, do not exhibit statistically significant differences in most comparisons, with high p-values indicating similarity in SERS intensities between the categories. This lack of significance across multiple peaks implies that the photonic crystal structure may not contribute consistently to the SERS intensity across all bands.

Interestingly, certain peaks, such as 613, 1186, 1598 and 1644 cm^{-1} in the D vs. F comparison, show significantly different behaviour, even though the silicon peak at 520 cm^{-1} is not significantly different between these two categories. The similarity in the silicon peak at 520 cm^{-1} is expected because, in both categories D and F, the laser is aligned with the edge of the PBG, which means that the impact of the PBG on the silicon signal is the same, resulting in no significant difference in the silicon response. However, the distinct behaviour of other peaks suggests that there is a non-negligible influence of PBG on Raman shifted bands in the sample

category D, since when the laser is aligned with the low-frequency edge of the PBG, the whole spectrum lies outside the reflectance peak of the PBG.

Overall, while some peaks like 520 cm^{-1} demonstrate distinct SERS profiles between the categories, the lack of significant differences at many other peaks suggests that the influence of the photonic crystal structure on SERS enhancement is not uniform across all bands. This variability raises questions about the effectiveness of the photonic crystal structure in achieving consistent SERS enhancement across the spectrum, especially since some peaks are relatively unaffected by the modifications in sample categories D and F compared to A.

The enhancement of the SERS signal by PhCs was determined using the final results presented in Table 7.17 and illustrated in Figure 7.25. The mean intensity for the eight most prominent R6G SERS bands in the spectrum was calculated by averaging approximately 675 spectra per sample category, resulting in a total of over 2000 spectra recorded across the three sample categories of interest for the SERS experiment. The results in presented in the table are rounded for clarity, which can sometimes lead to a larger relative error than it would be with unrounded data. For example, the intensity of the SERS R6G band at 1313 cm^{-1} for sample category D is listed as 6000 ± 7000 . However, the unrounded values are comparable, giving a relative error of 100%, whereas the rounded values give a deviation closer to 120%. The error bars in Figure 7.25 present the standard deviation for each band. The enhancement factors (EFs) were determined in the same way as in the Raman experiment analysis - by dividing the number of counts for a particular band and a particular sample category by the corresponding number of counts for sample category A. As discussed in Chapter 5, previous studies have typically reported findings based on the analysis of only a few spectra, often focusing on a single SERS band.

Table 7.17 Mean intensities of the main R6G SERS bands and ~ 520 cm^{-1} Si band for sample categories A, D, and F, with the corresponding enhancement factors calculated with respect to the sample category A

Mean SERS intensity (counts) and EFs R6G SERS bands (cm^{-1})	I_A	I_D	EF (D)	I_F	EF(F)
520	1800 ± 400	3000 ± 400	1.7 ± 0.5	4000 ± 2000	2 ± 1
613	9000 ± 3000	9000 ± 3000	1.0 ± 0.5	4000 ± 1000	0.5 ± 0.2
773	5000 ± 2000	5200 ± 900	1.0 ± 0.4	4000 ± 2000	0.7 ± 0.4
1186	11000 ± 5000	14000 ± 3000	1.3 ± 0.7	4000 ± 3000	0.4 ± 0.4
1313	7000 ± 5000	10000 ± 9000	2 ± 2	4000 ± 2000	0.6 ± 0.6
1360	10000 ± 4000	11000 ± 8000	1.1 ± 0.9	7000 ± 4000	0.7 ± 0.5
1511	5000 ± 2000	6000 ± 2000	1.3 ± 0.7	4000 ± 2000	0.8 ± 0.5
1598	7000 ± 4000	8000 ± 4000	1.2 ± 0.9	2000 ± 100	0.3 ± 0.3
1644	7000 ± 4000	6000 ± 2000	1.0 ± 0.6	1600 ± 900	0.2 ± 0.2

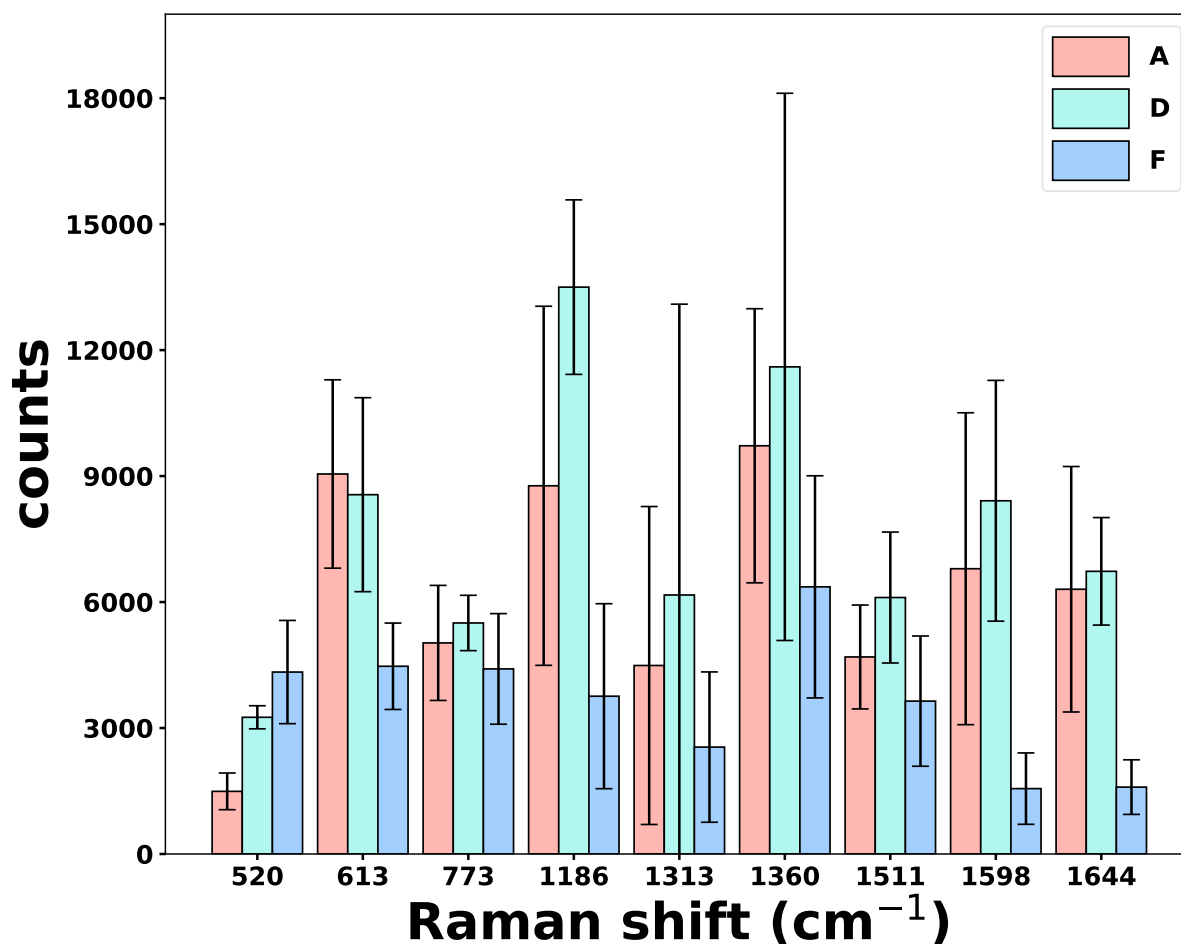


Figure 7.25 Bar plot illustrating the final mean intensities of the main R6G SERS bands for sample categories A, D, and F. Error bars represent the standard deviation for each band

The analysis of the SERS signal enhancement is organized in the same way as the analysis of Raman signal enhancement: the first part focuses on the intensity of the $\sim 520\text{ cm}^{-1}$ peak, which corresponds to the Raman peak of silicon and gives information about the changes in the intensity of the SERS signal obtained from the constituent material. The second part of the analysis examines the SERS signal originating from the probe molecule. Both sections of the analysis emphasize the effect of aligning the laser excitation with the specific position of the PBG.

7.4.1 Silicon $\sim 520\text{ cm}^{-1}$ Raman band

Just as in the Raman experiment, the intensity of the silicon band at $\sim 520\text{ cm}^{-1}$ was used to verify the relative alignment between the laser excitation and the PBG. The Raman experiment results identified sample categories D and F that correspond to the alignment of the laser excitation with the high- and low-frequency edges of the PBG, respectively, as the categories of interest for the subsequent SERS analysis. The results from section 7.2 showed that the increased light-matter interaction and minimal reflectance when the laser is aligned with the edge of the PBG enhance signal intensity, including the intensity of the $\sim 520\text{ cm}^{-1}$ silicon band. Thus, the variation in intensity between sample category A and sample categories D and F again serves as a reference.

The SERS substrates based on ordinary pSi corresponding to sample category A showed the intensity variations of the $\sim 520\text{ cm}^{-1}$ peak of 60% among samples A1, A2 and A3, as shown in Figure 7.24 and in Table 7.13. From Table 7.17, it can be seen that the average intensity of the $\sim 520\text{ cm}^{-1}$ silicon peak is ~ 1500 counts, meaning that the variation within the sample category A is $\pm 30\%$ from the average value. Although higher than in the Raman experiment, this variation still indicates a relatively high degree of reproducibility in the preparation and measurements of these samples. The higher variation in SERS results compared to the Raman experiment is expected, primarily due to the inherently variable nature of the signal enhancement mechanism in SERS.

Additionally, it is important to highlight that one of the key differences between the Raman and SERS experiments is the significantly lower intensity of the silicon 520 cm^{-1} band in the SERS spectra compared to the standard Raman spectra, as clearly visible by comparing Figure 7.11 with Figure 7.24, and Figure 7.14 with Figure 7.25, as well as the corresponding tables. This reduction in intensity can be attributed to the plasmonic effects inherent to the SERS technique. In the SERS experiment, plasmonic enhancement was achieved by the deposition of gold nanoparticles on the top of the pSi and pSi PhC samples, which creates localized EM fields that enhance the Raman signal of molecules near the metal surface. However, gold nanoparticles exhibit high reflectance in a near-infrared region, which reduces the amount of incident light that penetrates into the underlying (photonic) structure. Consequently, only a fraction of the incident light interacts with the silicon in the porous layer and crystalline bulk, resulting in a lower observed intensity of the silicon band in the SERS spectra.

The mean intensity of the $\sim 520\text{ cm}^{-1}$ silicon peak for sample categories D and F is higher than that of the control category A, as shown in Figure 7.25. This enhancement of the silicon band, representing the constituent material of PhC, was expected and in agreement with the results obtained from the Raman experiment since it can be attributed to the longer light-matter interaction time, leading to a higher probability for Raman scattering. However, the SERS experiment showed different behavior. When the laser excitation was aligned with the high-frequency side of the PBG, corresponding to the sample category D, an increase of (1.7 ± 0.5) times was observed. In contrast, the SERS signal was enhanced (2 ± 1) times when the laser excitation overlapped with the low-frequency side of the PBG, corresponding to the sample category F. This finding is confusing since the results from the Raman experiment showed a higher enhancement when samples from the sample category D were used. The stronger $\sim 520\text{ cm}^{-1}$ peak observed in category F may be attributed to the predefined uncertainty intervals (Figure 7.1) and the possibility that the overlap between the laser excitation and the low-frequency edge of the PBG was more precisely tuned. This improved overlap likely resulted in a more significant increase in light-matter interaction, leading to a higher $\sim 520\text{ cm}^{-1}$ signal intensity for sample category F.

Nevertheless, it is important to note that despite the differences between the Raman and SERS experiments, the consistent finding in both experiments is that the enhancement of $\sim 520\text{ cm}^{-1}$ silicon peak when the laser excitation overlaps with either the high or low-frequency side of the PBG is between 1.7 and 2 times, where higher enhancement corresponds to better preparation and measurement conditions. This consistency suggests that we can generally expect an approximately 2 times enhancement of the signal when the laser overlaps with the PBG edge, which is a reliable outcome.

7.4.2 Eight most prominent R6G SERS bands

The analysis of the intensity of the R6G SERS bands is based on the results illustrated in Figure 7.25 and numerically represented in Table 7.17. Similar to the findings from the Raman experiment, the signal enhancement across R6G SERS bands is not completely uniform. The SERS technique relies on the presence of hotspots where the EM field is significantly enhanced. These hotspots are often not uniformly distributed, leading to increased variability in signal intensity from one spot to another. Additionally, the amount of probe molecules adsorbed at or near these hotspots can vary, also contributing to fluctuations in the detected SERS signal intensity. In the following analysis of signal enhancement, the mean intensities from sample category A will again serve as a reference point.

The SERS measurement showed that the strongest SERS signal enhancement was obtained when the laser excitation was aligned with the high-frequency edge of the PBG, which is in agreement with the results from the Raman experiment. All analyzed R6G SERS bands exhibited the most significant enhancement when samples from sample category D were used. This result can be attributed to the localization of high-frequency modes in low-refractive index sections of the PhC structure. Since the gold nanoparticles did not entirely cover the surface of PhCs, the laser was able to penetrate into the underlying photonic structure. By averaging the EFs across the entire spectrum, the calculated enhancement is (1.1 ± 0.2) . This enhancement is somewhat smaller than the enhancement obtained in the Raman experiment. The obtained reduction was expected and can be explained by plasmonic effects inherent to the SERS technique, which may overshadow the photonic effects, since the intensity of the SERS signal is more than the order of magnitude higher than the intensity obtained in the Raman experiment. It is important to mention that all SERS substrates were prepared in the same manner, so the influence of plasmonic effects on the signal enhancement is expected to be consistent across different sample categories, and much stronger than the influence of the underlying photonic structure. This effectively results in a significantly lower contribution from the photonic structure in the case of the SERS experiment. Additionally, the metal nanoparticles exhibit strong reflection, which prevents the incident radiation from effectively entering the photonic structure. Moreover, the extensive coverage of the surface of PhCs by metal nanoparticles results in smaller amount of a probe molecule infiltrating the photonic structure. Consequently, the expected contribution of the photonic structure was up to 5%, however the signal obtained from sample category D was approximately 10% higher compared to sample category A. This observed enhancement may have originated from molecules located within a narrow superficial

layer of the photonic structure, positioned close enough to the metallic nanoparticles to experience the significantly increased EM field. Additionally, the SERS spectrum of R6G was recorded in the range $(350 - 1700) \text{ cm}^{-1}$, which means that it completely falls within the PBG width in the case of sample category D, as illustrated in Figure 7.26, meaning that the influence of PBG may have also contributed to the signal enhancement.

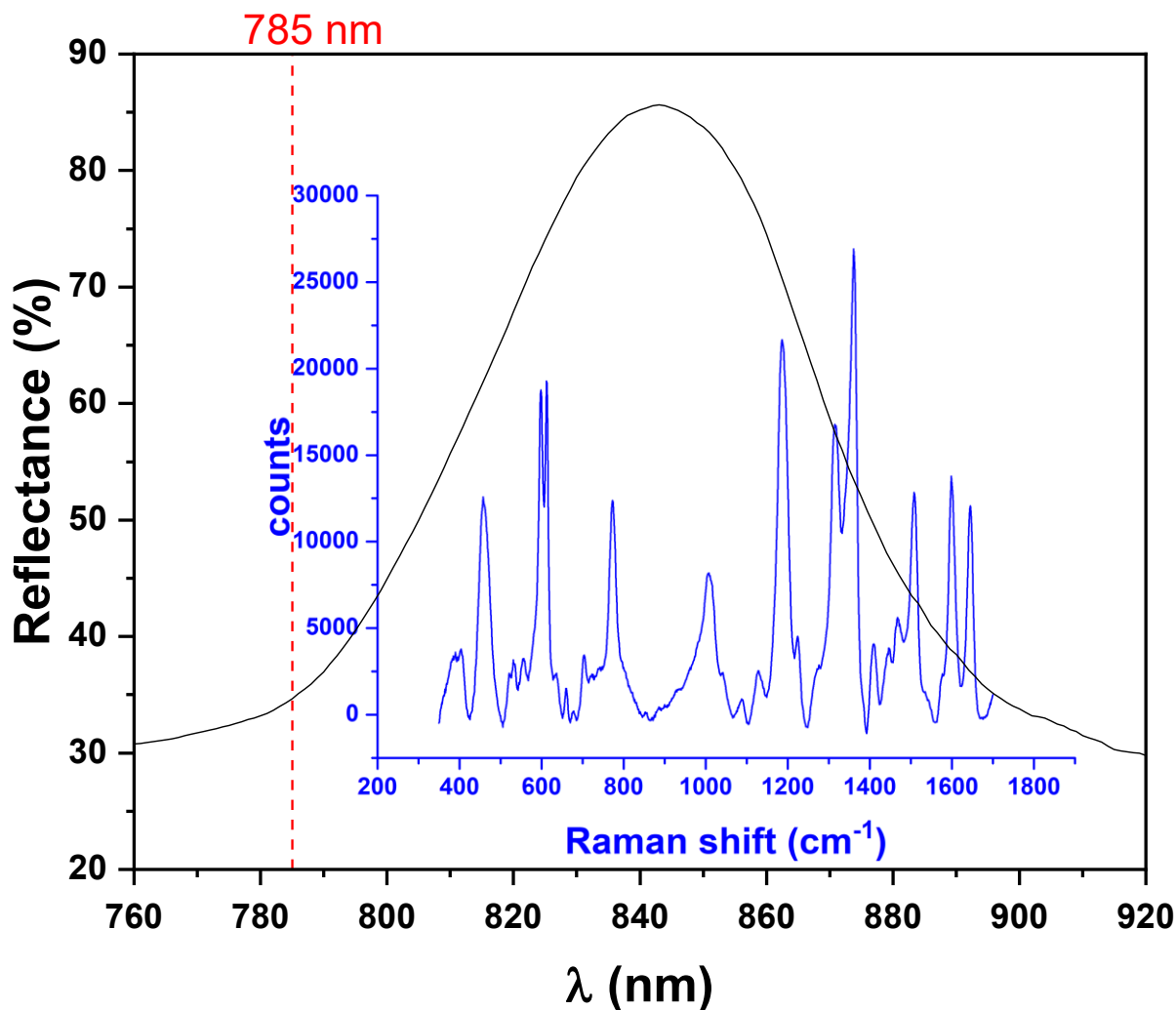


Figure 7.26 Overlay of the reflectance spectra of the PhC for sample category D with the SERS spectra of the R6G probe molecule, along with the 785 nm laser excitation wavelength (indicated by the red dashed line). In this sample, the laser overlaps with the high-frequency edge of the reflectance peak, illustrating how different Raman bands experience varying levels of reflection from the PhC, which may impact the enhancement observed for each band

On the other hand, the signal intensity for sample category F is for some bands slightly lower than the intensity from the reference category A, while the intensity of bands at 613, 1186, 1598 and 1644 cm^{-1} is significantly lower than the intensity obtained from the reference sample category A, with the average EF of (0.4 ± 0.1) . This unexpected result is particularly surprising

because the $\sim 520\text{ cm}^{-1}$ peak for sample category F was stronger than the one observed for samples from sample category D. The most probable explanation for the lack of enhancement and the low signal intensity lies in the imperfect preparation conditions. It is likely that a smaller amount of the probe molecule remained on the SERS substrate after rinsing in MQ water after the incubation of the samples in the probe molecule.

Despite the unexpected result for sample category F, several important insights that can be derived from the above findings. Firstly, the analysis of the SERS measurement implies that the maximum enhancement achievable from the 1D PhC-based SERS structure is approximately 1.1 times. Moreover, it is important to find a balance between the plasmonic and photonic effects. If the PhC structure is completely covered by nanoparticles, the photonic effect would be completely overshadowed, thus diminishing the overall enhancement potential. Furthermore, as indicated by the results from the Raman experiment, the enhancement is predominantly associated with molecules that have penetrated into the 1D photonic structure. Moreover, the findings highlight the importance of using a sufficiently large number of spectra to scientifically validate the influence of PhC on signal enhancement. A single band or a small number of spectra recorded from a limited number of samples cannot be considered sufficient for scientific verification due to the presence of outliers, signal fluctuations, and the impact of specific experimental conditions.

Overall, this study provides essential insights into the enhancement potential of 1D PhC-based SERS structures. The results underscore the interplay between plasmonic and photonic effects, emphasizing the need for careful structural balance to achieve optimal signal enhancement. By demonstrating how the use of PhCs influences signal intensity and highlighting the role of molecular penetration into the photonic structure, our findings lay a solid groundwork for further exploration in this field. Future studies will build on these insights to refine our understanding of enhancement mechanisms, aiming to optimize PhC-based structures for more consistent and effective SERS applications.

Conclusion

The study focused on the influence of photonic crystals on Raman and SERS signal enhancement, with a particular emphasis on the alignment between laser excitation and the photonic bandgap of photonic structures. The analysis of the results obtained from the Raman experiment is structured in two sections: the first part pertains to the examination of the intensity of the $\sim 520 \text{ cm}^{-1}$ peak that corresponds to the Raman peak of silicon. This section gives information about the changes in the intensity of the Raman signal obtained from the constituent material. The second part investigates the Raman signal from the probe molecule. Both sections of the analysis focus on the effect of the alignment of the laser excitation with the specific position of the PBG. Additionally, the influence of the PBG on the Raman-shifted bands is also discussed.

The Raman signal intensity of silicon at $\sim 520 \text{ cm}^{-1}$, associated with transversal-optical phonons at the center of the Brillouin zone was used to verify the relative alignment between the laser excitation and the PBG. When the laser aligns with the center of the PBG, most incident radiation is reflected, leading to a lower Raman signal of the $\sim 520 \text{ cm}^{-1}$ band. Conversely, alignment with the photonic bandgap edges, characterized by the increased density of states and minimal reflectance, resulted in enhanced signal intensity of the Raman silicon band. Therefore, variations in the intensity of the $\sim 520 \text{ cm}^{-1}$ peak across sample categories served as a control, while the consistent position and shape of this band across all categories suggest that phonon confinement effects were negligible.

For ordinary pSi (sample category A), the intensity of the $\sim 520 \text{ cm}^{-1}$ peak varied by less than 10% between samples A1 and A4, indicating high reproducibility in sample preparation and measurements. The penetration depth of the 785 nm laser into pSi samples is approximately 10 μm , while the porous layer thickness is approximately 7.5 μm . Therefore, a significant portion of the Raman signal at $\sim 520 \text{ cm}^{-1}$ originates from scattering in the underlying crystalline silicon, implying that the Raman intensity has contributions from both the porous layer and the substrate.

In sample category B, where the laser aligns with the center of the photonic bandgap, more than 80% of the incident radiation is reflected, resulting in a mean Raman intensity approximately five times lower than in sample category A. This significant reduction is consistent with the high reflectivity of the photonic crystals at the photonic bandgap center, which effectively reduces the available light for Raman scattering.

Sample categories D and F that correspond to the alignment of the laser with the high- and low-frequency sides of the photonic bandgap, respectively, showed higher mean Raman intensities of the $\sim 520\text{ cm}^{-1}$ peak compared to category A, with an increase of approximately 2.2 and 1.4 times, respectively. This enhancement has been theoretically predicted and previously observed and is attributed to increased light-matter interaction due to the higher density of optical states and decreased group velocity at the PBG edges.

The study also analyzed the influence of the PBG on the Raman-shifted bands of crystal violet as a probe molecule. The signal enhancement across the CV Raman bands was not uniform, with some bands exhibiting significantly different behavior. When the laser overlapped with the center of the reflectance peak of the PhC, the expected EF was slightly lower than 2 due to contributions from both incident and back-reflected light. However, contrary to expectations, the mean intensities for most CV bands in sample category B were similar to those in category A, suggesting that the 1D PhC structure may not effectively enhance SERS signals where both metal nanoparticles and probe molecule are adsorbed on the surface of the PhC.

The strongest Raman signal enhancement was observed when the laser was aligned with the PBG edge. Four out of ten CV bands showed the strongest enhancement at the high-frequency edge of the PBG, while three bands were enhanced at the low-frequency edge. The average EFs for sample categories D and F were approximately 2.5 and 2.3, respectively. The variations in enhancement observed at different PBG edges were interpreted using PhC theory, which predicts that lower-order modes prefer high-dielectric regions while higher-order modes occupy low-dielectric regions. Moreover, the concentration gradient of a probe molecule resulted in more CV molecules in the low-refractive index layers. In addition, when samples from sample category D were used, the whole Raman spectrum fell within the PBG width, which may have also contributed to the stronger enhancement at the high-frequency edge.

For sample categories C and E, where the laser aligns with approximately half of the reflectance peak's height, the Raman intensities were about 50% lower for category C and 40% lower for category E compared to category A. The differences in intensities were attributed to the variations in reflectance between these categories and ordinary pSi. The EF for category C was unexpectedly higher than for category E, even though in the case of sample category E, the Raman spectrum partially falls at the low-frequency PBG edge, where a longer light-matter interaction time was anticipated.

Overall, the study highlights several key insights regarding Raman signal enhancement in PhCs. The relative position between the laser excitation wavelength and the PBG is crucial for

observing enhancement, and the enhancement is predominantly associated with molecules that have penetrated into the 1D photonic structure. However, the maximum enhancement observed was up to 150%, significantly lower than theoretical predictions.

Furthermore, the study emphasizes that a single Raman band or a small number of spectra recorded from a limited number of samples cannot be scientifically accepted as verification of the PhC's influence on Raman signal enhancement due to potential outliers, signal fluctuations, and experimental conditions. Insights from EDS measurements suggest that probe molecules penetrate up to approximately 3 μm into the PhC structure, affecting about 40% of the total PhC thickness. Future work will explore the potential for greater enhancement by using thicker pSi PhCs, lasers with different penetration depths, and varying infiltration depths of probe molecules. These experiments aim to optimize the design and application of PhCs in Raman spectroscopy, providing a more detailed understanding of the mechanisms behind Raman signal enhancement in PhCs.

In the SERS experiment, samples corresponding to sample categories A, D, and F were utilized because they demonstrated an enhancement of the Raman signal in the Raman experiment. Substrates corresponding to ordinary pSi (sample category A) exhibited approximately 30% variation in the $\sim 520\text{ cm}^{-1}$ peak intensity from the average value, which is slightly higher than in the Raman experiment, but still within acceptable limits. This variation is attributed to the inherently variable nature of the SERS enhancement mechanism, including the distribution of hotspots and variability in probe molecule adsorption. Another significant difference was the significantly lower intensity of the silicon band in SERS spectra compared to standard Raman spectra. This reduction is due to the plasmonic effects of gold nanoparticles, which, while enhancing the Raman signal near the metal surface, also reduce the penetration of incident light into the underlying photonic structure, thus diminishing the silicon band intensity. Interestingly, in the SERS experiments, sample category F showed a stronger enhancement (~ 2.5 times) compared to category D (~ 1.7 times), which was contrary to the Raman experiment results. This discrepancy may be due to the more precise alignment of the laser with the low-frequency PBG edge in category F, leading to enhanced light-matter interaction.

For the probe molecule R6G, the strongest enhancement was observed when the laser was aligned with the high-frequency PBG edge, consistent with the Raman results. However, the SERS enhancement was lower, likely due to plasmonic effects overshadowing the photonic contributions. On the other hand, sample category F unexpectedly showed lower intensity. This inconsistency was likely due to variations in the preparation conditions and the number of probe

molecules that remained on the SERS substrate after rinsing in MQ water as part of the sample preparation.

Despite the discrepancies between the Raman and SERS experiments, the study demonstrated that the signal enhancement when the laser overlaps with the PBG edge is approximately 2.5 and 1.1 times, respectively. The smaller enhancement factor in the SERS experiment is in line with our expectations since it results from a significantly stronger plasmonic influence, which overshadowed the effect of the photonic structure. This consistency indicates that PhCs can provide a predictable enhancement factor, which is crucial for designing and optimizing SERS-based sensing platforms. The study also showed that while plasmonic effects play an absolutely dominant role in SERS, the photonic structure or the possible synergy between the plasmonic and photonic effects can further enhance the signal.

The results of this study emphasize the potential of photonic crystals, particularly pSi PhCs, as effective platforms for enhancing Raman and SERS signals. The ability to tune the PBG and control the light-matter interaction within the PhC structure opens up new possibilities for designing highly sensitive and specific spectroscopic tools.

Future work should focus on conducting a more detailed and systematic analysis of SERS signal enhancement, particularly addressing the variability in sample preparation and the influence of different PhC configurations. Additionally, exploring the integration of PhCs with various plasmonic materials and probe molecules could lead to further improvements in signal enhancement and the development of more versatile SERS substrates.

In conclusion, this research has provided valuable insights into the role of photonic crystals in enhancing Raman and SERS signals, highlighting the importance of precise control over PhC fabrication and the alignment of the laser with the PBG. These findings contribute to the knowledge in the field of photonic structures and their applications in advanced spectroscopic techniques.

The study for this doctoral thesis was designed to be conducted as independently as possible by using the experimental equipment available at the Department of Physics and Biophysics, School of Medicine, University of Zagreb, and Division of Materials Physics at Ruđer Bošković Institute. The research also relied on extensive knowledge about porous silicon and even porous silicon photonic crystals, including their preparation and characterization, which has been developed through scientific work conducted at the Department of Physics and Biophysics over the past 10-15 years. This approach ensured that the study was based on both practical experience and a solid understanding of the fundamental principles about porous silicon and

porous silicon photonic crystals that have been established by previous research within the department.

The future belongs to those who believe in the beauty of their dreams.

(E. Roosevelt)

Bibliography

1. Y. Qi, E.X. Chen, D. Hu, Y. Yang, Z. Wu, M. Zheng, et al. Applications of Raman spectroscopy in clinical medicine. *Food Frontiers*. John Wiley and Sons Inc, 2024. 392–419. 10.1002/fft2.335.
2. E.G. Bartick, P. Buzzini. “Raman Spectroscopy in Forensic Science”. *Encyclopedia of Analytical Chemistry*. Wiley, 2009. 10.1002/9780470027318.a9098.
3. N. Stone, C. Kendall, J. Smith, P. Crow, H. Barr. “Raman spectroscopy for identification of epithelial cancers”. *Faraday Discuss.* 2004. 126(1): 141–157. 10.1039/b304992b.
4. A. Smekal. “Zur Quantentheorie der Dispersion.” *Naturwissenschaften* 11. 1923. 873–875. 10.1007/BF01576902.
5. C. Raman, K. Krishnan. “A New Type of Secondary Radiation”. *Nature* 121. 1928. 501–502. 10.1038/121501c0.
6. D.A. Long. *The Raman Effect: A Unified Treatment of the Theory of Raman Scattering by Molecules*. Wiley, 2002. 10.1002/0470845767.
7. “Edinburgh Instruments”. n.d. <https://www.edinst.com/blog/what-is-raman-spectroscopy/> [Sep 2 2024].
8. R. Aroca. *Surface-Enhanced Vibrational Spectroscopy*. Wiley, 2006.
9. J.M. Hollas. *Modern Spectroscopy*, 4th Edition. Wiley, 2003.
10. E. Smith, G. Dent. *Modern Raman Spectroscopy: A Practical Approach*. 2019. 10.1002/9781119440598.
11. M. Diem. *Modern Vibrational Spectroscopy and Micro-Spectroscopy: Theory, Instrumentation and Biomedical Applications*. John Wiley & Sons, Inc., 2015. 10.1002/9781118824924.
12. M. Škrabić. *Fotonički kristali od poroznog silicija kao SERS podloge za blisku infracrvenu pobudu*, Doktorska disertacija. 2020.
13. M. Cardona. Resonance phenomena. In: Cardona, M., Güntherodt, G. (eds) *Light Scattering in Solids II*. Topics in Applied Physics. Berlin, Heidelberg, 1982. 10.1007/3-540-11380-0_14.
14. A. Compaan, H.J. Trodahl. “Resonance Raman scattering in Si at elevated temperatures”. *Phys Rev B*. 1984. 29(2). 10.1103/PhysRevB.29.793.

15. J.D. Joannopoulos, S.G. Johnson, J.N. Winn, Meade R.D. Photonic Crystals: Molding the Flow of Light - Second Edition. 2007. 10.2307/j.ctvc4gz9.
16. Q. Gong, H. Xiaoyong. Photonic Crystals Principles and Applications. 1st Edition. Pan Stanford Publishing, New York, 2014. 10.1201/b15654.
17. R.S. Dubey, D.K. Gautam. "Propagation of electromagnetic waves in 1D finite photonic crystals for the investigation of linear properties". J Mod Opt. 2009. 56(4): 487–495. 10.1080/09500340802484051.
18. E. Yablonovitch. "Inhibited Spontaneous Emission in Solid-State Physics and Electronics". Phys Rev Lett. 1987. 58(20). 10.1103/PhysRevLett.58.2059.
19. S. John. "Strong localization of photons in certain disordered dielectric superlattices". Phys Rev Lett. 1987. 58(23). 10.1103/PhysRevLett.58.2486.
20. K. Sakoda. Optical Properties of Photonic Crystals. Springer, 2001.
21. A. Bardaoui, R. Chtourou, M. Amlouk. Porous Silicon Multilayers: Synthesis and Applications. 2012.
22. S. Kasap. Optoelectronics & Photonics: Principles & Practices. 2012.
23. E. Yeganegi, A. Lagendijk, A.P. Mosk, W.L. Vos. "Local density of optical states in the band gap of a finite one-dimensional photonic crystal". Phys Rev B Condens Matter Mater Phys. 2014. 89(4). 10.1103/PhysRevB.89.045123.
24. J.M. Bendickson, J.P. Dowling, M. Scalora. "Analytic expressions for the electromagnetic mode density in finite, one-dimensional, photonic band-gap structures". Phys Rev E. 1996. 53(4). 10.1103/PhysRevE.53.4107.
25. S. V. Gaponenko. "Effects of photon density of states on Raman scattering in mesoscopic structures". Phys Rev B Condens Matter Mater Phys. 2002. 65(14): 1–4. 10.1103/PhysRevB.65.140303.
26. S.M. Barnett, R. Loudon. Sum Rule for Modified Spontaneous Emission Rates. 1996. 10.1103/PhysRevLett.77.2444.
27. G. Vincent. "Optical properties of porous silicon superlattices". Appl Phys Lett. 1994. 64(18): 2367–2369. 10.1063/1.111982.
28. C. Vinegoni, M. Cazzanelli, L. Pavesi. Porous silicon microcavities In: H.S. Nalwa. Silicon-Based Material and Devices. Academic Press, 2001. 10.1016/B978-012513909-0/50015-5.

29. L. Pavesi. "Porous silicon dielectric multilayers and microcavities". Springer, 1997. Pp. 1–76. 10.1007/BF02877374.
30. M.J. Sailor. Porous Silicon in Practice: Preparation, Characterization and Applications. Wiley-VCH, 2012. 10.1002/9783527641901.
31. S. Iadanza, C. Devarapu, A. Liles, R. Sheehan, L. O’Faoláin. "Hybrid external cavity laser with an amorphous silicon-based photonic crystal cavity mirror". Applied Sciences (Switzerland). MDPI AG, 2020. 10(1). 10.3390/app10010240.
32. M.A. Butt, S.N. Khonina, N.L. Kazanskiy. Recent advances in photonic crystal optical devices: A review. Optics and Laser Technology. Elsevier Ltd, 2021. 10.1016/j.optlastec.2021.107265.
33. M.G. Daher, Y. Trabelsi, A. Panda, A.H. Gevorgyan, K.M. Abohassan, L.K. Smirani, et al. "Design of a Highly Sensitive Detector Using a Ternary Photonic Crystal (PC) Based on Titanium Nitride Sandwiched between Si and SiO₂ for the Creatinine Concentration Detection in the Blood Serum". Optics. MDPI, 2022. 3(4): 447–461. 10.3390/opt3040038.
34. E. Lorenzo, C.J. Oton, N.E. Capuj, M. Ghulinyan, D. Navarro-Urrios, Z. Gaburro, et al. Porous silicon-based rugate filters. 2005. 10.1364/AO.44.005415.
35. B.G. Bovard. "Rugate filter theory: an overview". Appl Opt. 1993. 5427–5442. 10.1364/AO.32.005427.
36. J.E. Lugo, H.A. Lopez, S. Chan, P.M. Fauchet. Tunable Porous Silicon Photonic Band Gap Structures. 2001. 10.1557/PROC-637-E4.6.
37. B.H. King. "Medium-wavelength infrared gas sensing with electrochemically fabricated porous silicon optical rugate filters". J Nanophotonics. SPIE-Intl Soc Optical Eng, 2011. 5(1): 051510. 10.1117/1.3558740.
38. W.H. Southwell. Spectral response calculations of rugate filters using coupled-wave theory. J. Opt. Soc. Am. A. 1988. 10.1364/JOSAA.5.001558.
39. A.G. Imenes, D.R. Mckenzie. Flat-topped broadband rugate filters. 2006. 10.1364/ao.45.007841.
40. X.G. Zhang. "Morphology and Formation Mechanisms of Porous Silicon". J Electrochem Soc. The Electrochemical Society, 2004. 151(1): C69. 10.1149/1.1632477.
41. L. Mikac. Surface-Enhanced Raman Scattering: From the Colloid to the Stable Substrate, Doktorska disertacija. 2016.

42. L. Canham. Handbook of Porous Silicon. Handbook of Porous Silicon. 2nd ed. Springer International Publishing, 2018. 10.1007/978-3-319-04508-5_38-1.
43. V. Lehmann, U. Gösele. "Porous silicon formation: A quantum wire effect". Appl Phys Lett. 1991. 58(8): 856–858. 10.1063/1.104512.
44. F. Ptashchenko. "Electrochemical etching of porous silicon – DFT modeling". Comput Mater Sci. Elsevier B.V., 2021. 198. 10.1016/j.commatsci.2021.110695.
45. V. Đerek. Hibridni spoj strukturiranoga silicija i organskoga poluvodiča za detekciju infracrvene svjetlosti, Doktorska disertacija. 2016.
46. A.G. Cullis, L.T. Canham, P.D.J. Calcott. The structural and luminescence properties of porous silicon. Journal of Applied Physics. American Institute of Physics Inc., 1997. 909–965. 10.1063/1.366536.
47. M. Kosović. Nanostrukturalna svojstva visoko luminiscentnoga poroznoga silicija, Doktorska disertacija. 2015.
48. J. Vukajlović Pleština, V. Đerek, L. Francaviglia, F. Amaduzzi, H. Potts, M. Ivanda, et al. "Nanoporous silicon tubes: The role of geometry in nanostructure formation and application to light emitting diodes". J Phys D Appl Phys. Institute of Physics Publishing, 2017. 50(26). 10.1088/1361-6463/aa7196.
49. S. Um, J. Yang, T.E. Choi, H. Cho, S. Jin, H. Sohn. Fabrication and optical characterization of full color stop band based on rugate-structured porous silicon. Microelectronic Engineering. 2012. Pp. 100–103. 10.1016/j.mee.2011.03.143.
50. R. Moretta, L. De Stefano, M. Terracciano, I. Rea. Porous silicon optical devices: Recent advances in biosensing applications. Sensors (Switzerland). MDPI AG, 2021. 1–26. 10.3390/s21041336.
51. F. Cunin, T.A. Schmedake, J.R. Link, Y.Y. Li, J. Kom, S.N. Bhatia, et al. "Biomolecular screening with encoded porous-silicon photonic crystals". Nat Mater. European Association for Cardio-Thoracic Surgery, 2002. 1(1): 39–41. 10.1038/nmat702.
52. C. Pacholski. Photonic Crystal Sensors Based on Porous Silicon. Sensors (Switzerland). 2013. 4694–4713. 10.3390/s130404694.
53. J.O. Estevez, V. Agarwal. "Porous silicon photonic crystals". Handbook of Porous Silicon. Springer International Publishing, 2014. Pp. 805–814. 10.1007/978-3-319-05744-6_82.

54. K. Kneipp, Y. Wang, H. Kneipp, L.T. Perelman, I. Itzkan, R.R. Dasari, et al. Single Molecule Detection Using Surface-Enhanced Raman Scattering (SERS). 1997. 10.1103/PhysRevLett.78.1667.
55. K.H. Rieder, S. Nie, S.R. Emory. Probing Single Molecules and Single Nanoparticles by Surface-Enhanced Raman Scattering. *Angew. Chem. Int. Ed. Engl.* Springer, 1994. 10.1126/science.275.5303.1102.
56. J.R. Lombardi, R.L. Birke. “A unified view of surface-enhanced raman scattering”. *Acc Chem Res.* 2009. 42(6): 734–742. 10.1021/ar800249y.
57. A. Otto, I. Mrozek, H. Grabhorn, W. Akemann. Surface-Enhanced Raman Scattering. *J. Phys.: Condens, Matter.* 1992. 10.1088/0953-8984/4/5/001.
58. G.C. Schatz, R.P. Van Duyne. Handbook of Vibrational Spectroscopy Electromagnetic Mechanism of Surface-Enhanced Spectroscopy. 2006. 10.1002/0470027320.s0601.
59. D. Ciialla-May, X.S. Zheng, K. Weber, J. Popp. Recent progress in surface-enhanced Raman spectroscopy for biological and biomedical applications: From cells to clinics. *Chemical Society Reviews.* Royal Society of Chemistry, 2017. 3945–3961. 10.1039/c7cs00172j.
60. N. Gao, Q. Wang, J. Tang, S. Yao, H. Li, X. Yue, et al. “Non-invasive SERS serum detection technology combined with multivariate statistical algorithm for simultaneous screening of cervical cancer and breast cancer”. *Anal Bioanal Chem.* Springer Science and Business Media Deutschland GmbH, 2021. 413(19): 4775–4784. 10.1007/s00216-021-03431-3.
61. M. Jahn, S. Patze, I.J. Hidi, R. Knipper, A.I. Radu, A. Mühlig, et al. Plasmonic nanostructures for surface enhanced spectroscopic methods. *Analyst.* Royal Society of Chemistry, 2016. 756–793. 10.1039/c5an02057c.
62. K.D. Sattler. Handbook of Nanophysics Nanoparticles and Quantum Dots. 2010. 10.1201/9781420075458.
63. S.A. Maier. Plasmonics: Fundamentals and Applications. Springer, 2007.
64. J.D. Jackson. Classical Electrodynamics. 3rd ed. Wiley, 1998.
65. E.C. Le Ru, P.G. Etchegoin. Principles of Surface-Enhanced Raman Spectroscopy and Related Plasmonic Effects. Elsevier, 2008.
66. K.L. Kelly, E. Coronado, L.L. Zhao, G.C. Schatz. “The Optical Properties of Metal Nanoparticles: The Influence of Size, Shape, and Dielectric Environment”. *Journal of Physical Chemistry B.* 2002. 107(3): 668–677. 10.1021/jp026731y.

67. H. Jing, L. Zhang, H. Wang. Geometrically Tunable Optical Properties of Metal Nanoparticles In: UV-VIS and Photoluminescence Spectroscopy for Nanomaterials Characterization. 2013. 10.1007/978-3-642-27594-4_1.
68. “Futura Tech”. n.d. <https://www.futura-sciences.com/tech/dossiers/technologie-revolution-nanotechnologies-790/page/4/> [Oct 4 2017].
69. C. Bréchnignac, P. Houdy, M. Lahmani. Nanomaterials and Nanochemistry. Springer, 2007.
70. M.M. Alvarez, J.T. Khoury, T.G. Schaaff, M.N. Shafigullin, I. Vezmar, R.L. Whetten. Optical Absorption Spectra of Nanocrystal Gold Molecules. 1997. 10.1021/jp962922n.
71. P.K. Jain, M.A. El-Sayed. “Plasmonic coupling in noble metal nanostructures”. Chem Phys Lett. 2010. 487(4–6): 153–164. 10.1016/j.cplett.2010.01.062.
72. X. Huang, S. Neretina, M.A. El-Sayed. Gold nanorods: From synthesis and properties to biological and biomedical applications. Advanced Materials. 2009. 4880–4910. 10.1002/adma.200802789.
73. H. Jing, L. Zhang, H. Wang. “Geometrically tunable optical properties of metal nanoparticles”. UV-VIS and Photoluminescence Spectroscopy for Nanomaterials Characterization. Springer Berlin Heidelberg, 2013. Pp. 1–74. 10.1007/978-3-642-27594-4_1.
74. N. Félidj, J. Aubard, G. Lévi, J.R. Krenn, A. Hohenau, G. Schider, et al. “Optimized surface-enhanced Raman scattering on gold nanoparticle arrays”. Appl Phys Lett. 2003. 82(18): 3095–3097. 10.1063/1.1571979.
75. J. Grand, S. Kostcheev, J.L. Bijeon, M.L. De la Chapelle, P.M. Adam, A. Rumyantseva, et al. Optimization of SERS-active substrates for near-field Raman spectroscopy. Synthetic Metals. 2003. Pp. 621–624. 10.1016/S0379-6779(03)00276-5.
76. N. Guillot, B. Fremaux, H. Shen, O. Péron, E. Rinnert, T. Toury, et al. Surface Enhanced Raman Scattering optimization of gold nanocylinder arrays: Influence of the Localized Surface Plasmon Resonance and excitation wavelength. AAPP Atti della Accademia Peloritana dei Pericolanti, Classe di Scienze Fisiche, Matematiche e Naturali. 2011. 10.1478/C1V89S1P043.
77. F.J. Colas, M. Cottat, R. Gillibert, N. Guillot, N. Djaker, N. Lidgi-Guigui, et al. “Red-Shift Effects in Surface Enhanced Raman Spectroscopy: Spectral or Intensity Dependence of the Near-Field?” Journal of Physical Chemistry C. American Chemical Society, 2016. 120(25): 13675–13683. 10.1021/acs.jpcc.6b01492.

78. S. Link, M.A. El-Sayed. "Spectral Properties and Relaxation Dynamics of Surface Plasmon Electronic Oscillations in Gold and Silver Nanodots and Nanorods". *Journal of Physical Chemistry B*. American Chemical Society, 1999. 103(40): 8410–8426. 10.1021/jp9917648.
79. L. Gunnarsson, T. Rindzevicius, J. Prikulis, B. Kasemo, M. Käll, S. Zou, et al. "Confined plasmons in nanofabricated single silver particle pairs: Experimental observations of strong interparticle interactions". *Journal of Physical Chemistry B*. 2005. 109(3): 1079–1087. 10.1021/jp049084e.
80. H. Mertens, J. Verhoeven, A. Polman, F.D. Tichelaar. "Infrared surface plasmons in two-dimensional silver nanoparticle arrays in silicon". *Appl Phys Lett*. 2004. 85(8): 1317–1319. 10.1063/1.1784542.
81. P.K. Jain, W. Huang, M.A. El-Sayed. "On the universal scaling behavior of the distance decay of plasmon coupling in metal nanoparticle pairs: A plasmon ruler equation". *Nano Lett*. 2007. 7(7): 2080–2088. 10.1021/nl071008a.
82. J. Langer, D.J. de Aberasturi, J. Aizpurua, R.A. Alvarez-Puebla, B. Auguie, J.J. Baumberg, et al. Present and future of surface-enhanced Raman scattering. *ACS Nano*. American Chemical Society, 2020. 28–117. 10.1021/acsnano.9b04224.
83. H. Lin, J. Mock, D. Smith, T. Gao, M.J. Sailor. "Surface-enhanced Raman scattering from silver-plated porous silicon". *Journal of Physical Chemistry B*. 2004. 108(31): 11654–11659. 10.1021/jp049008b.
84. S. Chan, S. Kwon, T.W. Koo, L.P. Lee, A.A. Berlin. "Surface-Enhanced Raman Scattering of Small Molecules from Silver-Coated Silicon Nanopores". *Advanced Materials*. 2003. 15(19): 1595–1598. 10.1002/adma.200305149.
85. H. V. Bandarenka, K. V. Girel, S.A. Zavatski, A. Panarin, S.N. Terekhov. Progress in the development of SERS-active substrates based on metal-coated porous silicon. *Materials*. MDPI AG, 2018. 10.3390/ma11050852.
86. R. Hérino. "Nanocomposite materials from porous silicon". *Materials Science and Engineering B*. 2000. 69–70: 70–76.
87. E. Nativ-Roth, K. Rechav, Z. Porat. "Deposition of gold and silver on porous silicon and inside the pores". *Thin Solid Films*. Elsevier B.V., 2016. 603: 88–96. 10.1016/j.tsf.2016.01.020.
88. F.A. Harraz, T. Tsuboi, J. Sasano, T. Sakka, Y.H. Ogata. "Metal Deposition onto a Porous Silicon Layer by Immersion Plating from Aqueous and Nonaqueous Solutions".

- J Electrochem Soc. The Electrochemical Society, 2002. 149(9): C456.
10.1149/1.1498841.
89. N.G. Greeneltch, M.G. Blaber, G.C. Schatz, R.P. Van Duyne. “Plasmon-Sampled Surface-Enhanced Raman Excitation Spectroscopy on Silver Immobilized Nanorod Assemblies and Optimization for Near Infrared ($\lambda_{\text{ex}} = 1064 \text{ nm}$) Studies”. *Journal of Physical Chemistry C*. 2013. 117(6): 2554–2558. 10.1021/jp310846j.
90. H. Kearns, N.C. Shand, W.E. Smith, K. Faulds, D. Graham. “1064 nm SERS of NIR active hollow gold nanotags”. *Physical Chemistry Chemical Physics*. Royal Society of Chemistry, 2015. 17(3): 1980–1986. 10.1039/c4cp04281f.
91. E.J. Liang, X.L. Ye, W. Kiefer. “Surface-Enhanced Raman Spectroscopy of Crystal Violet in the Presence of Halide and Halate Ions with Near-Infrared Wavelength Excitation”. *J Phys Chem A*. 1997. 101(40).
92. B. Nikoobakht, M.A. El-Sayed. “Surface-Enhanced Raman Scattering Studies on Aggregated Gold Nanorods†”. *J Phys Chem A*. 2003. 107(18): 3372–3378.
93. R. Smith, K.L. Wright, L. Ashton. Raman spectroscopy: An evolving technique for live cell studies. *Analyst*. Royal Society of Chemistry, 2016. 3590–3600.
10.1039/c6an00152a.
94. I. Notingher, S. Verrier, H. Romanska, A.E. Bishop, J.M. Polak, L.L. Hench. “In situ characterisation of living cells by Raman spectroscopy”. *Journal of Spectroscopy*. IOS Press, 2002. 16(2): 43–51. 10.1155/2002/408381.
95. D. Rout, R. Vijaya. “Role of Stopband and Localized Surface Plasmon Resonance in Raman Scattering from Metallo-Dielectric Photonic Crystals”. *Plasmonics*. Springer New York LLC, 2017. 12(5): 1409–1416. 10.1007/s11468-016-0400-5.
96. M. Ashurov, A. Baranchikov, S. Klimonsky. “Photonic crystal enhancement of Raman scattering”. *Physical Chemistry Chemical Physics*. Royal Society of Chemistry, 2020. 22(17): 9630–9636. 10.1039/d0cp00781a.
97. D.A. Mamichev, K.A. Gonchar, V.Y. Timoshenko, G.K. Mussabek, V.E. Nikulin, T.I. Taurbaev. “Enhanced Raman scattering in multilayer structures of porous silicon”. *Journal of Raman Spectroscopy*. John Wiley and Sons Ltd, 2011. 42(6): 1392–1395. 10.1002/jrs.2865.
98. K.A. Gonchar, G.K. Musabek, T.I. Taurbayev, V.Y. Timoshenko. “Enhancement of photoluminescence and raman scattering in one-dimensional photonic crystals based on porous silicon”. *Semiconductors*. 2011. 45(5): 614–617. 10.1134/S1063782611050113.

99. D. Qi, L. Lu, L. Wang, J. Zhang. “Improved SERS sensitivity on plasmon-free TiO₂ photonic microarray by enhancing light-matter coupling”. *J Am Chem Soc. American Chemical Society*, 2014. 136(28): 9886–9889. 10.1021/ja5052632.
100. V.S. Gorelik, P.P. Sverbil, V. V. Filatov, D. Bi, G.T. Fei, S.H. Xu. “Transmission spectra of one-dimensional porous alumina photonic crystals”. *Photonics Nanostruct. Elsevier B.V.*, 2018. 32: 6–10. 10.1016/j.photonics.2018.08.004.
101. Y. Almohamed, R. Barille, A.I. Vodchits, Y.P. Voinov, V.S. Gorelik, A.D. Kudryavtseva, et al. “Reduction of the threshold of stimulated Raman scattering in Raman-active media introduced into pores of a globular photonic crystal”. *JETP Lett. Maik Nauka-Interperiodica Publishing*, 2015. 101(6): 365–370. 10.1134/S0021364015060028.
102. Z. Li, D.J. Gosztola, C.J. Sun, S.M. Heald, Y. Sun. “Exceptional enhancement of Raman scattering on silver chlorobromide nanocube photonic crystals: Chemical and photonic contributions”. *J Mater Chem C Mater. Royal Society of Chemistry*, 2015. 3(11): 2455–2461. 10.1039/c5tc00077g.
103. M. Fränzl, S. Moras, O.D. Gordan, D.R.T. Zahn. “Interaction of One-Dimensional Photonic Crystals and Metal Nanoparticle Arrays and Its Application for Surface-Enhanced Raman Spectroscopy”. *Journal of Physical Chemistry C. American Chemical Society*, 2018. 122(18): 10153–10158. 10.1021/acs.jpcc.8b02241.
104. K.I. Zaytsev, G.M. Katyba, E. V. Yakovlev, V.S. Gorelik, S.O. Yurchenko. “Band-gap nonlinear optical generation: The structure of internal optical field and the structural light focusing”. *J Appl Phys. American Institute of Physics Inc.*, 2014. 115(21). 10.1063/1.4880299.
105. O. Deparis, S.R. Mouchet, B.L. Su. “Light harvesting in photonic crystals revisited: why do slow photons at the blue edge enhance absorption?” *Physical Chemistry Chemical Physics. Royal Society of Chemistry*, 2015. 17(45): 30525–30532. 10.1039/c5cp04983k.
106. S. V. Gaponenko. “Effects of photon density of states on Raman scattering in mesoscopic structures”. *Phys Rev B Condens Matter Mater Phys.* 2002. 65(14): 1–4. 10.1103/PhysRevB.65.140303.
107. R.G. Zaporozhchenko, S.Y. Kilin, A.G. Smirnov. “Stimulated Raman scattering of light in a photonic crystal”. *Kvantovaya Elektronika.* 2000. 30(11): 1001. 10.1070/qe2000v030n11abeh001851.

108. G. Von Freymann, S. John, S. Wong, V. Kitaev, G.A. Ozin. “Measurement of group velocity dispersion for finite size three-dimensional photonic crystals in the near-infrared spectral region”. *Appl Phys Lett*. 2005. 86(5): 1–3. 10.1063/1.1857076.
109. K.X. Wang, Z. Yu, V. Liu, A. Raman, Y. Cui, S. Fan. “Light trapping in photonic crystals”. *Energy Environ Sci. Royal Society of Chemistry*, 2014. 7(8): 2725–2738. 10.1039/c4ee00839a.
110. V.S. Gorelik, V. V. Kapaev. “Electromagnetic-field amplification in finite one-dimensional photonic crystals”. *Journal of Experimental and Theoretical Physics. Maik Nauka-Interperiodica Publishing*, 2016. 123(3): 373–381. 10.1134/S1063776116070062.
111. M. Bertolotti. Wave interactions in photonic band structures: An overview. *Journal of Optics A: Pure and Applied Optics*. 2006. 10.1088/1464-4258/8/4/S02.
112. S.D. Abdurakhmonov, M.S. Ashurov, S.O. Klimonsky, N. V. Tcherniega, V.S. Gorelik. “Numerical Simulation of Optical Properties of One-Dimensional Photonic Crystals Based on Anodic Aluminum Oxide”. *Bulletin of the Lebedev Physics Institute. Pleiades Publishing*, 2022. 49(9): 294–301. 10.3103/S1068335622090020.
113. M. Ashurov, B. Abdusatorov, A. Baranchikov, S. Klimonsky. “Surface-enhanced Raman scattering in ETPTA inverse photonic crystals with gold nanoparticles”. *Physical Chemistry Chemical Physics. Royal Society of Chemistry*, 2021. 23(36): 20275–20281. 10.1039/d1cp02958d.
114. D. Yan, L. Qiu, M. Xue, Z. Meng, Y. Wang. “A flexible surface-enhanced Raman substrates based on cellulose photonic crystal/Ag-nanoparticles composite”. *Mater Des. Elsevier Ltd*, 2019. 165. 10.1016/j.matdes.2019.107601.
115. C. Yi Wu, C. Chi Huang, J. Sin Jhang, A. Chi Liu, C.-C. Chiang, M.-L. Hsieh, et al. Nanostructure fabrication; (240.6695) Surface-enhanced Raman scattering; (350.4238) Nanophotonics and photonic crystals. of pyridine adsorbed at a silver electrode. *Adv. Funct. Mater. Mater*, 1974.
116. T. Van Nguyen, D.C. Vu, V.H. Pham, T.B. Pham, V.H. Pham, H. Bui. “Improvement of SERS for detection of ultra-low concentration of methyl orange by nanostructured silicon decorated with Ag nanoparticles”. *Optik (Stuttg). Elsevier GmbH*, 2021. 231. 10.1016/j.ijleo.2021.166431.

117. G. Chen, K. Zhang, B. Luo, W. Hong, J. Chen, X. Chen. “Plasmonic-3D photonic crystals microchip for surface enhanced Raman spectroscopy”. *Biosens Bioelectron.* Elsevier Ltd, 2019. 143. 10.1016/j.bios.2019.111596.
118. S. Guddala, S.A. Kamanoor, A. Chiappini, M. Ferrari, N.R. Desai. “Experimental investigation of photonic band gap influence on enhancement of Raman-scattering in metal-dielectric colloidal crystals”. *J Appl Phys.* 2012. 112(8). 10.1063/1.4758315.
119. J. Bi, G. Fan, S. Wu, X. Su, H. Xia, S.F. Zhang. “Fabrication of Poly(styrene-co-maleic anhydride)@Ag Spheres with High Surface Charge Intensity and their Self-Assembly into Photonic Crystal Films”. *ChemistryOpen.* Wiley-VCH Verlag, 2017. 6(5): 637–641. 10.1002/open.201700118.
120. L. Dac Tuyen, A. Chi Liu, C.-C. Huang, P.-C. Tsai, J. Hung Lin, C.-W. Wu, et al. “Doubly resonant surface-enhanced Raman scattering on gold nanorod decorated inverse opal photonic crystals”. *Opt Express.* Springer, 2012. 20(17): 29266. 10.1364/OE.20.029266.
121. X. Ma, H. Cheng, J. Hou, Z. Jia, G. Wu, X. Lü, et al. “Detection of breast cancer based on novel porous silicon Bragg reflector surface-enhanced Raman spectroscopy-active structure”. *Chinese Optics Letters.* Shanghai Institute of Optics and Fine Mechanics, 2020. 18(5): 051701. 10.3788/col202018.051701.
122. H. Wang, Y. Wu, H. Song. “Synergistic effects of photonic crystal and gold nanostars for quantitative SERS detection of 3-Phenoxybenzoic acid”. *Appl Surf Sci.* Elsevier B.V., 2019. 476: 587–593. 10.1016/j.apsusc.2019.01.061.
123. X.G. Wang, J. Wang, Z.J. Jiang, D.W. Tao, X.Q. Zhang, C.W. Wang. “Silver loaded anodic aluminum oxide dual-bandgap heterostructure photonic crystals and their application for surface enhanced Raman scattering”. *Appl Surf Sci.* Elsevier B.V., 2021. 544. 10.1016/j.apsusc.2020.148881.
124. S. Narayanan, P. Sahani, J. Rathod, V.R. Soma, R. Yalla, B.V.R. Tata. “Thin photonic crystal templates for enhancing the SERS signal: a case study using very low concentrations of dye molecules”. *Phys Scr.* Institute of Physics, 2024. 99(3). 10.1088/1402-4896/ad23b2.
125. J. Wang, Z. Jia, Y. Liu. “Improvement of SERS by the Optical Modulation of Photonic Crystal”. *IEEE Sens J.* Institute of Electrical and Electronics Engineers Inc., 2019. 19(23): 11221–11227. 10.1109/JSEN.2019.2937092.

126. F. Zhong, Z. Wu, J. Guo, D. Jia. "Porous silicon photonic crystals coated with Ag nanoparticles as efficient substrates for detecting trace explosives using SERS". *Nanomaterials*. MDPI AG, 2018. 8(11). 10.3390/nano8110872.
127. J. Yang, F. Ren, X. Chong, D. Fan, S. Chakravarty, Z. Wang, et al. "Guided-mode resonance grating with self-assembled silver nanoparticles for surface-enhanced Raman scattering spectroscopy". *Photonics*. MDPI AG, 2014. 1(4): 380–389. 10.3390/photonics1040380.
128. V. Gašparić. "Utjecaj prostornog ograničenja fonona na fotoluminescenciju nanostrukturiranog silicija, Diplomski rad". 2017.
129. "PVEducation". n.d. <https://www.pveducation.org/pvcdrom/materials/optical-properties-of-silicon> [Sep 2 2024].
130. A. Goksu, M.K. Tanaydin. "Adsorption of hazardous crystal violet dye by almond shells and determination of optimum process conditions by taguchi method". *Desalination Water Treat.* Desalination Publications, 2017. 88: 189–199. 10.5004/dwt.2017.21364.
131. "Wikipedia". n.d. https://en.wikipedia.org/wiki/Rhodamine_6G [Sep 2 2024].
132. S.N. Agbo, P. Sutta. "Preferred Crystal Orientation in Thin-Film Nanocrystalline Silicon Determined by Raman Spectroscopy". *Dig J Nanomater Biostruct.* 2013. 8(4): 1461–1473.
133. W.S. Yoo, H. Harima, M. Yoshimoto. "Polarized Raman Signals from Si Wafers: Dependence of In-Plane Incident Orientation of Probing Light". *ECS Journal of Solid State Science and Technology*. The Electrochemical Society, 2015. 4(9): P356–P363. 10.1149/2.0061509jss.
134. A.G. Imenes, D.R. Mckenzie. "Flat-topped broadband rugate filters". *Appl Opt.* 2006. 45(30).
135. W.H. Southwell. "Spectral response calculations of rugate filters using coupled-wave theory". *Journal of the Optical Society of America A*. 1988. 5(9). 10.1364/JOSAA.5.001558.
136. M. Škrabić, M. Krajačić, M. Gotić, N. Baran, L. Mikac, T. Jurkin, et al. "Gold-coated porous silicon as a SERS substrate for near-infrared excitation: Off- and on-resonant conditions". *Appl Surf Sci.* Elsevier B.V., 2024. 644. 10.1016/j.apsusc.2023.158820.

137. D. Devashish, S.B. Hasan, J.J.W. Van Der Vegt, W.L. Vos. “Reflectivity calculated for a three-dimensional silicon photonic band gap crystal with finite support”. *Phys Rev B*. American Physical Society, 2017. 95(15). 10.1103/PhysRevB.95.155141.
138. F. Galisteo-López, E. Palacios-Lidón, E. Castillo-Martínez, C. López. “Optical study of the pseudogap in thickness and orientation controlled artificial opals”. *Phys Rev B Condens Matter Mater Phys*. 2003. 68(11). 10.1103/PhysRevB.68.115109.
139. Y.A. Vlasov, M.A. Kaliteevski, V. V Nikolaev. “Different regimes of light localization in a disordered photonic crystal”. *Phys Rev B*. 1998. 60(3). 10.1103/PhysRevB.60.1555.
140. A. Wathukarage, I. Herath, M.C.M. Iqbal, M. Vithanage. “Mechanistic understanding of crystal violet dye sorption by woody biochar: implications for wastewater treatment”. *Environ Geochem Health*. Springer Netherlands, 2019. 41(4): 1647–1661. 10.1007/s10653-017-0013-8.
141. K. Lai, Y. Zhang, R. Du, F. Zhai, B.A. Rasco, Y. Huang. “Determination of chloramphenicol and crystal violet with surface enhanced Raman spectroscopy”. *Sens Instrum Food Qual Saf*. 2011. 5(1): 19–24. 10.1007/s11694-011-9106-8.
142. L. Angeloni, G. Smulevich, M.P. Marzocchi. “Resonance Raman Spectrum of Crystal Violet”. *Journal of Raman Spectroscopy*. 1979. 8(6): 305–309. 10.1002/jrs.1250080603.
143. S.A. Dyakov, T. Perova, K.A. Gonchar, V. Timoshenko. “Resonance Enhancement of Raman Scattering from One-Dimensional Periodical Structures of Porous Silicon”. *Journal of Nanoelectronics and Optoelectronics*. 2012. 7(6): 591–595. 10.1166/jno.2012.1398.
144. V. Gorelik, D. Bi, N. Klimova, S. Pichkurenko, V. Filatov. The electromagnetic field distribution in the 1D layered quasiperiodic dispersive media. *Journal of Physics: Conference Series*. Institute of Physics Publishing, 2019. 10.1088/1742-6596/1348/1/012060.
145. S.N. Agafilushkina, O. Žukovskaja, S.A. Dyakov, K. Weber, V. Sivakov, J. Popp, et al. “Raman signal enhancement tunable by gold-covered porous silicon films with different morphology”. *Sensors (Switzerland)*. MDPI AG, 2020. 20(19): 1–11. 10.3390/s20195634.

146. P. Hildebrandt, M. Stockburger. "Surface-Enhanced Resonance Raman Spectroscopy of Rhodamine 6G Adsorbed on Colloidal Silver". *J Phys Chem.* 1984. 88(24): 5935–5944. 10.1021/j150668a038.
147. M. Majoube, M. Henry. "Fourier transform Raman and infrared and surface-enhanced Raman spectra for rhodamine 66". *Spectrochim Acta A.* 1991. 47(9–10): 1459–1466. 10.1016/0584-8539(91)80237-D.

Information about the supervisor

Asst.Prof. Marko Škrabić was born on July 4, 1986, in Split, Croatia. He graduated Physics from the Faculty of Science, University of Zagreb, in 2011, and completed his PhD in 2020, specializing in Atomic and Molecular Physics. Since 2014, he has been working at the Department of Physics and Biophysics at the School of Medicine, University of Zagreb, where he teaches six courses for first- and fourth-year students. In 2024, he was appointed to the position of Assistant Professor.

Asst.Prof. Marko Škrabić has authored or co-authored 16 scientific papers, 11 of which are in Q1 journals, with 117 citations and an h-index of 7, according to the Web of Science database. His scientific and professional interests include the application of vibrational spectroscopy to the study of biological materials and other systems, as well as semiconductor physics, with a focus on the preparation, characterization, and application of porous silicon.

He has collaborated with the Scientific Center of Excellence for Advanced Materials and Sensing Devices (CEMS) within the research unit for New Functional Materials and has participated in two Croatian Science Foundation projects, one bilateral project, and several national and international conferences. In 2015, as a member of the Department of Physics and Biophysics, he received the University of Zagreb's Award for Multimedia Content in E-courses, and in 2023, he was honored with the Dean's Award for exceptional contribution as a member of the Admissions Committee at the School of Medicine in Zagreb.

Asst.Prof. Škrabić is also a co-author of two manuals for medical students and an active member of three committees at the School of Medicine. He is married and the father of two daughters, and in his free time, he enjoys playing tennis.

Curriculum vitae

Maria Krajačić was born in September 1993, in Zagreb, Croatia. In 2011, she completed her music education at Music High School Karlovac, specializing in flute as her primary instrument and piano as an additional focus. In 2012, she graduated from Gymnasium Karlovac and began her studies at the Department of Physics, Faculty of Science, University of Zagreb.

In 2018, she was awarded the Rector's Award for her work "Individual and Collective Neural Dynamics." She also participated in "Brainhack Zagreb 2018," where data processing results obtained in collaboration with the Theoretical Cognitive Neuroscience Lab, Center for Memory and Brain, Boston University, were presented. She graduated in the same year and started working as a research and teaching assistant at the Department of Physics and Biophysics, School of Medicine, University of Zagreb. She has been involved in teaching first-year subjects for students of the School of Medicine (Physics and Biophysics) and the School of Dental Medicine (Physics) on both, Croatian and English. From 2018 to 2022, she was also involved in teaching fourth-year students of the School of Medicine in the subject Physics of Medical Diagnostics.

In 2019, she was part of the organization team for the Physics Summer School in Veli Lošinj. She started her doctoral studies in 2019 in Atomic, Molecular, and Optical Physics at Faculty of Science, University of Zagreb. Her scientific interests include porous silicon photonic structures and the use of photonics and vibrational spectroscopy in studying biological materials.

Maria was a member of the Center of Excellence for Advanced Materials and Sensors, New Functional Materials. She has authored or co-authored six scientific papers indexed in Current Content, and has participated in several symposiums and international conferences.

List of publications

1. **Krajačić, Maria**; Baran, Nikola; Tolić, Ana; Mikac, Lara; Ivanda, Mile; Gamulin, Ozren; Škrabić, Marko. Influence of One-Dimensional Photonic Crystal on Raman Signal Enhancement: A Detailed Experimental Study // *Applied Spectroscopy* (2024); 0(0). doi: 10.1177/00037028241258101
2. Škrabić, Marko; **Krajačić, Maria**; Gotić, Marijan; Baran, Nikola; Mikac, Lara; Jurkin, Tanja; Šegedin, Nikola; Ivanda, Mile; Gamulin, Ozren. Gold-coated porous silicon as a SERS substrate for near-infrared excitation: Off- and on-resonant conditions // *Applied surface science*, (2023), 644; 158820-x. doi: 10.1016/j.apsusc.2023.158820
3. Gamulin, Ozren; Oroz, Katarina; Ćoric, Luka; **Krajačić, Maria**; Škrabić, Marko; Dretar, Vilim; Štrbe, Sanja; Talapko, Jasminka; Juzbašić, Martina; Krezić, Ivan; et al. Fourier Transform Infrared Spectroscopy Reveals Molecular Changes in Blood Vessels of Rats Treated with Pentadecapeptide BPC 157 // *Biomedicines*, 10 (2022), 12; 3130, 11. doi: 10.3390/biomedicines10123130
4. Serec, Kristina; Šegedin, Nikola; **Krajačić, Maria**; Dolanski Babić, Sanja. Conformational transitions of double-stranded DNA in thin films // *Applied sciences* (Basel), 11 (2021), 5; 2360, 18. doi: 10.3390/app11052360
5. Gamulin, Ozren; Škrabić, Marko; Serec, Kristina; Par, Matej; Baković, Marija; **Krajačić, Maria**; Dolanski Babić, Sanja; Šegedin, Nikola; Osmani, Aziz; Vodanović, Marin. Possibility of human gender recognition using Raman spectra of teeth // *Molecules*, 26 (2021), 13; 3983, 16. doi: 10.3390/molecules26133983
6. Plazibat, Milvija; Katušić Bojanac, Ana; Himelreich Perić, Marta; Gamulin, Ozren; Rašić, Mario; Radonić, Vedran; Škrabić, Marko; **Krajačić, Maria**; Krasić, Jure; Sinčić, Nino et al. Embryo-derived teratoma in vitro biological system reveals antitumor and embryotoxic activity of valproate // *The FEBS journal*, 287 (2020), 21; 4783-4800. doi: 10.1111/febs.15248